Electrical Potential Changes and Acoustic Emissions Generated by Fracture and Fluid Flow during Experimental Triaxial Rock Deformation.

By

Oswald Conan Clint

A thesis submitted to the University of London
for the degree of Doctor of Philosophy.

Department of Geological Sciences
University College London

November 1999

Abstract

Natural electrical potential signals have been recorded from numerous seismically active areas around the world and therefore have been proposed as a potential earthquake prediction tool. The streaming potential is being used to locate sub-surface water reservoirs, to monitor steam fronts during enhanced oil recovery techniques, and to delineate the anisotropy of fractures in geothermal and oil reservoirs. The generating mechanism for these signals is still unclear although plausible theories include:

- Piezoelectric fields produced through stress changes on piezoelectric materials, such as quartz, found in many rocks.
- Electrokinetic currents induced through a pressure gradient and caused by electrical charge transport within a moving fluid.
- Less well-established theories for instance involving current carrying mobile O^- charges.

To investigate the relative significance of these mechanisms, I have measured the direct current electrical potential and acoustic emissions during constant strain rate rock deformation under simulated crustal conditions of pressure and pore fluid pressure. Some sixty-one experiments were done on rock samples of quartz rich Darley Dale and Bentheim sandstone and quartz free basalt from Iceland. A computer and servo-controlled conventional triaxial cell was used to deform dry, water-saturated and brine-saturated rock samples at confining pressures between 20 and 200MPa, pore fluid pressures between 10 and 50MPa and strain rates from 10^{-4} s^{-1} to 10^{-6} s^{-1}.

I identify the primary sources of the electrical potential signals as being generated by (i) piezoelectricity in dry sandstone experiments and (ii) electrokinetic effect in saturated basalt experiments. I show that electrical potential signals from the other proposed methods are not detectable above the background noise level. It can therefore be argued that the electrokinetic effect is the main electrical potential generating mechanism within the upper crust.

Both precursory and coseismic signals to dynamic rupture exist for pure water-saturated samples. However for brine saturated rock samples, the increased ionic mobility of the charges is suspected as the cause of absence of precursory signals. Increasing effective pressure decreases the pre-seismic electrical potential anomaly and is found to increase the co-seismic electrical signal. These results are explained in terms of the number of electrical and hydraulic pathways available for electrical current flow.

Variations of electrical potential difference and acoustic emission change markedly with strain between the compaction and dilatancy phases of rock deformation, and show dependence on both effective pressure and strain rate. Differences between streaming potential and hydraulic permeability during deformation are explained using a model of varying electrical and hydraulic tortuosity. Intergranular and intragranular cracking can be distinguished using the electrical potential generated from brine saturated rocks. The electrical and streaming potential signals occurring during deformation are found to reflect the accumulating and accelerating damage prior to fracture and the localisation of damage at dynamic fracture.

Table of Contents

List of Figures

List of Tables

Acknowledgements

This investigation has been completed in the Rock and Ice Physics Laboratory, University College London. In this achievement, special thanks must go to my parents who through their endless and unrewarding hard work have provided me with all the best opportunities. In completion of this piece of work, I would like to mention and thank a number of people. I would like to express my gratitude to my supervisors, firstly Dr Peter Sammonds for his constant intellectual support and the financial support, which allowed me to attend numerous conferences and build important new apparatus as, required. Secondly Dr Shingo Yoshida who I worked with for the first six months and together we learned quickly the experimental techniques required. My trips to the Earthquake Research Institute, University of Tokyo will be fondly remembered through his kind hospitality and endless enthusiasm. I also thank Professor Phil Meredith for his consistent support and invaluable advice throughout all stages of this work. I would also like to jointly thank them all for stimulating my interest in rock physics.

Experimental studies are by their very nature, difficult and frustrating. Though through the willingness, enthusiasm and high level of expertise offered to be by our experimental officers, Neil Hughes, John Bowles and Steve Boon, this was minimised. Special thanks to Neil Hughes for his ability to complete work quickly which played a strong part in this project being completed on time. I also thank these above named persons for making my time as part of the Rock and Ice Physics Group enjoyable, educational and memorable.

Never a dull moment was experienced at UCL and this was due to some great people namely Franck Belloni, John Bowles, Dr Steve Covey-Crump, Wilson Crichton, Dan Herron, Andy Howard, Neil Hughes, Neil McKearney, Dave Parkinson, Dr Rhodri Thomas, and Dr Dave Upton. Others such as Matt Balme, Emma Bowden, Dave Hodgson, Paula Martin, Nigel Moreland, Dr Anita Odedra, Matt Philips, Valentina Rocchi, Dr Ruth Sidall, Dr John Street, Pim, Zuwena have shared with me, some great times. I acknowledgement with gratitude the help of the administrative section (Ron, Celine and Lisa) of the Department of Geological Sciences.

I acknowledge support by the National Environment Research Council through the award of an NERC studentship, and additionally the British Council, UCL Graduate School and the Inoue Masuri Scholarship (UCL).

1. Introduction

1.1 Introduction

In recent years there has been increased interest in monitoring electrical potential signals in the earth's crust in such fields as earthquake prediction, geothermal engineering, hydrogeology and petroleum reservoir engineering. Electrical potential signals or self-potential signals of the order of mV are recorded from water level changes in lakes (Perrier et al., 1998), leaking water dams (Al-Saigh et al., 1994), under deforming glaciers (Blake and Clarke, 1999) and are associated with shallow earthquakes (Corwin and Morrison, 1977; Varotsos and Alexopoulos, 1984). The mechanism for these particular signals is still unclear and therefore laboratory experiments are important to help understand the underlying physical processes. These experiments involve applying a stress to both dry and fluid-saturated rock samples. The applied stress may be uniaxial or triaxial and is used to cause brittle deformation while the change in the electrical fields are monitored using near-field antennas or electrodes, thereby recreating similar conditions to those employed in field monitoring.

Field monitoring of naturally occurring electrical potential has shown anomalous variations preceding major seismic events (Derr, 1973; Tate and Daily, 1989; Varotsos and Lazaridou, 1991; Varotsos et al., 1993; Varotsos and Alexopoulos, 1991, 1984a, 1984b). The precursory signals, coined as seismo electric signals (SES) by Varotsos and Alexopoulos (1984a), are attributed to stress and strain changes leading up to major earthquakes. They are observed over areas of the order of $1km^2$. It is proposed by Varotsos and Alesopoulos (1984a), that these phenomenon offer a successful earthquake prediction tool. This is termed the VAN earthquake prediction technique. Difficulties arise in validating these predictions due to the sensitivity of the measurement position and artificial and atmospheric noise contamination (Michael, 1997). As an example, Morat and Le Mouel (1992) have shown that electrical potential signals larger than 50mV can arise in partially saturated rocks in response to variations of atmospheric pressure. The question of statistical significance i.e. whether the VAN does statistically better than randomly sampling the earthquake catalogue is contentious. The results from statistical tests by Aceves et al. (1994) show the VAN method to outperform random chance models, while Mulgaria and Gasperini (1992) show random chance models were better than the VAN method. Evidence has mounted that earthquakes are non-linear, chaotic, scale-invariant phenomena (Bak and Tang, 1989) and therefore prediction is not possible (Kagan, 1997, 1999). A review of earthquake prediction research over the last decade by Geller (1996) reveals that no single precursory signal exhibiting statistical significant correlation with individual earthquakes has been found, nor argues Geller (1997) is likely to be found. Main (1997) therefore suggests earthquake prediction in the future remains highly unlikely and earthquake mitigation measures could also be prone to failure.

Two major problems in understanding electrical field anomalies associated with earthquakes concern firstly the generation of the electrical field and secondly the propagation mode of the electromagnetic EM

waves. These are important questions, which need to be solved and current experimental work has a significant contribution to make. Several mechanisms have been proposed for the causes of SES, d.c. electrical potential changes and electric field variations. One of the most commonly used explanations of electrical potential precursors to earthquakes is the electrokinetic or streaming potentials produced by fluid flow in conductive regions connecting source regions to recording positions (Bernard, 1992; Morgan, 1990). Models based on EM waves propagation are also proposed (Ikeya et al., 1997) as are motion of charge dislocations across conductive regions (Mavromatou and Hadjicontic, 1994) and transfer of point defects (Freund et al., 1994). Laboratory studies have confirmed the existence of streaming potentials under simulated crustal conditions and have provided useful relationships between important physical properties such as pressure, permeability, fluid concentration, flow rate, pore matrix geometry and stress state (Jouniaux and Pozzi, 1995a, 1995b, Lorne et al., 1999a, 1999b, Revil et al., 1999a). Deformation of rocks without pore fluid shows that strain-induced piezoelectricity of some naturally occurring crystals can also create measurable electrical fields (e.g. Cress et al., 1987 and the research of the author in Yoshida et al., 1997). The effect of an applied stress on rock produces electromagnetic emissions from microscopic crack-tips (Yamada et al., 1989) and if the stress state is altered sufficiently it can produce mobile electronic charges capable of producing charged surfaces even within insulating materials (Freund et al., 1994). These studies enable numerical models to be developed, which can be compared to observations from field scale structures. One such application utilised experimentally determined electrokinetic parameters to determine macroscopic constitutive equations (Bernabe, 1998), which predict electrical potential anomalies in agreement with those recorded from geothermal environments (Ishido and Pritchett, 1999; Revil et al., 1999b).

It seems likely that in tectonically active areas naturally occurring electrical potential signals are detectable on the surface. This is demonstrated by the large volume of electrical and associated phenomena observed including earthquake lights, SES and anomalous animal behaviour (Mogi, 1985). The earth, however, is highly heterogeneous due to the diversity of rock types and fault patterns. As a consequence, the paths of fluid flow (Kosakowski and Berkowitz, 1999) and therefore electric currents also are heterogeneous (Brown, 1989; David, 1993). The heterogeneity is continually evolving due to crustal deformation. Stress changes will have a direct influence on crack properties such as crack aperture, fracture permeability and crack connectivity. Stress changes also cause new surfaces to be created which are assumed to emit EM waves and capable of increasing ionic charge transfer. It can therefore be seen that any of the above electrical potential generating mechanisms could operate during rock deformation and hence a fundamental understanding of these signals is essential.

1.2 Purpose and Scope of Investigation

Even though considerable research in the laboratory has been undertaken, as indicated above, a number of aspects of electrical potential phenomena are still not well understood. In particular how the electrical potential difference changes during a typical earthquake cycle. This is because the start of an earthquake

cycle cannot be easily identified in the field. In the laboratory a rock deformation experiment can exhibit the processes of compaction, dilatancy and shear fracture which are thought to be characteristic of crustal deformation during the earthquake cycle (Mogi, 1985). The permeability changes during these phases of deformation have been previously studied (Tuefel, 1987; Zhu and Wong, 1996; Keaney, 1998) and more recently the relationship between permeability and streaming potential (Jouniaux and Pozzi, 1995b; Lorne et al., 1999b) using pore fluids of varying concentration on sandstone. The electrical potential evolution during these this type of deformation has not been investigated to date or how strain rate, effective pressure and pore fluid salinity affect these types of signals. The change in acoustic emission activity during rock deformation has also been extensively investigated (Lockner et al., 1991; Aves, 1995; Read et al., 1995) and related to earthquake processes (Sammonds et al., 1992), however no studies measuring simultaneously acoustic emissions and electrical potential have been attempted. This will allow a more comprehensive understanding of how the micromechanical processes affect transport processes.

Numerous data is available in the literature concerning AE and streaming potentials on unconfined rocks in this study however triaxial deformation experiments have been conducted which more accurately describes crustal deformation processes. Specifically I have investigated the response of the electrical potential field of porous rocks undergoing deformation within the brittle regime using a computer and servo-controlled triaxial deformation apparatus. Using a novel recording system, the electrical potential is recorded continuously during deformation at four electrodes and acoustic emissions are recorded at eight transducers. This allows source location techniques to map out the spatial evolution of acoustic emissions and the electrical potential field. I have addressed the following questions. Do electrical potential differences on the surface of a stressed rock sample reflect destructive micro-tectonic processes like rupture and if so what are the signs of such a reaction in space and time? For a brittle shear rupture process, is there evidence of precursory, co-process electrical activity? For a brittle shear fault zone, how is its location on the surface related to the spatial distribution of electrical potential? The elucidation of damage mechanisms and resulting electrical potential signals requires the complementary input from microstructural analysis of deformed specimens. These results together provide a key understanding of how electrical potential signals are generated, what processes cause them to change and what factors control their generation. Each parameter investigated in

1.3 Thesis Description

This thesis is divided into eleven chapters, which describe in detail the collection of electrical potential data and acoustic emission data, the main results, their interpretation and conclusions drawn.

In chapter 2 a review of the theories of rock physics is given. The relatively new field of the application of electrical potential measurement techniques is reviewed in chapter 3. Also in this chapter an outline of the main theories of the generation of electrical potential signals such as piezoelectricity and electrokinetic phenomena is outlined. In chapter 4 a description of the experimental program and techniques used to collect, calibrate and process the large quantities of accurate experimental data is

given. The modifications made to the existing experimental apparatus to allow measurements to be made at elevated pressures are described. This is followed by the description of the design and implementation of a pore fluid separator which allowed corrosive fluids such as brine to be used as pore fluids in the rock deformation so better representing crustal conditions. A full understanding of the results using these fluids was only possible after the effects of deionised water alone was established. A comprehensive list of all the experiments discussed in this thesis is presented in Appendix C. The tables include all experimental conditions and lists of the figures in which the data is plotted and the experiment number is included in the appropriate figure caption. In chapters i.e. chapters 5, 6, 7, 8 and 9 I give the main experimental results obtained. Electrical potential difference and acoustic emissions generated during rock deformation are given while confining pressures, strain rates, pore fluid salinity, rock type and stages of deformation are changed.

In chapter 10 I discuss the results from the previous chapters. This involves applying existing theories, making comparisons with previous research and developing conceptual models, which describe how electrical potential signals are generated under a wide range of geological conditions. Applications of electrical potential methods to exploration, earthquake forecasting and current day statistical physics earth models are proposed.

2. The Development of Rock Physics as an Investigative Tool

2.1 Introduction

Changes in the stress-strain field are responsible for deformation and the style of faulting found within tectonic regions and also in laboratory experiments. The analysis of stress and strain is imperative to allow interpretation of rock physics properties within the framework of rock mechanics. For example, tectonic stresses, responsible for the state of stress in the upper lithosphere can be determined indirectly from earthquake focal mechanism studies (Scholz, 1996) and directly from stress-induced borehole breakouts (Edwards, 1998). Hydraulic fracturing of boreholes and stress-relief measurement techniques applied to rock core are also used to provide in-situ stress measurements. Directions of fault slip or volcanic alignment can be used as reliable direction indicators. Some of these techniques have been used to produce maps of global stress patterns (Zoback et al., 1989).

It is however difficult to make these in situ measurements because the necessary drilling and manually pumping fluids into rock involved in these measurements alters the actual rock deformation stress-strain paths. It is therefore more appropriate to indirectly measure physical properties of the rocks, which reveal details of the microstructural processes. These properties include electrical resistivity studies, monitoring acoustic emissions (AE), elastic wave velocity analyses and permeability and pore fluid volumometry investigations.

For example in laboratory experiments the acoustic emission results from Lockner et al. (1992) clearly show pre-nucleation activity, fault nucleation and fault propagation. Using statistical b-values determined from the number of AE events, earthquake activity can be correlated with laboratory behaviour (Sammonds et al., 1992) while information on the stress levels can be obtained from the fractal dimension, D, of the size distribution of AE events (Meredith et al., 1990). P and S wave velocities are related to the stress induced damage (Sammonds et al., 1989) and crack orientations during deformation may also be used to distinguish between micro-cracking and crystal plasticity (Jones, 1989). The importance of these velocity changes to stress is suggested as a possible *in situ* monitor of differential stress by utilising shear wave splitting (Zatsepin and Crampin, 1997; Crampin and Zatsepin, 1997). Permeability measurements also reveal information on pore/crack shapes and the tortuous nature of the pore network, for which crack aperture is found to be the controlling factor (Walsh, 1981). Since permeability is dependent on confining and pore pressures (David and Darot, 1989, Jones et al., 1998) it clearly responds to the microscopic porosity components of the rock, a characteristic critical for recovery rates of oil and water and is essential for radioactive storage capabilities. Pore volumometry allows external measurement of the total specimen volume change by volumetric displacement of fluid and can be used at elevated effective pressures under drained and undrained conditions. The volume changes during compaction and dilatancy are attributed to micro-structural changes and are directly related to the permeability (Fischer and Paterson, 1992; Keaney, 1998).

Electrical resistivity measurements are also sensitive to changes in the pore network during deformation (Jouniaux et al., 1992) and complex measurements can reveal the microscopic surface areas of the pore network (Ruffet et al., 1991) and the level of induced damage (Glover et al., 1997). These complex measurements have also been used to produce anisotropic crack damage parameters, which accurately describe the stress/strain fields in rocks (Glover et al., 1996). The change of electrical resistivity with compaction and dilatancy has been suggested as a method of monitoring dilatancy in the source region of an impending earthquake (Lockner and Byerlee, 1986). Other mechanisms of electrical conductivity change during stress variations and fracture are however possible such as carbon enhancing electrical pathways (Roberts et al., 1999).

These measurements are all based on the fact that changes occur in the pore structure of saturated rock. Changes during stress cycles produce a number of effects, which are related and can be measured in a variety of ways. This chapter will describe in some detail the pore structure of saturated rocks, then detail the theories of brittle deformation, outlining the information obtainable through rock physics measurements from saturated rocks under stress. This will provide a solid knowledge base for the analysis of electrical potential signal and acoustic emission data during simulated crustal deformation.

2.2 Crustal Conditions

The complex evolution and dynamics of the upper crust leads to it being a strongly heterogeneous body. Indirect measurements through seismological forward modelling methods indicate an average thickness of 35km for the earth's continental crust with an average P-wave velocity of 6.5kms^{-1}. The thickness however increases to around 80km beneath young fold mountain belts and thins to approximately 20km beneath some tectonically active areas. This velocity varies with depth as shown in Figure 2-1. The increase with depth is due to the increase in lithostatic overburden pressure. This is the vertical component of stress acting on a buried rock mass. It is generated by the overburden of rock but can be modified by up to 50% near the earth surface due to residual stresses (Price, 1975). Overburden pressure, σ_l, is calculated by

$$\sigma_l = \rho . g . h \qquad (2\text{-}1)$$

where ρ is rock density, g is gravitational acceleration and h is depth.

Assuming that crustal rocks have an average density of 2500 kg/m^3, this equation gives the geobaric gradient to be 25MPa/km and can vary depending on tectonic setting due to pressure and temperature effects on rock density (Fowler, 1990). This value will be used in any extrapolation of results to depth. As rocks are compacted through increasing overburden pressure the rock matrix is deformed. This increase of pressure with depth causes an increase in the bulk modulus, rigidity and density of rocks. The effect is especially important within the uppermost 5km of the crust as existing pores, fractures and joints are closed. At deeper levels thermal expansion methods tend to counteract these effects leading to smaller effects. The increasing vertical stress also increases the pore fluid pressure within the rock

matrix. The highly pressurised pore fluid reduces the lithostatic stress allowing thrust faulting to occur (Hubbert and Rubey, 1959). The influence of high pressure, high temperature fluids has important effects on the elastic properties of rocks including mineral reactions, phase transitions and changes of rock microstructure (Lebedev et al., 1996).

Estimates of the temperature gradient vary widely from 5°C/km in a subducting slab to >100°C/km in volcanic areas. Borehole measurements provide an estimate of the temperature gradient of 25°C Km^{-1} (Bott, 1982). At the Moho and below, this gradient decreases rapidly due to the radioactive decay of K^{40}, U^{235} and Th^{232} isotopes, which provide large heat sources.

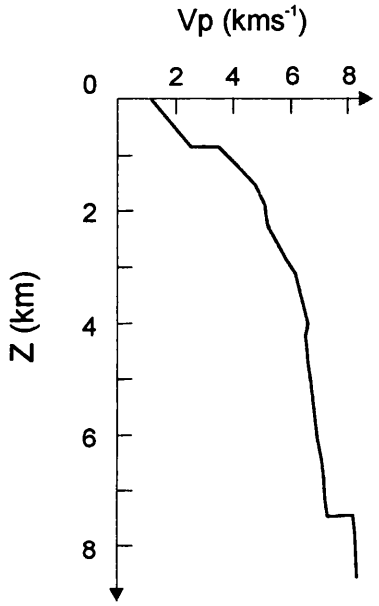

Figure 2-1 Variation of P-wave velocity (Vp) with crustal depth (z) (Taken from Fowler 1990).

Differential Stress and Pore Pressure

Stress maps are determined from crustal stress orientations produced using borehole measurements and earthquake focal mechanisms (Zoback et al., 1989). These maps indicate the presence of relatively small differential stresses. An average value of 25MPa was determined by Ambrasey (1970) which is an order of magnitude smaller than dry compressive strengths (Paterson, 1978). This can be explained using highly pressurised pore fluids, which reduce the effective confining pressure acting on any element of the rock. Evidence supports the presence of fluids down to 12km (Extracted from, The Role of Fluids in Crustal Processes, 1990) and large volumes may be present at shallow depths (Nur and Walder, 1990). There is also evidence for suprahydrostatic pore pressures formed through sealed fault compartments or impermeable rock formations (Nur and Walder, 1990) and also in compressional tectonic regions (Price and Cosgrove, 1990) which would allow fracture to occur at low values of differential stress due to rock

weakening. The pore pressure influences are complicated by the effects of low permeability and fluid chemistry. Brittle deformation processes are enhanced by hydrating and weakening of the Si-O-Si bonds leading to more rapid crack growth (Atkinson and Meredith, 1987).

Electrical Conductivity

The electrical conductivity of the crust has been measured using electromagnetic field techniques. It is routinely split into three regions, (a) a high conductivity surface layer associated with the saturated sediments, (b) a lower conductivity layer corresponding to the metamorphic basement and (c) a deeper high conductivity layer. (Figure 2-3). Field values obtained between 10^{-4} Sm^{-1} to 10^{-2} Sm^{-1} do not correspond with laboratory values of 10^{-6} Sm^{-1} obtained by Brace (1971). Shankland and Ander (1983) suggest that the processes of crack closure controlling conductivity under drained conditions is not necessarily the mechanism operating in the crust. If the lower crust is envisaged as an overlap of saturated highly conductive lamellae (observed from seismic interpretations of the lower crust, Reston, 1987) then model results compare quantitatively with laboratory results (Merzer and Klemperer, 1992). Interpretations other than saline fluids, to explain the high conductivity lower crust include one suggesting carbon enhanced conduction pathways created during compaction (Glover and Vine, 1992), a result confirmed by experiments on non-weathered crustal rocks recovered from the KTB boreholes (Duba et al., 1994; Shankland et al., 1996). In contrast results from experiments on granite and hornblende schist by Olhoeft (1981) suggested low volumes of conductive fluids or massive volumes of good conducting materials, such as graphite, are responsible.

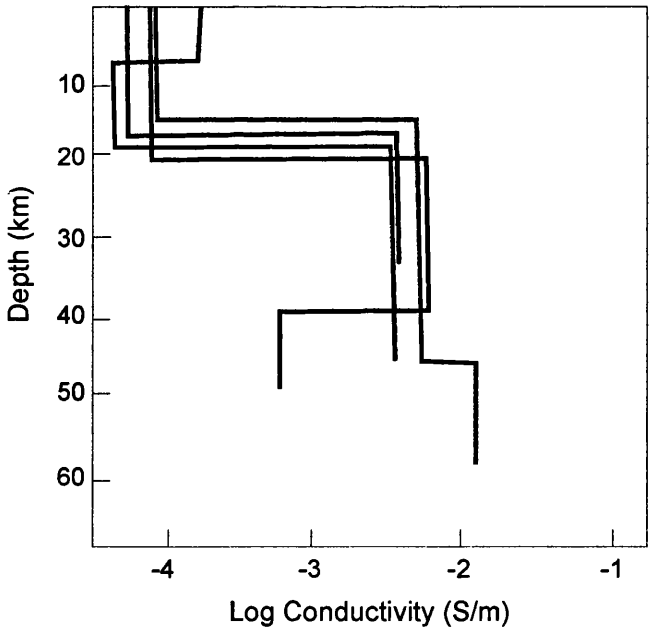

Figure 2-3 Variation of electrical conductivity with depth of the continental crust showing three distinct areas of electrical structure (from Shankland and Ander, 1983).

Strain Rates

Estimates of the strain rates in accretionary wedge-type thrust systems are of the order 10^{-15} s^{-1} (Bucher et al., 1996) and 10^{-14} s^{-1} in foreland fold and-thrust type orogenic systems (Kligfield et al., 1986). Slip rates on the San Andreas fault within the Pajaro network measured between 1990 and 1996 are now 9-10 mm/a compared to about 7mm/a ($\approx 10^{-14}$ s^{-1}) before the Loma Prieta earthquake suggesting continual stress loading on this section of the fault. These values are deduced from considerations of plate tectonic motions and geodetically observed recent crustal movements and are probably related to mantle displacement rates. Since these processes may take thousands of years to many million years to occur, the strain rate in different areas may alter significantly. Lower strain rates of 10^{-15} s^{-1} and 10^{-16} s^{-1} are required to model the deformation history of metamorphic rocks extracted from the Ocean Drilling Program (Platt et al., 1998).

Strain rates down to 10^{-8} s^{-1} are obtainable within the laboratory but to understand geological processes extrapolation to realistic strain rates (10^{-14} s^{-1}), based on theoretical models, must be applied (Rutter, 1995, Covey-Crump, 1998). Heard (1963) using this principle showed that the strength of marble at 25°C would decrease by 20% using a linear extrapolation to a strain rate of 10^{-14} s^{-1}. Strain rates between 1.5 x 10^{-4} and 1.5 x 10^{-6} s^{-1} were used in this investigation and hence a strain rate effect may be expected. The effects of strain rate on frictional slip and the shear rupture nucleation zone show that by increasing strain rate the frictional strength increases logarithmically and the nucleation zone size decreases (Kato et al., 1992).

2.3 Deformation of the Crust

Rocks behave elastically (to a first approximation) at low temperature and pressure and for high strain rate experiments show linearity between stress and strain. Rheological equations including the physical properties discussed above allow the description of deformation and flow of a material and is reviewed by Ranalli (1995). This is achieved by relating kinematic and dynamic quantities of the body. The basic kinematic property is strain rate and stress is the corresponding dynamic quantity. These quantities and material coefficients can be grouped in constitutive equations of the form

$$R(\varepsilon, \dot{\varepsilon}, \sigma, \dot{\sigma}, ..., \{M\}) = 0 \qquad (2\text{-}2)$$

where ε is strain, $\dot{\varepsilon}$ is strain rate (first order in this case but can be higher), σ is stress, $\dot{\sigma}$ stress rate, M denotes the material coefficients and R is the rheological function.

2.3.1 Statistical Physics Approaches

Early views of the crust were of a homogeneous elastic-brittle medium (Reid, 1910) in which strain accumulations in fault zones were caused by tectonic movements. When the local shear stresses exceed

the local strength of the particular fault, rupture is initiated and propagates catastopically resulting in an earthquake. However it has come to be established that the crust does not behave in this time-predictable manner (Main, 1996).

Certain geometrical properties of earthquake populations (except characteristic earthquakes), for instance fault lengths, together with other examples in earth sciences have been observed to be scale invariant (see review by Turcotte 1992). This means the geometrical characteristics are independent of the measuring scale hence the ubiquity of geological hammers in geological photographs. Sammis et al. (1986) have suggested that tectonic processes have caused a fragmentation of the lithosphere into a fractal distribution of block sizes over a wide range of scales. This fragmentation is attributed to comminution of the lithosphere due to the geometrical incompatibility of plate evolution. This hypothesis has important implications for the frequency-size distributions of faults and earthquakes.

A scale-invariant object can be described by a fractal dimension, which quantifies the static geometry of an object. An important (defining) property of a fractal is self-similarity, which refers to an infinite nesting of features and structures on all scales. A distribution of features with a characteristic scale invariant length can only, be described by a power law (Mandelbrot, 1982). This takes the form

$$N(l) = Cl^{D} \tag{2-3}$$

where N is the number of fractures or cracks in this scenario within a discrete length interval $l - \delta l/2 \leq l < l + \delta l/2$. C is a constant and the power law exponent D is known as the fractal dimension of the system (Mandelbrot, 1982).

Seismological investigations utilise a fractal interpretation i.e. the relationship between the number of earthquakes and their magnitude is given as

$$\log n = a - bm \tag{2-4}$$

where N is the number of earthquakes in the magnitude range $m - \delta m/2 \leq m < m + \delta m/2$ and a, b are empirical constants . This relationship results from a constant stress drop over a power law distribution of fault lengths and is known as the Gutenberg-Richter relation. Main et al. (1990) shows that the seismological b value is related to the power law exponent D by

$$D = 3\,b/c \tag{2-5}$$

It has been found that for intermediate earthquakes that $c = 3/2$ (Kanamori and Anderson, 1975) therefore $D = 2b$ while some experimental studies suggest a value of c = 3 leading to b = D (Main et al., 1989). This result suggests that a power law distribution of seismic event magnitudes imply a power-law distribution of crack or fault sizes.

These results have allowed theoretical models to be constructed between the b-value, stress intensity factor and stress and crack length (Meredith et al., 1990; Main et al., 1990). Agreement between the models, earthquake statistics and experimental results was reached by relating the b-value derived from acoustic emissions measured in the laboratory (Sammonds et al., 1992).

Fault populations can also be described as power-law size distributions over several orders of magnitude (Scholz et al., 1993, Schlische et al., 1996) although exponential distributions have been observed (Cowie et al., 1993). Experimental evidence supports both exponential and power law distributions and suggests this may be related to different strain regimes (Spyropoulos et al., 1999). It has also been suggested that the total offset on a fault is related to its length in a fractal manner, although this may be more typical of the static fault dimensions and not of active fault growth (Cartwright et al., 1996; Moreland and Roberts, 1999). Finally a further observation of this scale invariance is depicted in Figure 2-4 where a linear relationship is found between stress drop associated with earthquakes and source dimension on a log-log plot (Abercrombie, 1995).

Self-organised Criticality

The concept of self-organised criticality was introduced by Bak et al. (1988) and is defined as a natural system in a marginally stable state which, when perturbed from that state, will evolve back to the state of marginal stability. Input to the system is continuous, but the loss occurs in a discrete set of events that satisfy fractal frequency-size statistics. The scaling properties of such a system are required to be relatively insensitive to the details of the dynamics. These scaling properties show remarkable similarities to populations observed at the critical points in statistical physics, i.e., the Curie temperature of magnetic materials. Seismicity therefore appears to be an example of self-organised criticality (Bak and Tang, 1989) and as a result Scholz (1991) argues that the lithosphere is everywhere in a state of self-organised criticality and on the brink of failure. Barriere and Turcotte (1991, 1994) have presented a cellular-automata model for distributed seismicity with a fractal distribution of box sizes; model runs were shown to generate foreshocks, aftershocks and satisfy Gutenberg-Richter statistics.

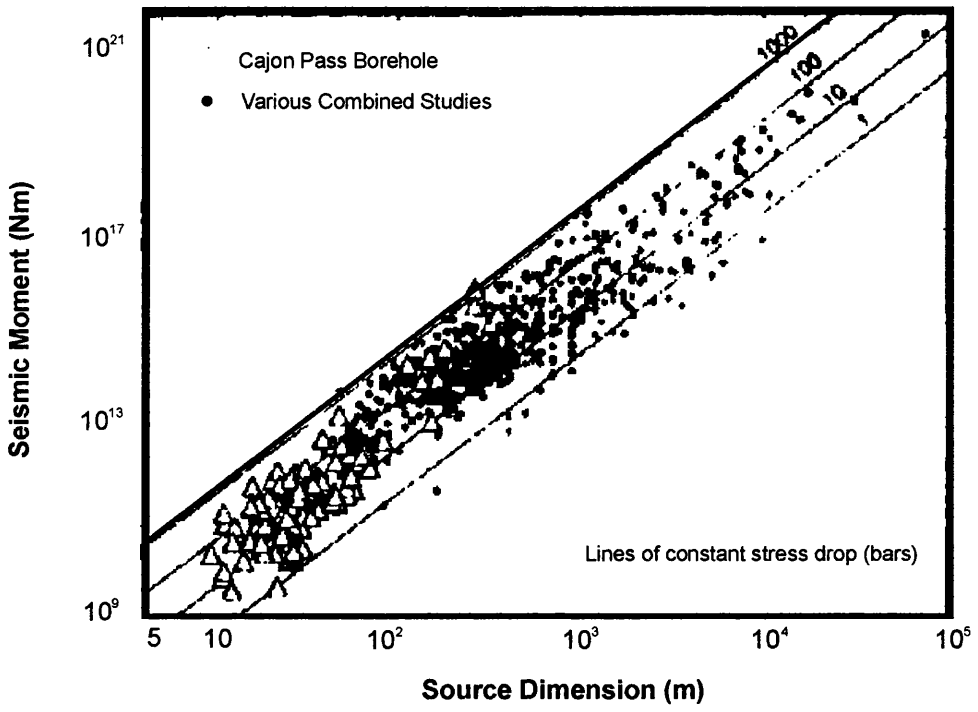

Figure 2-4 Seismic moment data taken from boreholes and earthquakes plotted as a function of the source dimension. The straight lines are predicted scaling laws at different stress drops (in bars) from dislocation model of the seismic source (Taken from Abercrombie, 1995).

There have been questions however about applicability of self-organised criticality to some systems (Sykes et al., 1999). For instance, the probability of occurrence of the largest earthquakes is reduced in comparison with an extrapolation of the Gutenberg-Richter trends and Hatton et al. (1994) argue against the range of applicability of the total offset to fault length relationship. Such systems are more accurately described as 'subcritical' (Main, 1996) and are sensitive to external conditions.

Measurements of fractal dimension, b-value, correlation length and cellular automaton approaches determined from the process of fault formation, nucleation and propagation can be explained in the framework of critical point phenomena. An analogue model by Cowie et al. (1993) successfully show the progression from fault nucleation to a subcritical growth of earthquakes during fault growth. This organised pattern of faulting produced from the model rests only on the statistical physics of elastic-brittle interactions in heterogeneous granular materials.

In the laboratory, crack coalescence and interaction to form a macroscopic fault is associated with a decreasing b-value (Sammonds et al., 1992) and the effects are influenced by stress intensity, a measure of the stresses at crack tips, and secondly by the presence of fluids (Meredith et al., 1990). Fault nucleation therefore, cannot be classed as a process of self-organised criticality because a non-changing b-value is expected, implying a subcritical process. Interestingly the b-value does become roughly constant after fracture during frictional sliding (Sammonds and Ohnaka, 1998).

Earthquake Prediction

The ultimate aim of earthquake prediction is to predict the exact location, size and time of a major slip event from precursory events. If earthquake generating processes can be described as self-organising critical systems (SOC) then they are in a state of marginal stability and insensitive to the dynamics of the system. This SOC model suggests that any small earthquake has some probability of cascading into a larger earthquake and therefore both long-term and short-term prediction would be unreliable. The poor reliability of precursors is reviewed by (Geller, 1996). Often they do not hold against rigorous statistical validation (Michael, 1997) and can usually be explained by random noise or by chance coincidence. The failure of proposed predictions is also due to the immense complexity of earthquake rupture phenomena and lack of rigor in the empirical analysis of seismicity (Kagan, 1996, 1999). The difficulty also increases because patterns vary greatly from one earthquake to the next, anomalies are measurable at only a few points over the entire source region and finally no quantitative mechanism relating the precursory activity to the forthcoming earthquake is available (Turcotte, 1991). I believe the development of more rigorous procedures for testing proposed patterns of earthquake occurrence and comparing them to predictions of theoretical and computer modelling are required. Moreover these can only be undertaken in the framework of a thorough understanding of the physical basis for the manifestation of precursors.

The dilatancy-diffusion hypothesis was the first such mechanism to attempt to explain velocity changes in a earthquake preparation zone (Nur, 1972; Scholz, Sykes, and Aggarwal, 1973) but no natural example has been found to confirm the theory (Geller, 1996). Varotsos (1996) claims to have predicted successfully earthquakes in Greece using geoelectrical measurements but tests show lack of statistical significance (Kagan and Jackson, 1996) and contamination through noise Gruszow et al. (1996). Cuomo et al. (1998) also point out that geoelectrical time series can show fingerprints of self-organised systems but earthquake prediction using one such electrical precursor is routinely difficult. In conclusion recent mechanical models investigating the complex dynamics of earthquake populations show that theoretically the prediction of magnitude, time and position of earthquakes under certain conditions cannot be ruled out (Shaw, 1992).

2.4 The Mechanics of Rock Deformation

2.4.1 Porous Media

Porosity

The porosity (ϕ) of a rock sample is a controlling factor in transport (David, 1993), mechanical (Dunn et al, 1973) and acoustical properties (Ayling et al., 1995) of rocks and is defined as the pore volume per unit rock volume. The initial value is dependent on grain size and distribution, initial deposition conditions, secondary porosity alteration methods and of course on the rock type.

Specific Surface Area

The specific surface area (S_c) of a porous medium is defined as the pore surface area in a sample divided by the total volume of the sample. It depends on the grain packing type and is found to be equal to $S = 3(1-\phi)/R$ for 'spherical' grains where R is the grain radius. The surface area can be correlated to permeability (Walsh and Brace, 1984) which stems from the fact that it is inversely proportional to capillary size.

Surface Roughness

In reality, rock surfaces and associated fractures are always rough and exhibit scale invariance (Brown and Scholz, 1985a). This roughness affects the properties of the rock. For example roughness affects the hydraulic properties of the flow system by increasing frictional resistance to flow and by channelling of flow along fracture surfaces. It also affects the transport properties of a medium by changing the dimension of the flow paths that particles take (Glover et al., 1998), as well as by increasing the total area available on the fracture surface for chemical reactions. In addition to the hydraulic properties, roughness, including asperity distributions, affects the shear strength and the compressibility of rocks.
The roughness of pore surfaces of sandstones on microscopic levels has been shown to be fractal over four orders of magnitude (Katz and Thompson, 1985) and the fractal relationships allow accurate predictions of electrical conductivity (Katz and Tugman, 1988). The authors suggest this self-similarity is produced through steady state crystal growth during rock formation. However the inclusion of a fractal description of surfaces in models of electrical conductivity is not always appropriate (Ruffet et al., 1991).

Surface Adsorption

The interaction between a liquid solution and a solid surface is modelled as an adsorption of ions or atoms onto the solid surface (Revil and Glover, 1997). In shaly sandstones, the exchangeable cations in the clay fraction become solvated when they are immersed in water and form a diffuse charge layer at the pore-grain interface. For sandstone, the free ions in the fluid are attracted to the solid surface by electrostatic forces. The result is an electrical double layer (EDL) which is the physical basis behind electrokinetic phenomena (EDL and electrokinetic phenomena are discussed in Chapter 3) and electrical currents in rocks. Surface adsorption has also been shown to have an effect on effective elastic modulii of porous solids (Schmidt, 1988).

2.4.2 Stresses

Two different types of forces act upon a continuous medium: body forces which are due to the acceleration due to gravity and surface forces acting on a particular surface area. The limiting value of the ratio $\partial F/\partial A$ as ∂A approaches zero is called the stress vector at that point where F is an applied force and A is the area acted on by that force

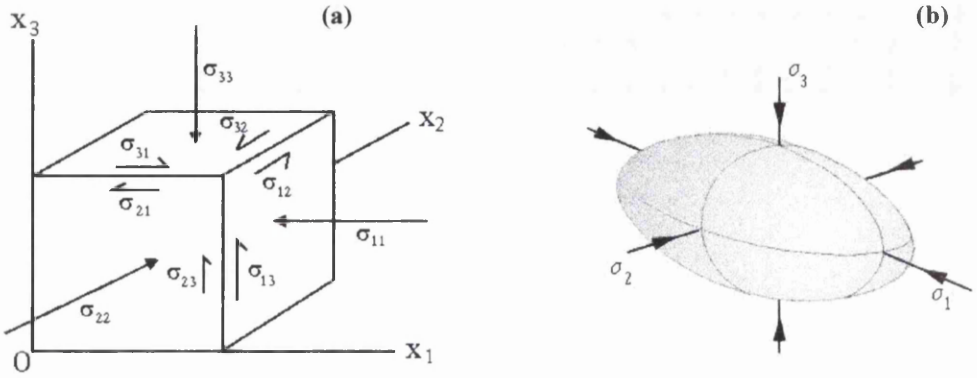

Figure 2-5 Schematic diagrams showing (a) nine stress components required to describe stress at a point and (b) the stress ellipsoid produced if all possible stresses through a point are plotted.

Stress at a point is a second-order tensor, which means that it takes (in 3D space) nine components to describe, or six independent components for an isotropic homogeneous body.

The nine components required to identify the stress (σ_{ij}) at a point are represented in Figure 2-5a and expressed in matrix form in equation 2-6.

$$\sigma_{ij} = \begin{bmatrix} \sigma_{11} & \sigma_{12} & \sigma_{13} \\ \sigma_{21} & \sigma_{22} & \sigma_{23} \\ \sigma_{31} & \sigma_{32} & \sigma_{33} \end{bmatrix} \tag{2-6}$$

where σ_{23} represents the stress component acting on the face normal to X_2 in the direction of X_3. If all possible stresses through a point are plotted then an ellipsoid is obtained known as the stress ellipsoid (Figure 2-5b, N.B. σ_{xx} is represented as σ_x).

2.4.2 Isotropic, Deviatoric and Principal Stresses

The stress tensor can be separated into an isotropic and deviatoric component (see Ranalli, 1995). The isotropic part is defined as

$$\sigma_{ij}^{0} = \tfrac{1}{3}\sigma_{kk}\delta_{ij} \tag{2-7}$$

where σ_{kk} is the sum of the on-diagonal components of the stress tensor and δ_{ij} is the identity matrix which is equal to one when $i = j$ and zero when $i \neq j$. The deviatoric stress is defined by

$$\sigma_{ij}^{'} = \sigma_{ij} - \sigma_{ij}^{0} \tag{2-8}$$

which determines the resultant stress when the isotropic part has been removed and is calculated using the off-diagonal components of the stress tensor.

The stress tensor can therefore be expressed as

$$\sigma_{ij} = \tfrac{1}{3}\sigma_{kk}\delta_{ij} + \sigma'_{ij} \tag{2-9}$$

The principal stresses are an important representation of the stress state in structural geology and rock mechanics. When the principal stress axes are known, they allow a stress co-ordinate frame to be adopted. The principal axes are those where the only non-zero components of the stress tensor are the on-diagonal components and represent axes that define planes of no shear stress normal to them. The principal stresses are the values of the on-diagonal components.

To determine the principal stress axes a suitable transformation must be found which reduces the stress tensor to a diagonal matrix, i.e.,

$$\sigma_{ij} = \begin{Bmatrix} \sigma_{11} & \sigma_{12} & \sigma_{13} \\ \sigma_{21} & \sigma_{22} & \sigma_{23} \\ \sigma_{31} & \sigma_{32} & \sigma_{33} \end{Bmatrix} T' = \begin{Bmatrix} \sigma_{11}^P & 0 & 0 \\ 0 & \sigma_{22}^P & 0 \\ 0 & & \sigma_{33}^P \end{Bmatrix} \tag{2-10}$$

where σ_{ij}^P is the principal stress. The principal stresses are denoted σ_1, σ_2 and σ_3 and the convention is used where compression is taken to be positive.

2.4.3 Compressive Failure

The stress state in conventional triaxial deformation experiments (where $\sigma_1 > \sigma_2 = \sigma_3$) is represented in Figure 2-8. The compressive stress σ_1 causes failure on one or two planes lying at an angle to σ_1 and the normal and shear stresses acting on these surfaces are given by

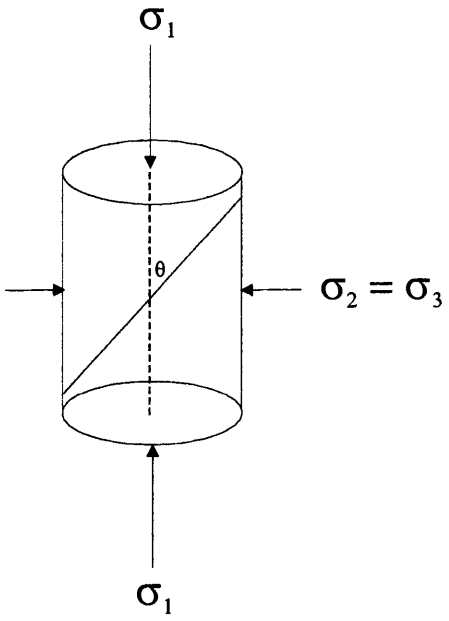

Figure 2-8 Principle of a triaxial test.

$$\sigma_N = \frac{\sigma_1 + \sigma_3}{2} + \frac{\sigma_1 - \sigma_3}{2}\cos 2\theta \qquad (2\text{-}11)$$

$$\sigma_S = \tau_s = \frac{\sigma_1 - \sigma_3}{2}\sin 2\theta \qquad (2\text{-}12)$$

The quantity $(\sigma_1 + \sigma_3)/2$ is the mean stress, $(\sigma_1 - \sigma_3)/2$ is the deviatoric stress, i.e., the non-hydrostatic component, $(\sigma_1 - \sigma_3)$ is the differential stress and θ is the angle between the normal to the inclined plane and the principal axial stress direction.

2.4.5 Fracture Criteria

The development of theoretical models used to describe observed rock deformation characteristics is traced in this section. The early empirical models are described followed by the micromechanical models dealing with single crack growth and finally the 'Damage Mechanics' theories, which attempt to profile the complete process of deformation from crack growth to coalescence and fault formation. Statistical developments in these models are also described. A review of the first two types of models is given by Jaeger and Cook, 1979).

Empirical Theories

In order to describe the strength of rock under stress conditions a fracture criterion must be developed i.e. a relationship such that

$$\sigma_1 = f(\sigma_2, \sigma_3) \qquad (2\text{-}13)$$

If normal stress (equation 2-11) is plotted as a function of shear stress (equation 2-12) a circle can be constructed known as the Mohr circle (Figure 2-10). For a given stress state, we can generate a Mohr circle that represents the normal and shear stress components on planes of all possible orientations through a point.

If a range of differential stresses is conducted, a linear envelope can be fitted to the constructed Mohr circles of the form

$$\tau_s = S_c + \mu' \sigma \tag{2-14}$$

where S_c is the cohesive strength (1-10MPa for most rocks) and μ' is the coefficient of internal friction. This equation, known as the Coulomb-Navier fracture criterion can be plotted in shear/normal stress space as two straight lines intersecting the shear stress axis at ±S with slopes equal to tan ϕ_f. The value ϕ_f is the angle of friction and is equal to $\pi/2 - 2\theta$, therefore predicting two different orientated planes of possible failure. The relationship of all these parameters are shown in Figure 2-10. The maximum shear stress in a rock is generally observed at an angle of θ = 30 - 60° and this angle is related to the coefficient of friction by

$$tan(2\theta) = \frac{1}{\mu'} \tag{2-15}$$

The Coulomb criterion does not incorporate any understanding of the internal microscopic processes involved in rock fracture and represents a purely empirical model.

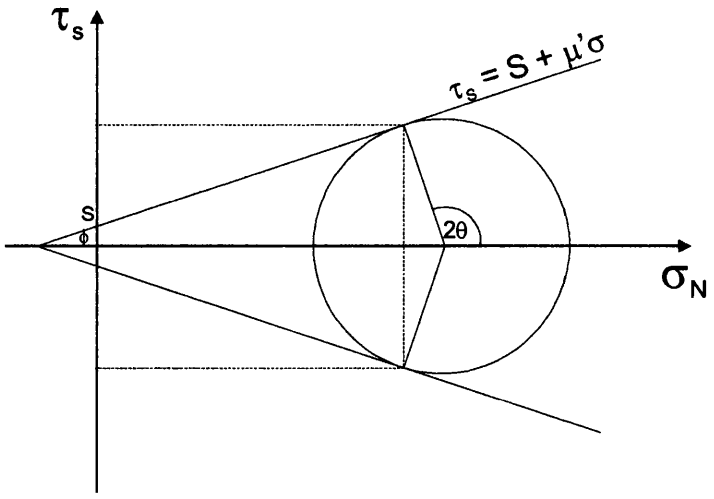

Figure 2-10 Mohr circle and the Coulomb-Navier criterion for shear fracture.

Griffith Single Crack Analysis

By explaining the weakness of glasses as being a result of the existence of crack and flaws, Griffith (1924) proposed a fracture criterion, which incorporated physical processes of crack initiation in a biaxial stress field. Considering the tangential stresses on elliptical cracks in two-dimensions he proposed that failure takes place when the maximum tensile stress in the crack of most favourable orientation reaches a critical value. Murrell (1963) provided an empirical extension of the two-dimensional Griffith theory to the three-dimensional case. It was further modified by McLintock and Walsh (1962) and Murrell (1964) who considered the effect of crack closure under sufficiently high compressive stresses and the frictional interaction between closed crack faces. This treatment showed agreement with the Coulomb criterion when cracks are closed and also provided a physical meaning to the coefficient of friction where it is now the coefficient of sliding friction of the crack surfaces.

Murrell and Digby (1970) provided a three-dimensional treatment for closed cracks with internal pore pressure by considering the general case of an ellipsoidal crack in an arbitrary triaxial stress field. This yields a crack initiation curve of the form,

$$(\sigma_1 - \sigma_3)^2 - 2(2-\nu)T_0(\sigma_1+\sigma_3) = U(4-U)(2-U)_2T_0^2 \qquad (2\text{-}16)$$

$$\text{for } \sigma_1 > -A^*\sigma_3 \quad \text{(or a compressive system)}$$

where A^* is a constant of order 1 when ν=0.3, and U is the Poisson's ratio. An important conclusion from this treatment is the independence of the failure criterion on intermediate stress.

This allows for a more accurate description of fracture as the Griffith criterion only deals with two-dimensional open cracks and neglects crack face friction. From this criterion the ratio of uniaxial compressive strength to uniaxial tensile strength is equal to 12 which is more realistic and the coefficient of internal friction becomes the physically realistic coefficient of sliding friction on crack surfaces.

These modified Griffith criteria, to describe rock failure are significant advances and actually rely on the physical processes involved though they are still unable to account for:

- Single crack models.
- Effects of plasticity.
- The effect of heterogeneity, anisotropy and specimen size, which also causes growth of less favourable, orientated cracks.
- But most importantly, they are fracture initiation criteria and can't describe crack interaction and linkage.

Damage Mechanics Approaches

The above criteria only deal with crack initiation and therefore cannot represent crack extension and crack interaction. Damage mechanics models include similar fundamental theories of Griffith theory such that they consider isolated cracks in an otherwise homogeneous medium, which initiate at the most favourable

positions. Cracks then occur at a high angle to the initial crack creating 'wing cracks'. These cracks grow when a stress intensity factor K becomes greater than the fracture toughness K_c of the surrounding medium (Digby and Murrell, 1975; Horrii and Nemat-Nasser, 1985).

The stress intensity factor K is derived from considering a stress field surrounding a crack tip isolated within a linear elastic medium. Using polar co-ordinates r, Θ the stress (σ) perpendicular to the crack is,

$$\sigma = K/(2\pi r)^{\frac{1}{2}} f(\Theta) \tag{2-17}$$

where $f(\Theta)$ is a known function of the angle Θ. Therefore the stress field surrounding a crack tip can be fully described if the value of K is known.

The model of Horrii and Nemat-Nasser (1985) and Costin (1985) who follows the same analytical approach incorporates all the observed features of brittle failure together with the effects of confining pressure and temperature. Crack interaction and faulting is understood in these models as the effects of more distributed cracking which amplifies the stress intensity factor (K) allowing crack growth under lower differential stresses. This theory can therefore explain the strain softening period post peak stress.

Sammis and Ashby (1986) use fracture mechanics and beam theory approaches to describe crack growth and crack interaction, extending it to consider cracks interacting with a free surface of a sample. An important feature of the model is the consideration of crack growth from three-dimensional pores which allows more representative stress/strain curves to be produced. The growth of cracks in an axial direction also causes the experimentally observed anisotropy to be created in the sample. Wong (1990) shows using a 'wedge' crack model that crack growth in this way may be aided by piling up of dislocations around a wedge crack until an equilibrium crack length is reached, under compressive stresses.

The model of Costin (1985) incorporates a time-dependent component by including the effects of 'stress corrosion' (see Atkinson 1984, for an extensive review) by chemically active fluids at crack tips to be analysed. Cracks can therefore grow subcritically at values of K well below K_c. The crack interaction and coalescence is now assumed to occur in an unstable, organised and subcritical fashion. The subcritical crack growth causes more distributed damage around a propagating crack compared to dynamic fracture which is consistent with high fractal dimensions (D) found for distributed shear faults (Shaw and Gartner, 1986). The fractal dimension inferred from the b-value and the stress intensity show strong correlation (Main et al., 1989) which represents how stress intensity and fracture toughness cause a fractal distribution of damage. The effects of this sub-critical crack growth have been incorporated into the modified Griffith theory using a mean field approach (Meredith et al., 1990; Main, 1991) and applied to compressive failure (Main et al., 1993).

2.4.6 Failure Modes during Experimental Triaxial Deformation

Rocks, under stress, fail in different ways depending on the temperature and pressure. At low temperatures and high strain rates rocks are brittle-elastic. They deform elastically at stresses up to about 50% of their strength then crack propagation becomes dominant and eventually the rock fails as cracks coalesce to form a large fracture or failure surface (Jaeger and Cook, 1979) (Figure 2-11). This occurs due to stress concentrations arising at crack tips leading to initiation and propagation of cracks as explained above.

At low confining pressures (representing shallow depths) or near free surfaces, vertical-splitting (1) is the usual failure mode. At higher confining pressures (deeper), a single shear plane develops (2). At even higher confining pressures, networks of inclined shears develop (3).

At low strain-rates, elevated temperatures and very high confining pressures the stress strain curve does not have a distinct maximum to indicate failure. Samples show the continuous deformation under load characteristic of ductile-plastic materials. Failed rock core samples have a characteristic "barrel" shape. The transition from brittle-elastic behaviour to ductile-plastic behaviour known as the 'brittle to ductile transition' is favoured by increasing pressure, temperature.

2.5 The Deformation of Fluid Saturated Rocks

2.5.1 Application of Pore Pressure

A natural rock formation contains levels of pore fluid of varying salinity, temperature and pressure within the interconnected pore and crack network. The fluid can affect the rock both mechanically and chemically. Mechanically the rheological behaviour of the rock then depends on the total macroscopic stress and pore pressure which creates important implications in large scale faulting (Hubbert and Rubey, 1968; Sibson, 1980). The concept gives rise to an effective pressure σ^e_{ij} (Jaeger and Cook, 1979, Berryman, 1992a) defined as

$$\sigma^e_{ij} = \sigma_{ij} - p_f \delta_{ij} \tag{2-18}$$

if the rock is fully saturated and where σ_{ij} is the total macroscopic stress and p_f is the pore pressure and δ_{ij} is a constitutive relation of poroelasticity called the effective stress coefficient. If the value of $\delta_{ij} = 1$ therefore for an incremental increase in the pore fluid pressure the pore opens by the same amount as it would given a decrease in the normal pressure on the fracture by the same amount. If $\delta_{ij} \neq 1$ then Nur and Byerlee (1971) show how it can be determined through the relationship

$$\delta_{ij} = 1 - \frac{K}{K_s} \tag{2-19}$$

where K is the bulk modulus of the rock frame containing pores and K_s is the bulk modulus of the solid rock. Substituting equation 2-22 into 2-19, 2-20 or 2-21 and providing that fluid pressure is fully communicated within the connected porosity, it is seen that the effective normal stresses that control crack growth, macroscopic fracture and friction are reduced by the magnitude of the fluid pressure.

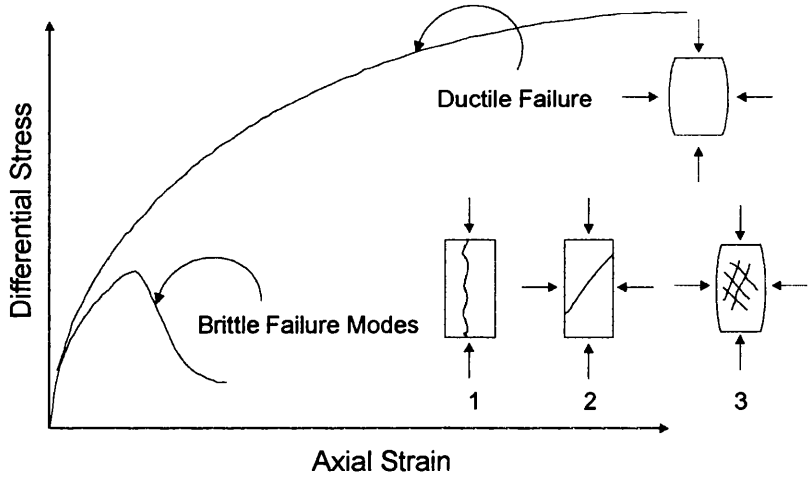

Figure 2-11 Characteristic stress-strain curves for brittle and ductile deformation and associated failure modes for the rock samples (1) tensile axial fault, (2) inclined shear fault and (3) network of inclined shear fractures.

The effective stress principle can be described graphically, using the experimental results shown in Figure 2-12. Zoback and Byerlee (1975) however found a value of $\delta_{ij} = 4$ in Berea sandstone from permeability measurements. This result suggests that the permeability is more strongly influenced by fluid pressure than confining pressure.

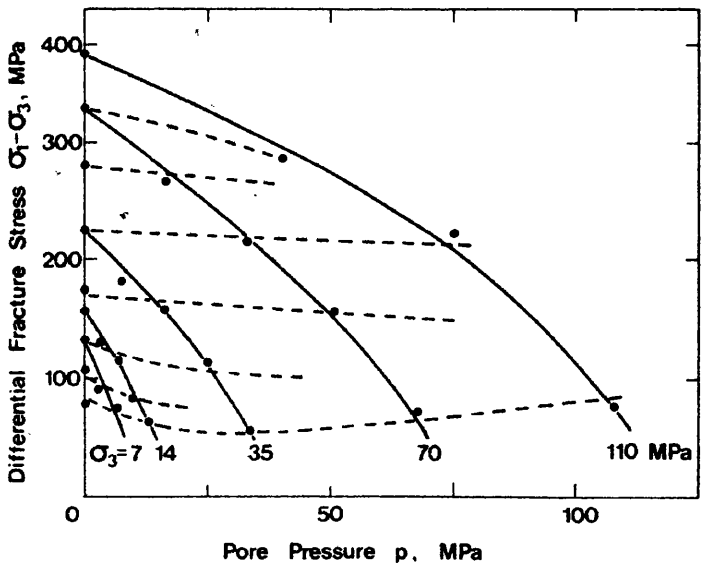

Figure 2-12 Influence of pore fluid pressure on the fracture strength of sandstone under triaxial deformation. The hashed lines are lines of constant effective stress as described by the effective stress law, equation 2-22 (Taken from Murrell, 1965).

Berryman (1992b) shows that these results cannot be explained using an 'equivalent homogeneous rock' model but in principle can be explained by a 'two-constituent homogeneous' paradigm for microscopically homogeneous rocks. For inhomogeneous rocks a rigorous analyses suggests that the pore fluid pressure is least effective at counteracting the changes caused by confining pressure.

2.5.2 Chemical Effects

A reactive fluid at a certain pressure and temperature creates the conditions necessary for what is known as subcritical crack growth (Murrell, 1965; Atkinson, 1982, Atkinson and Meredith, 1987) which involves crack extension occurring at a stress intensity value lower than a critical stress intensity. The mechanisms responsible include stress corrosion, hydrolytic weakening and pressure solution, of which stress corrosion is the most heavily investigated. It is the weakening of strained molecular bonds by a chemically active fluid hence chemical reaction kinetics can be used to explain the dependence of crack growth rates in various environments (Freiman, 1984).

The relationship between the crack propagation velocity (v_c) and the normalised stress intensity factor K consists of three regions. In the first region crack velocity is controlled by the stress corrosion rate while in region 2 the cracking rate is limited by the rate at which the chemically active fluids can reach the crack tip. Finally in region 3 the mechanical effects dominate and chemical effects are reduced considerably. A review of the experimental data concerning subcritical crack growth in a range of geological materials is given by Atkinson (1984).

2.5.3 Permeability Changes

Permeability is one of the most important rock characteristics in relation to hydrocarbon production, geothermal recovery rates and radioactive storage procedures. It is measured using fluid flow techniques. The coefficient of permeability (k) in saturated media relates the fluid flux to the applied pressure gradient. This relation is quantified in Darcy's law, which states

$$q_x = -\frac{k}{\eta}\frac{dP}{dx} \tag{2-20}$$

where q is the Darcy velocity and η is the viscosity of the fluid in the x-direction. Since dimensional analysis reveals k to have units of m^2, the permeability can be thought of as an effective cross-section for flow. This equation is valid only for $R_e << 1$ where R_e is the Reynolds number given by

$$R_e = \rho v l / \eta \tag{2-21}$$

where ρ is the fluid density and l is a characteristic length of the pore space.

Transport properties such as permeability and electrical currents are dependent on the connected pore space in the rock. It is known that increasing normal and effective stress closes pores and microcracks in intact granites (Batzle et al., 1980), jointed granites (Brown and Scholz, 1986) and that this closure affects the fluid flow rate in fractures (Tsang and Witherspoon, 1981). For example the model used by Glover et al. (1998) shows how the mean aperture of a synthetic fracture can close by 5 orders of magnitude with a closure pressure of 13.5MPa. The measurement of k therefore reveals much information about the shape of pores and cracks in rocks. These effects will therefore affect the permeability of a rock as shown in Figure 2-13a where an increasing confining pressure reduces k through porosity reduction. These effects are summarised in equation 2-22 (Scheidegger , 1974) for a capillary model

$$k = c\frac{\phi^3}{S_i^2 \tau^2} \tag{2-22}$$

where S_i^2 is the specific internal area, τ is the tortuosity, ϕ is porosity and c is a constant dependent on pore geometry.

Permeability also increases in response to an increase in pore pressure as shown in Figure 2-13b. This plot also illustrates the application of the effective pressure law although the value of $\delta_{ij} = 1$ is not found. Increasingly investigations now find that the value of δ_{ij} varies with rock type, confining and pore fluid pressures.

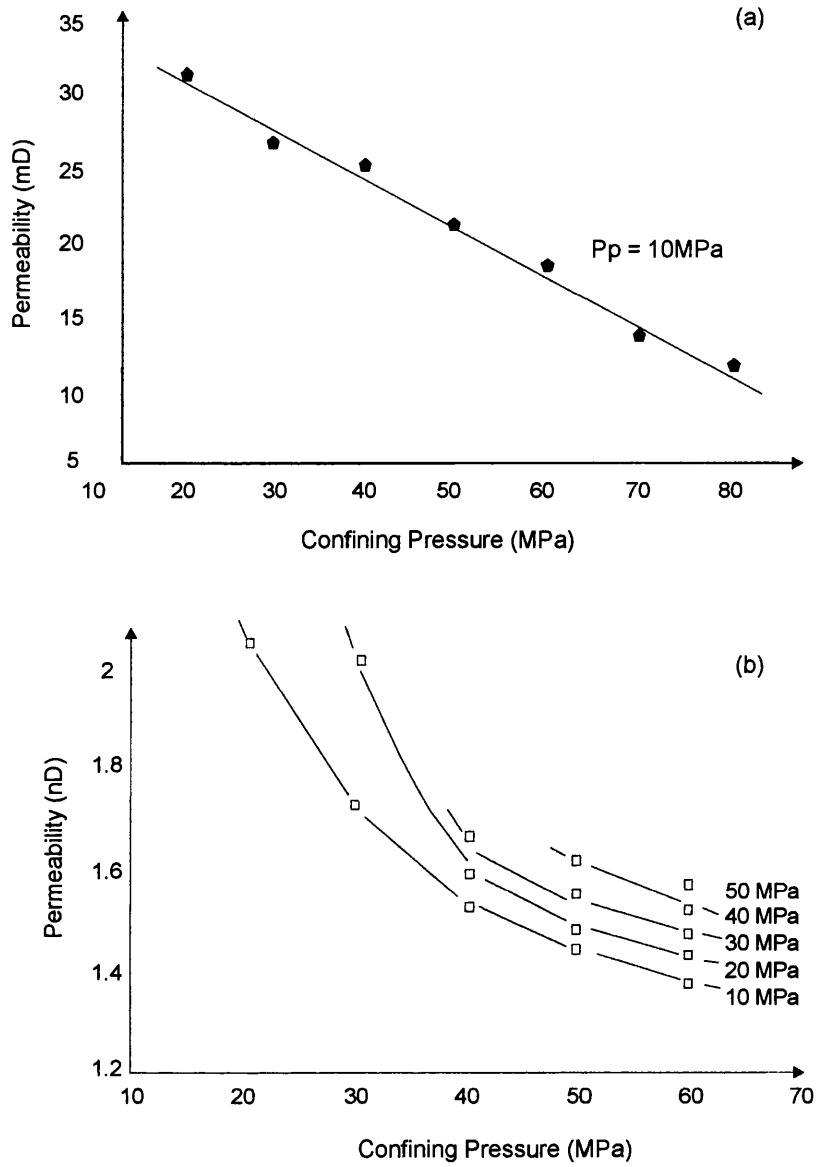

Figure 2-13 Influence of hydrostatic pressure on permeability for (a) isotropic pores and (b) pore and crack porosity of sandstone (taken from David and Darot, 1989).

Permeability is reduced due to porosity closure during compaction (Trimmer et al., 1980) and increased significantly due to microcrack opening and formation during dilatancy (Zoback and Byerlee, 1975). These studies relate to crystalline rocks and are generally accepted. In sedimentary rocks permeability evolution is considered more complex, (Zhu and Wong, 1996; Keaney, 1998) resulting in permeability decreases during dilatancy. Network models consisting of tubular pores and stress induced cracks can adequately describe this behaviour (Zhu and Wong, 1996) and without regard to network dimensionality or pore radii distribution (Bernabe and Bruderer, 1998).

2.5.4 Acoustic Emission

Acoustic emissions (AE) are elastic waves, which are emitted from newly forming crack tips, twin formation and dislocation pile up in response to increasing stress within the brittle regime. The number of AE increases with increasing stress especially as macroscopic failure is approached and AE frequency characteristics have been used to characterise the microfracturing process in uniaxial compression (Ohnaka and Mogi, 1982) and triaxial deformation (Scholz, 1966; Sammonds et al., 1992; Lockner, 1993). The consequences of these studies confirmed the earlier work of Brace (1966b), which revealed accurate predictions of the onset of dilatancy at two thirds to seventy-five percent of peak stress and a close correlation between AE activity and stress-strain behaviour. The onset of AE during uniaxial compression also shows correlation with high frequency electromagnetic emissions and appear to be formed through tensile cracking rather than shear micro-fracturing (Yamada et al., 1989).

Source location experiments show that there is significant inhomogeneity in the spatial distribution of AE events during rock deformation. Mogi, 1968 used 3D source location techniques to locate the source of acoustic emission to build up a spatial map of the increasing deformation. The method is similar to that used in global seismic networks and employs four or more transducers at which the first arrival of the p-wave must be detected. Lockner et al. (1992) controlled the AE event rate shows how 3D source located AE allow crack nucleation, coalescence, fault generation and propagation to be monitored clearly (Figure 2-14). In this study and others the distribution of AE events is fairly homogeneous until failure is approached where a clustering around weak spots is observed. Nishizawa et al. (1985) found similar results in uniaxial compression of granite and explain it in terms of stress corrosion cracking where subcritical crack growth is environmentally induced.

Plotting magnitudes of AE occurrences as a function of their occurrence reveal a similar relation to that found in seismological investigations namely the decrease of occurrence frequency with increasing magnitude. The slope of the log linear frequency-magnitude distribution is the b-value, which is routinely plotted for AE studies and has been showed explicitly to follow a robust model describing AE in terms of the underlying time-varying applied stress and corrosion-enhanced crack growth under drained and undrained conditions (Sammonds et al., 1992). Figure 2-15 displays the b-value variation during deformation of Darley Dale sandstone under drained conditions. A decrease of the b-value is exhibited during stress-induced dilatancy corresponding to an increasing number of large amplitude events as the rock approaches failure. Recovery of the b-value occurs post-failure as frictional sliding dominates the deformation sequence.

The statistical models of Scholz (1968) found b-values to be dependent on stress levels which offers important implications in earthquake studies where earthquake and laboratory behaviour can be correlated (Main et al., 1989). Microstructural information on mean aspect ratio of propagating cracks can be determined from AE rates and velocity changes (Read et al., 1995) and these crack sizes can be used to predict mechanical behaviour (Cox and Meredith, 1993). A damage state variable produced from the

measurements was used in damage models of Bruner (1976) and Walsh (1965) to predict stress-strain relations during rock deformation, agreeing with the models of Scholz (1968).

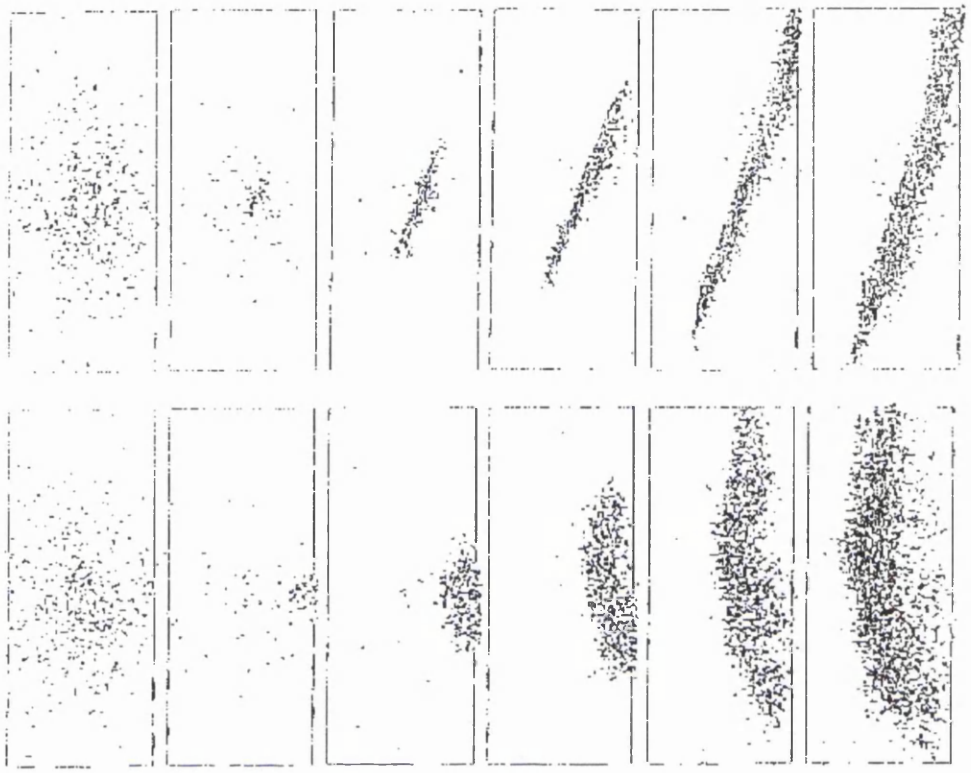

Figure 2-14 Initial nucleation propagation and formation of fault plane from source located AE events during triaxial deformation. Upper and lower row shows evolution in time from two orthogonal directions.

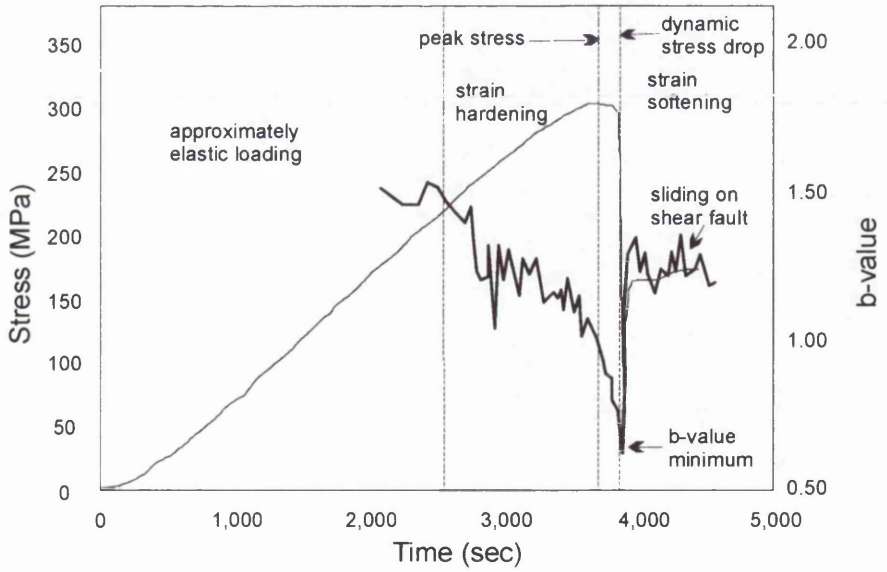

Figure 2-15 Evolution of b-value during triaxial deformation of Darley Dale sandstone showing decrease to approximate value of 0.5 at dynamic failure and subsequent recovery. A confining pressure of 50MPa was used with water as pore fluid and a strain rate of 1×10^{-5} s^{-1} (Redrawn from Sammonds et al., 1992).

2.5.5 Electrical Conductivity and Resistivity of Rocks and Fluids

Effects analogous to those shown in permeability are also shown in the electrical conductivity of fluid saturated rocks. Conductivity, a measure of the electrical current density due to an applied electric field has a range of 10^{10} S m^{-1} for rocks (Figure 2-16) and minerals and is calculated from equation 2-23 for isotropic materials.

$$J_i = \sigma_{ij} E_j \tag{2-23}$$

where J_i is the electrical current density, σ_{ij} is the conductivity and E_j is the applied electric field.

In geological solids conduction is mainly through diffusive ionic displacement given by

$$Ji = -D_p \frac{\partial \eta_f}{\partial x} + vn \tag{2-24}$$

where $D_p \, {}^{\partial \eta_f}/_{\partial x}$ is a flux due to diffusion (Fick's Law) and vn is a convective transport term involving v the average particle velocity.

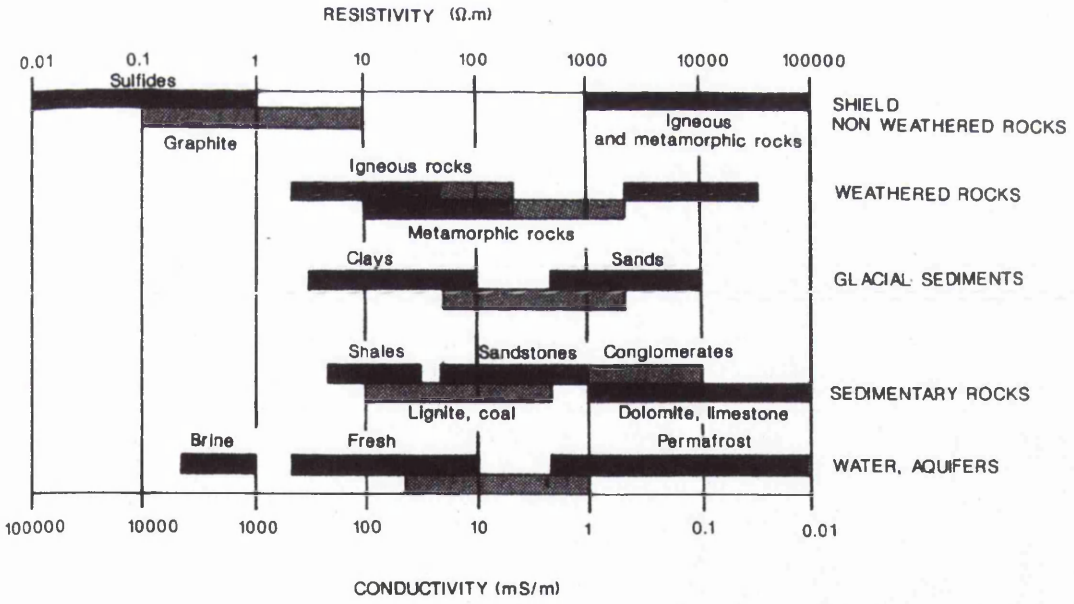

Figure 2-16 Typical values of conductivity and resistivity for geological materials (from Palacky, 1987).

In geological salt bearing fluids, dissociated ions e.g. Na^+, Cl^- move independently under applied electric fields creating electrical currents through conduction mechanisms. The conductivity is proportional to the ionic concentration of the fluid as shown in Figure 2-17 for a range of ionic fluids and is given empirically by (Worthington et al., 1990),

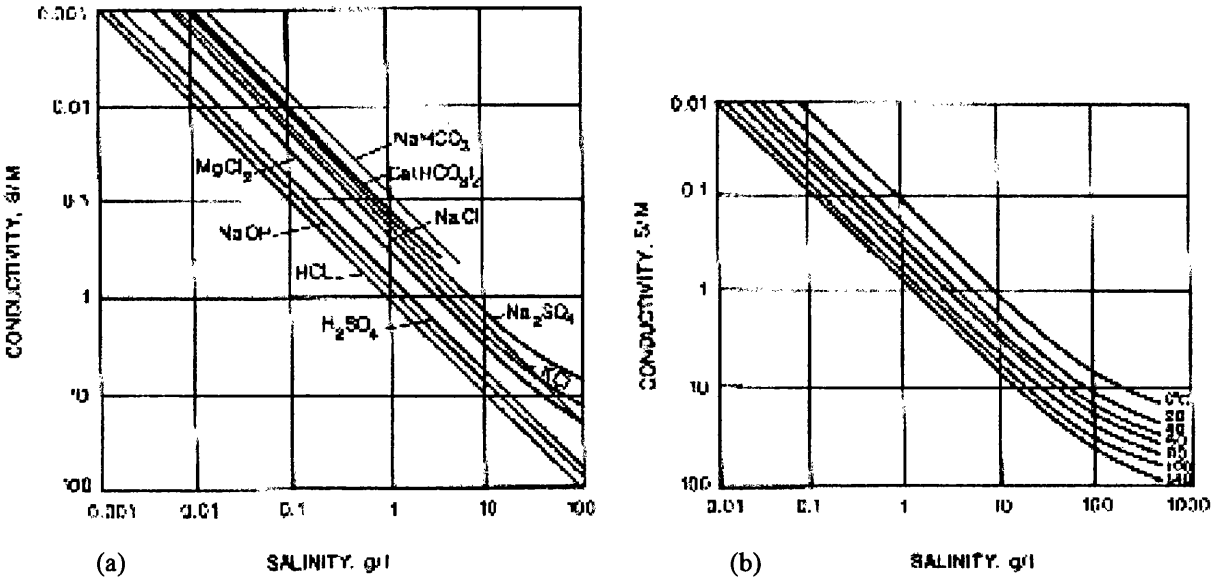

Figure 2-17 Conductivity as a function of fluid concentration for (a) different salts at 20°C and (b) for NaCl solution at varying temperatures (Keller, 1987).

$$log\ (c)\ (\text{in mol/l}) = -1.03024 + 1.06627\ log\ c + 2.41239 \times 10^{-2}\ [log\ (\sigma_f)]^2 + 3.68102 \times 10^{-3}\ [log\ (\sigma_f)]^3 + 1.46369 \times 10^{-4}\ [log\ (\sigma_f)]^4 \quad (2\text{-}25)$$

where σ_f is the pore fluid conductivity and c is the fluid concentration.

Hydrostatic Deformation

Hydrostatic pressure increases the d.c resistivity of saturated crystalline rocks by three orders of magnitude over a range of 1GPa (Brace and Orange, 1966). This result clearly shows how electrical conductivity is dependent on the connected pore structure. Use of higher frequency resistivity measurement reveal only a factor of 2 difference in these values (Lockner and Byerlee, 1985) while also showing that resistivity of granite is more sensitive than sandstone.

These results suggest the importance of crack, pore aspect ratios and porosity on the electrical resistivity. An empirical relationship between resistivity and porosity is expressed in Archie's law (equation 2-26) (Archie, 1942).

$$F = \frac{\rho_r}{\rho_f} = a\phi^{-m} \quad (2\text{-}26)$$

where $F = \rho_r / \rho_f$ is the formation factor, ρ_r is the resistivity of the rock, ρ_f is the resistivity of the solution in the pores, ϕ is the porosity. a the coefficient of saturation and m, the cementation factor are constants dependent on the rock type.

Complex conductivity measurements in the range 1kHz to 1MHz reveal a good correlation with specific surface area of pores, which also exhibit fractal geometry (Ruffet et al., 1991). This indirect observation is confirmed by SEM and optical microscopy (Katz and Thompson, 1985). This scaling quantity of the electrical conductivity is also found for permeability and depends on the skewness of the pore-size distributions (Wong et al., 1984)

Permeability is related to porosity and hence electrical conductivity through the empirical Kozeny equation

$$k = c\frac{\phi^3}{S_0^2} \tag{2-27}$$

and hence allows electrical conductivity to be modelled by percolation theory (Pike and Seager, 1974).

Triaxial Deformation

During triaxial deformation, resistivity increases slightly before then decreasing at approximately half the fracture stress value (Brace and Orange, 1966; Jouniaux et al., 1992; Glover et al., 1997; Lorne et al., 1999b) with the effects being more pronounced than elastic properties, due to the strong dependency of resistivity on pore structure. The results are attributed to a closing of cracks during compaction and dilatant opening of new cracks. Newly forming cracks are used to explain an increase in electrical conductivity with time during creep experiments (Lockner and Byerlee, 1986). Similar resistivity changes have been recorded for granites and sandstones deforming in carbonaceous environments, where carbon films deposited on fracture surfaces during deformation are proposed to act as a conductivity enhancement agents (Roberts et al., 1999).

Surface Conductivity and Effects of Clays

The assumption that electrical conductivity in rocks is controlled by the electrolyte within the pores is inaccurate, especially so in clay rich sandstone (Ruffet et al., 1995). In these rock types the clay particles act as a separate conduction path in addition to the electrolyte path. The resistance of this additional path is low and the origin of the high conductivity lies in the formation of an electrical double layer (EDL) of ions described in detail in the Chapter 3.

The EDL consists of a rigid inner monolayer of cations and an outer diffuse layer of ions, whose density drops off exponentially. It is this outer layer which is free to move under the influence of an applied electric field and results in increased surface conductivity. Since clay minerals have high ion-exchange capacities and surface areas compared to quartz (Figure 2-18) they exhibit this property to a high degree.

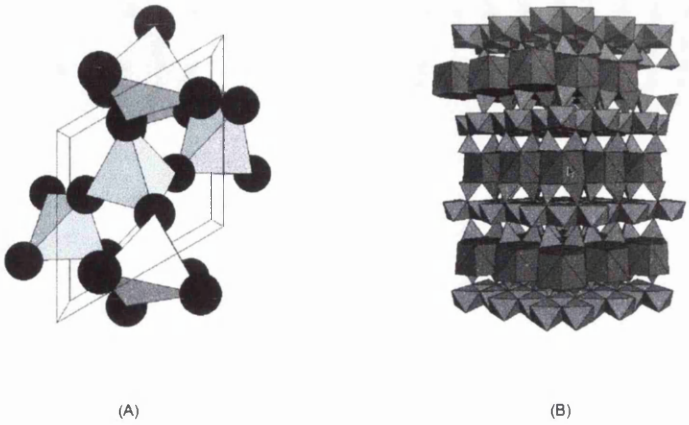

Figure 2-18 Crystal structure of (A) quartz and (B) clay.

Surface conductivity is dominant when low conductivity fluids are used (Bussian, 1983; Glover et al., 1994). It has been shown that the value of surface conductivity extrapolated to low conductivity values is greater for rocks containing higher percentages of clays. This is demonstrated in Figure 2-19, which shows a higher surface conductivity for clay bearing Darley Dale sandstone than for the non clay bearing Berea sandstone.

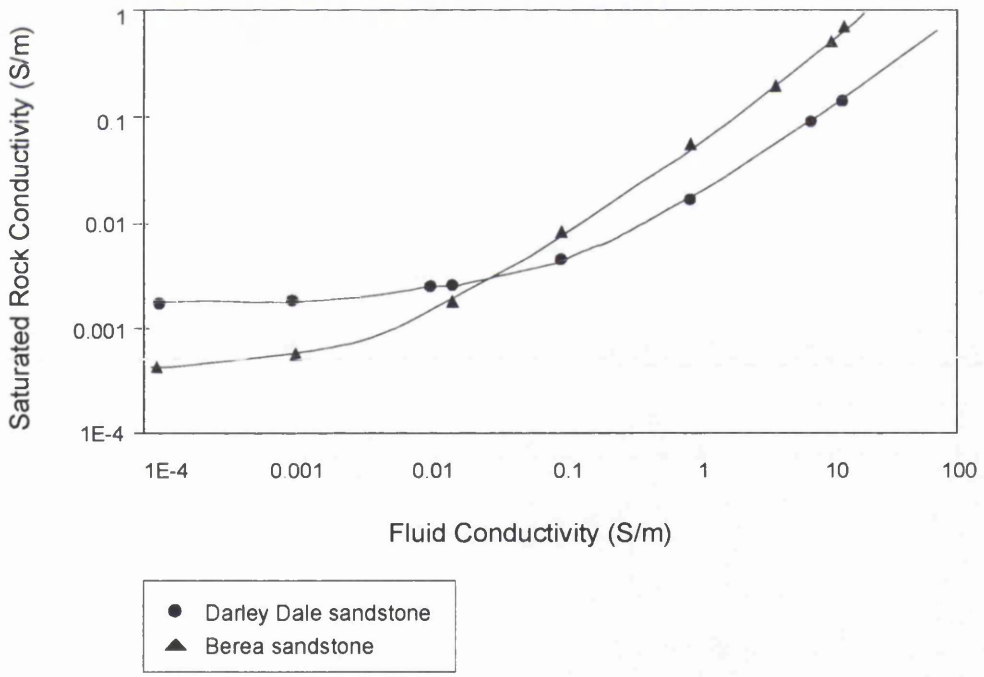

Figure 2-19 Saturated bulk conductivity as a function of fluid conductivity for a clay bearing sandstone, Darley Dale sandstone and a non-clay-bearing sandstone, Berea sandstone (Taken from Glover et al., 1994).

The mechanism of surface conductivity in a rock-fluid system has been shown to involve conduction in the electrical diffuse layer, conduction in the adsorbed layer on the crystal surface and a fluid independent process operating directly on the mineral surface (Revil and Glover, 1998).

Clays and porosity content play an important role in self potential (SP) log interpretation where they were found to increase the electrical potentials of shaly sands. This was subsequently explained using the cation-exchange capacity of the rock and saturating water salinity (Smits, 1968). The increased conductivity due to the clay effect is also important in monitoring steam fronts during enhanced oil recovery where it has been found to be elevated by temperature increases (Butler and Knight, 1998). The results from experiments and well logs have led to the development of various models to predict permeability from electrical conductivity, these include statistical models of tubes and fissures describing rock fluid connectivity, Kirkpatrick's model (Kirkpatrick, 1973) based on solving the microscopic electrostatic equations and the widely used percolation models (David et al., 1990).

2.5.6 The Brittle Deformation Cycle

Rock deformation during the typical brittle cycle is a result of microscopic to macroscopic processes. Theses processes have different effects on all the physical properties described in this chapter. In Figure 2-20 the change in some of the variables with increasing strain is shown. Five specific areas can be recognised, as first proposed by Brace (1964), and the resulting microscopic processes can be described from the bulk rock physics measurements.

Stage 1

In stage I, a concave upward trend in the stress-strain curve occurs causing compaction. This stage may however be absent for intermediate to high confining pressures. This mechanism is probably due to the closing of the most favourable orientated microcracks (i.e. high angles to the applied stress direction) and the elastic velocities V_p and V_s then increase. The pore volume also decreases during crack closure causing lower hydraulic permeabilities and low levels of AE.

Stage 2

Quasi-linear elastic deformation is dominant during stage II and further pore volume decrease occurs. Crack closure is therefore still prevalent causing permeability and electrical conductivity decreases while V_p and V_s parallel and perpendicular to the maximum stress axis remain fairly constant. Little or no AE activity can be detected during this stage and the deformation is considered reversible although some hysteresis can occur.

Stage 3

The stress-strain curve begins to deviate from linearity becoming concave downwards and a process of strain hardening occurs. It marks the onset of the growth of widely distributed newly forming axial orientated microcracks. The microcracking is anisotropic causing V_p parallel and perpendicular to the major stress axis to decrease and at a faster rate than V_s. AE rate begins to increase exponentially at this point which can be between 50-75% of peak stress and the sample becomes dilatant. This causes pore

volume and permeability to increase. A marked decrease in electrical resistivity occurs during dilatancy and is one of the physical properties most strongly affected.

Stage 4

The curve now indicates that the rock sample undergoes strain softening as its ability to withstand further increases in stress is reduced. V_p and V_s in all directions continue to decrease while AE show a period of quiescence associated with maximum damage accumulation and saturation of the AE recorder. The b-value decreases rapidly from a slowly decreasing value in stage 3 to a value of approximately 0.5. This period therefore represents a stage of accelerated crack growth and coalescence to form a macroscopic fault plane. Permeability and electrical conductivity will continue to increase during this stage as a linkage of the new microcracks provides fluid, and hence electrical, pathways.

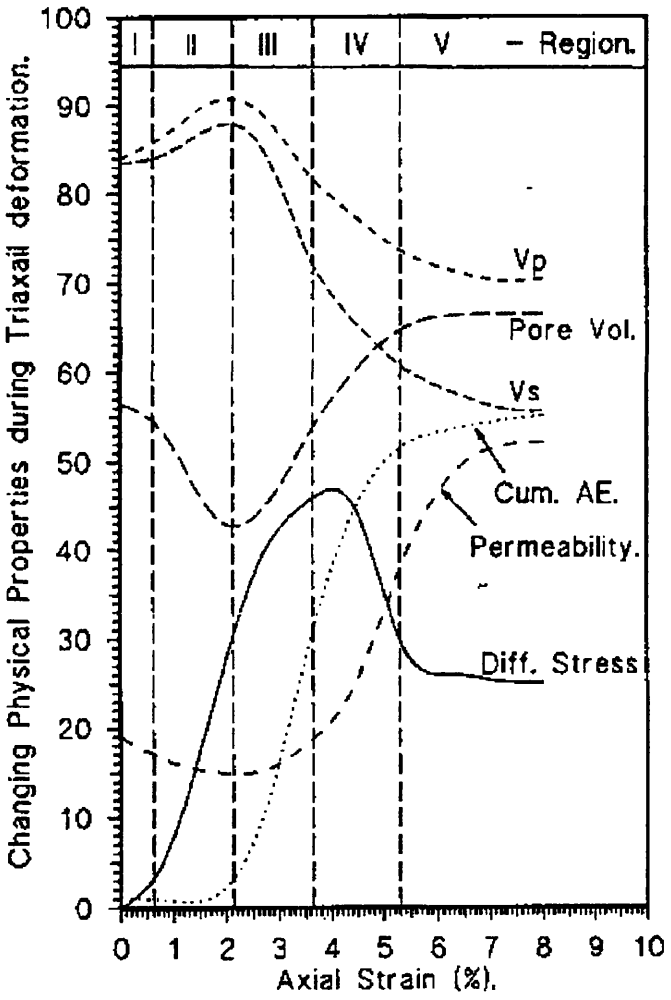

Figure 2-20 Variation of a number of physical properties with axial strain during a typical deformation cycle (Taken from Aves, 1995).

Stage 5

Stable sliding occurs on the macroscopic fault plane and stress becomes independent of strain. The curves indicate electrical resistivity, pore volume change, permeability and elastic velocity changes all become constant. The b-value recovers to an intermediate value while AE activity is reduced to a lower level. This is probably due to the translation of the fault surfaces across one another rather than continued cracking and results in an approximately constant coefficient of friction.

3. Overview and Theory of Seismo Electric Signals (SES)

3.1 Introduction

Seismo electric signals (SES) are anomalous changes in the electric potential measured by electrical dipoles from which there is no simultaneous variation in the earth's magnetic field. SES include electrical, magnetic and electromagnetic (EM) signals with frequencies from d.c. to megahertz frequencies, generated in the upper crust. The number of mechanisms proposed to explain these phenomena include piezoelectricity, contact electrification, exoelectron emission, streaming potential, EM excitation of water droplets and fault zones acting as EM waveguides.

These types of observation and explanations are the basis of emerging research into the use of electrical signals as pre-earthquake indicators and fluid flow monitors. This specific research concentrates on the electrical potential signals produced from the brittle upper crust. This current chapter introduces the SES signals by means of a review of field and laboratory measurements. The development of the theory applicable to the interpretation and a discussion of electrical and streaming potential signals is presented which will be used to interpret later experimental results obtained.

3.2 Electrical Phenomena in the Field

3.2.1 Electrical Signals Associated with Geological Hazards

Derr (1973) collated the evidence that earthquake lights appear to be associated with earthquakes. Within the review are claims of fluorescent lights above quartz-diorite mountains some distance away from the rupture area during the Matsushiro 1965 - 1967 earthquake swarm. The conclusion is that there are electrical disturbances generated from quartz crystals in the rock formation. A radio emission of 2.56 x 10^{-6} W Hz^{-1} total spectral power was observed six days before the great Chilean earthquake of 1960, on a network of widely spaced radio receivers in Colorado (Warwick et al., 1982). This EM signal, again a far-field anomaly, was explained using a mechanism involving stress-induced fracture of quartz-bearing rocks. This signal was also reproduced by means of a theoretical model incorporating pressure variations and fluid saturation (Khatiashvili and Perel'man 1989).

Numerical calculations were applied to model reasonable mechanisms for EM propagation within the earth's interior (Sumitomo, 1994), such as the radio emissions of Warwick et al. (1982). The deviations between model predictions and field results suggest difficulties in detection, which arise due to interference of EM waves from natural and artificial sources. Using telluric currents allows more realistic predictions to be made and may offer a more reliable signal for monitoring. d.c. electrical potential signals have since been measured in seismically sensitive areas around volcanoes (Hashimoto et al., 1994; Nishida et al., 1996) and preceding earthquakes, when precursors of 40mV (Miyakoshi, 1986) and 90mV (Corwin and Morrison, 1977) were reported. Recent quantitative modelling of electric and magnetic

signals provides good agreement with field measurements from the La Fournaise volcano (Adler et al., 1999) and also show how heterogeneity can influence the spatial electrical potential signals.
The dilatancy-diffusion hypothesis for earthquakes (Scholz et al., 1973) can be employed as an interpretative tool for electrical signals recorded in seismic areas. The fluid flow occurring in these areas is due to the build up of critical pressure compartments (Byerlee, 1993) which rupture when hydrostatic pressures exceed the lithostatic pressure. This fluid flow carries electrical currents generating electrical signals, commonly referred to as streaming potentials (SP). Fenoglio et al (1995) using this model, calculated magnitudes of electrical and associated magnetic signals which show quantitative agreement with magnetic signals recorded prior to the magnitude 7.1 Loma Prieta 1989, earthquake.

When claims of successful earthquake prediction arose from these d.c. electrical potential measurements (Varotsos et al., 1984a, 1984b), the validity of the predictions was called into question (Geller (ed), 1996; Lighthill (ed), 1996). As in EM wave propagation through ionospheric waveguides, artificial noise is evident in the crust, causing interpretation problems (Gruszow et al., 1996, Pham et al., 1998). Even if noise can be eliminated from the data, the possibility of electrical potential signals forecasting a seismic cycle is questionable due to the large number of dynamical equations which govern the system (Cuomo et al., 1998). With this disagreement a plausible theory is difficult to construct, though further calculations show the time varying strain field prior to an earthquake may be large enough to induce fluid instabilities, and so create measurable streaming potential signals (Bernard, 1992). From this theory, whereby fluid flow can generate an electric field, it was considered that earthquake activity could be controlled by reducing fluid pressure and hence effective pressure through the application of an external electric field (Mizutani et al., 1976). While the source of these SES signals is still unknown, a statistical analysis shows in some cases the predictions are better than a random analysis of the earthquake catalogue. Park (1996) suggests that a causative mechanism could be given by monitoring water table fluctuations, magnetic fields, d.c. resistivity and strain as well as electrical potentials. It is clear that an interpretation based on all these properties will be more plausible.

3.2.2 Electrical Potential Exploration Methods

The 'electroseismic effect' has been used to describe the change in electrical current with elastic deformation (Thompson, 1936; Long and Rivers, 1975). During exploration of a geothermal area, Anderson and Johnson (1976), using copper electrodes 300ft apart and a high impedance voltmeter, recorded dc electrical potential gradients in the Long Valley caldera, California. Spatial mapping of these signals allowed fault delineation to be traced, although the origin of the signals was not obvious. Recently however signals observed from a geothermal well have been reproduced using an Gauss-Seidel iteration procedure incorporating pressure, temperature, vapour saturation, flow rate and ionic concentration (Ishido and Pritchett, 1999). Observations of net potential gradients of 900mV were recorded over a volcanic basement and explained in terms of electrical streaming potentials produced by moving saline fluids at varying temperatures. The results could not be correlated with other geophysical measurements and the magnitudes appear to be of the same order as theoretical electrical potentials calculated for surface measurements from crustal sources (Nourbehecht, 1963). In other exploration areas,

fluid induced streaming potentials have been recorded from high viscosity oil reservoirs and geothermal wells in Takinoue, Japan (Dorfman et al., 1977; Ishido et al., 1983). Corwin and Hoover (1979) document a review of streaming potential signals generated in geothermal areas.

It is therefore suspected that fluid flow is a major contributor to electrical potentials measured at the surface. Butler et al. (1996) make the same conclusion following an investigation of shallow rock formation boundaries and rule out any other generating mechanisms such as piezoelectricity or resistivity modulation. Understanding of electroseismic phenomena is increasing and the measurement of electrical signals due to applied elastic waves is presently being investigated as a tool to locate zones of high fluid mobility (permeability) and to understand fluid chemistry. Mikhailov et al. (1997) are able to fit synthetic reflection electroseismic waveforms to field data; this technique is incompatible with the field experiments of Beamish (1999) which require refracted waves to account for the irregular moveout velocities. In both investigations, improved measurement techniques are proposed for further studies including noise reduction techniques (Mikhailov et al., 1997) and enhanced electrode characteristics (Beamish, 1999). A maximum depth of investigation of 300m is obtainable from a standard shot and offset recorder arrangement (Thompson and Gist, 1993). The underlying mechanism is explained in terms of charge separation due to an applied seismic wave transmitted through fluid bearing porous media. It can therefore be expected that formation boundaries and discontinuities such as fractures would produce a corresponding signal change in electroseismic measurements. Russell et al. (1997) mapped delineation of a sulphide ore body and quartz veins in Canada using the electroseismic method, adding support to this proposal.

3.2.3 Electrical Potential Investigation of Crustal Structures

In many crustal settings such as sedimentary basins or metamorphic environments, fractures provide large fluid pathways with the potential for immense fluid fluxes. The fluids will travel more rapidly through these discontinuities and therefore electrical potential signals could be expected, as discussed in the preceding sections. This reasoning is also used in the explanation of streaming potentials in accretionary prisms (Heinson and Segawa, 1997) since fluid flow expelled during compaction cannot create streaming potentials large enough to account for the magnitudes obtained. Using finite element models, the authors calculate electrokinetic potentials of the order of 1mV and conclude that the SP magnitudes increase with depth and arcward from a deformation front. Other measurements over large scale structures include electric potential variations of 120mV recorded over a ridge separating two lakes in the Alps (Perrier et al, 1998), where the variation correlates with the changes in annual water levels, also suggesting a fluid flux/streaming potential generating mechanism. Within glacial environments an excellent correlation between natural electrical potentials and fluid pressure from the ice-bed interface is obtained (Blake and Clarke, 1999). The most interesting application of this study is the possibility of mapping subglacial topography and the ability to calculate flow rates.

3.3 Electrical Phenomena in the Laboratory

To understand these field electrical signals and allow quantitative interpretations to be made, laboratory methods have been employed. Early experiments conducted without fluids under uniaxial stress regimes recorded EM signals due to fracture of piezoelectric minerals and rocks (Nitsan, 1977). The generating mechanism could qualitatively be explained by charge separation through piezoelectrification. Fracturing granite through application of a bending force also produced EM emissions (Ogawa et al. 1985) and the electrical dipole moment calculated could be quantitatively explained using piezoelectric models or contact electrification.

Similar uniaxial deformation experiments showed clear electrical precursors seconds before the failure of the rock sample (Enomoto et al., 1994) and highlighted the potential use of the signals in earthquake prediction. In this study electrical charge was detected from granite, gabbro and quartz free serpentinite indicating that a piezoelectric effect was a minor contributor to the generating mechanism. These results showed the electrical signals measured from granite to be approximately eighty times greater than serpentinite. This is confirmed in the dry fracture and slip experiments of Yoshida et al. (1994), where the signals from granite are approximately one hundred times larger than in a gabbro. Further still, they found a strong correlation between the location of quartz crystals, determined using AE source location techniques, and EM occurrence. Their model to explain these results predicts that the EM waveform from wet rocks will rapidly decay compared to a dry rock situation. This model was developed further (Yoshida et al., 1997) when pre and coseismic electrical potential signals were observed during stress drops, with and without slip, along a failure plane. The electrical signals were observed within areas of high strain, suggesting firstly, that a casual relationship between crack growth and electrical potential is possible and secondly, that spatial information may be obtained from mapping electrical potentials. This conclusion also rules out dislocation theories where it is proposed that slip of discontinuities within crystals produce EM emissions. A recent study performed during triaxial stress deformation concluded that the piezoelectric effect must operate in order to explain the dependence of electrical potential magnitude on the loading time and on the magnitude of the stress drop (Sasaoka et al., 1998).

The above investigations were conducted without the presence of pore fluids but it is known that free water exists in the crust, though the depth of existence is still a matter of debate (Nur and Walder, 1990). The streaming potentials measured in the field correlate with changes in lake water levels, flood steam front displacements and fluid flow rates therefore it can be assumed that a strong controlling factor on electrical potential signals is water movement. Early laboratory tests show the streaming potential to vary linearly with applied fluid flow rate, for porous sandstone and siltstone, up to 9MPa, after which a non-linear increase with incremental pressure is observed (Tuman, 1963). The cause of this non-linearity is suggested to be as a result of turbulent flow but it was felt that this would be insufficient to explain fully the observed effects. A linear relationship was also found between pressure head drop and the resulting streaming potential across a simulated fissured sample made from quartz glass plates (Bogoslovsky and Ogilvy, 1972). It is known that the effects of electrode polarisation and airflow in a system may cause spurious results; Ross and Shain (1956) attribute the variation of their electrical potential measurements to this effect. A reliable method of performing streaming potential experiments is therefore required.

Korpi and Bruyn (1972) outline a method and present results showing an increase of streaming potential with applied pressure, up to 17MPa.

With a direct measurement technique in hand, further development of the streaming potential theory was possible and aided by a comprehensive description and experimental study of the phenomenon by Overbeek (1952). The most important parameter of the streaming potential theory is the zeta potential (Figure 3-2) which is the electrical potential and the slipping plane between the inner and outer layers of an electrical double layer (EDL). The relationship between zeta-potential, a controlling parameter of the streaming potential magnitude, and fracture strength showed a positive correlation for quartz diorites (Ishido and Mizutani, 1980). A quantitative study of this effect might therefore have important consequences in engineering and drilling procedures. It was subsequently shown that the subcritical crack growth rate increases as the zeta-potential decreases (Ishido and Nishizawa, 1984). Ishido and Mizutani (1981) demonstrated that the streaming potential coefficients increase with temperature (30-70°C) and decrease with saturating fluid pH. The results agree well with their proposed theory. Later studies on Westerly granite (Morgan et al., 1989) show temperature independence of the streaming potential coefficient between 5-70°C while a decrease in zeta potential with temperature is found for barium sulphate above 70°C. Morgan et al. also include in their study surface conduction effects of saline solutions together with the enhancing effect of salt compound (NaCl + $CaCl_2$) flow on streaming potentials. An investigation involving two-phase (water + vapour) flow with applications to volcanic systems found measurable signals which are enhanced by temperatures up to 60°C (Antraygues and Aubert, 1993).

Under hydrostatic confinement Jouniaux et al. (1994) found streaming potential to depend on the permeability of claystones and that the relationship is stronger for low conductivity fluids (Jouniaux and Pozzi 1995a). They present a model which explains the behaviour using surface conductivity, as suggested by Morgan et al (1989). Under deviatoric stress, the evolution of the streaming potential coefficient were found to be related to changes of permeability in Fontainebleau sandstone (Jouniaux and Pozzi, 1995b). The measured streaming potential coefficient showed a general decrease until approximately 72-86% of the sample yield stress upon which an increase in streaming potential coefficient occurred. The author speculated that this point represented the onset of localisation of newly forming dilatant microcracks. A similar study on Fontainebleau sandstone (Lorne et al., 1999b) also showed similar streaming potential changes during triaxial deformation. They propose an explanation based on independent evolution of hydraulic and electrical tortuosity. A relationship between streaming potential and absolute permeability however was not established.

Investigation of electrokinetic phenomenon as an exploration tool has also been studied in the laboratory. The temporal streaming potential variation across a porous plug was shown to be identical to a differential fluid pressure pulse, so allowing elastic properties, permeability and porosity, of the sample to be determined (Chandler, 1981). The variation of uniaxial low stress cyclic loading can also be directly linked to the variation of the electric field in a number of rock types (Migunov et al., 1992). These results offer quantitative interpretations of the field results and open the possibility for development of downhole

exploration techniques. This idea was investigated using a finite element model based on time varying streaming potentials which concluded that measurable signals are produced through hydraulic fracturing and that fracture directions may be determined owing to increased signal magnitudes in the opening directions (Wurmstich et al., 1995). Finally the applications to hydrogeology appear to be evident as shown in a study by Brown and Haupt (1997). They show streaming potential signals exhibiting good correlation with fluid velocity while the magnitude of the streaming potential is dependent on the distance between the two measuring electrodes.

3.4 Mathematical Development of Seismoelectric Theory

Piezoelectricity has been used to locate quartz veins and to explain electrical phenomena while electrokinetic phenomena has been utilised extensively in chemistry and in the investigations of fluid flow in earth systems (Overbeek, 1952). The following discussion presents the theories that have been developed to describe the various seismoelectric phenomena and derive constitutive relations.

3.4.1 The Theory of Piezoelectric Phenomenon

Since Becquerel in 1820 noticed the existence of charge by simple stretching of rubber and hypothesised the same occurrence in crystals, the piezoelectric effect has been extensively studied. It is the phenomena exhibited when an applied pressure across a piezoelectric material generates an electric field or conversely the formation of a pressure difference due to an applied electric field. Cady (1964) defines a piezoelectric crystal as 'one that becomes electrified on squeezing; or as one that becomes deformed when in an electric field'. The former effect is known, as the direct piezoelectric effect (Equation 3-1) while the latter is the converse effect (Equation 3-2). The electric polarity generated on the crystal surface is determined by the mode of deformation, i.e., compression, tension or shearing.

Experimental investigation of electromagnetic emissions from rocks have led to the application of piezoelectric theory to rocks (Warwick et al., 1982; Ogawa et al., 1985; Yoshida et al., 1994).
The fundamental equations describing piezoelectricity in rock samples are

$$D = d\sigma + \varepsilon_p^{\sigma} E \tag{3-1}$$

$$\varepsilon = \frac{1}{C^E}\sigma + dE \tag{3-2}$$

where D is the electric polarisation, d the piezoelectric constant, σ is the stress, ε_p is the permittivity, E is the electric field, ε is the strain and C is the elastic constant.
A quantitative model (Yoshida et al., 1997) describes the generation of electrical potential signals through piezoelectricity for stick-slip experiments and is described below. It is seen from Equation 3-1 that the electrical polarisation is directly proportional to the applied stress gradient when strain is zero, giving

$$D_i^0 = d_{ijk}\sigma_{jk}^0 \tag{3-3}$$

where D_i is the *i*th component of the polarisation vector, d_{ijk} is this time the piezoelectric modulus of the third order tensor. Sasaoka et al. (1998) estimated the value of d_{ijk} to be 1.4 x 10^{-15} C/N for granite by measuring the peak height of the electrical potential change with increasing stress.

The initial polarisation of a typical quartz crystal is neutralised by mobile bound charges in the rock (Figure 3-1a) and hence a measurable electrical potential cannot be obtained on the sample surface. When a rapid stress drop occurs, $\Delta\sigma_{jk}$, the polarisation of the quartz crystal is reduced to

$$p_i = c_{ijk}(\sigma_{jk}^0 - \Delta\sigma_{jk}) \tag{3-4}$$

where c_{ijk} is the piezoelectric modulus of the material.

The difference between the initial polarisation and the stress-induced polarisation appears as an effective polarisation (Figure 3-1b) P_{eff} given by

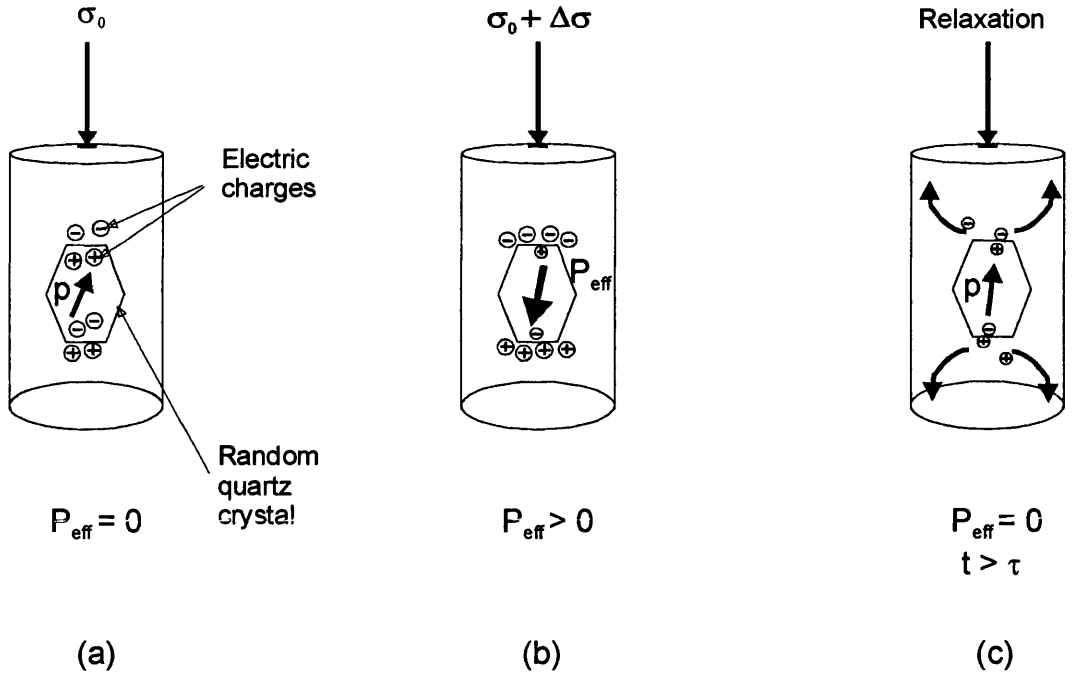

Figure 3-1 Initially stress induced polarisation of quartz crystals is (a) neutralised by mobile bound charges on the charge surface. A rapid stress change (b) induces an effective polarisation in the crystal, which decays (c) through a relaxation process with time constant $\tau = \varepsilon/s$ where s is the electric conductivity (Redrawn form Yoshida et al.,1997).

$$P_{eff} = p_i - p_i^0 = -c_{ijk}\Delta\sigma_{jk} \tag{3-5}$$

If the process occurs at a speed greater than the decay time τ for the bound charges to neutralise the effective polarisation then this signal can be measured on the sample surface (Figure 3-1c). Yoshida et al. (1997) propose a theoretical relation which utilises the electrical potential from a ensemble of quartz crystals and is given as

$$\varphi(t) = \frac{1}{4\pi\varepsilon_p} \sum_m \frac{-b^{(m)} r_i^{(m)} c_{ijk}^{(m)} \sigma_{jk}^{(m)}(t) * g(t)}{\left|r^{(m)}\right|^3} \tag{3-6}$$

where b is the a quartz crystal volume, r is the distance to the measuring point, c is the piezoelectric modulus of quartz, σ is the stress drop, ε_p is the permittivity of the medium and '* g(t)' is a Fourier transform operation. They proceed to show the frequency response of this model and how the signal is dependent on the measuring position as a consequence of the random orientation of quartz electrical axes in granite.

3.4.2 The Theory of Electrokinetic Phenomenon

Electrokinetic phenomenon involve a coupling between fluid flow and electrical current flow in a solid-liquid system. The theory rests upon the existence of a charged solid -liquid interface, known as an Electrical Double Layer (EDL), between the two phases, which is related to the electrokinetic properties of the dual phase system (Overbeek 1952). In a two-phase system of solid and liquid phases, four main electrokinetic effects (Shaw 1996) involving charge flow exist. They are (i) electro-osmosis, which is the movement of a liquid past the solid phase due to an applied electrical potential gradient, (ii) streaming potential, which describes the electrical potential gradient produced on application of an applied pressure gradient causing generation of electricity from a tangential movement of two phases past one another, (iii) electrophoresis, the movement of colloidal particles in an applied electric field and (iv) sedimentation potential which is the generation of an electric field through the movement of charged particles. The application of applied electrical fields will not be discussed further in this study since we are interested only in natural occurring electrical signals in geological systems.

The Electrical Double Layer and Zeta Potential

The mechanics of electrokinetic phenomenon as described above can be explained through the generation of an electrical double layer at the solid-liquid interface. When the two phases are placed in contact, an electrical potential difference develops between them. A number of mechanisms are assumed to occur, such as ionisation of surface groups, adsorption of species and dipole orientation, all which cause charge separation. In a rock/pore fluid dual system the solid phase has an excess charge of one polarity with a compensating oppositely charged distribution of counterions existing in the near fluid phase. The concentration of ions in this layer is statistically organised following a Boltzmann distribution pattern. This manifests itself through an exponential concentration profile into the bulk fluid where electroneutrality is reached. Currently accepted theoretical models of the physical description were first developed by Chapman (1913) and Gouy (1917) and further developed by Stern (1924).

The Structure of the Electrical Double Layer

The electrical double layer is composed of an inner adsorbed layer and a diffuse outer layer as shown in Figure 3-2 (Ishido and Mizutani, 1981; Morgan et al., 1989)

Solid Inner Layer

The rigid inner monolayer of molecular ions in the plane of the solid surface forms due to the attraction of ions from the liquid phase. The adsorbed ions in the inner layer are held by electrostatic attraction, which fully populate the solid surface of the crystal. An electric potential is set up (Ψ_0) on the surface which decreases to a lower value, the zeta potential (ζ), at the slipping plane (S_2) plane, as shown in Figure 3-2.

The Diffuse Outer Layer

The counter-ionic charge density in the immediate liquid phase is physically described as a diffuse layer. The plane S1 in Figure 3-2 shows the approximate position of this layer. This outer layer is composed of positively and negatively charged ions with a typical thickness of 3000Å following a Boltzmann distribution. The actual thickness can be calculated from the reciprocal Debye length κ^{-1}

$$\kappa^{-1} = \sqrt{\frac{\varepsilon_p k_b T}{2e^2 C_f}} \tag{3-7}$$

where ε_p is the permittivity of the electrolyte (7.072×10^{-10} for water), k_b is Boltzmann's constant (1.381×10^{-23} J/°K), T is the temperature (291°K), e is the elementary charge of an electron (1.6×10^{-19} C) and C_f is the concentration (m^{-3}) (Revil et al., 1996). The thickness of the diffuse layer can therefore be seen to decrease with increasing concentration (Figure 3-3). As an example, a 0.2M NaCl solution at room temperature has a Debye length of approximately 7 Å. In general these values are much smaller than pore radii in the majority of rocks and soils with the exception of materials like clays (Pride and Morgan, 1991).

In the case of a fairly homogeneous rock, such as, sandstone, the quartz grains are separated by pore space. Since an electrical double layer exists at the interface between the sandstone grains and the saturating pore fluid, an interaction between the EDL's of opposite grains can be expected as depicted in (Figure 3-4).

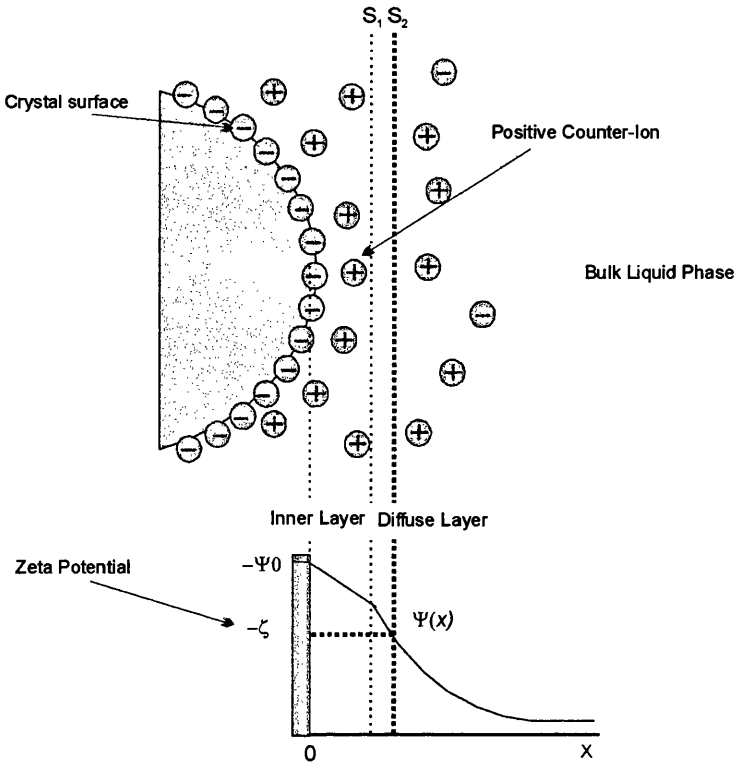

Figure 3-2 Formation of electrical double layer (EDL) on quartz crystal (symbols on lower graph explained in the text).

Numerical analysis by Ohshima et al., 1986 shows that the interaction of two parallel charged surfaces produces an electrical potential considerably smaller than model predictions and therefore, it can be assumed that the zeta potential will not behave according to theoretical requirements.

When non-uniform charged surfaces come into contact Cohen and Radke (1991) showed that the charged surfaces distort the electrical field and can increase the zeta potential by up to 30%

Zeta Potential

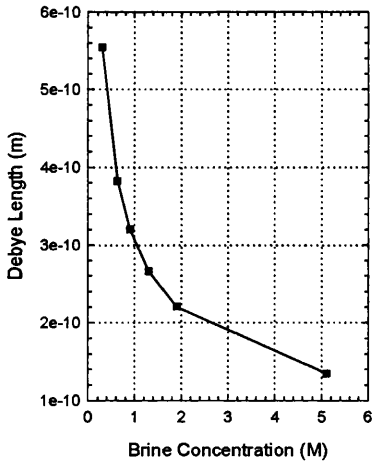

Figure 3-3 Influence of concentration on the Debye length of the electrical double layer.

The solid rigid layer and the diffuse outer layer are separated electrically by a plane characterized by the zeta potential. This is the most common and easiest to measure parameter of the EDL, in certain circumstances being more important than the surface potential of the solid phase. It is defined as the point where the potential difference across the interface ceases to be uniform, i.e., where the diffuse layer begins (Chandler, 1981). The zeta potential is related to the electrostatic repulsion energy between the inner and outer layers and therefore is of importance in mineral extraction, drilling fluids and ceramics where details of the attraction of particles with solutions is critical (Zeta-Meter Inc.).

Most silicate minerals and rocks exhibit negative values of the zeta potential (Ishido and Mizutani, 1981) although the addition of surface-active species can increase it to values above zero (Ishido and Mizutani, 1980). The presence of surface conductance has also been noted to decrease the zeta potential (Ishido and Mizutani, 1981), while a clear dependence of ionic strength on the zeta-potential was found for crushed quartz samples (Johnson, 1999). Typical zeta potentials for quartz sand vary from –55mV up to –15mV for industrial quartz and became more negative with increasing pH (Johnson, 1999), and also observed by Ishido and Mizutani (1981). In a consolidated sandstone for example, a value of –97mV was calculated from experimental data for a Fontainebleau sandstone specimen (Jouniaux and Pozzi, 1995a).

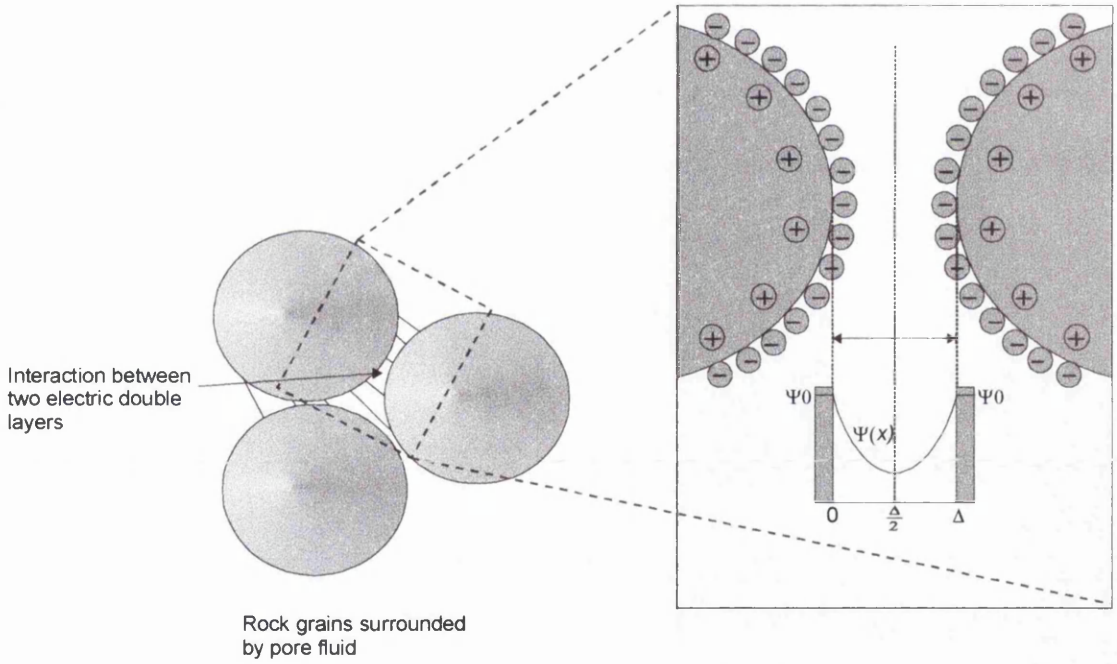

Figure 3-4 The interaction of two electrical double layers showing the resulting electrical potential.

The dependence of the zeta potential on the streaming potential coupling coefficient is shown in Figure 3-5. Results obtained with 0.63M NaCl brine.

Two fundamental first-order equations exist; one, Gauss's law, describes the relationship between the electric field and the total enclosed charge over a surface S, is given in differential form as

$$\nabla \cdot E = \frac{\rho}{\varepsilon_p} \tag{3-8}$$

The second equation relates the electrical potential and the electrical charge density

$$E = -\nabla\varphi \tag{3-9}$$

Combining equations (3-8) and (3-9) we obtain a second order partial differential equation known as Poisson's equation.

$$\nabla \cdot \nabla\varphi = \frac{-\rho}{\varepsilon_p} \tag{3-10}$$

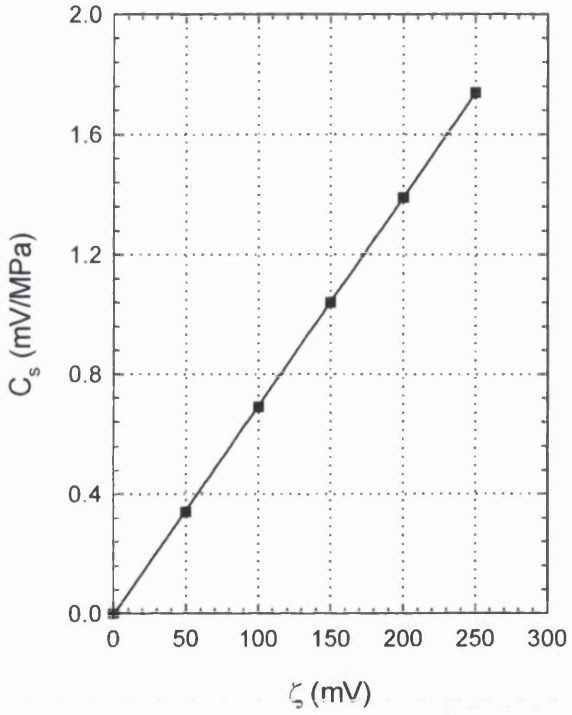

Figure 3-5 Dependence of streaming potential coupling coefficient (C_s) as a function of the zeta potential (ζ).

or using the Laplacian scalar differential operator

$$\nabla^2\varphi = -\frac{\rho}{\varepsilon_p} \tag{3-11}$$

where the electrical potential (ϕ) has a value φ_0 at the electrical interface, between solid and liquid phases, due to a charge density ρ in a medium of electric permittivity ε. Therefore the spatial electrical potential is determined by the charge density.

The distribution of ions in the liquid phase can be described through the Boltzmann statistical equation, which expresses that at places of positive electrical potential the negative ions are concentrated and the positive ions are repelled, with the opposite case being true.

$$n_i = n_0 \exp\left[\frac{-z_i e\varphi}{k_b T}\right] \tag{3-12}$$

where n_i is the concentration of either positive or negative ions of charge e and valence z at a position of electric potential difference φ with n_0 representing the ionic concentration of the bulk solution.

Assuming the solid-liquid interface to be smaller than the radius of curvature of a crystal surface, the interacting surface can be treated as a planar surface. The Laplacian, in Cartesian co-ordinates, reduces from three dimensions to one, i.e. $\partial^2/\partial x^2$.

The space charge density ρ is given by the algebraic sum of the ionic charges per unit volume

$$\rho = \sum z_i e n_i \tag{3-13}$$

and so we can write Poisson's equation (equation 3-8) as

$$\Delta\varphi = -\frac{1}{\varepsilon}\sum z_i e n_i \exp\left[\frac{-z_i e\varphi}{k_b T}\right] \tag{3-14}$$

If we multiply each side of equation 3-11 by $2\,d\varphi/dx$ and integrate twice using the boundary conditions as $x \to \infty$ then $\varphi \to 0$ and $d\varphi/dx \to 0$

Then

$$\frac{d\varphi}{dx} = -\sqrt{\frac{4nk_bT}{\varepsilon_p}}\left[\exp\left(\frac{ze\varphi}{2k_bT}\right) - \exp\left(\frac{-ze\varphi}{2k_bT}\right)\right] \tag{3-15}$$

This relationship shows that the electric potential decreases exponentially in value, from the interface, to zero in the bulk solution as a function of position x.

The theory was improved by accounting for the finite ionic size (Stern, 1924) of ions adsorbed to the solid phase.

3.4.3 Streaming Potentials

When a pressure difference is applied across a saturated porous sample, the diffuse layer of the EDL is forced to move in the direction of transport of the liquid. An electrical current (I_A), convective in nature,

is produced which accumulates charge at one end of the sample. This electrical current generates an electric field producing a secondary electrical current (I_B) opposing the primary current. This current takes all possible routes through the rock sample including the bulk of the solution and the rigid part of the electrical double layer (Figure 3-6). Therefore in the steady state situation, the two currents will be equal and opposite, i.e., $I_A = -I_B$. The potential difference that develops between the ends of the sample is called the streaming potential.

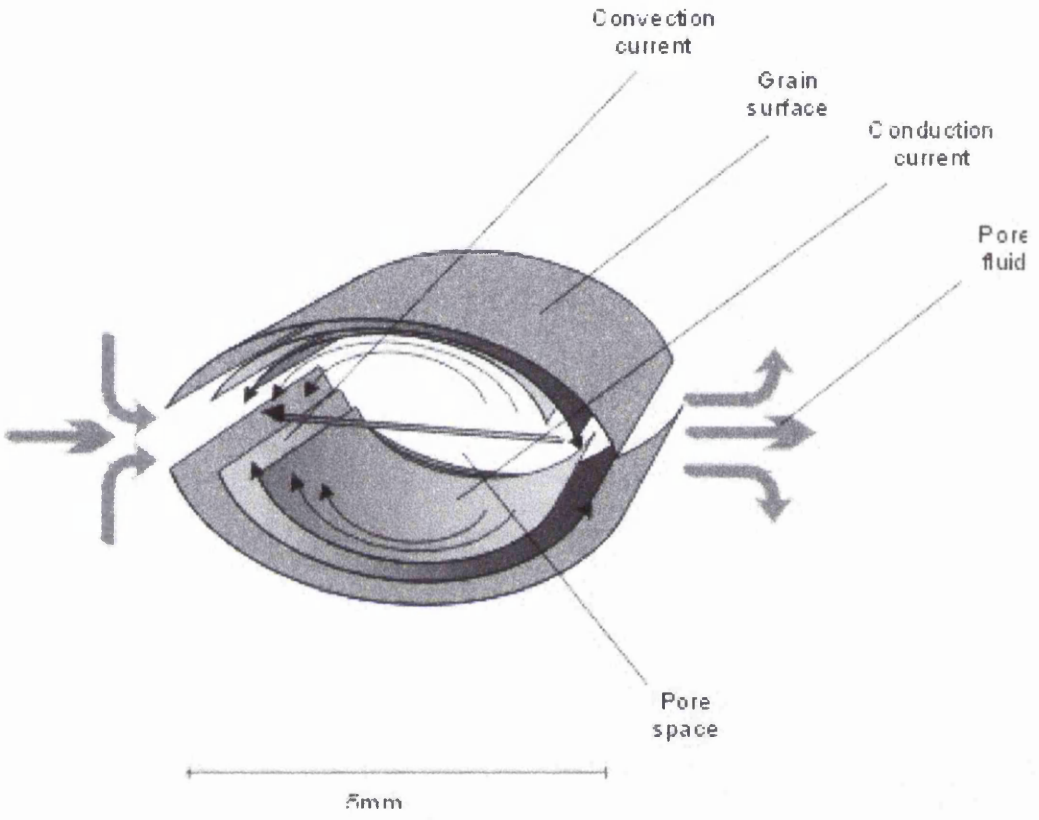

Figure 3-6 Schematic diagram showing the convection and conduction current produced through application of a pressure gradient across a typical rock pore.

To derive the streaming potential equations we assume a single circular capillary of radius r and length l, the potential difference across the ends of the capillary is V developed due to a pressure gradient P/l. Flow within the capillary is governed by Poiseuille's equation, which relates the velocity u, of the pore fluid as a function of the distance x away from the wall, given as

$$u = \frac{P\left(r^2 - x^2\right)}{4\eta l} \tag{3-16}$$

where η is the pore fluid viscosity.

The moving part of the electrical double layer at a distance *(r-δ)* from the centre of the tube, moves with velocity u_δ given by

$$u_\partial = \frac{P}{4\eta l}\left[r^2 - (r-\delta)^2\right] \tag{3-17}$$

$$= \frac{P}{2\eta l}\left(2r\delta - \delta^2\right) \tag{3-18}$$

therefore we have

$$u_\delta \approx \frac{Pr\,\delta}{2\eta l} \qquad \text{since} \qquad \delta^2 \langle\langle\, 2r\delta \tag{3-19}$$

As the movement of the diffuse component of the EDL occurs, a current I is produced which is the product of the total charge q through a unit length of tube with speed u_δ. Therefore the velocity of the moving part of the layer can be derived from

$$I = 2\pi r q u_\delta \tag{3-20}$$

Substituting equation 3-19 we obtain

$$I = \frac{\pi r^2 q\,\delta P}{\eta l} \tag{3-21}$$

If the pore fluid has conductivity σ_f, an expression for the conductance of the pore fluid is $\pi r^2 \sigma_f / l$ and therefore the resistance is the inverse. Using Ohm's Law the streaming potential, V, is arrived at and given as

$$V = \frac{Il}{\pi r^2 \sigma_f} \tag{3-22}$$

Substituting for the current I from equation 3-21

$$V = \frac{q\delta P}{\eta \sigma_f} \tag{3-23}$$

If we assume the diffuse layer can be represented by a simple parallel plate condenser then the potential in the solution is zero and that on the S_2 plane is ζ. This value is known as the zeta potential (units in V)

and is fundamental in all electrokinetic phenomena (Mazur and Overbeek, 1951) and has a negative value for earth materials. The potential difference is therefore given by

$$\zeta = \frac{q\kappa^{-1}}{\varepsilon_p} \tag{3-24}$$

Assuming the Debye length (κ^{-1}) to equal δ, the distance at which shearing of the diffuse layer occurs, we have $q\delta = \zeta\varepsilon_p$ and substituting into equation (3-23), we can write the streaming potential (V) as

$$V = \frac{\zeta\varepsilon_p}{\eta\sigma_f} P \tag{3-25}$$

This equation describes a situation where the flow is laminar and the pore fluid volume conductance is large in caparison to the surface conductance. It is known as the Helmoltz-Smoluchowski equation and predicts that the streaming potential under an applied pressure gradient is therefore dependent on the zeta potential of the rock-fluid system. Since this value is negative for most rocks the potential gradient will be in the opposite direction to the pressure gradient. Overbeek derived equation 3-25 equation for a curved capillary of variable cross-section and showed how it can be applied to the streaming potential generated in porous media such as soils and rock. The additional parameters in equation 3-26 introduce the dependency on pore radii, which removes the scale invariance of equation 3-24.

The surface conductivity mentioned acts to enhance the conductivity of the diffuse zone and is most important for low pore fluid salinity. It is not difficult to make the necessary corrections for the surface conductance applicable to this model; the return current is proportional to $\pi r^2\sigma_f + 2\pi r\Sigma_s$ where Σ_s is the specific surface conductance (Overbeek, 1952) and therefore the streaming potential can be described as (Revil et al., 1999b)

$$V = \frac{\varepsilon_p\zeta}{\eta(\sigma_f + \frac{2\Sigma_s}{r})} P \tag{3-26}$$

For a porous medium which is more representative of a rock sample, the surface conductivity effect on the streaming potential can be determined by considering the bulk conductivity (σ_b) of a fluid saturated plug containing a bundle of capillaries. This modification accounts for the conduction through the fluid and along the solid grains of the matrix.

Two other significant multiplicative factors, which must be introduced, are the porosity of the sample (ϕ) and the tortuosity (τ) (later described individually as electrical and hydraulic tortuosity) of the pore network. The former accounts for the fact that only a fraction of the plugs cross-sectional area is accessible to fluid flow and the latter considers the reduction of fluid flow due to the sinuous nature of

pore fluid pathways. More specifically the tortuosity is defined as $\tau = L'/L$ where L' is the real length of the path along which fluid travels and L is the apparent path length. The parameter can be determined in the laboratory through measurement of the bulk formation factor (F_0), which is equal to τ^2/ϕ, where ϕ is porosity.

An expression for the streaming potential can now be given as

$$V = \frac{\phi}{\tau^2}\frac{\varepsilon_p \zeta}{\eta \sigma_b} P \tag{3-27}$$

A commonly plotted variable is the streaming potential coupling coefficient, C_s, that is defined as the ratio of the streaming potential to the applied pressure gradient ($\Delta V/\Delta P$). It is clear from the above equations that C_s does not depend on the geometrical properties of the media and therefore it has been suggested that it can be used to interpret field measurements (Jouniaux and Pozzi, 1995b). However a numerical study by Bernabé (1998) shows that C_s is not scale invariant but shows a permeability dependence which is controlled by Johnson and Schwartz's (1989) weighted average length scale.

More information can be obtained from measurements in low frequency regions. Neev and Yeatts (1989) include the effects of streaming potentials in the Biot theory of fluid saturated poroelastic media and solve the equations using plane wave solutions. The solutions reveal a number of frequencies which are characteristic of physical properties of the fluid and the solid-liquid interface, i.e., EDL. Experiments have also revealed the behaviour of fluid compositions and concentrations, pH of fluids, solid grain size and geometry on the EDL (Revil et al., 1996). Due to these large number of properties affecting the electrical double layer it has not been a simple process to provide complete agreement between theoretical predictions and experimentally determined results.

3.4.4 Electrokinetic Coupled Phenomena

The theoretical framework developed for the quantitative treatment of electrokinetic coupling is known as irreversible thermodynamics (Overbeek, 1953). The coupling between electrical charge and the flow of liquid can be described by

$$\begin{bmatrix} Q \\ J \end{bmatrix} = \begin{bmatrix} L_{11} & L_{12} \\ L_{21} & L_{22} \end{bmatrix} \begin{bmatrix} \nabla\varphi \\ \nabla P \end{bmatrix} \tag{3-28}$$

for a capillary tube where Q is the fluid flux (Darcy velocity), J is the current density, P is the fluid pressure, φ is the electrical potential and L_{ij} are hydraulic, electrokinetic coupling and electrical coefficients. When $i = j$ the equations become the generalised relations between flows and their direct driving forces. When $i \neq j$ the constants are known as the coupling coefficients and relate flows to the indirect driving forces.

The coefficients represent important physical properties of the rock fluid system; L_{11} is the hydraulic mobility (obtained from Darcy's Law and equal to k/η where k is the permeability and η is the fluid viscosity), L_{22} is the electrical conductivity from Ohm's Law. The relation $L_{ij} = L_{ji}$ is the basis of Onsager reciprocity which reduces the number of coupling coefficients which must be determined and therefore the coupling coefficients L_{12} and L_{21} are both equal to $-\varepsilon_p\zeta/\eta$ where ε_p is the permittivity, ζ is the zeta potential.

If we expand equation (3-28) for current and fluid flow in all directions we obtain the following two coupled equations for porous networks.

$$Q = -\frac{k}{\eta}\nabla P - \frac{\varepsilon_p \zeta}{\eta}\nabla \varphi \tag{3-29}$$

$$J = -\frac{\varepsilon_p \zeta}{\eta}\nabla P - \sigma_f \nabla \varphi \tag{3-30}$$

Since the permeability and fluid conductivity are variables in these coupled equations, it can be assumed that electrical currents and streaming potentials may be sensitive to heterogeneity in porous media (Sill, 1983).

Following Sill's approach it is assumed that the first term on the right hand side of equation 3-29 is dominant in controlling the fluid flow then

$$Q = -\frac{k}{\eta}\nabla P \tag{3-31}$$

and writing the total current density in equation (3-30) as the sum of a pressure induced convective current and a compensating ohmic conduction current we have

$$J_{total} = J_{convection} + J_{conduction} \tag{3-32}$$

If no external current sources exist and a steady state system is in place (i.e. $\partial/\partial t = 0$) then all the charge in the system is conserved, i.e., $\nabla . J_{total} = 0$ and we can write equation 3-32 as

$$\nabla . J_{conduction} = -\nabla . J_{convection} = S \tag{3-33}$$

where S is an electrokinetic source which can exist without net current sources. The significance of this electrokinetic source is that local convective sinks equilibrate the local conductive sources, although the current magnitudes are not necessarily equal in magnitude.

The heterogeneity which cause electrokinetic sources can be found by substituting (3-30) into (3-33)

$$\nabla.J_{conduction} = \nabla.(\frac{\varepsilon_p \zeta}{\eta} \nabla P) \tag{3-34}$$

$$\nabla.J_{conduction} = \nabla \frac{\varepsilon_p \zeta}{\eta}.\nabla P + \frac{\varepsilon_p \zeta}{\eta} \nabla^2 P \tag{3-35}$$

using equation 3-28 to find $\nabla^2 P$ and substituting into equation 3-35 yields

$$\nabla.J_{conduction} = \nabla\left(\frac{\varepsilon_p \zeta}{\eta}\right).\nabla P - \frac{\varepsilon_p \zeta}{k}\left(\nabla \frac{k}{\eta}.\nabla P\right) - \frac{\varepsilon_p \zeta}{k}(\nabla.Q) \tag{3-36}$$

Therefore it is possible to identify three sources for induced conduction currents and hence streaming potentials generated through steady state flow. They are (a) the position of gradients in the cross-coupling coefficient L_{21}, (b) positions of change in permeability k and (c) sources or sinks of fluid flow. To account for the seismically induced streaming potentials (Neev and Yeats, 1989, Pride, 1994, Haartsen et al., 1998) a fourth term should be added to equation 3-32 if the assumption of slowly varying flows are operating or alternatively a solution to the equations obtained using the correct charge conservation statement; $\nabla.J = -\partial q / \partial t$.

From the above equation it is evident sources are strongly dependent on heterogeneities and they assume fluid and current to flow in similar fashion through the pore geometry. This has been questioned as numerical investigations show the critical paths for hydraulic and electrical flow to be different (David, 1993) and indicate varying electrical and hydraulic spatial patterns in fractures (Brown, 1989, Brown and Thompson, 1991) and give poor estimates of hydraulic flow rates in fractures using electrical analogues (Sundaram and Frink, 1983). These conclusions signal the caution required in predicting permeability from electrical current measurements such as the empirical relation $k \propto l_c^2 / F$ (l_c^2 is a length scale) of Thompson (1986). To account for this, a more accurate length scale involving information about electrical and momentum transport was derived which provides a rigorous link between fluid permeability and electrical conductivity (Avellaneda and Torquato, 1991).

4. The Acquisition of Experimental Data

4.1 Introduction

Rocks are inherently heterogeneous due to the presence of cracks, joints, fractures and induced fabrics. It is this property which controls the mechanical behaviour of the rock formation. As explained in Chapter 2.4.2, stresses acting on rocks involve a combination of shear and normal stresses. Triaxial deformation techniques can provide these natural principal stresses, which are combinations of both shear, and normal stresses. The stress variations encountered alter the geometry of the rock matrix causing, electrical changes, fluid interactions, elastic wave emissions and chemical changes. Measuring these properties provides indirect information on the behaviour of the rock and the microscopic processes involved. This leads to a determination of how these processes produce macroscopic deformation. The advantage of laboratory studies is that they allow the independent measurement of the dynamic variables causing deformation and so provide a method for discriminating between different mechanisms.

A high-pressure fluid medium triaxial deformation vessel was used to deform samples of sandstone and basalt under crustal stresses. The vessel and experimental set-up in the laboratory is shown in Figure 4-1. The experiments done in this study are quasistatic tests and can last from 1 minute to several days depending on strain rate. In general these tests are carried out in a triaxial pressure cell and are designed to determine the deformation behaviour of rocks. Material failure strength, pore volume changes, elastic modulii, and dilatant cracking variations can all be used to describe this deformation behaviour. Microacoustic tests have been done to monitor crack formation and through source location techniques, we can observe the fault plane formation. These data provide an important pool of information, which can be utilised to understand the complex physics of rock deformation and electrical potential generation.

In this chapter I will describe all the experimental apparatus used and the data logging procedures together with sources of experimental error in the data. Sample sizes vary from 2 to 150mm in diameter and 6 to 300mm in length in experimental rock physics, a safeguard designed to ensure statistical homogeneity. A sample size of 100mm in length and 40mm in diameter is used here which ensures a statistically large number of grains and cracks and of sufficient length to ensure a central homogeneous strain region away from any inhomogeneous end effects. In saturated conditions, typical pore fluids used are deionised water and brines of varying concentration. The temperature variation effects are also important but are left to future work as the understanding of electrical potential signals at room temperatures, is considered an important primary step.

I have made significant modifications to the apparatus, which I describe in this chapter. Firstly, to increase the simulated depth of observation of electrical potential signals, a novel lead through design was designed and commissioned. Secondly to analyze the effects of more typical crustal fluid, e.g., brines, a pore fluid separator was designed and implemented. The measurement system and experimental

technique are described followed by the data reduction methods. Finally a detailed error analysis is presented along with the apparatus calibration techniques. For a review of the practical problems encountered during triaxial deformation experiments see Tullis & Tullis (1986).

4.2 Triaxial Deformation Apparatus

To simulate the natural stress state within the crust a triaxial deformation apparatus is used. Von Kármán (1911) first used this approach and improved capabilities of these vessels were further developed by the 'unsupported area' sealing mechanism of Bridgman (1949). To achieve deeper crustal conditions, high temperature and pressure equipment was developed (Murrell, 1958, Paterson, 1970). A concise review of triaxial testing machines is given by Paterson (1978).

The triaxial cell used in this investigation was designed by Dr. P. Sammonds in the Rock and Ice Physics Laboratory at University College London based on an earlier design (Sammonds et al., 1991). It uses oil as the confining medium with a stepped balanced ram arranged in vertical position situated inside a servo-controlled load frame. Figure 4-2 shows schematically the thick walled pressure vessel constructed from 3.5% nickel chrome alloy steel. It has a 130mm internal diameter and is fully heat-treated to approximately 37 Rockwell C hardness.

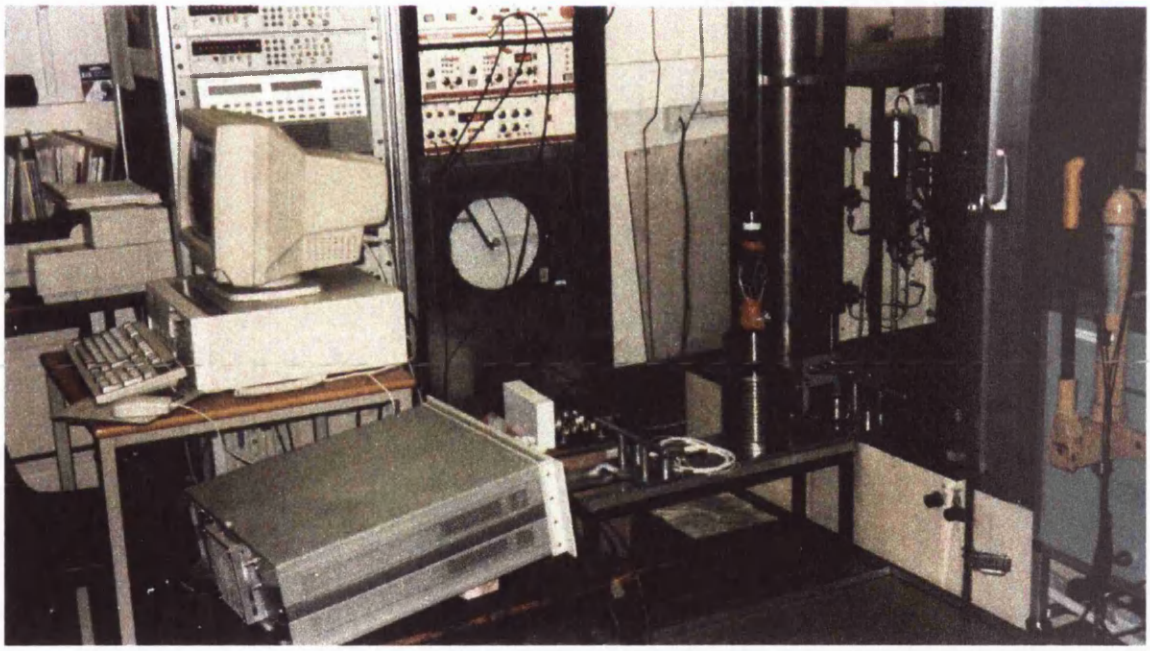

Figure 4-1 Laboratory set-up for triaxial deformation of rocks at high pressure and for the measurement of electrical potential difference, acoustic emission, stress, strain and pore fluid volumometry.

Under test conditions the pressure vessel sits in a plastic safety guard shield and is attached to the actuator and load cell via a yoke (Figure 4-2). Upper and lower rams are separated by the rock sample arrangement as described in Chapter 4.4. The upper ram is pressure balanced, i.e. the pressure applied to the bottom surface is equilibrated by an equal pressure on the upper surface. This design has the

advantage of requiring a less powerful actuator, to overcome greater confining pressures, hence load measurements are more accurate. Loading occurs through the upper piston and the upper ram. The sealing of closures and pistons is done with an O-ring and mitre ring arrangement, which are chosen due to their excellent elastic properties.

The apparatus is able to operate in different modes using the actuator to maintain a constant stress or strain rate. An alternative mode is achieved when the actuator is locked in position allowing relaxation experiments to be performed. To achieve these various deformation modes, the rate of advance of the actuator is controlled through a feedback signal from a linear variable displacement transducer, which is continuously referenced with a programmed signal. This control loop also helps to create a stiff loading apparatus, i.e., one, which unloads at a rate faster than the rock sample. 'Non-stiff' deformation systems can result in premature catastrophic failure of the rock (Rist et al., 1991).

4.3 Pressure Application Systems

4.3.1 Confining pressure

A silicone oil medium with viscosity of 100 cS is used to apply the confining pressure. This pressure is achieved using a two-stage hydraulic pump built by Stanstead Fluid Power, Stanstead, UK which can attain a maximum confining pressure of 400MPa. The confining oil is bled to vacant volumes along the loading ram annulus above an intermediate region of the upper piston. This procedure is the basis of the balanced ram, which ensures all parts of the sample receive equal hydrostatic stress before any deviatoric stresses are applied. The oil is isolated from the rock sample by the jacketing system, described below, and the pump is controlled via electrical contacts so that confining pressure can be automatically maintained regardless of any leaks at the required setting. Initially this setup did introduce noise contamination into the electrical measurement system but with the design of the improved electrical feed-throughs, this effect was eliminated (see chapter 4.4.4). Some physical properties of the silicone oil are given in Table 4-1.

Property	100cS Silicone Oil
Specific Gravity	0.960 (25°C)
Coefficient of Volume Expansion	0.00096
Surface Tension	20.9 (25°C)
Boiling Point	150°C

Table 4-1 Physical properties of the silicone oil used as confining medium.

The confining medium maintains pressure in two of the main principal stress directions namely the intermediate and least directions (σ_2 and σ_3). When the set confining pressure, as indicated by a pressure transducer, required for the experiment is reached, the vessel is then isolated from the pump which is then

switched off. The confining pressure is then allowed to equilibrate. The error in the measurement of the confining pressure is ± 2MPa.

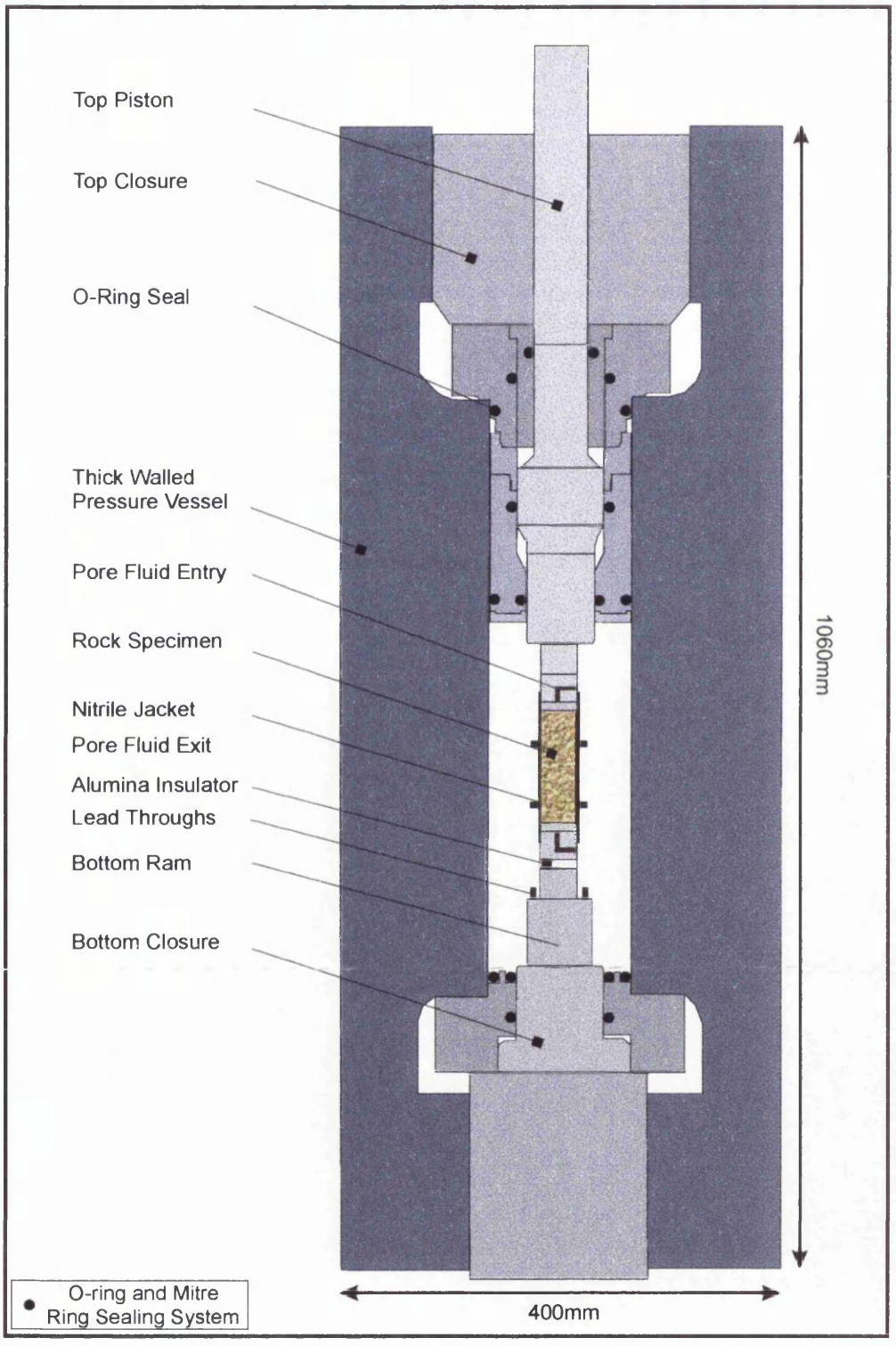

Figure 4-2 Schematic diagram of thick walled pressure cell used in this study. The position of the sample is shown between top and bottom rams. Internal sealing is accomplished using mitre ring represented by solid filled black circles. See text for discussion of main components.

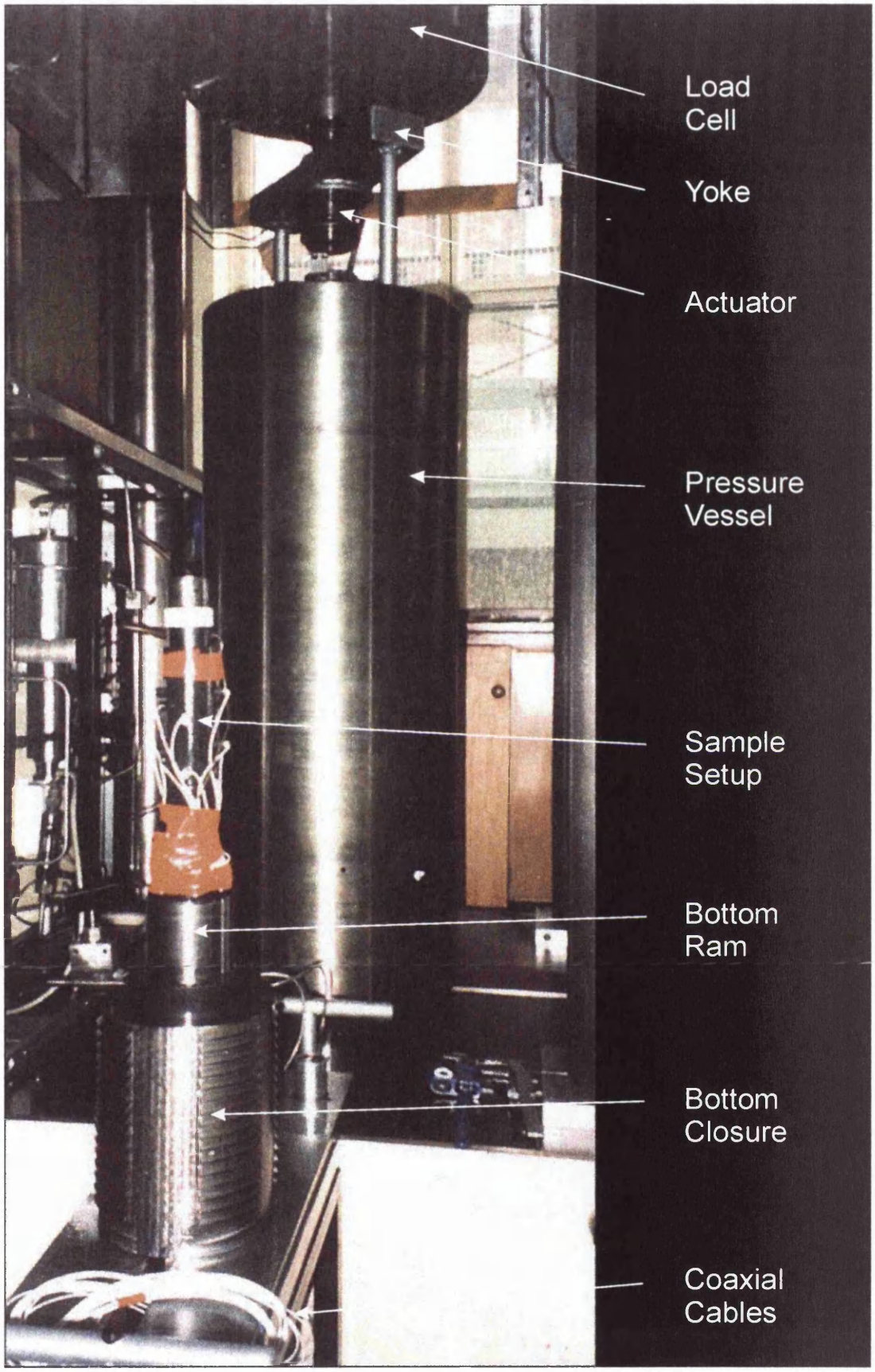

Figure 4-3 Photograph showing main components of the triaxial deformation equipment. The sample set-up is shown outside the pressure vessel, which is enclosed in a safety cubicle.

4.3.2 Pore Pressure

The application and control of pore pressure is important in brittle failure experiments as discussed in Chapter 2. Pore pressure regulation is achieved using a pressure intensifier system. A servo-controlled piston with displacement transducer attached and sealed within the intensifier, moves to apply pressure to small volumes of pore fluid. The internal volume is 10ml and this is capable of achieving 400MPa maximum fluid pressure. Pore fluid is introduced to the sample through externally plastic coated piping attached to the top of the sample arrangement. The necessity for plastic coated piping is described in section 4.4.3. Since porosity and permeability changes produce small relative changes in the pore fluid pressure and volume, highly sensitive transducers are required in the intensifier system. The transducers used here are capable of detecting variations of $\pm$ 0.02MPa.

4.3.3 Pore Fluid Separator

The current pore fluid intensifier cannot operate with salt solutions, which cause rust and corrode the internal seals and materials. A separator was therefore designed and implemented. It was introduced into the pore fluid system to provide a means of determining the effect of different brine concentrations on the generating mechanism of electrical potential signals.

Figure 4-4 shows the main components of the separator. It is essentially a pressure vessel with a moving inner plug (*shuttle*). The plug is sealed using a central piston GLYD seal with wear rings on the outer ends. The seal system employed can operate up to 80MPa of pore fluid pressure on either side. Two outer flanges, on the separator, are sealed with mitre rings and screwed into position.
The insertion of the separator into the pore fluid system is shown schematically in Figure 4-5. The pore fluid piping from the outlet of the intensifier is connected to the one side of the separator. When fluid is passed the central *shuttle* is displaced to the outlet. Using a manual pump, brine is introduced to the outlet, pushing the *shuttle* back. At approximately the midpoint, priming of brine is stopped and the outlet closed. The pressure can now be applied. Pore fluid piping is now connected from the outlet to the pore fluid piping around the rock sample. A calibrated pressure transducer monitors the pressure in this side of the separator.

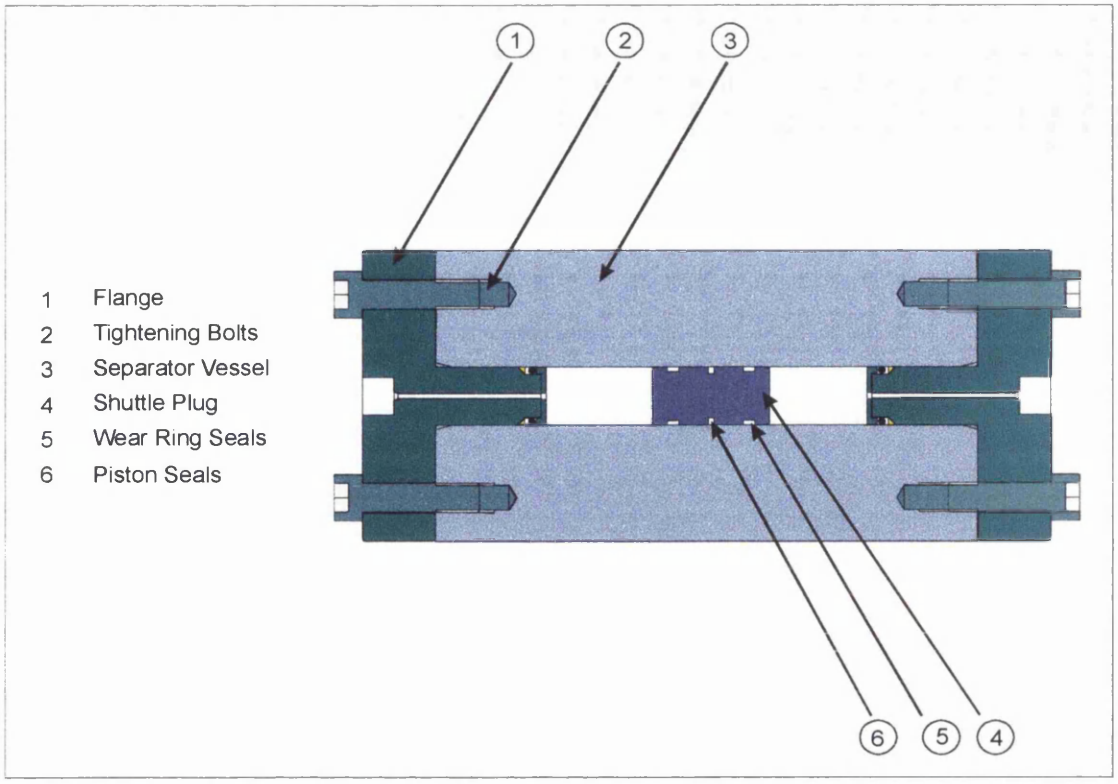

Figure 4-4 Diagram of pore fluid separator design. A moving shuttle plug separates corrosive brine fluids from distilled fluids and is sealed using standard piston and o-ring seals. Pore fluid pressures up to 80MPa can be used in this arrangement.

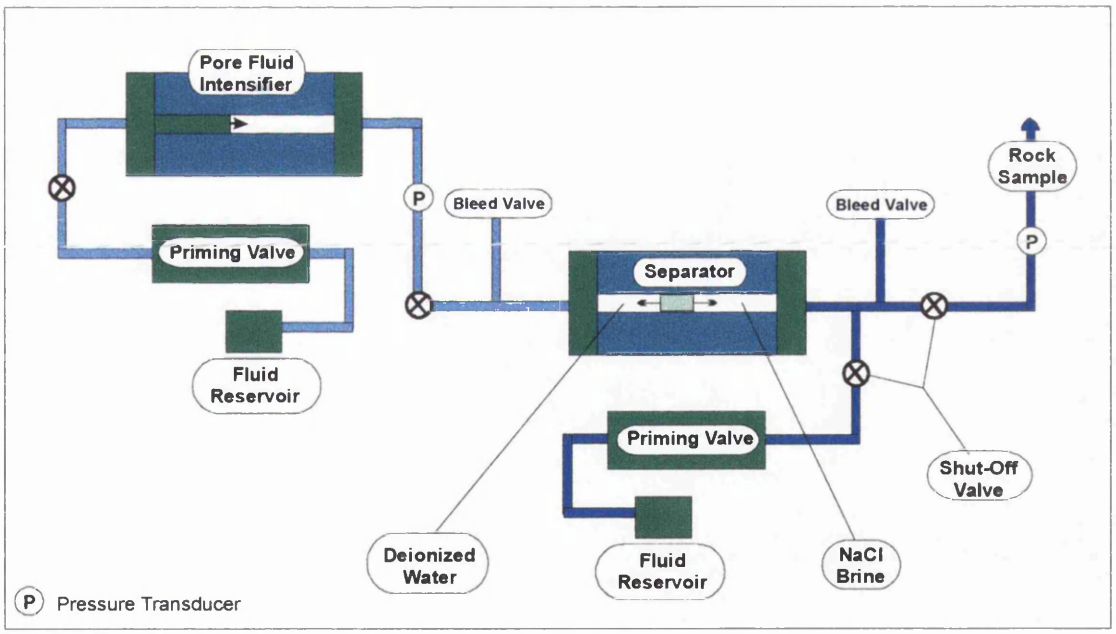

Figure 4-5 Schematic diagram displaying pore fluid system incorporating a separator. The right side of the system is primed with NaCl brine isolated from de-ionised water in the left of the system by the shuttle plug. Pore pressure is applied from the servo-controlled pore fluid intensifier and transmitted to the brines.

4.4 Rock Sample Arrangement

The sample assembly (Figure 4-3 and Figure 4-7) must be carefully constructed so that the rock is completely isolated from the confining pressure medium. It is also important that pore fluid can penetrate the rock homogeneously and that the pore fluid piping is isolated for electrical potential measurements. The jacketing, pore fluid and isolation systems are detailed now.

4.4.1 Jacketing System

A jacketing system designed by Dr. P. Sammonds and L. Lombos is required to prevent the silicone oil confining medium from entering the rock pores and cracks, thereby allowing pore fluid to be varied independently.

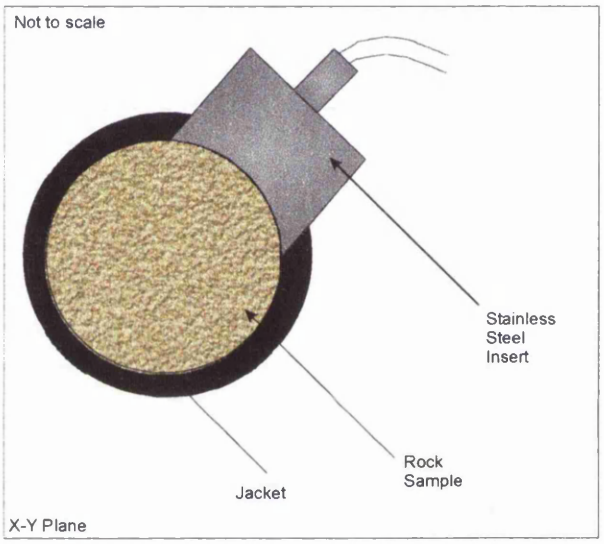

Figure 4-6 Expanded view of jacket and stainless steel inserts used to attach transducers and electrodes.

The jacketing system has been constructed of fluoroelastomer nitrile and can seal the rock efficiently from confining pressures up to 400MPa and temperatures up to 100°C. Specially designed holes, with internal o-rings in the circumference, allow stainless steel inserts to be placed in contact with the rock surface (Figure C-1 Appendix C). Each insert has been machined with a concave surface to allow increased surface contact with the rock (Figure 4-6).

The jacket is sealed by stretching two nitrile clasps around the jacket at the extreme top and bottom of the jacket. This has the effect of forcing the jacket against the sample and the pore fluid endcaps when confining pressure is applied. This method proved highly successful with only 3% of the experiments being abandoned due the problem of seal failure. The system is reusable unless frictional sliding on the fault surface occurs. This condition induces grooves on the inner surface of the jacket, which could allow increased local fluid flow along the rock surface. In this study the deformation path up to and during shear faulting was the subject of investigation and so this source of error was considered unimportant.

4.4.2 Pore Fluid Piping

Standard 1/16"inch high pressure pore fluid piping is attached to a pore fluid endcap allowing pore fluid to be introduced to the sample. The pressurized fluid permeates through the sample under the applied pressure forces from the top of the sample to the bottom and is the same for all the following experiments.

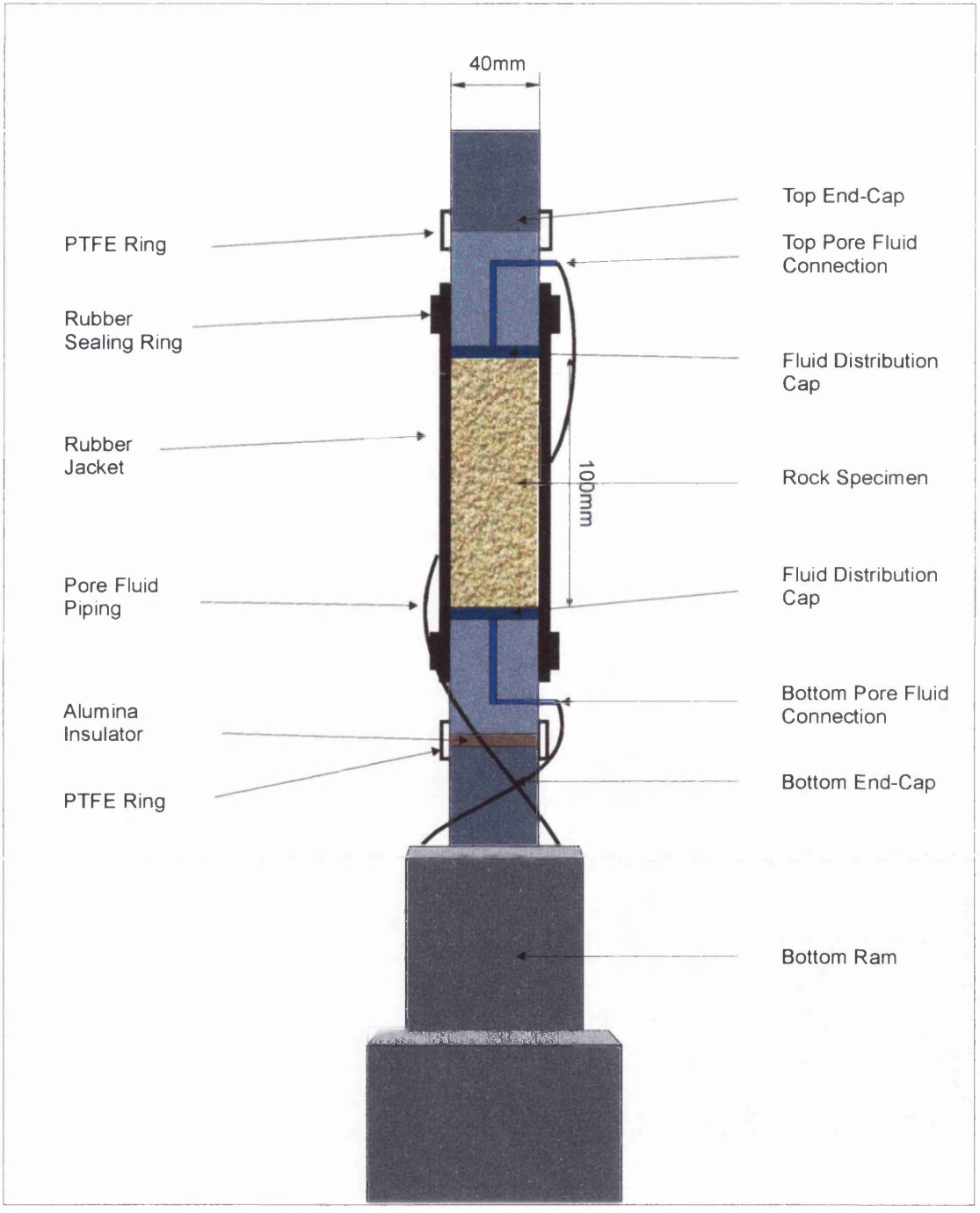

Figure 4-7 Experimental set-up for a typical triaxial deformation test. Pore fluid enters through a top pore fluid endcap, is disbursed through the sample evenly by means of a fluid distribution cap and exits at a bottom pore fluid endcap. A jacket isolates the sample from the confining oil and the bottom ram is used to align the vessel. The alumina insulator is necessary for electrical potential measurements (see text for explanation).

The endcaps are made from stainless steel, hardened through quenching to prevent deformation from the applied axial loads. They are located within the ends of the jacket system and therefore isolated from the confining medium. The piping exits from the vessel via cone seals located in the bottom closure.

4.4.3 Electrical Isolation

Electrical isolation is important for the measurement of electrical potential therefore an electrical grounding point must exist to eliminate noise. This is made available when the electrically grounded upper ram is in contact with the upper surface of the sample setup. The electrical potential difference between ground and four known electrode positions is then measured. To prevent charge leakage through the lower regions of the sample setup and the bottom ram an insulating alumina disk is placed below the lower pore fluid endcap (Figure 4-7). The coaxial cables used to record the electrical potential pass through lead-though plugs positioned within the bottom closure. The bottom closure is in contact with the triaxial vessel, which is also grounded. The methods used to pass data signals from the sample, to the logging instruments is described in the following section.

It may be possible for the stainless steel pore fluid-piping wound around the sample to be in contact with the electrodes, which would alter the measured signal. To prevent this a polyolefin heat shrink material surrounds all pore fluid piping for its entire length inside and outside the triaxial cell.

.

4.4.4 Modified Lead-through Design

I designed and implemented an improved lead through system, which allowed accurate data to be measured over long periods of time repeatedly. The initial lead-through design is shown in Figure 4-8. It has the unique design that three coaxial cables pass through the plug increasing the data acquisition capabilities. The central wires are unobstructed as they pass through the plug while the shielding wires are in contact with the plugs inner surface, which is grounded.

The coaxial wires are sealed from the confining pressure with a high strength epoxy resin. In practice this method was suitable at confining pressures up to 40MPa, though repeated experiments would induce cracking in the resin, leading to eventual failure.

In order to continue the experimental investigation to higher pressures a much-improved design was required. The main difficulty centred around maintaining the high data acquisition capability. The design shown in Figure 4-9 was finally implemented and repeatedly proved successful to confining pressures of 400MPa.

Separate coaxial wires are connected to the ends of the stainless steel connector pins. This pin is completely isolated from the plug utilising an ULTEM (see Table 4-2) insulating cone and ULTEM insulator. ULTEM is a low cost, high strength polymer with a high dielectric strength produced by the Polymer Corporation (USA).

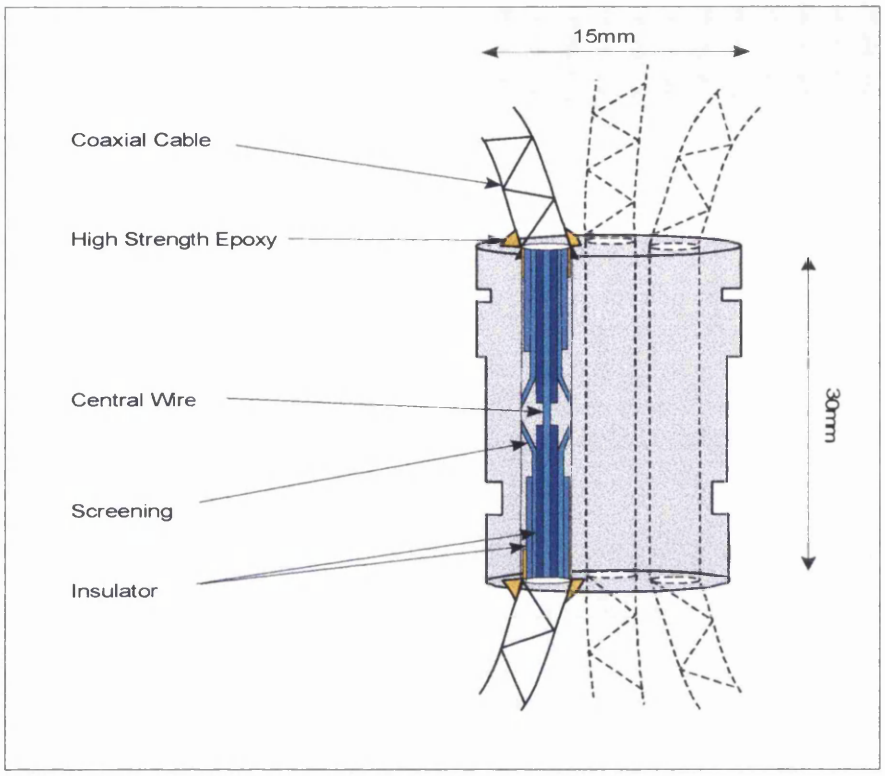

Figure 4-8 Lead-through design incorporating three separate coaxial cables passing through one plug. The sealing mechanism utilises a high strength epoxy resin. The central wire passes unobstructed through the plug while the shielding is attached to the grounded inner surface of the plug. Insulating coatings are also shown.

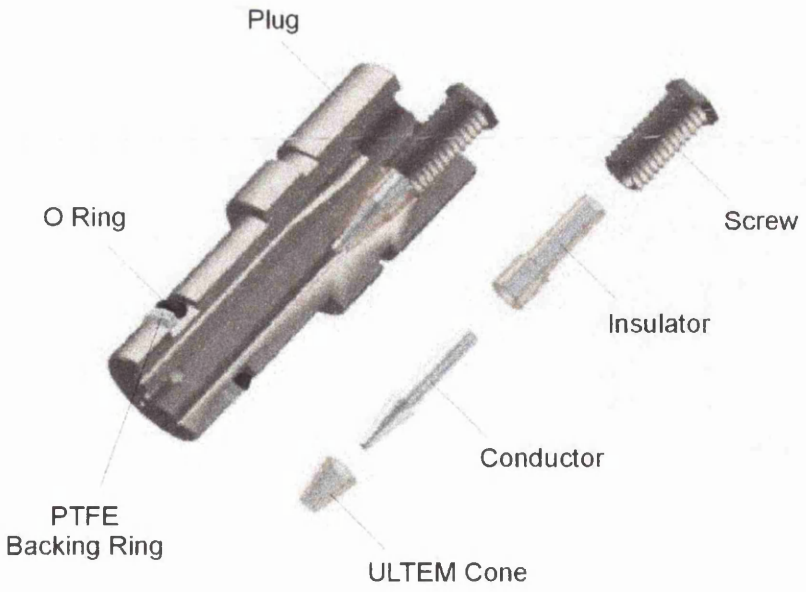

Figure 4-9 Improved lead-through plug design which operated successfully during experiments at elevated confining pressures up to 400MPa. The miniature components allowed three coaxial cables per plug maintaining the high number of data channels. See text for explanation of individual components.

Properties of ULTEM 1000	
Compressive Modulus	2877 MPa
Tensile Modulus	2945 MPa
Dielectric Strength (in oil)	710 V/mil
Volume Resistivity	6.7 E19 Ωm

Table 4-2 Physical properties of ULTEM 1000 relevant to the implementation of the improved lead-through design. The polymer acts as an insulator and as a seal within the plug.

The ULTEM cone seals deforms under pressure to create a seal against an internal machined shoulder in the plug. Under zero pressures a screw over the ULTEM insulator is used to perform initial sealing. Electrical isolation of the central coaxial wire is created using these ULTEM components. The shielding wires, of the coaxial cable, are made long enough to attach to screws positioned in the middle of the plug. The plug itself seals using a standard O-ring and PTFE backing ring arrangement.

4.5 Rock Type Description

The rock types selected were Darley Dale sandstone, Bentheim sandstone and Icelandic basalt. The rocks used in this study have been carefully selected because (1) their mineral content is useful to highlight certain effects, (2) the rock type shows good repeatability and (3) physical properties, such as approximate homogeneity are approached.
The mineralogical and micro-structural elements of each rock are now described.

4.5.1 Description of Darley Dale Sandstone

A photograph of Darley Dale sandstone shown in Figure 4-11a displays the microscopic mineral content under cross-polarized light. It can be described as poorly graded quartz-feldspathic sandstone bound with siliceous cement. Quartz dominates the matrix, accounting for approximately 75% of the mineral content, with 10% feldspar (plagioclase and microcline) and 15% clay and other minerals forming the remainder. The grains show angular to sub-angular geometry with diameters ranging between 8 - 800μm. As can be seen from Figure 4.11a, the quartz grains are approximately homogeneous with only a small degree of cracking visible in some crystals. The porosity of the rock varies between 13-17% and has a permeability of the order $10^{-15}m^2$.

4.5.2 Description of Bentheim Sandstone

Bentheim sandstone shown in Figure 4-11b can be seen to be predominantly composed of quartz crystals. The crystals, totalling approximately 95%, are held together with siliceous cement. The porosity is much greater in this particular rock and varies between 21 and 24% and notably no clay constituent minerals are present. The grain size varies between 0.1mm and 0.5mm and the grains are sub-rounded in character. As in the Darley Dale sandstone, the undeformed crystals are relatively homogeneous with little or no cracking evident.

4.5.3 Description of Icelandic basalt

Figure 4-11c shows Icelandic basalt microscopically, it is composed of plagioclase feldspar and pyroxene with some accessory minerals. This mineral composition can categorise the rock as tholeiitic basalt. It is a compact, high-density rock with porosity estimated at 3% and a permeability of the order $10^{-20}m^2$.

4.6 Rock Sample Preparation

4.6.1 Coring and Grinding

Right-circular cylindrical samples, taken perpendicular to bedding were prepared by primarily machining a 130mm length using a coring drill of 40mm radius and then ground down to a length of 100mm. To ensure the load was applied uniformly the top and bottom ends of the samples were ground flat to within ± 0.02mm using a diamond sintered grinding wheel. This was performed by repeatedly grinding off layers of 0.2mm until the required length was obtained.

The grinding process used a water/oil emulsion as a cooling and lubricating agent and therefore the samples were oven dried at 60°C for 2 days to eliminate all presence of these and any existing fluids.

4.6.2 Saturation Techniques

If the sample was to be used in a wet-saturated experiment, it was left in the required pore fluid under a vacuum of 10^{-3} Tor. The saturation time under vacuum was however dependent on the permeability of the rock. The sandstone samples remained in the vacuum for 2 days while the basalt samples required 7 days to be confident of high levels of saturation.

4.6.3 Preparation for Electrical Measurements

To create an improved electrical contact between the electrodes and the rock, a thin layer of silver paint was painted on the rock (Figure 4-10) in the form of a grid. This allowed for improved electrical contact while maintaining unrestricted surface area for fluid percolation.

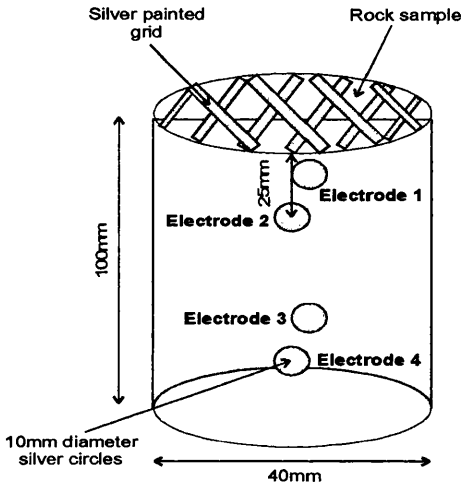

Figure 4-10 Schematic diagram showing rock sample preparation for electrical measurements. A thin silver grid is painted on the top and bottom surfaces while small circles are painted at the positions of the measuring electrodes to improve electrical contact.

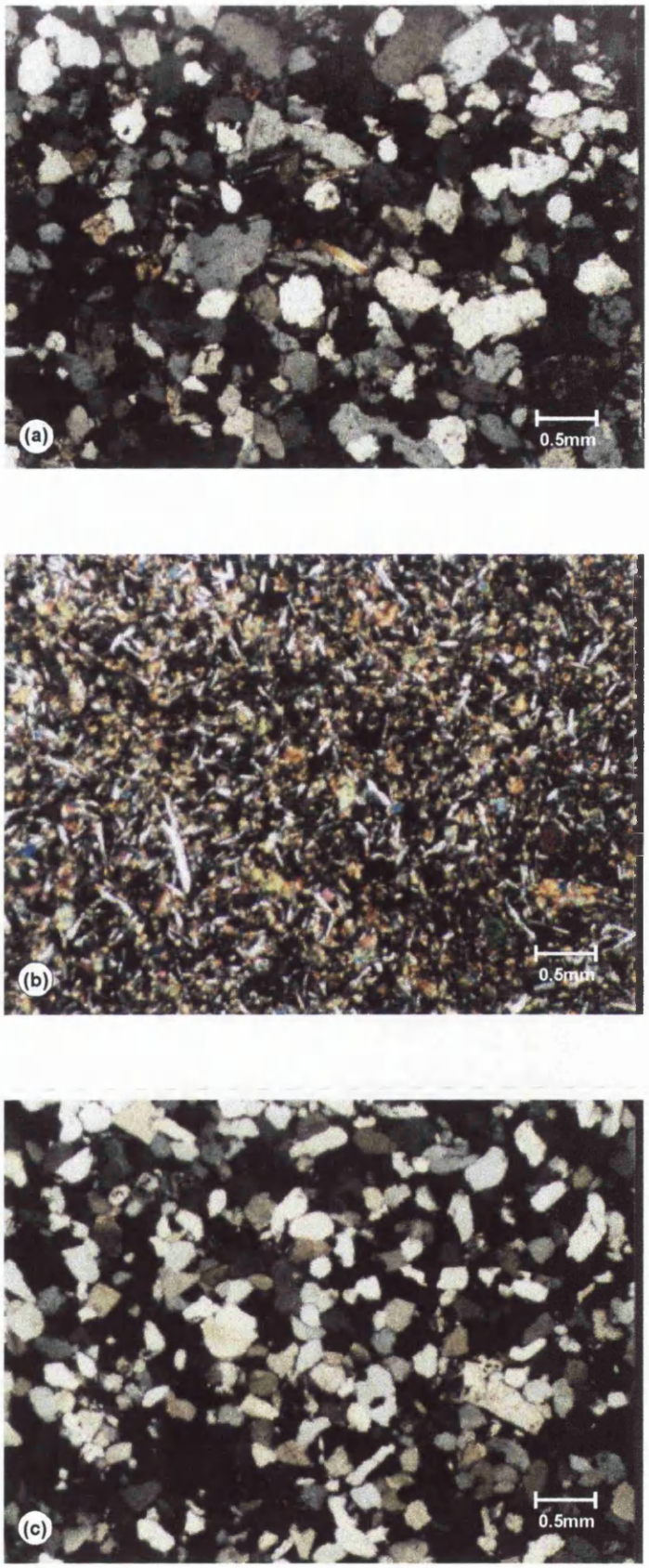

Figure 4-11 Photomicrographs of (a) Darley Dale sandstone, (b) Icelandic basalt and (c) Bentheim sandstone under cross-polarised light.

4.7 Measurements and Data Logging

The acquisition of data together with noise reduction techniques is described in this section. Figure 4-12 shows a block diagram of the measurement instrumentation, i.e. the electronic recording equipment connected to the triaxial cell.

4.7.1 Logging Systems

Data are acquired using a National Instruments LABview AT-MIO data acquisition card. Digital input values of axial load, axial displacement, pore pressure and pore fluid piston displacement were used. These values were output from the electronic servo-controller, which controls the load cell, LVDT's and pore fluid intensifier. Sampling rate was 10Hz but increased to 1kHz as dynamic failure was approached during deformation experiments. Electrical potential signals transmitted from the electrodes were primarily pre-amplified before sampling.

The LABview card was controlled using a National Instruments data acquisition module, which provides a digital waveform displayed within LABview graphical programming software. A display program was written to provide a graphical output of all input signals. Data was recorded to five decimal places.

AE were detected continuously using a 1MHz resonant frequency lithium niobate pressure wave piezoelectric transducer. Properties of the acoustic wave recorded by the analyser were amplitude, energy, and duration. Eight channels of AE were measured enabling 3D source location techniques, which aid the visualisation of spatial and temporal microcracking.

4.7.2 Load Measurements

A servo-controlled actuator applied a compressive force to the end of the sample set-up. The absolute value of this force was obtained using an external load cell, which determines the load from accurate resistance changes across a vertical strain gauge. This measurement was output as a voltage corresponding to the applied force. The calibration of the load cell is discussed in chapter 4.8.1.

To allow for uneven loading occurrences a hemispherical seat is placed between the loading actuator and the upper ram assembly. The main effect was to correct for distortion of angles between these surfaces. This distortion can arise from a rock surface, which is not completely smooth.

4.7.3 Displacement Measurements

Within this study brittle deformation is of primary importance, therefore low values of strain are recorded in this research. The upper ram and sample set-up shown in Figure 4-2 comprise the loading column, which is deformed by the axial differential load. Any displacement change is recorded using a pair of linear variable differential transducers situated between the pressure vessel and the top crosshead and then

calibrated to 0.01mm. The average measurement value is output and then converted to a displacement using the calibration outlined in chapter 4.8.1. It was necessary to correct the displacement for apparatus distortion, which for the setup used amounts to 0.004mm/1000kg of the differential load applied.

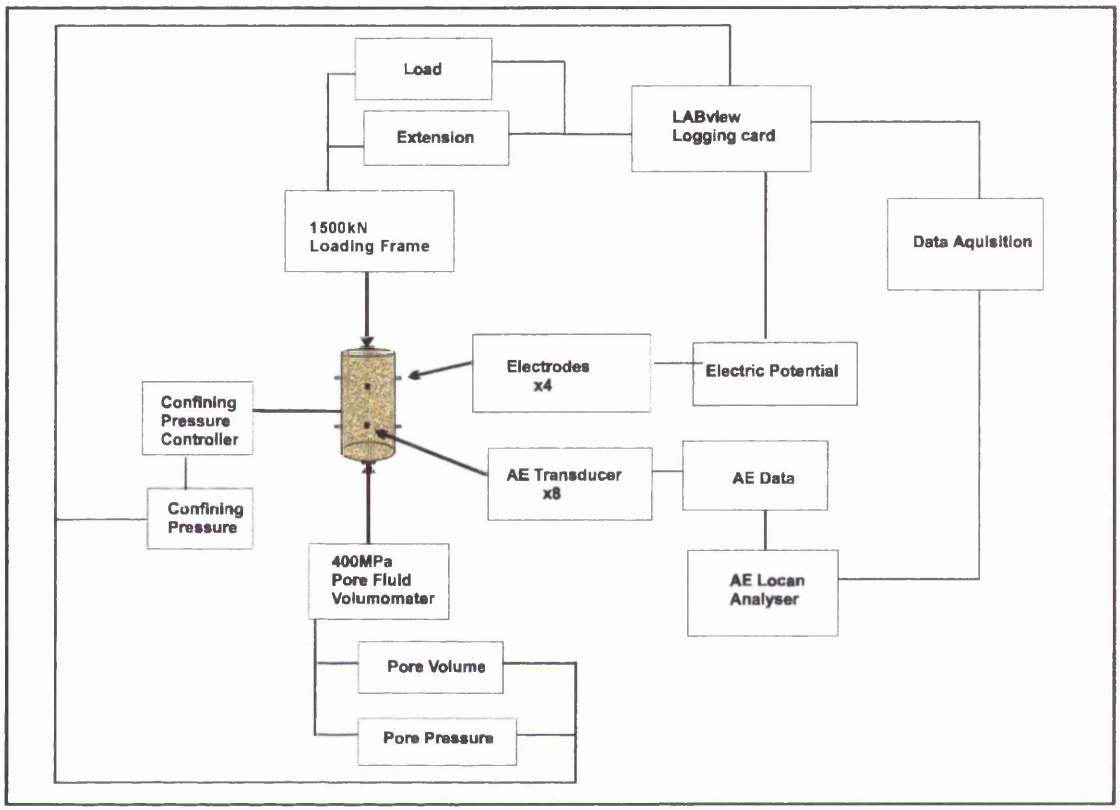

Figure 4-12 Block diagram showing main instrumentation involved in a triaxial deformation experiment and the resulting data acquired.

This displacement value is converted to normal strain, ε, using equation 4-1

$$\varepsilon = \frac{\Delta l}{l_0} \tag{4-1}$$

where Δl is the change in length of the original sample length l_0.

4.7.4 Pore Volume and Pore Pressure Measurements

The change in pore volume during triaxial deformation was quantified using the movement of a piston in a pore fluid intensifier. The intensifier has a volume of 10ml therefore the calibration of the displacement transducer was set to have a range of 10V. By monitoring changes in piston displacement, volume changes could easily be calculated.

The pore pressure was measured and monitored using a pressure transducer situated in the fluid-piping network close to the sample (Figure 4-6). The voltage output from the transducer was converted to a representative SI pressure using a calibration of 1V = 40MPa.

4.7.5 Electrical Potential Measurements

Electrical potential measurements were recorded from stainless steel electrodes in contact with the sample surface. Rock has a very high dielectric constant, which makes direct measurements difficult. The contact area was therefore lined with a thin film of conductive paint to improve the electrical contact. The difference between each electrode and the ground was measured using an electronic circuit with high input impedance of $10^{13}\Omega$. Electrodes were subject to polarisation due to ionic processes occurring near the contacts. At d.c. conditions this is negligible and not considered further.

The electrode potentials may fluctuate during the administration of a confining pressure and pore pressure fluid application, therefore sufficient time was given to allow the potential to stabilise. In the results chapters, some electrode magnitudes are given relative to a base value. This value is a constant value reached under hydrostatic conditions. In some data plots the electrical potential change is given. This is the difference between values recorded from the top and bottom electrodes (Figure 4-10). This is considered important because increasing the deviatoric stress will increase the surface resistance between rock sample end-cap assembly. This will undoubtedly increase the measured voltage at electrode positions and therefore presenting an electrode difference between, for example, electrode 3 and 1 will eliminate this effect.

A streaming potential is a constant voltage produced under a constant pressure gradient. Typical streaming potentials are shown in Figure 4-13, when a pressure gradient of 20MPa is applied to the sample. The streaming potential magnitude is given as the difference between the potential produced by the gradient and the nominal base value and presented, as is usual in the literature, in mV.

4.7.6 Acoustic Emission Measurements

Acoustic emissions are elastic waves spanning a range of frequencies emitted from the fracturing of crystals or the opening of a crack tip. These acoustic pulses are transmitted through the rock sample and recorded using piezoelectric transducers, which convert the mechanical energy of the wave to electrical signal. The transducers used were 3mm in diameter and were attached to the stainless steel insert with epoxy glue. This was to minimise the loss of acoustic energy at the transducer-insert interface. Signals were pre-amplified with a 40dB gain being applied.

Measurements in the frequency range 100 to 300kHz are generally used for 90% of AE testing in engineering disciplines, in areas of fluid flow however, the noise produced requires measurements in the range 500kHz. To record only signals of interest and reduce noise, 1MHz transducers were selected and each measurement point is grounded at the source. A description of the frequency response of these transducers can be found in Read et al. (1995).

The emitted signals were filtered, amplified and passed to a LOCAN AT Analyser. The LOCAN acquisition system described in chapter 4.5.1 is hit driven, storing AE information in grouping bins when an acoustic wave arrives. The bins when filled are stored to disk and the analyser is reset. The device

records properties of an acoustic wave with amplitude above set electronic amplitude threshold. The set threshold value is dependent on the background noise at the beginning of the experiment and usually a value between 45-50dB was chosen. With eight channels of AE data, it was noted that high hit rates could cause the bins to saturate with the possibility of data loss. This observation will be discussed further in the result chapters. For b-value calculations and mean crack analysis a numerical threshold is chosen to (1) normalise the experimental data to the same amplitude level and (2) prevent errors introduced through least-significant-bit noise in the a-d converter measuring the signal amplitudes. The consequence of this is that data at the bottom of the amplitude range are incompletely recorded. Under recording of events are discussed in detail by Cox and Meredith (1993) and taken into account by Sammonds et al. (1994).

4.7.7 Angle of Failure

The angle between the vertical corresponding to the axial compressive stress direction and the fracture plane is measured using a protractor. An error of 0.5 degrees is associated with each measurement. Some fault traces were curvilinear and not used in any analysis of shear fault angles.

4.7.8 Measurement Errors

Only the experiments, which produced useful data or results (Appendix C), which amounts to 61 out of a total of 75, are described in this thesis. A number of experiments could not be used. Reasons for the failure of an experiment include electrical shorting, noise from external motors, environmental noise, broken electrical lead-throughs, confining pressure leaks, failure of seals in pore fluid intensifier and instrument failure (electrical cut-outs).

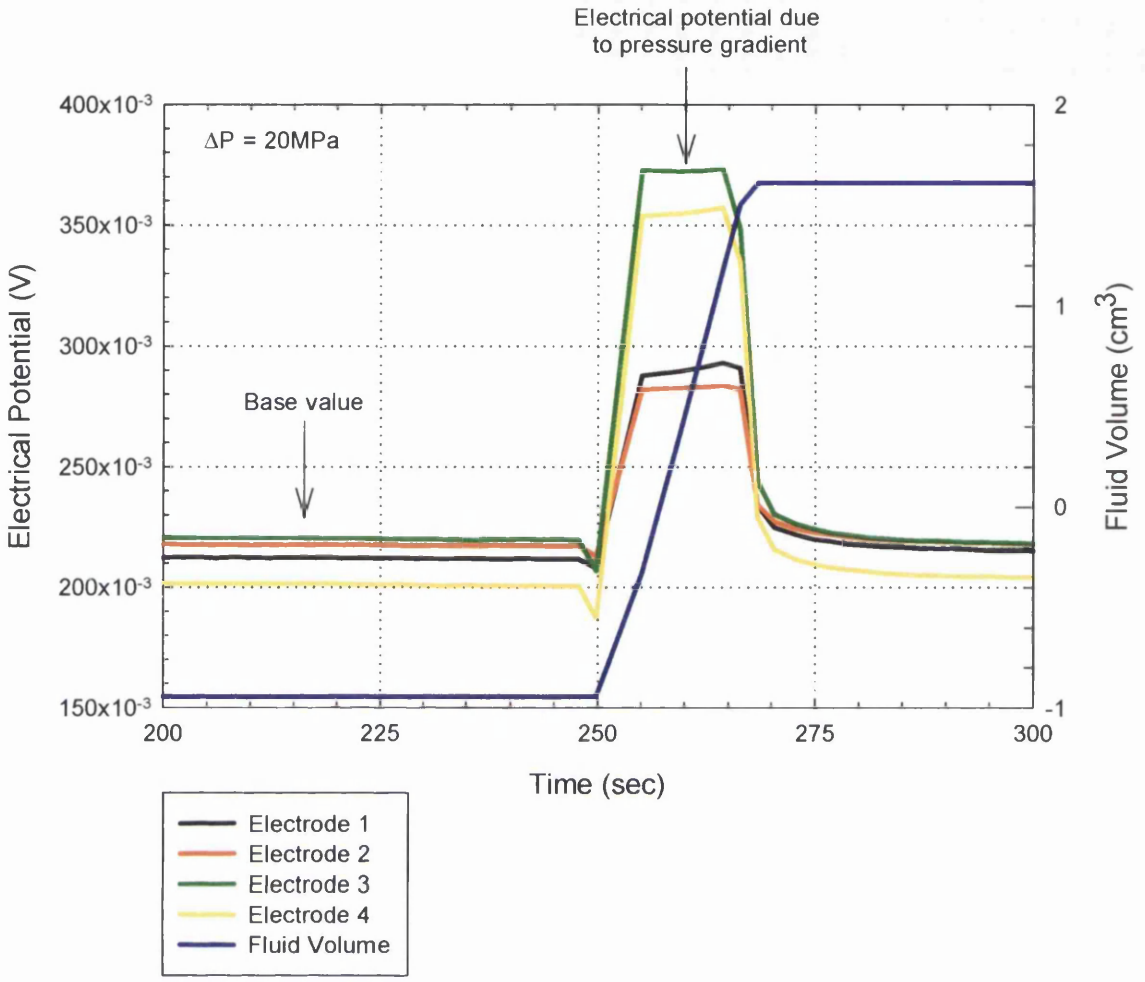

Figure 4-13 Plot showing streaming potentials generated by applying a 20MPa pressure gradient across a Darley Dale sandstone sample under hydrostatic conditions. The streaming potentials at electrode 3 and 4 are greater because the top surface of the sample is grounded.

4.8 Experimental Procedure

The procedure of performing a triaxial experiment is outlined. Initially the rock sample is prepared as described in Chapter 4.6. It is then placed between the fluid distribution plates and the pore fluid endcaps within the nitrile jacket as shown in Figure 4-6, with the nitrile seal in place. Piezoelectric transducers are then glued to eight of the stainless steel inserts and the central wire of the coaxial cable is soldered to the transducer. Screening wires from the coaxial wire are soldered to the insert. Four extra coaxial cables are attached to the remaining four inserts and acts as electrodes for the electrical potential measurements. All wires are carefully enveloped around the jacket, alignment is assured using a spirit level and the sample is placed inside the vessel.

A quarter turn on the bottom closure seals the vessel to the sample set-up. Confining fluid is pumped into the vessel and bleeds through to all areas including the area above the central piston so that the piston is

pressure-balanced. When the vessel is filled the intensifier automatically begins to pumps the oil medium and so increase the confining pressure. With the improved lead-through design the vessel can be isolated from the pump when the required pressure is reached and the pump switched off.

Coaxial wires are connected to individual amplifiers and logging computers. The balanced piston is now moved into contact with the top of the sample set-up and the external linear variable displacement transducers (LVDT) positioned and zeroed. The pore fluid, which is at pressure, is then let into the sample. The fluid is allowed to exit the vessel and then the outlet is closed. This procedure ensures that the fluid will saturate the entirety of the rock. The movement of the pore fluid intensifier piston is monitored and when it ceases movement, saturation is assumed to be complete. The time period for this operation is generally 1-2 hours. The servo-control is set for the particular type of experiment i.e. drained or undrained. The servo-controlled actuator is now changed to a ramp-generating mode, which allows constant strain rate to be maintained. The strain rate is set, logging initiated and deformation is begun.

For streaming potential and permeability measurements the ramp generator is stopped and equilibrium state is achieved. In this study these measurements were only performed under drained experimental conditions and therefore the rock can still be considered saturated. The outlet of the pore fluid network is then opened while a constant pressure gradient is maintained across the sample. The electrodes at this stage, will record the streaming potential and the displacement of the intensifier piston can be used to calculate the permeability using the volume change. After a measurement has been completed the sample is re-saturated and deformation is allowed to continue by starting the ramp function generator.

4.9 Error Analysis

Random errors are the unavoidable errors that enter into every measurement. To ensure the accuracy of the data in this study, the sources of error and corresponding uncertainties are presented in this chapter. Calibration techniques, routinely carried out, are outlined.

Table 4-3 presents some physical parameters, which are measured and set at the beginning of an experiment together with their associated uncertainties. These variables are determined from the appropriate measuring devices.

The effects of jacket strength are discussed by Ismail (1974). A calculation based on the stress acting on the jacketed and unjacketed sample is used to predict that for the case of rubber, its strength has negligible effect on the mechanical properties of the deforming sample.

Variable	Absolute Uncertainty
Confining Pressure	± 0.1MPa
Pore Pressure	± 0.4MPa
LVDT	± 0.005mm
Mass of Sample	± 0.005g
Length of Sample	± 0.01mm
Parallelism of Sample	± 0.01mm
Angle of Failure	± 0.5°
Conductivity of Pore Fluid	± 1μS

Table 4-3 List of physical variables measured and set at beginning of experiments together with absolute uncertainties.

4.9.1 Calibration Techniques

The uncertainty in the pore pressure, confining pressure and LVDT readings are dependent on accurately calibrated transducers. Stress, which is determined from the applied load, relies on the accuracy of the load cell.

The **load cell** was calibrated using a proving ring, which had maximum scale deflection equivalent to 200kN and was calibrated on purchase by Harry Stanger, Material Consultants (UK). An incrementing load was applied in stages to the proving ring using the servo-controlled actuator. The value of the applied load was read from the proving ring and the resulting voltage output was read from the load cell. Measurements were performed three times and the average voltage recorded. The results are plotted in Figure 4-14 as mean voltage ± standard mean error and show an excellent linear response. The slope of the regression line provided a calibration constant used to calculate axial stress.

The **LVDT's**, that measure the vertical displacement of the sample and upper loading ram, are calibrated using a micrometer head. A displacement is applied to the LVDT and the output voltage is read for a particular displacement. This average voltage is plotted against displacement (Figure 4-15) and a calibration of 1V = 1mm is obtained.

Changes in the volume of the **pore fluid intensifier** are representative of the change of the rock pore volume. Therefore the initial volume must be known so that the digital readings from transducers correspond to realistic volume changes. By priming the intensifier fully and forcing the fluid out into a measuring cylinder, the meniscus was found to lie along the 10ml graduation. The displacement transducer which records movement of the piston was then set to have a range of 10mm, providing a 1mm = 1ml calibration constant.

The pore pressure is measured using a pressure transducer, connected to the pore fluid piping system depicted in Figure 4-5. To obtain a calibration constant for this transducer, a dead weight tester applied a

series of pressures to a column of oil, producing a corresponding voltage output. The values are plotted in Figure 4-16 and shown a linear dependence of voltage output on pressure.

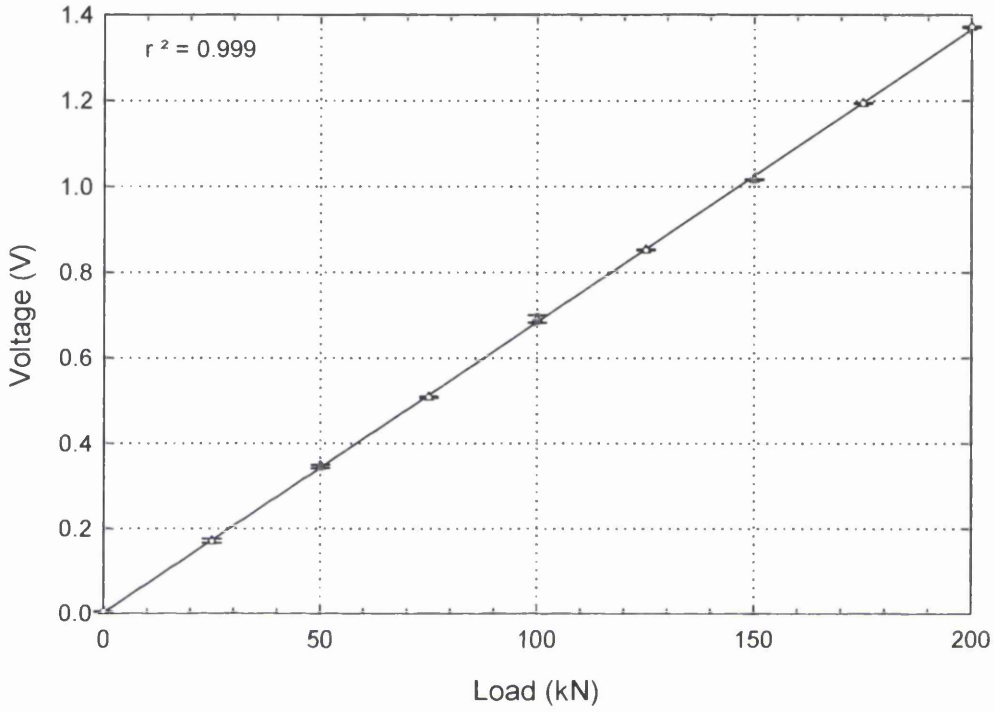

Figure 4-14 Calibration of the load cell used to determine axial differential stress plotted in the result chapters. The voltage output from a digital voltmeter is plotted against the applied load using a proving ring. The values plotted are $\bar{x} \pm \sigma_{\bar{x}}$ and $r^2 = 0.999$.

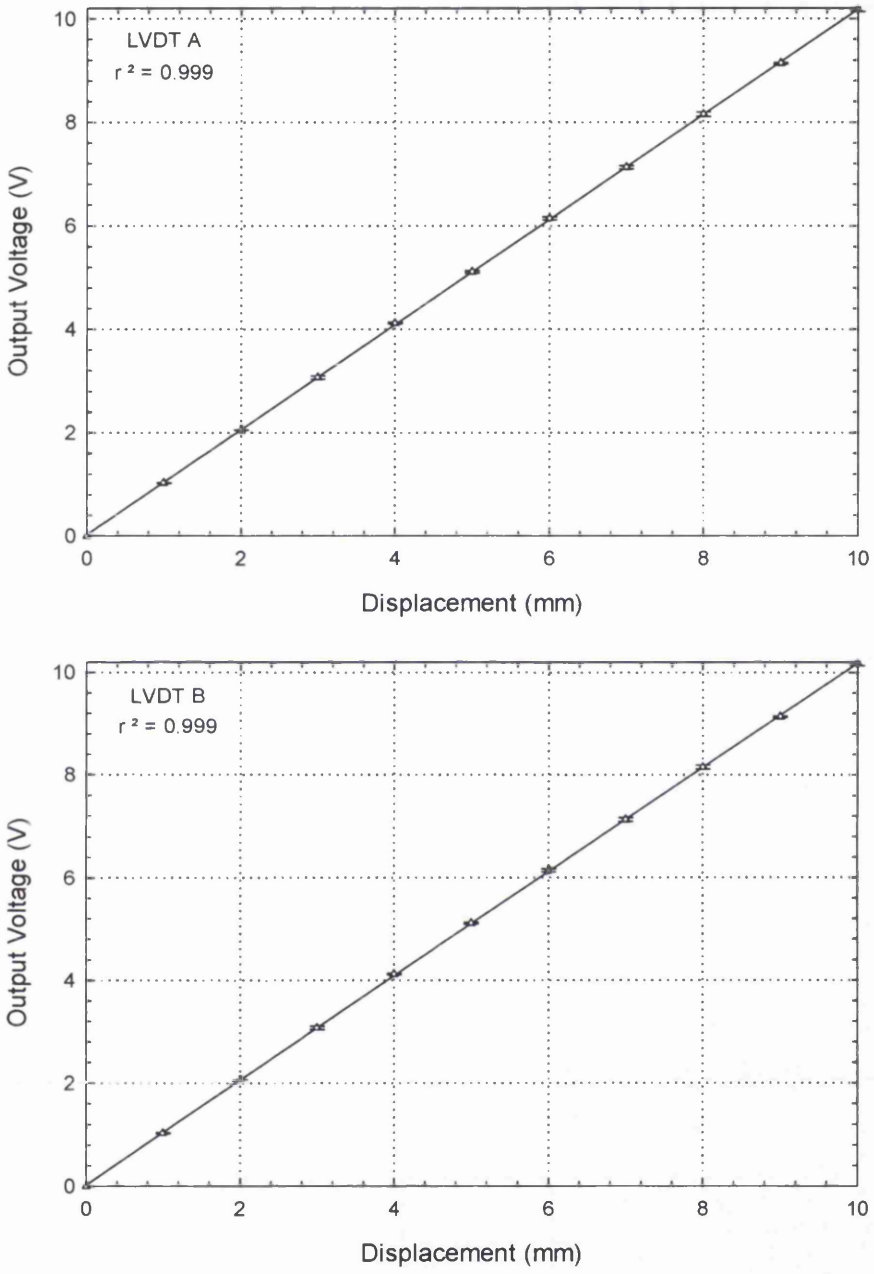

Figure 4-15 Calibration of linear variable displacement transducers used to determine axial strain applied to the sample set-up. Upper plot shows LVDT A and below is LVDT B, the strain was computed from the average of the two. The values plotted are $\bar{x} \pm \sigma_{\bar{x}}$ and $r^2 = 0.999$.

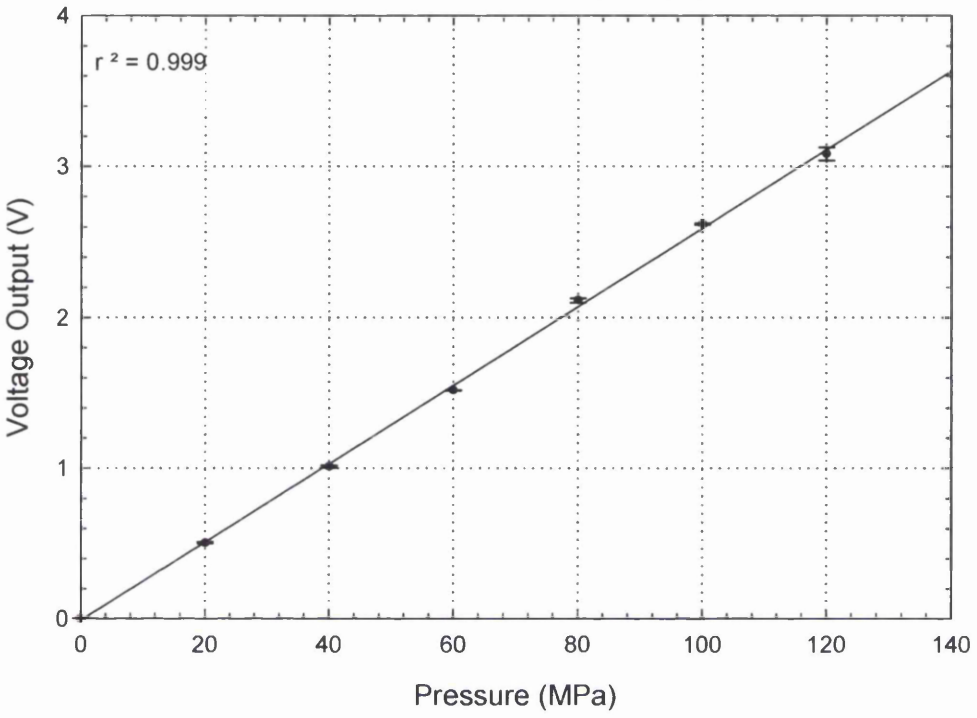

Figure 4-16 Voltage output from pore pressure transducer using dead-weight tester. The slope of the curve gives a calibration constant for experimentally measured values. The values plotted are $\overline{x} \pm \sigma_{\overline{x}}$ and $r^2 = 0.999$

5. Initial Observations of Electrical Potential Signals from Fracture of Crustal Rocks

5.1 Introduction

In this chapter I present a set of electrical potential results due to shear fracture of some typical crustal rocks. The rocks have been deformed at varying confining pressures using distilled water as pore-fluid under drained, undrained and water-free conditions at room temperatures.
The typical crustal rocks used are (i) Darley Dale sandstone which has approximately 75% quartz with the remainder being feldspars and clays, (ii) Bentheim sandstone which has approximately 99 % quartz and (iii) Icelandic olivine rich Basalt with no visible quartz. The porosity of these three rocks is 14%, 24% and 3% respectively and the hydraulic permeability is 10^{-17} m^2, 10^{-15} m^2 and 10^{-20} m^2 (see Chapter 4.5 for full rock descriptions). This study involves continuous measurements of electrical potential and acoustic emission through triaxial deformation on this suite of rocks.

The principal objective of this series of experiments was to identify the electrical potential signals and identify the signals due to the various likely generating mechanisms discussed in Chapter 3. The sandstone samples were used to observe the piezoelectric signal during deformation under water-free conditions and to record the expected changes when pore fluid was introduced, as electrokinetic mechanisms were then expected to operate. It was important to separate these two signals and this was possible by also observing and comparing with the electrical potential signal from fluid saturated quartz-free basalt. Finally the deformation of basalt, without any quartz or fluid should allow non-piezoelectric and non-electrokinetic signals to be observed if they exist.

A dynamic stress/strain curve for a typical deformation path has been described together with the associated d.c. electrical potential changes. Corresponding information on microcracking was obtained from acoustic emission (AE) data. Four electrodes were electrically coupled to the rock surface during all experiments and labelled electrodes 1 to 4 (Figure 4-10). The electrical potential difference from each electrode, 1 to 4 was measured. The signal magnitudes were plotted in mV to allow correlation with values in the literature, which report signals of the order of mV.
The electrical potential differences were plotted concentrating on values obtained during the period around dynamic fracture. This strain window was selected as it encompassed the largest stress change during catastrophic failure and so was expected to give rise to a maximum observable electrical potential signal as proposed in Chapter 3.4.1. The reasoning behind this assumption stems from electrical potential signals measured during slip on granite and the proposed model suggesting generation of piezoelectric signals from large stress drops (Yoshida et al., 1997). Also if electrokinetic phenomena (Ishido and Mizutani, 1981, Jouniaux and Pozzi, 1995b) are responsible for electrical potential signals, then dilatancy under drained conditions will create fluid movement in cracks (Scholz et al., 1973) causing an electrical convection current released during the co-seismic stress drop.

The results achieved aid in understanding the generating mechanism of these signals. The effects of varying salinity fluids, confining pressures, pore fluid pressures and strain rates will be discussed in the succeeding chapters.

5.2 Comparison of Electrical Potential Signals from Darley Dale Sandstone and Icelandic Basalt during Dynamic Failure under Drained Conditions

A typical stress strain curve for the mechanical deformation of Darley Dale sandstone is shown in Figure 5-1a [Experiment 7]. The curve shows a quasi-elastic linear phase between 0 and 0.5 strains. During this phase, compaction takes place, forcing closed existing pore and crack porosity as the rock attempts to accommodate the applied strain. This can be observed indirectly by a decreasing pore volume change as shown in Figure 5-2.

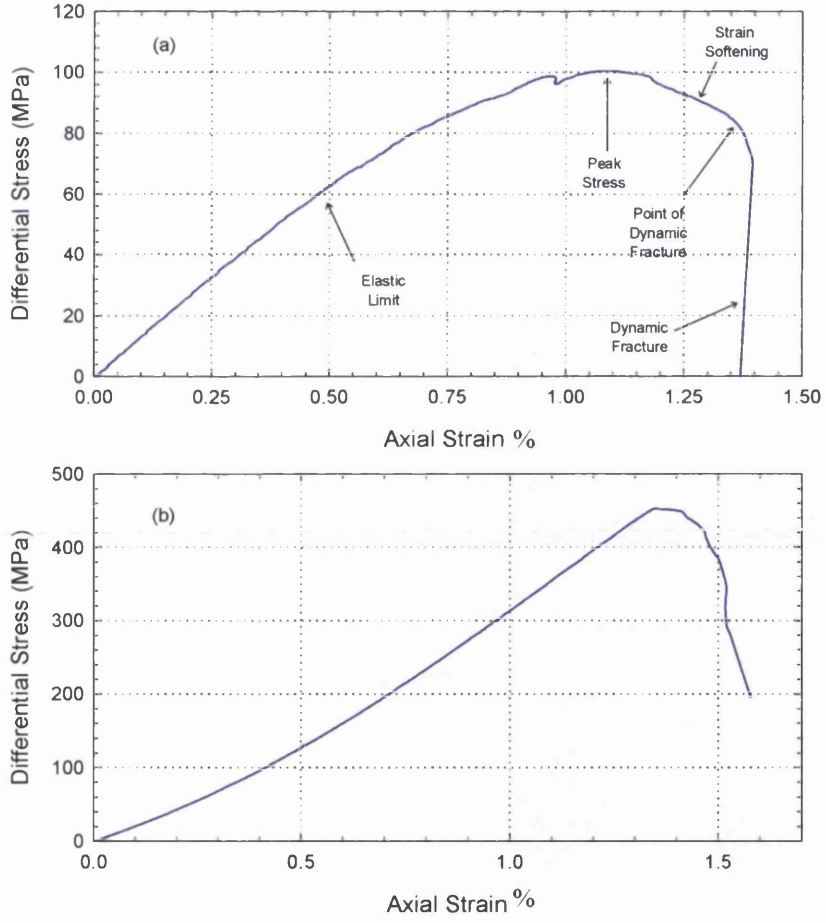

Figure 5-1 A typical stress-strain curve for triaxial deformation of (a) Darley Dale sandstone deformed at an effective pressure of 20MPa and (b) Icelandic Basalt at an effective pressure of 10MPa; both experiments were conducted at a strain rate of $1.5 \times 10^{-5} s^{-1}$. [Experiment No.: (a) 7, (b) 8]

A departure from linearity, representing strain hardening, is then observed until a peak stress is reached at 1.24 % strain. A period of strain softening ("rollover") then occurs leading to dynamic shear failure of the sample at 1.1% strain. This mechanical behaviour can be considered representative of Darley Dale sandstone and is observed throughout the majority of the experiments performed in this investigation as shown in Figure 5-3. The stress/strain behaviour for Icelandic basalt is plotted in Figure 5-1b and shows a quasi-elastic linear phase of increasing stress with strain up to approximately 450 MPa. Dynamic fracture occurs at this point with violent energy release causing damage to the sample setup.

In Figure 5-4 the d.c. electrical potential difference approaching failure and during dynamic fracture is plotted for experiments on both water-free and saturated Darley Dale sandstone and Icelandic basalt.

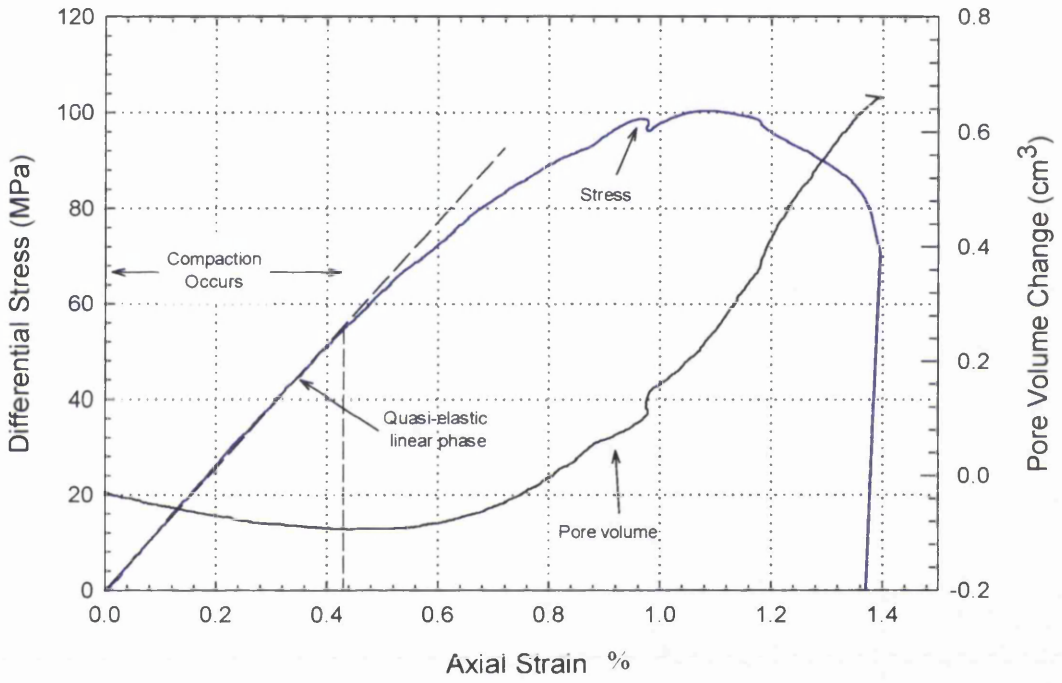

Figure 5-2 Differential stress and pore volume change as a function of axial strain. The quasi-elastic linear phase correlates well with a pore volume decrease in the rock and corresponds to compactive processes.

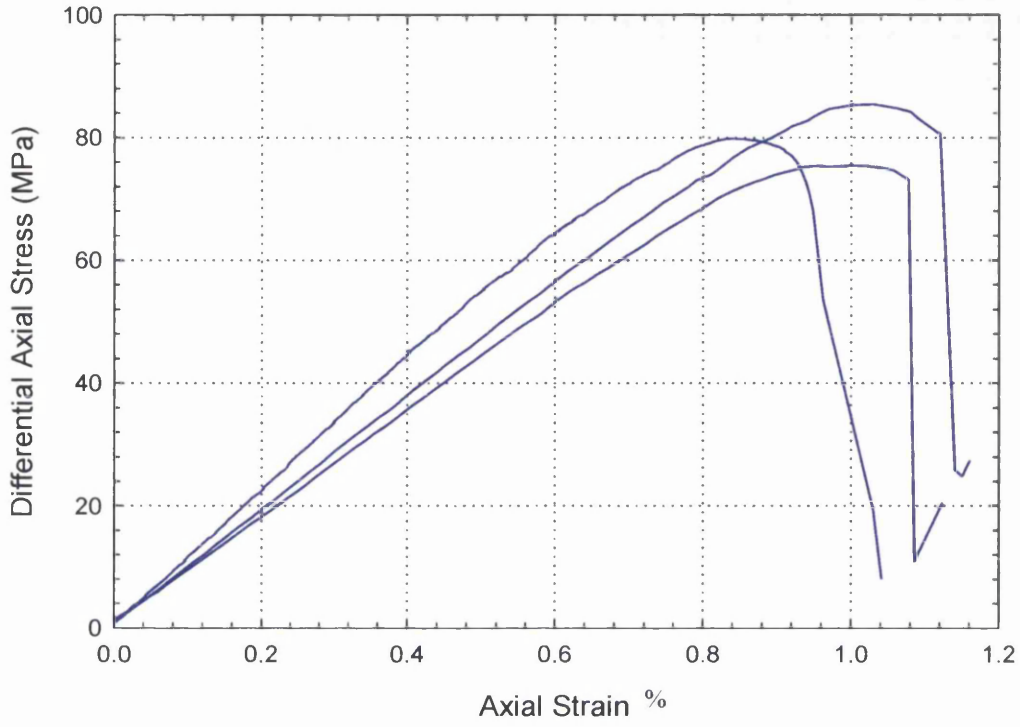

Figure 5-3 Differential stress as a function of axial strain for three identical experiments on Darley Dale sandstone showing the level of repeatability obtainable. [Experiment No.:7,15,23]

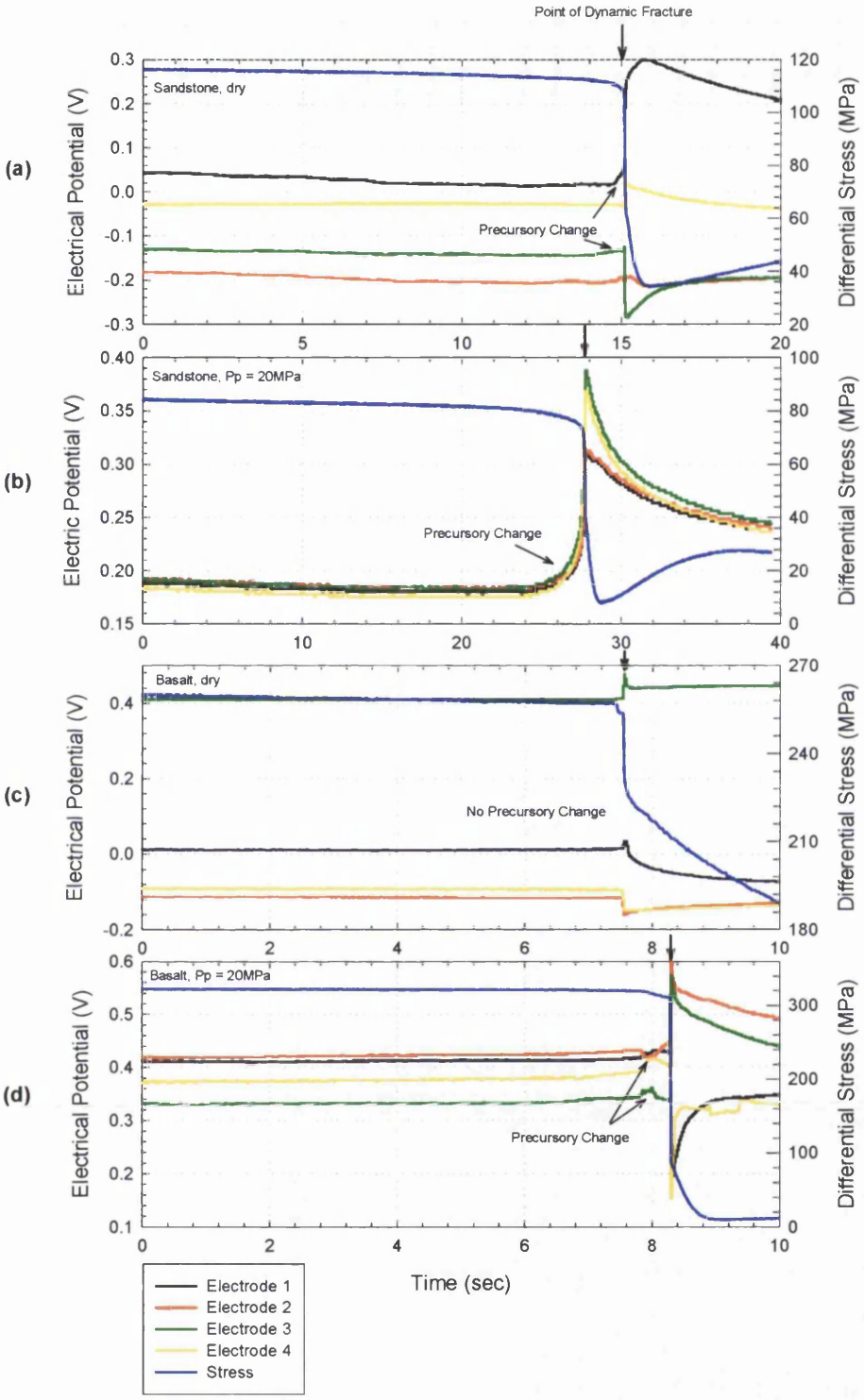

Figure 5-4 The electrical potential signals produced during strain softening and shear failure of Darley Dale sandstone (DDS) and Icelandic basalt (IB). (a) DDS, confining pressure (Cp) = 20MPa, no pore fluid. (b) DDS, Cp = 40MPa, pore pressure (Pp) = 20MPa, distilled water as pore fluid. (c) IB, Cp = 20MPa, no pore fluid. (d) IB, Cp = 30MPa, Pp = 20MPa, distilled water as pore fluid. The strain rate was $1.5 \times 10^{-5} s^{-1}$. [Experiment No.: (a) 11, (b) 6, (c) 9, (d) 8]

Figure 5-4a shows the electrical potential recorded from four positions on the sample surface from a dry sandstone. The experiment was conducted at a confining pressure of 20MPa on Darley Dale sandstone. The differential stress decreases slowly to 108 MPa and drops suddenly to 36 MPa, after which the servo-controlled loading ram achieves stable sliding at a residual stress level. Electrical potential signals show no observable deviations from the background noise level (3mV) during the decreasing pre-seismic period, until approximately 1-second before the stress drop. This change is manifested through small signal variations of the order of 20 mV displaying both positive and negative polarity. This polarity variation was not dependent on the electrode position and changed with each experiment performed under water-free conditions.

Corresponding with the dynamic stress drop is an abrupt increase in the electrical potential with an average magnitude of 107mV recorded between experiments; the polarities again depend on the individual measurement position. During the period when residual stress levels are approached, the electrical potential decays to a nominal base value. If a homogeneous charge distribution were present in the sample, electrodes 1 and 2 would show similar values while electrodes 3 and 4 would be approximately double due to the top of the sample set-up being grounded. I have therefore demonstrated that electrical signals during dynamic failure are not due to a homogeneous electrical field but rather local electrical dipoles.

In Figure 5-4b the strain-softening period was seen to decrease to 74 MPa followed by a co-seismic stress drop of 62MPa. In contrast to the water-free experiment, described previously, an electrical potential signal increase of approximately 100mV occurs 2 seconds before the co-seismic stress drop. The magnitude of the signal, corresponding with the stress drop, is approximately 115mV for electrodes 3 and 4, and 40mV for electrodes 1 and 2. Interestingly all four electrode show similar behaviour during the pre-seismic period and exhibit a spike and decay type signal at failure. The character of this signal appears to be produced by a different mechanism, which creates a net charge within the sample prior to and during dynamic failure.

Strain softening is also observed during an experiment conducted on water-free Icelandic basalt (Figure 5-4c). The stress decreases to approximately 258MPa, at which point a dynamic stress drop of 36MPa occurs. No existence of pre-seismic electrical signals can be determined, while co-seismic signals, with an average magnitude of 35mV, are evident for a stress drop of approximately 32MPa. In this experiment the hydrodynamically generated electrokinetic effects can be excluded and the absence of quartz rules out any piezoelectric effects suggesting alternative mechanisms in play.

Introducing distilled water at 20MPa as pore fluid and applying 30MPa confining pressure to the basalt resulted in the data shown in Figure 5-4d. Strain softening is not clearly defined in this experiment, though a small stress drop at 160MPa, one second before the ultimate dynamic stress drop, produced observable electrical potential signals. All four signals showed positive and negative polarities prior to dynamic failure with an average peak to peak amplitude of 20mV. With a stress drop of 220MPa, co-seismic electrical potential signals were produced with an average magnitude of 232mV. The

introduction of pore fluid did not appear to create a net charge in the basalt although pre and co-seismic signals have been observed, similar to those of the saturated sandstone experiment.

In Figure 5-5, the results from a experiment conducted at 75MPa confining pressure without pore fluid are presented. It can be observed that no pre-seismic or co-seismic signal can be detected on electrodes 1 and 2 while significant electrical potential changes are detected on the lower electrodes 3 and 4. It is noted that, in this case, the co-seismic stress drop is 360MPa, a factor of 12 greater than the situation represented by Figure 5-4c.

In contrast, Figure 5-6 shows data from thermally cracked Icelandic basalt sample deformed at the same conditions as Figure 5-4d. Since a network of cracks has been induced, the potential for fluid and current flow is greater and hence the sample is not considered a closed system. This has important consequences e.g. at peak stress of 480MPa the electrical potential begins to fluctuate and increase in magnitude until co-seismic signals are produced at dynamic failure of the sample. The occurrence of rapid increases in the pre-seismic period corresponds to a change in the stress rate and believed to be due to convection current flowing during episodic growth of the macroscopic fracture. This is caused by local enhancement of the pressure gradients assuming constnat zeta potential, fluid conductivity and pH.

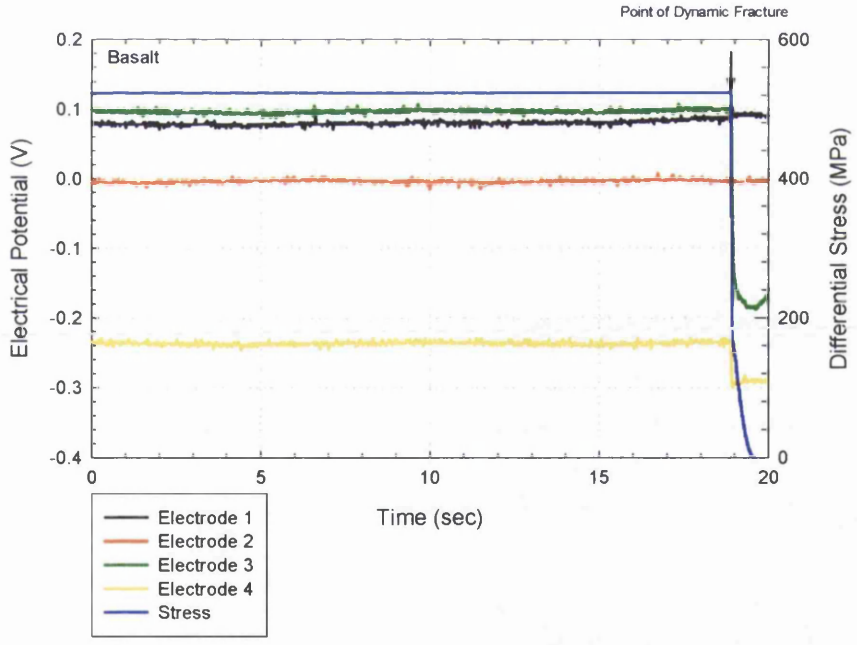

Figure 5-5 Electrical potential difference during the approach to failure and during dynamic shear fracture of Icelandic basalt. A confining pressure of 75MPa was used without the use of pore fluid. [Experiment No.: 31]

At ultimate failure, the average co-seismic signal magnitude is 333mV, which is higher than the co-seismic signal magnitude of the non heat-treated basalt sample by a factor of 1.5. The pre-seismic signal

observed (293mV) is a factor of ten greater than the non-thermally cracked rock. These results can be expected since more fluid pathways are created due to the presence of new cracks induced through the heat treatment which causes an enhancement of the local pressure gradients. The results are consistent with the previous experimental interpretations that the post peak stress region is associated with crack growth and linkage towards an ultimate macroscopic fault (Nur, 1972; Scholz et al., 1973).

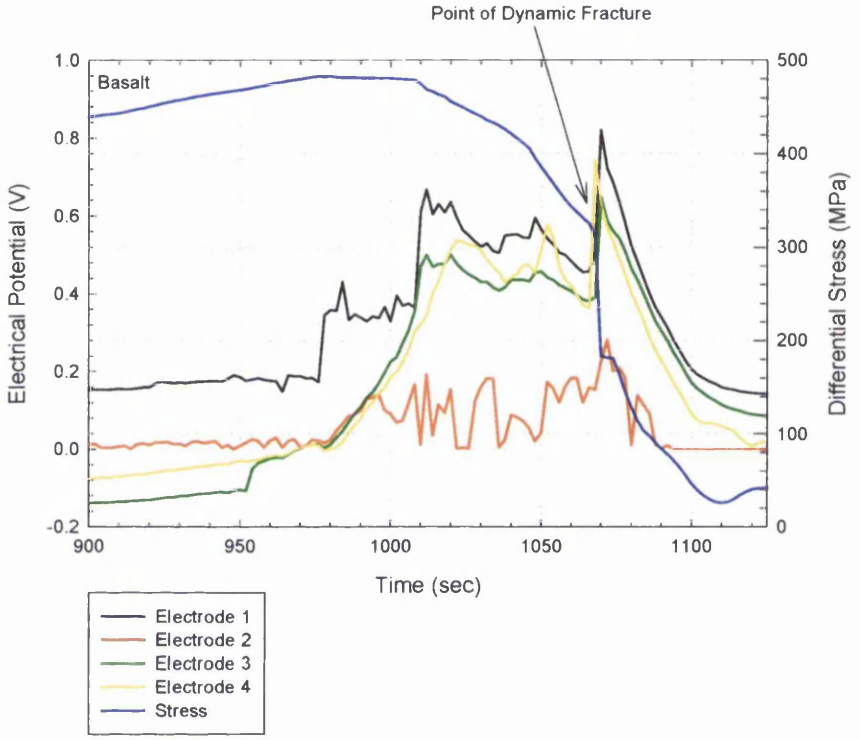

Figure 5-6 Electrical potential differences during strain softening and fracture for thermally cracked basalt. An effective confining pressure of 10MPa was used under drained conditions and a strain rate of 1.5×10^{-5} s^{-1}. [Experiment No.: 16]

The evolution of the earth's crust is strongly affected by the actions of fluids; by through mechanical effects, mineral and fluid phase reactions (Lebedev et al., 1996) and diagenesis. It is therefore important to include fluids during experimental deformation studies and the results obtained from these considerations can be used to understand the mechanics of the deforming crust. The current results therefore prove that electrical potential signals are generated under crustal conditions and strongly suggest that the electrokinetic effect is their dominant generating mechanism.

5.3 Comparison of Electrical Potential Signals from Bentheim Sandstone with Darley Dale sandstone During Shear Failure

The dynamic failure for a water-free Bentheim sandstone experiment is shown in Figure 5-7a. For a dynamic stress drop of 20MPa, equal to half that of water-free Darley Dale sandstone (Figure 5-4a), the pre-seismic electrical potential signals in Bentheim have a similar average magnitude of 20mV. The co-seismic electrical potential signals have an average magnitude of 40mV, which is an order of magnitude smaller than those detected in Darley Dale sandstone. Pre-seismic and co-seismic electrical potential signals vary in polarity depending on the measuring electrode. This result was found during all experiments conducted on Bentheim sandstone under water-free conditions.

Electrical potential differences during shear fracture of saturated Bentheim sandstone are presented in Figure 5-7b. The signals are similar in character to those measured from saturated Darley Dale sandstone and show concavity upwards followed by a peak and then an exponential decay to a residual value. The pre-seismic signals all show the same polarity, which is the same as the direction of movement of the pore fluid (Figure 5-2). They exhibit an average value of 30mV, smaller than those detected in Darley Dale sandstone. It is also noted that the pre-seismic signals are observed originating nearly 3.5 seconds before the main stress drop and therefore is comparable to the onset time of the pre-seismic electrical signals in Darley Dale sandstone.

Co-seismic electrical potential signals during dynamic shear fracture have an average value of 65mV. This value is an order of magnitude less than the average co-seismic signal found in Darley Dale sandstone even though the rock has a higher permeability and porosity. The zeta potential may also be different butis not expected to create such a large change since they are both quartz-water systems. The polarity of the signals is positive upwards and found on all electrodes.

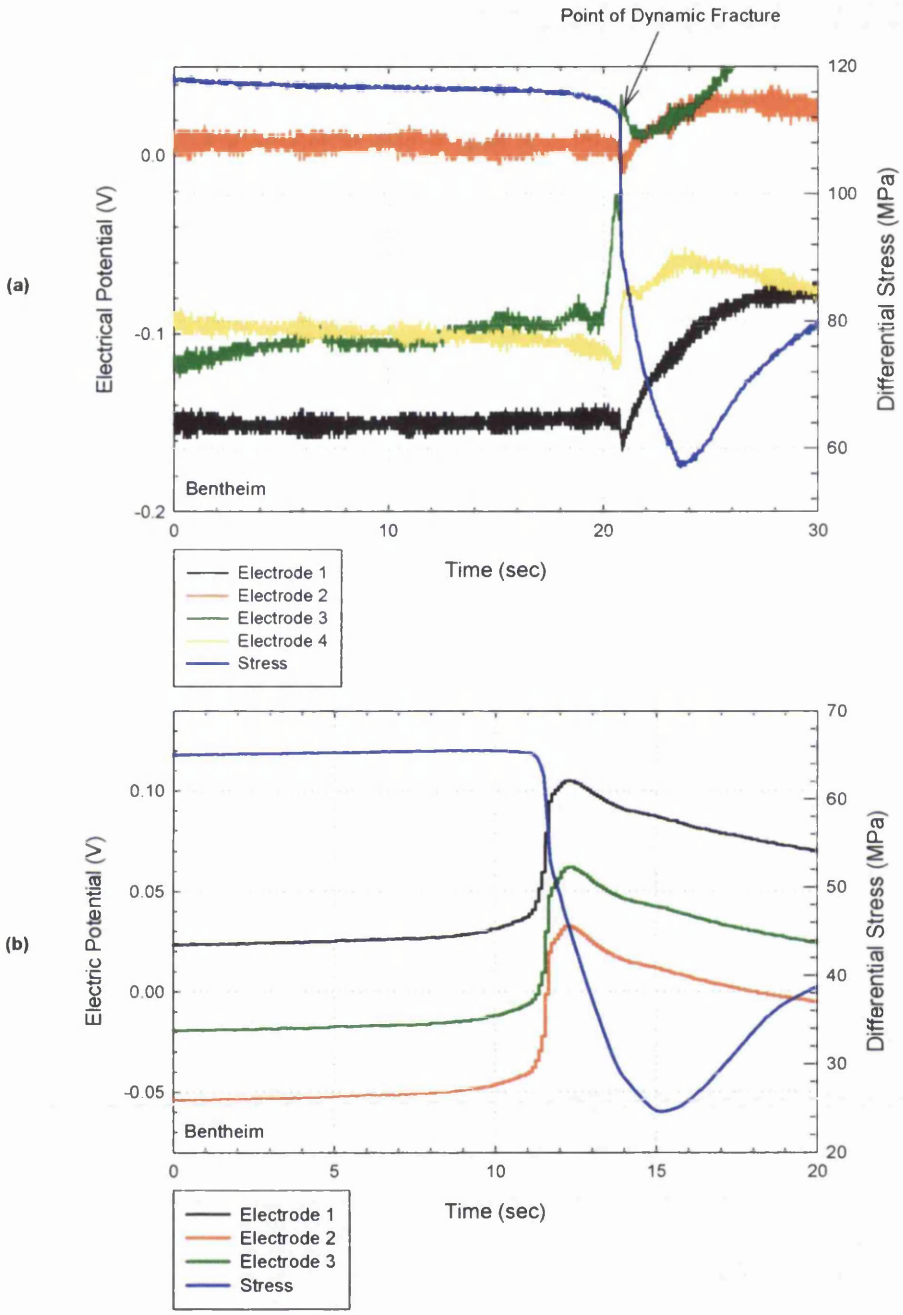

Figure 5-7 Electrical potential differences for Bentheim sandstone deformed at an effective pressure of 20MPa at 1.5 x 10^{-5} s^{-1} with (a) no pore fluid and (b) water as pore fluid. [Experiment No.: (a) 19, (b) 21]. N.B. Electrode 4 broke while placing the sample setup into the pressure vessel.

5.4 Effect of Undrained Conditions on the Pre-seismic and Co-seismic Electrical Potential Signals during Shear Fracture.

In Figure 5-8a the electrical potential during shear fracture, of Darley Dale sandstone under undrained conditions with a constant pore fluid volume is plotted. The electrical signals begin to either increase or decrease approximately 7 seconds before dynamic failure. Failure is characterised by a spike and decay type signal, which exhibit positive and negative polarities and average magnitudes of 27mV. The co-seismic signals have an average magnitude of 27mV and vary in a similar fashion to the electrical signals from saturated basalt under drained conditions (Figure 5-4d).

The electrical potential signals for Bentheim sandstone deformed under undrained conditions are shown in Figure 5-8b. The signals begin to show precursory changes approximately 4.5 seconds before dynamic failure with the amplitude variation remaining constant until 0.5 seconds before fracture. At this point the electrical signals show both positive and negative polarities. The average pre-seismic magnitude detected is 26mV and during shear fracture, an average value of 56 mV is found. The dynamic stress drop is approximately 41MPa for the drained and 17MPa for the undrained experimental condition.

The electrical potential differences during strain softening and dynamic fracture for all the experimental conditions and rock types are summarised in Table 5-1.

	Darley Dale Sandstone		**Bentheim Sandstone**		**Icelandic Basalt**	
	Pre-seismic	**Co-seismic**	**Pre-seismic**	**Co-seismic**	**Pre-seismic**	**Co-seismic**
Water Free	20	107	20	40	0	35
Drained	100	115	30	65	20	232
Undrained	27	27	26	56	-	-

Table 5-1 Absolute magnitude of pre-seismic and co-seismic signals for sandstone and basalt under a range of experimental conditions. All values are given in millivolt.

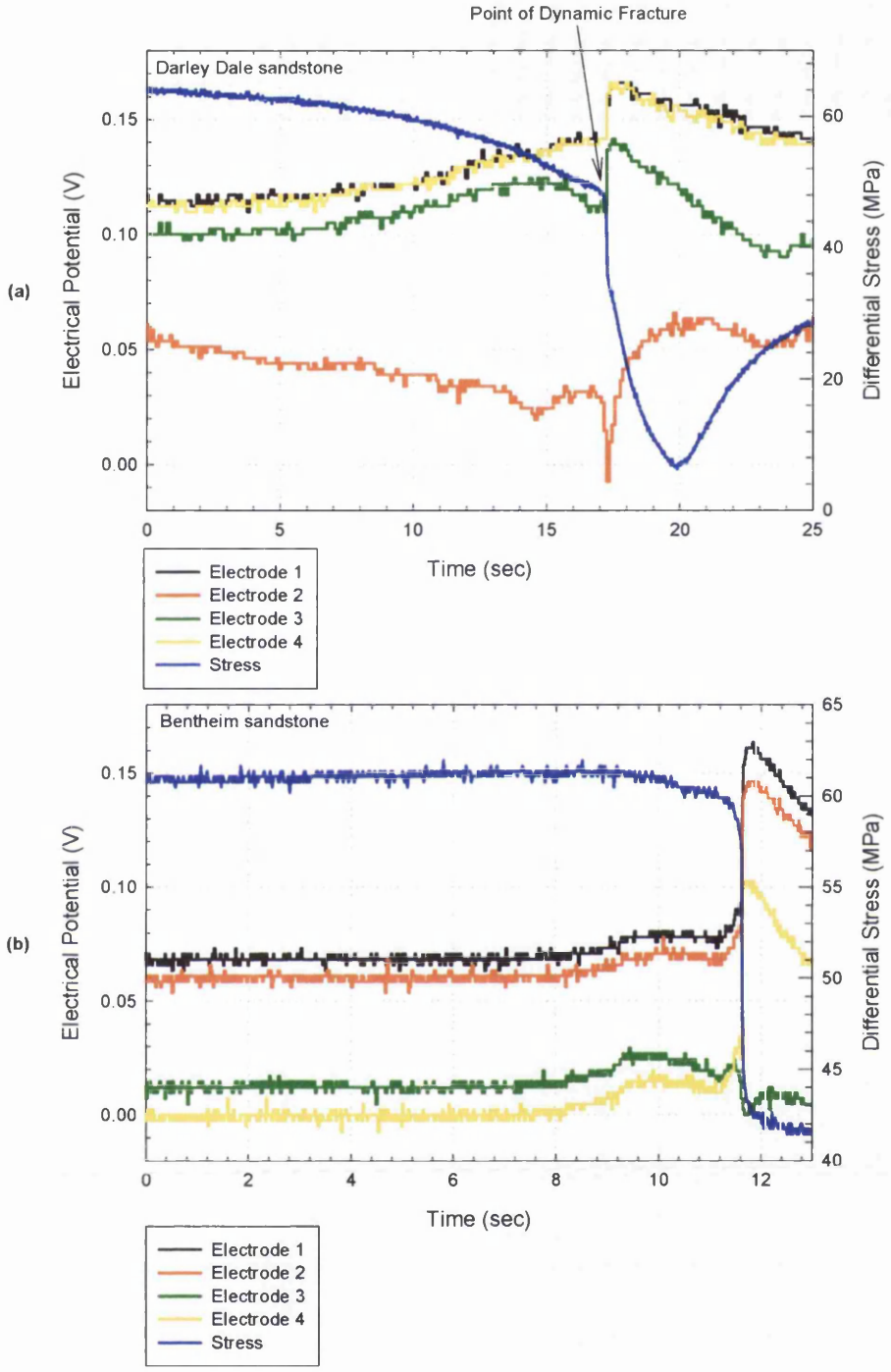

Figure 5-8 Electrical potential differences for deformation of (a) Darley Dale sandstone and, (b) Bentheim sandstone under undrained conditions. An effective pressure of 20MPa and strain rate of 1.5 x 10^{-5} s^{-1} was used. [Experiment No.: (a) 25, (b) 26]

5.5 Chapter Summary

I. Pre-seismic and co-seismic electrical potential signals have been observed for Darley Dale sandstone, Bentheim sandstone and Icelandic basalt. The signals occur during microcracking and shear fracture when new dilatant crack growth and linkage lead to the formation of a macroscopic fault.

II. The electrokinetic effect has been identified as a plausible electrical potential generating mechanism under upper crustal conditions. The piezoelectric effect was found to operate under water-free conditions but because the time constant of the electrical signals decrease with bulk electrical conductivity, it is considered to provide a negligible contribution to the measured electrical potential in fluid saturated rocks.

III. The electrokinetic effect, observable in igneous and sedimentary, rocks depends on the availability of fluid networks. Low permeability basalt acts as a closed system and generates localised current flow but when permeability is increased through thermal cracking, the electrical potential signals are increased, as fluid pathways become more continuous across the medium.

IV. The co-seismic electrical potential is higher for Darley Dale sandstone than Bentheim sandstone even though Bentheim sandstone has approximately 24% more quartz content. Their pre-seismic signals are however similar in magnitude.

V. Both drained and undrained conditions were investigated. In the drained situation, where fluid is flowing at a steady pressure into a dilatant zone, the electrokinetic potential is greater both in the pre-seismic and co-seismic periods. The undrained situation creates the conditions for a decreasing pore fluid pressure during dilatancy and therefore increasing effective stress deforming the rock. The rock can not saturate due to a lack of fluid and a uniform flow field can not operate. Local fluid flow will give rise to vari-directional convection currents and hence changing electrical potentials.

VI. Under drained conditions Darley Dale sandstone creates pre-seismic and co-seismic signals one order of magnitude greater than Bentheim sandstone while its initial permeability is two orders of magnitude lower. The deformation of the sandstone under undrained conditions produces similar pre-seismic and co-seismic signals in both Darley Dale and Bentheim sandstone.

6. Effect of Increasing Confining and Pore Fluid Pressures on Electrical Potential Signals.

6.1 Introduction

Variations of pore and confining pressures induce volumetric strain in rock. This fact is expressed in the theories of poroelasticity (Biot, 1941) and Terzaghis' law of effective stress derived for the undrained case by Nur and Byerlee (1971). The effect is known to be important in controlling a number of physical properties such as rock strength (Murrell, 1965), permeability (Tuefel, 1987, Keaney, 1998) and electrical resistivity (Morrow and Brace, 1981). The effective pressure is the resultant pressure that is effective in deforming a porous medium and is the difference between the applied pressure and the pore fluid pressure.

In this chapter experiments designed to investigate the effect of varying confining and pore fluid pressures on electrical potential signals are presented. The electrical potential signals from saturated rocks are deduced to result from electrokinetic mechanisms as concluded in Chapter 5.

The effect of pressure on precursory, co-seismic and electrical signals during deformation was investigated under elevated pressures. Consideration of mechanical deformation is made by analysis of acoustic emissions allowing relationships between brittle deformation and electrical potential generation to be drawn.

6.2 Deformation of Darley Dale Sandstone

The maximum confining pressure used to investigate the generation of electrical potential signals, detailed in Chapter 5, was 40MPa and a maximum pore fluid pressure exerted of 20MPa. This is equivalent to a depth of 1.6km and 0.8km respectively, in the earth's crust, which is the region of interest of many geological processes. Table 6-1 lists some typical crustal processes together with their estimated depth of occurrence; the data presented here provides evidence for the existence of pore fluids at high pressure and emphasises the need for experiments at conditions simulating these depths.

Indicator	Depth Range
Water table	0 to 2 km
Deep wells	To 12 km
Reservoir induced seismicity	To 12 km
Crustal low velocity zones	7 to 12 km
Crustal electrical conductivity zones	10 to 12 km
Crack healing and sealing	Not known
Crustal seismic attenuation zones	7 to 12 km
Silicic volcanism	Near surface
Low stress on faults	0 to 10 km

Table 6-1 The depth range of some typical crustal processes which suggest the presence of free fluids at high pressures. (Extracted from, The Role of Fluids in Crustal Processes, 1990)

6.2.1 'Dry' Experiments

In Figure 6-1 the stress strain curves for a range of experiments conducted at a strain rate of 1.5×10^{-5} s^{-1} and increasing confining pressures (Cp) without pore fluid are shown. The peak differential axial stress increases with confining pressure, for experiments conducted at 20, 75 and 100MPa.

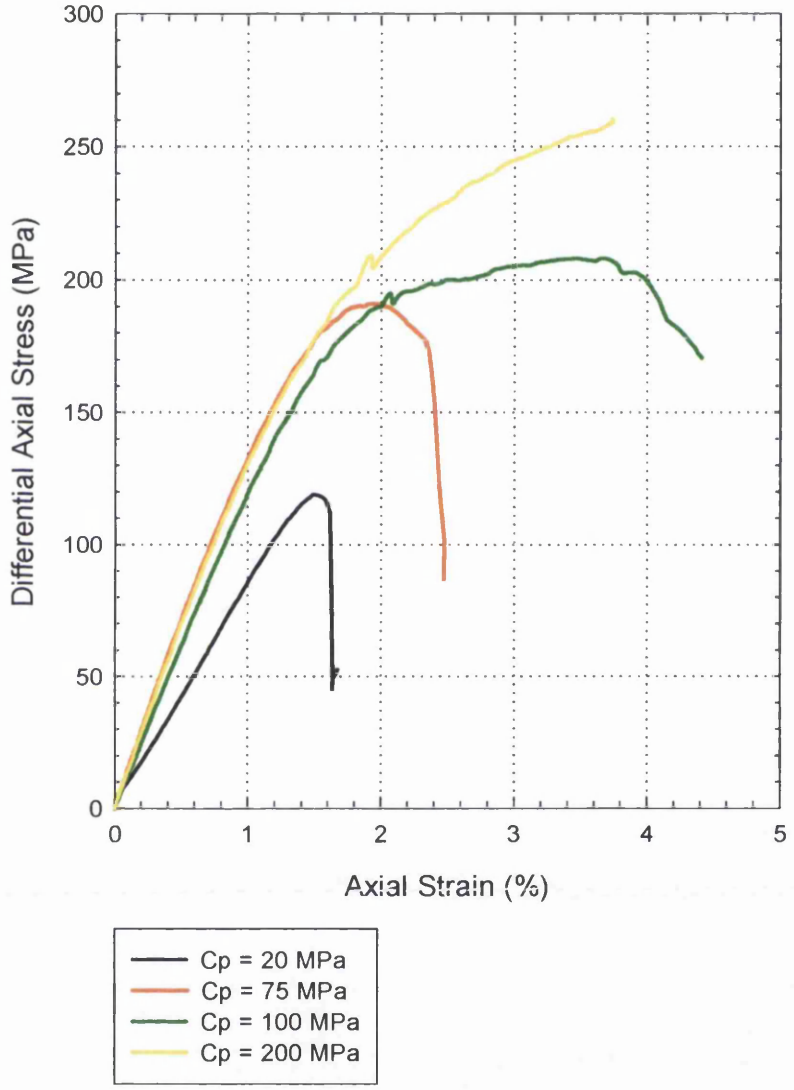

Figure 6-1 Stress-strain curves for deformation of Darley Dale sandstone under water-free conditions. [Experiment No.: 27, 28, 30, 33]

N.B. The experiment conducted at 200MPa (Expt. No. 27) does not reach a peak stress before 3.6% of the axial strain. Since rupture of the nitrile jackets is to be avoided and post-failure behaviour is not investigated in this study, deformation was stopped in this case. The stress strain curve obtained is characteristic of cataclastic deformation and the slight barrel shape of the sample with not obvious discontinuities confirms the occurrence of this form of deformation behaviour. The experiments conducted at the lower confining pressures (Expt. Nos. 6, 28 & 30) failed through brittle mechanisms

characterised by an audible dynamic stress drop. The strain accommodated by the samples increases with confining pressure. Shear faults are developed in all these samples: Expt. No. 6 done at 20MPa showed a sub-vertical fault in cross-section indicating a strong extension component while the samples deformed at 75 and 100MPa showed typical shear fractures. The angle of fracture in all cases is less than 45° to the maximum compressive stress direction (Table 6-1).

	Shear Fault Angle (°)		
Effective Pressure (MPa)	**Dry**	**Wet (CPP)**	**Wet (CPV)**
10	-	25	26
20	24	29	29
30	-	30	29
40	-	31	41
50	-	32	34
75	35	34	-
100	38	-	-

Table 6-2 List of inclination of shear fault to axial vertical stress direction. CPP represents drained experimental conditions and CPV, under undrained conditions. The error associated with these measured angles is ± 5°.

The electrical potential changes acquired are plotted in Figure 6-2. The data is displayed as the electrical potential gradient between two electrodes, situated one above the other and along one side of the sample. This type of plot is necessary to eliminate the effect of increasing differential stress on the contact resistance between the top end-cap and the sample surface.

It was discussed in Chapter 5 that a piezoelectric effect operates within dry sandstones because electrical potential changes occurred during strain softening and the dynamic stress drops for sandstone with a high quartz content and no pore fluid interaction. In this chapter the electrical potential difference is plotted throughout the deformation cycle. The behaviour pattern of the electrical potential is similar in Figure 6-2 a, b and c. A period of quiescence, relative to the base level noise, changes to a steady increase or decrease of the electrical potential gradient. The onset of this deviation occurs at 96%, 92% and 86% (Figure 6-2) for conditions a, b, c of the peak differential stress of the sample and occurs at a corresponding rate of -1.2 V/ % strain, 1.5 V/ % strain and 1.4 V/ % strain respectively. The electrical potential difference continues to increase or decrease until the sample fails indicated by to the differential stress drop. This generates a large co-seismic signal, which is greater for confining pressures up to 75MPa. In Figure 6-2d, the stress strain curve can be was described as typical of cataclastic behaviour and is characterised by a different mode of electrical potential difference signal. The electrical signal here increases throughout deformation, exhibiting fluctuations up to a maximum of 0.4V.

It is expected that the electrical potential difference should increase during loading as stress and strain increase if the piezoelectric effect was operating. This is evident for individual electrodes but the results could also be interpreted as a decrease in contact resistance between the sample surface and loading rams (as described above) or as capacitance changes between the electrode surface contact zone.

If the capacitance C is equal to $\varepsilon_0 A/d$ where A is the area of the contact zone and d is the distance between the electrode and rock surface then it can be seen that C is very sensitive to small changes in d, i.e. $\varepsilon_0 A/d+\Delta d$. Therefore the difference in distance between two electrodes is plotted to eliminate the contact resistance effect and at reasonably high confining pressures the capacitance effects may be less significant.

The change of electrical potential occurs at a position close to the peak strength of the sample as determined from the stress-strain data. To understand the physical nature of the onset of these signals further information is required. Figure 6-3 shows the electrical potential difference for increasing effective pressure together with AE event rate. Source located AE are plotted in Figure 6-3d. It is seen in Figures 6-3 a, b and c that the electrical potential gradient changes show good correlation with AE rate and the electrical potential differences increase or decrease with increasing AE event rate. The AE rate ranges between 0 and 50 s^{-1} with no obvious increase with confining pressure.

In Figure 6-3a an initial exponentially increasing AE event rate is observed which is also apparent in Figure-6-3b before a constant AE rate occurs when 2.2% strain is reached. The constant AE rate appears in Figure 6-3c at 2.4% strain following an exponential increase in activity. These constant levels are maintained until fracture. An increase in exponential activity is expected up to dynamic fracture (Sammonds et al, 1989; Ayling et al., 1995) and hence these regions represent saturation of the LOCAN AE detection equipment due to a high level of AE activity at the eight channels. This limitation in recording equipment is fully discussed by Cox and Meredith (1993). It is reasonable to assume that the AE rates would increase exponentially in a similar fashion to that depicted in Figure 6-3a.

A peak in AE event rate was observed to occur between 1 and 1.1 % strain for the test displayed in Figure 6-3c, the cause of this spike is unknown though it is likely to be a localised cracking event.

Where cataclastic deformation occurred (Figure 6-3d) the electrical potential gradient increases non-linearly throughout loading and suggests a different deformation mechanism is occurring. AE locations show the onset of AE activity, which commence at 1% strain and continue through the deformation until approximately 2.4% strain. The majority of the AE are spatially positioned along the length of the sample with a the bulk occurring between 30 and 70mm. The abrupt termination in the AE locations was due to the limitations of the AE measurement system at these high sampling rates, as discussed earlier.

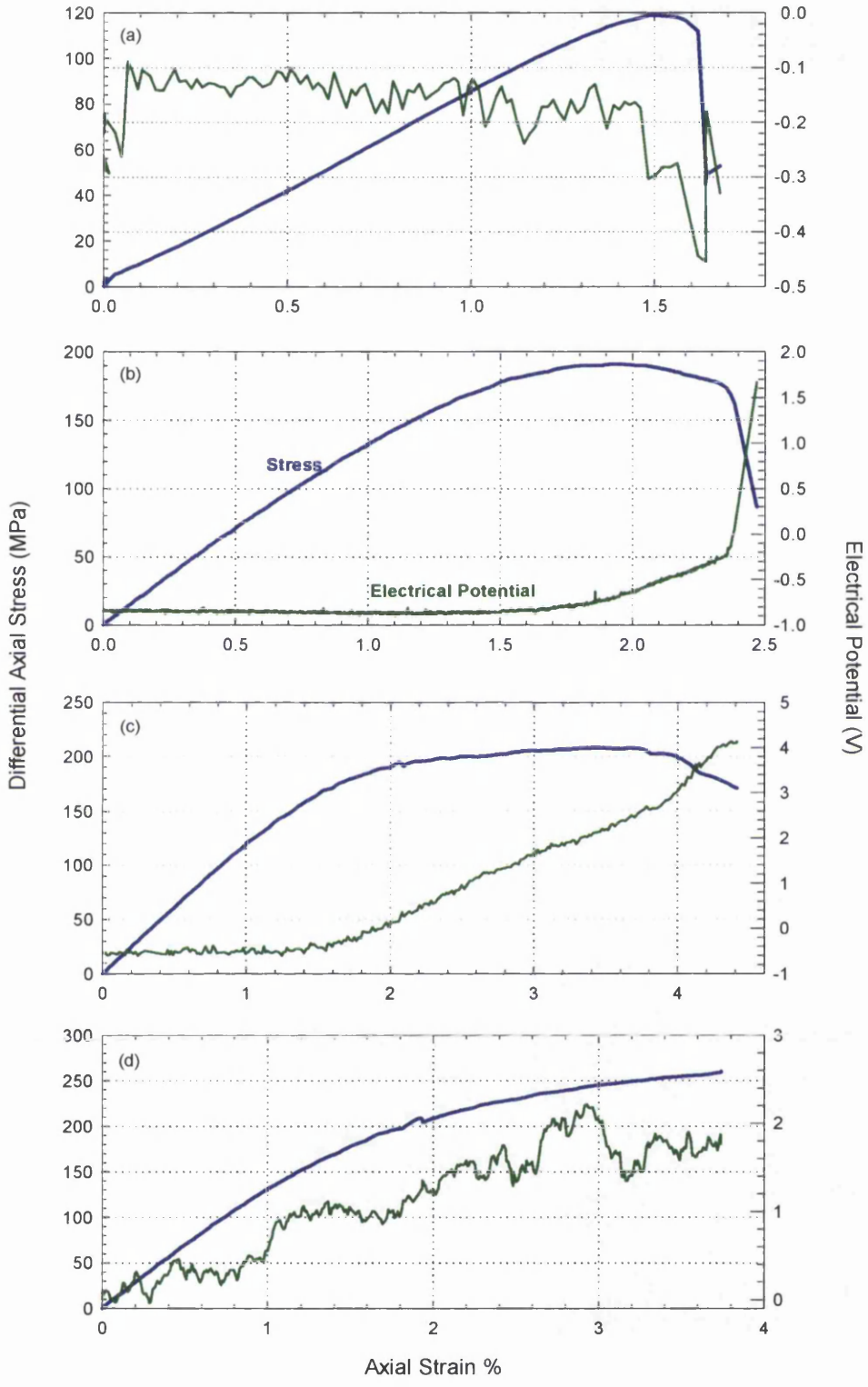

Figure 6-2 Differential stress and electrical potential gradients for the deformation of Darley Dale sandstone without pore fluids at (a) Cp = 20MPa (b) Cp = 75MPa (c) Cp = 100MPa (d) Cp = 200MPa using a strain rate of 1.5 x 10^{-5} s^{-1}. [Experiment No.: (a) 27, (b) 28, (c) 30, (d) 33]

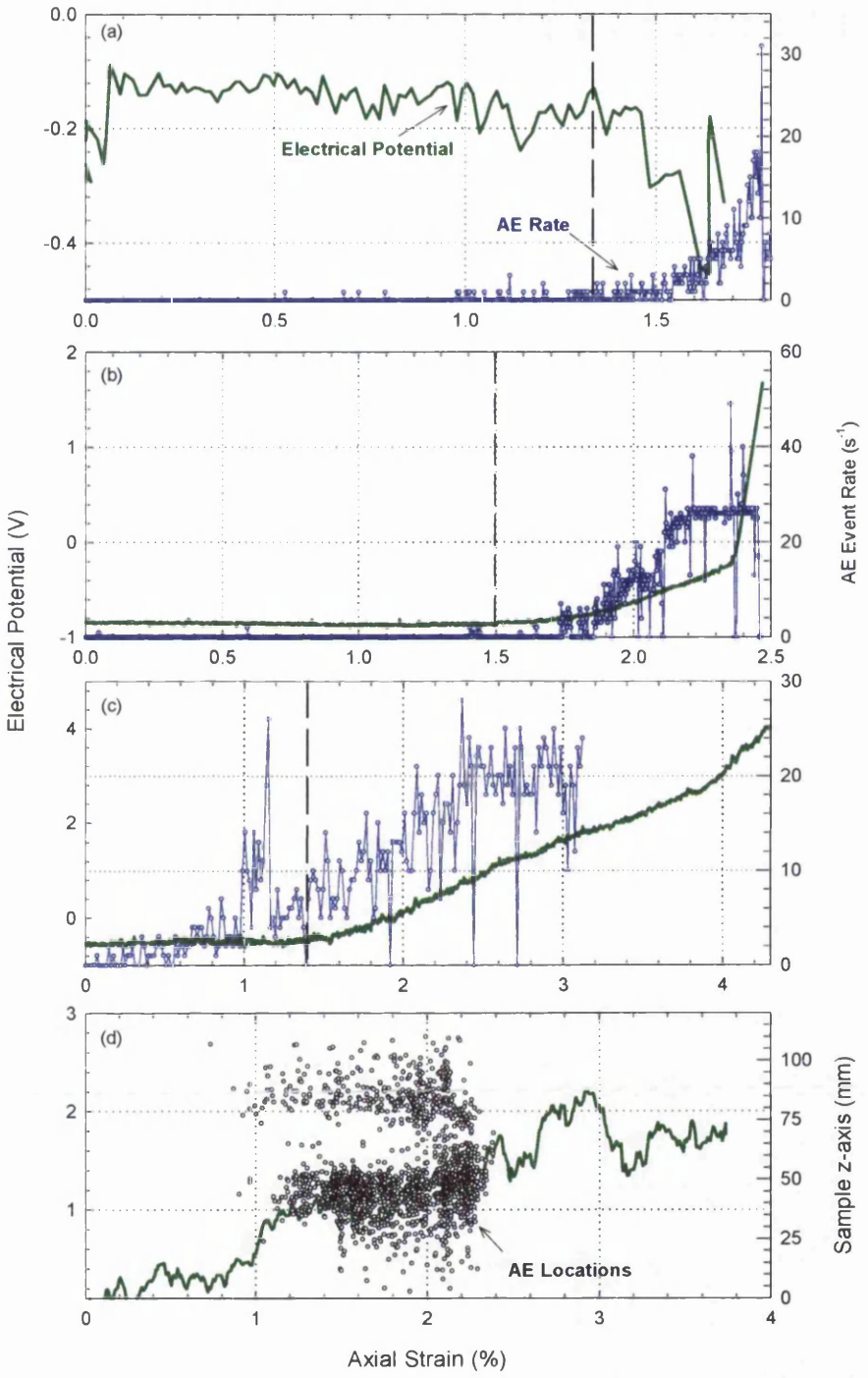

Figure 6-3 Electrical potential gradient and AE event rate or AE location for dry deformation of Darley Dale sandstone at (a) Cp = 20MPa (b) Cp = 75MPa (c) Cp = 100MPa (d) Cp = 200MPa using a strain rate of 1.5×10^{-5} s^{-1}. [Experiment No.: (a) 27, (b) 28, (c) 30, (d) 33]

6.2.2 'Wet' Experiments

A range of pore fluid and confining pressures were selected to investigate the effective pressure effect on the electrical potential during deviatoric deformation of a sample of Darley Dale sandstone. The data is plotted against strain, which is the same as time during constant strain rate experiments. The mechanical data for each of these experiments is plotted in Figure 6-4. Each curve shows a quasi-linear increase of differential stress with strain before undergoing a non-linear increase of stress with strain. During this phase a peak differential stress is reached followed by a decrease of stress with strain and ultimately a dynamic stress drop representing sample fracture.

The strength of the sandstone is best represented as a plot of maximum differential peak stress as a function of effective confining pressure (Figure 6-5). The plot shows a linear increase of peak stress with effective confining pressure, the dry data exhibiting the highest peak stress. Wet experiments, under drained conditions show higher peak stress than undrained conditions, the disparity between the two increasing with increasing effective pressure.

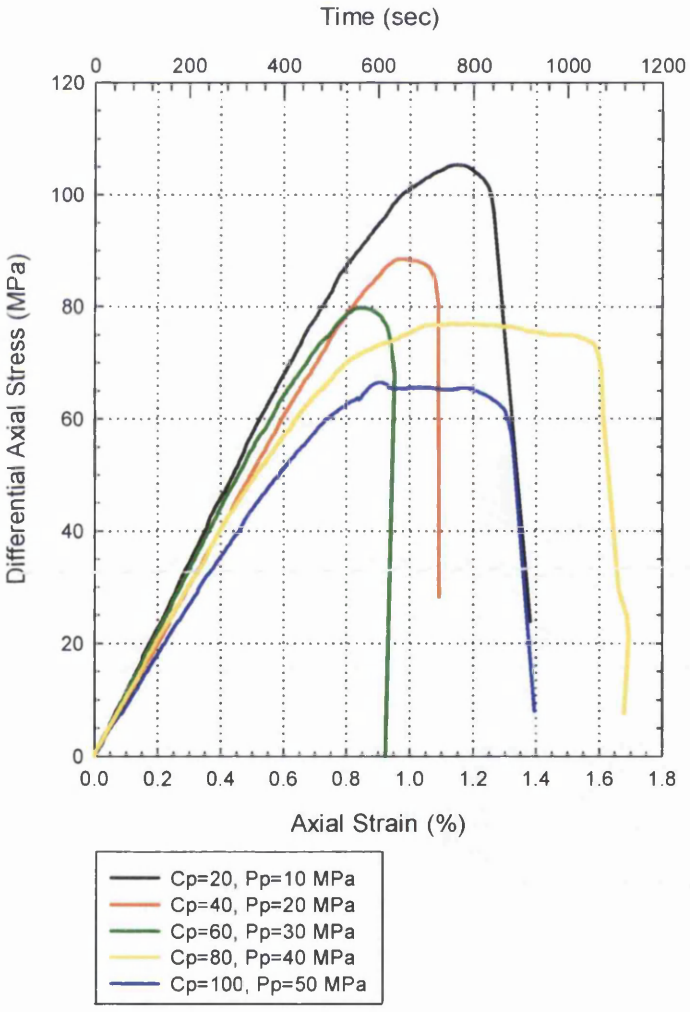

Figure 6-4 Stress-strain curves for deformation of Darley Dale sandstone under drained conditions using a strain rate of 1.5×10^{-5} s^{-1}. [Experiment No.: 23, 35, 36, 37, 38]

The temporal electrical potential data produced shows a good degree of similarity during deformation at all effective pressures investigated. A typical signal can be extracted and quantitatively analysed. Figure 6-6 displays typical electrical potential data together with differential stress, pore volume changes and b-value variations. The data are plotted for one representative value of effective pressure against axial strain. Both drained and undrained conditions are shown.

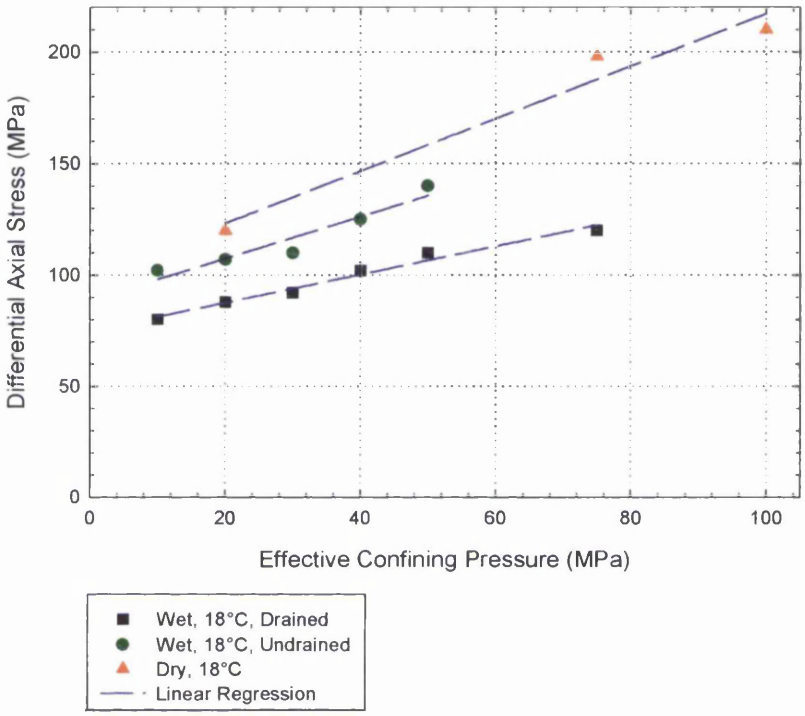

Figure 6-5 Maximum differential stress as a function of effective confining pressure for wet and dry experiments. Data is from deformation of Darley Dale sandstone. [Experiment No.: 11, 23, 24, 25, 28, 30, 35, 36, 37, 38, 45, 46, 47, 48]

The electrical potential change shown is the difference recorded between electrodes 4 and 2 or electrodes 3 and 1 in contact with the rock surface. Under drained conditions (Figure 6-6a) a decrease of approximately 2.5mV occurs initially as stress increases, which corresponds to a decrease in connected pore volume change of $0.06cm^3$. This period of pore volume decrease represents compaction when the deviatoric stress closes cracks and pores perpendicular to this direction.

Beyond this point the electrical potential after this point increases with increasing differential stress. After an increase in strain of 0.16% the pore volume within the rock also increases. During this increase an electrical potential change of 8mV up to the point of fracture corresponds to a $0.22cm^3$ pore volume change in the same period. A pore volume increase under increasing deviatoric stress is realised through dilatant microcracking. Microcracking is shown to occur through a decreasing b-value, which decreases from 1.2 to a value around 1.0 before a sudden drop at fracture to 0.7.

In Figure 6-6b, a similar experiment under undrained conditions is presented. In this case the change in pore fluid pressure is depicted instead of pore volume change. An increase in pore fluid pressure to 22MPa occurs with a quasi-linear increase in differential stress. No associated electrical potential change can be detected. At around 0.5% strain the pore pressure decreases which correlates with a deviation of the stress-strain curve from linearity. This point represents the onset of dilatancy and although a decrease in b-value occurs indicating AE activity, no significant electrical signal change can be observed.

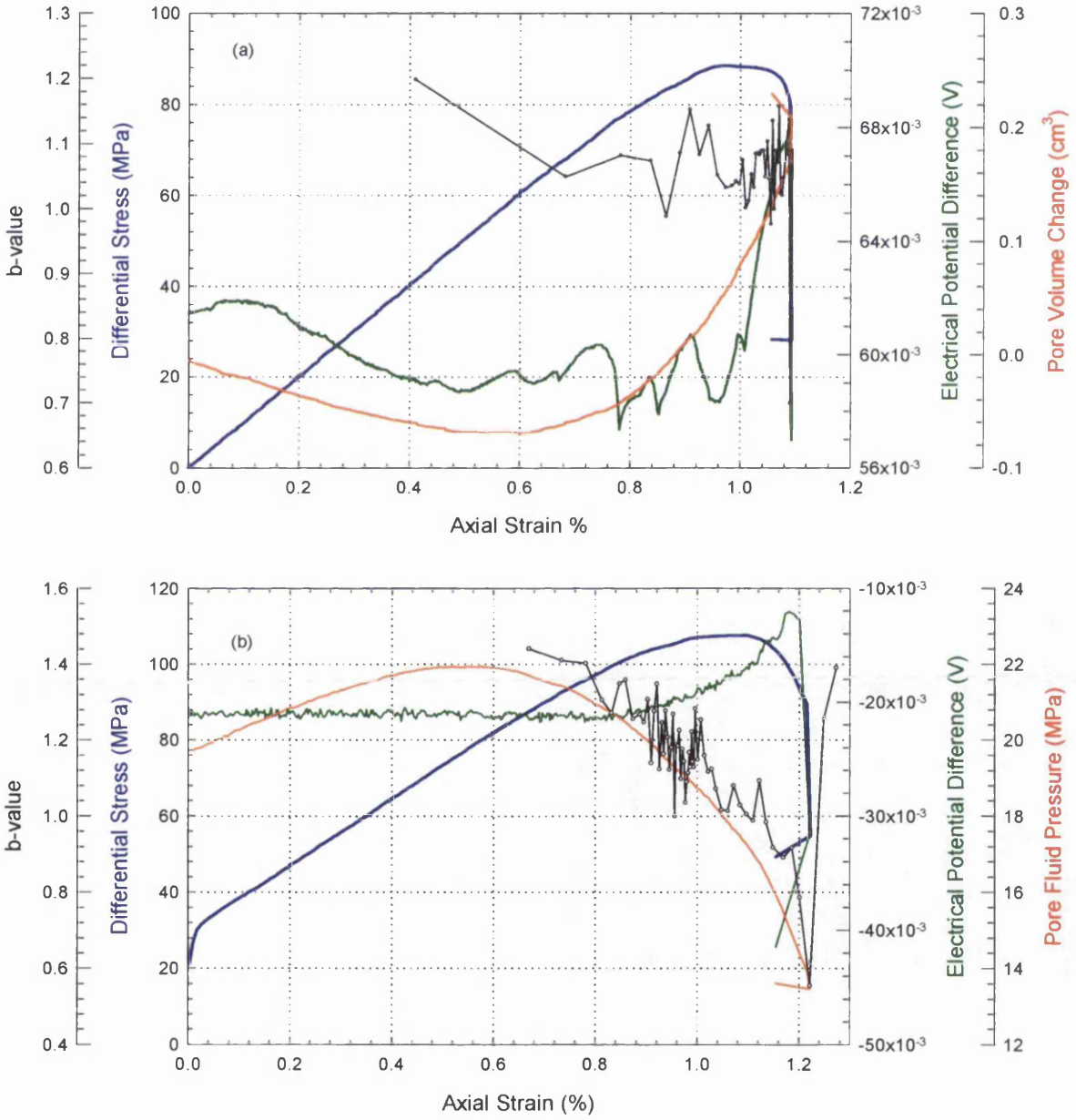

Figure 6-6 Electrical potential changes as a function of axial strain for (a) drained and (b) undrained experiments. Also shown are differential stress, pore volume change, pore pressure change and seismic b-value changes. [Experiment No.: (a) 41, (b) 25]

However an increase in the electrical potential difference begins to be observed at approximately 0.75% strain. An absolute change of 10mV, up to the point of fracture, is recorded during this period corresponding to a pore fluid pressure change of 7MPa. The onset of this change occurs concurrently with a rapidly decreasing b-value from 1.3 to approximately 0.5 at fracture.
It is important to quantify the electrical potential signals during the periods described above, i.e. during compaction, dilatancy and fracture. The behaviour up to dynamic fracture will be closely analysed because of the presence of precursory electrical signals observed for saturated rocks (described in Chapter 5).

6.3 Quantifying Effective Pressure Effects during Deformation

The effective pressure dependency of electrical potential changes under drained conditions is shown in Figure 6-7. The plots are arranged in two columns, the first column shows effects during compaction and the second shows effects during dilatancy.

The electrical potential change increases exponentially ($R^2 = 0.999$) as a function of effective pressure during compaction (Figure 6-7a). The values vary over 1 order of magnitude from 2.5mV to 32.5mV. A linear increase in pore volume change with increasing effective confining pressure (Figure 6-7b) occurs during compaction as greater stresses are effective in closing more of the connected porosity. Note that this measurement of the pore fluid is the quantity expelled from the sample.

During dilatancy the increase of electrical potential difference increases linearly with increasing effective pressure (Figure 6-7b) at a rate of 0.4mV/MPa. The pore volume change during dilatancy is plotted in Figure 6-7d and shows a constant volume change of $0.2 \pm 0.02 cm^3$. Therefore a change in fluid volume cannot be responsible for the electrical potential changes during dilatancy. Cumulative AE increase with effective pressure (Figure 6-7e) suggesting the formation of increasing number of axial cracks. It could be concluded therefore that the increased cracking would increase the pore volume though increased fluid volume change would also then be expected. As fluid volume does not change the possibility of connected channels of low aspect ratio and tight pore throats may be a plausible explanation.

Effective Pressure	Electrical potential change during compaction /mV	Error / mV	Electrical potential change during dilatancy MV	Error / mV	No of AE
10.00	2.50	1.00	8.50	1.00	3738.00
20.00	4.00	1.00	12.50	1.00	4100.00
30.00	4.50	1.00	16.00	1.00	4256.00
40.00	10.00	0.50	20.00	0.50	4489.00
50.00	32.50	0.50	26.50	0.50	4760.00

Table 6-3 The absolute change in the electrical potential difference during compaction and dilatancy with associated errors. The number of AE occurring in both periods is also given.

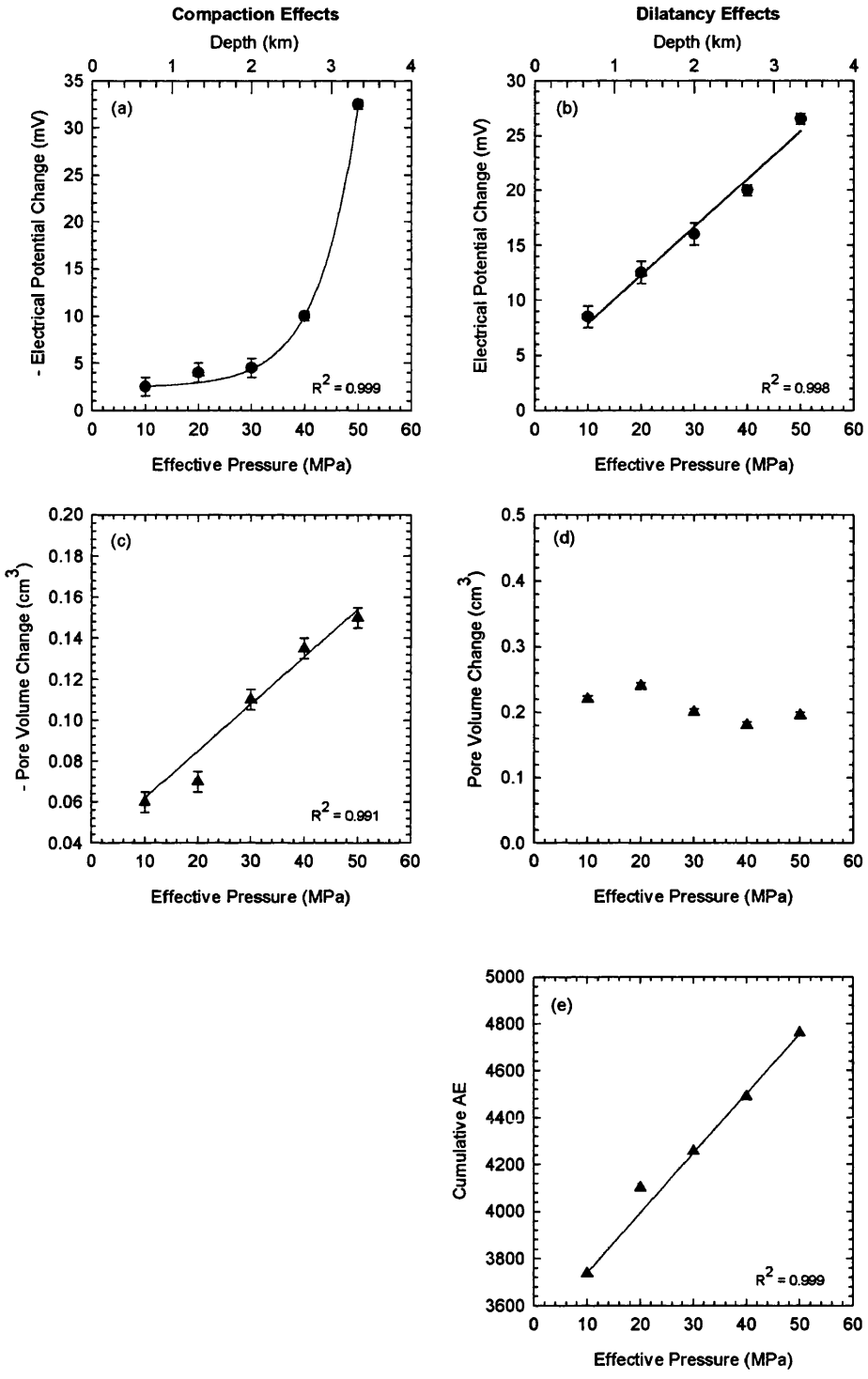

Figure 6-7 Effective confining pressure dependency on (a) electrical potential during compaction (b) electrical potential during dilatancy and up to fracture (c) pore volume change during compaction (d) pore volume change during dilatancy and (e) cumulative AE during dilatancy. [Experiment No.: 23, 35, 36, 37, 38]

6.3.1 Effective Pressure Dependency on Pre and Co-seismic Electrical Anomalies.

Figure 6-8 shows the effective pressure dependency on electrical potential anomalies preceding fracture and during macroscopic fault formation. The data shown represents the maximum change from a constant base value for each of the four electrodes similar to Figure 5-4b.

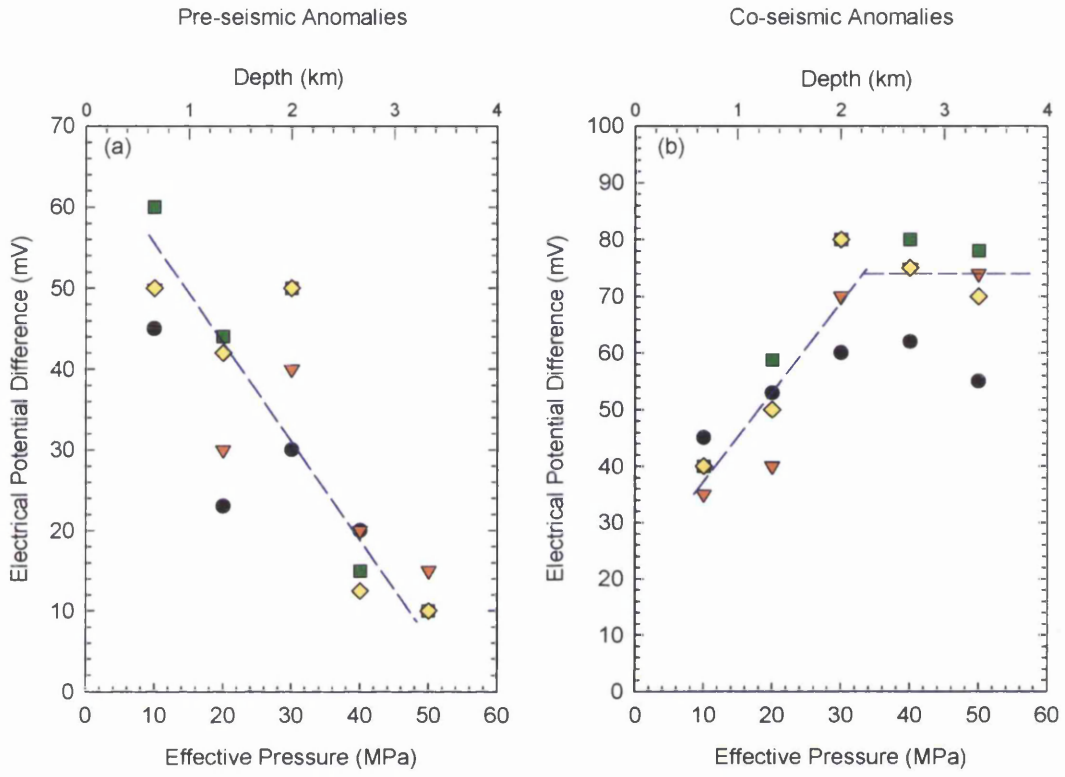

Figure 6-8 Effective confining pressure dependency on (a) pre-seismic electrical potential anomalies and (b) pre-seismic electrical potential anomalies. Other experimental conditions are the same as outlined in Figure 6-7. [Experiment No.: 23, 35, 36, 37, 38]. N.B. Error bars are within the symbols.

A decrease in the pre-seismic electrical potential signal occurs with increasing effective pressure under drained conditions (Figure 6-8a). The data are scattered which may be due to sample inhomogeneity or could be attributed to variations in spatial fluid flow occurring at each electrode. Typical pre-seismic magnitudes range between 10 and 60mV over a 40MPa effective pressure range.

The coseismic signals are plotted in Figure 6-8b for a set of drained experiments in the same range of effective pressures. An increase of the co-seismic electrical signal occurs initially up to 30MPa, further increases in effective pressure result in an almost constant value. The range of these co-seismic signals is between 20 and 80mV, a similar order of magnitude to the pre-seismic signals.

When considering precursory signals, the time period of the signal before fracture is important. Figure 6-9 shows the precursor time to failure as a function of effective pressure. A clear relationship between precursory time to failure and effective pressure is difficult to interpret. The undrained situation however, shows an increase of precursory time to failure with effective pressure although the values are lower.

	Drained Conditions							
	Pre-seismic Anomalies				Co-seismic Anomalies			
Stress	EL1	EL2	EL3	EL4	EL1	EL2	EL3	EL4
10.00	45.00	50.00	60.00	50.00	45.00	35.00	40.00	40.00
20.00	23.00	30.00	44.00	42.00	53.00	40.00	58.80	50.00
30.00	30.00	40.00	50.00	50.00	60.00	70.00	80.00	80.00
40.00	20.00	20.00	15.00	12.50	62.00	75.00	80.00	75.00
50.00	10.00	15.00	10.00	10.00	55.00	74.00	78.00	70.00

Table 6-4 Magnitudes of the pre-seismic and co-seismic electrical potential differences during shear fracture for drained conditions and varying effective stress.

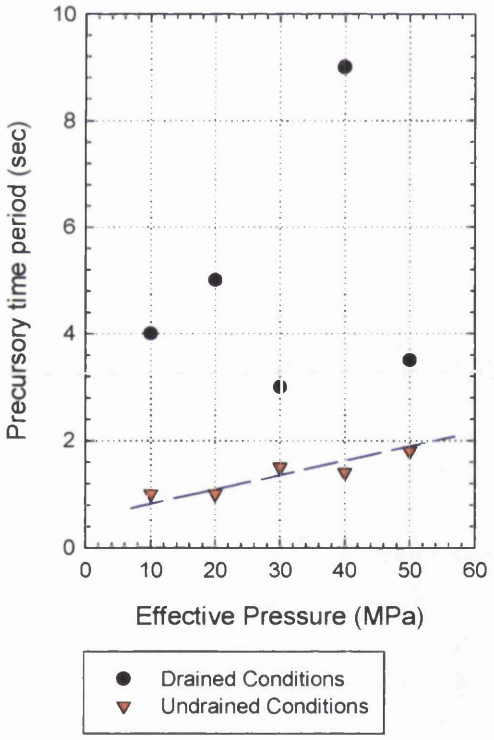

Figure 6-9 Plot showing precursory time to failure as a function of effective pressure for both drained and undrained conditions. [Experiment No.: 23, 25, 35, 36, 37, 38, 45, 46, 47, 48]

6.4 Correlation between Mean Crack Length and Electrical Potential Signals

The mean crack length, <c> of a fractal distribution of cracks can be calculated from

$$\langle c \rangle = \frac{\int_{c_0}^{c_1} c f(c) dc}{N_T} \tag{6-1}$$

where $f(c) = -dF(c)/dc$ is a density distribution of crack sizes and $N_T = \int_{c_0}^{c_1} f(c) dc$ is the number of aligned cracks (Main et al., 1993).

The variation of mean crack length during triaxial deformation is shown in Figure 6-10 and exhibits a non-linear increase reaching a maximum mean crack length at the point of dynamic fracture. The corresponding electrical potential difference as a function of mean crack length is plotted in Figure 6-11. The data was acquired during an experiment on Darley Dale sandstone at an effective pressure of 20MPa and strain rate of 1.5 x 10^{-5} s^{-1} under drained conditions.

The upper plot displays data during dilatancy and fracture and the lower graph re-plots the data during dilatancy up to the point of fracture on a larger axis scale.

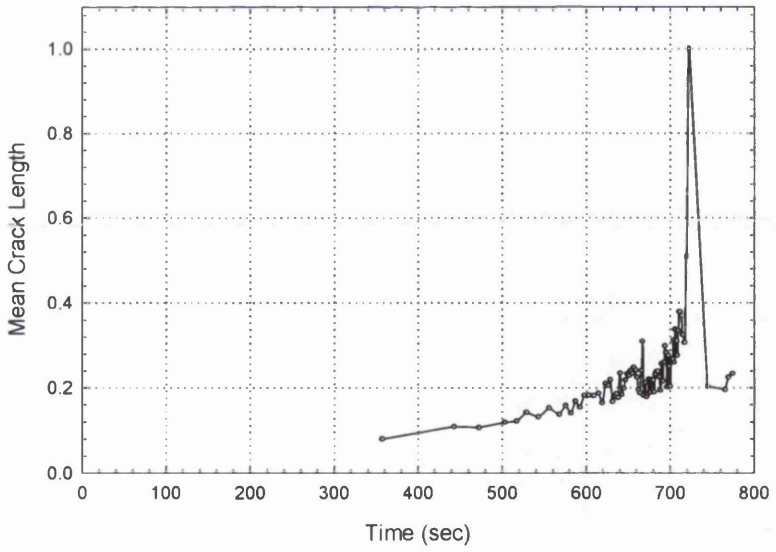

Figure 6-10 Variation of mean crack length and stress during triaxial deformation of sandstone under drained conditions. [Experiment No.: 41]

The electrical potential increases linearly with increasing mean crack length during dilatancy, which includes the period of strain softening after peak stress, observed on the stress/strain curves. An increase of 18mV occurs for a 33% increase in mean crack length during dilatancy.

Just before the fracture point an electrical potential change of 2mV occurs for a 60% increase in mean crack length. A large increase in the electrical potential occurs at fracture, approximately 45mV and is associated with an 80% decrease in instantaneous mean crack length. The continued deformation at the sample's residual strength causes a decrease in electrical potential of 10mV with no corresponding mean crack length observed.

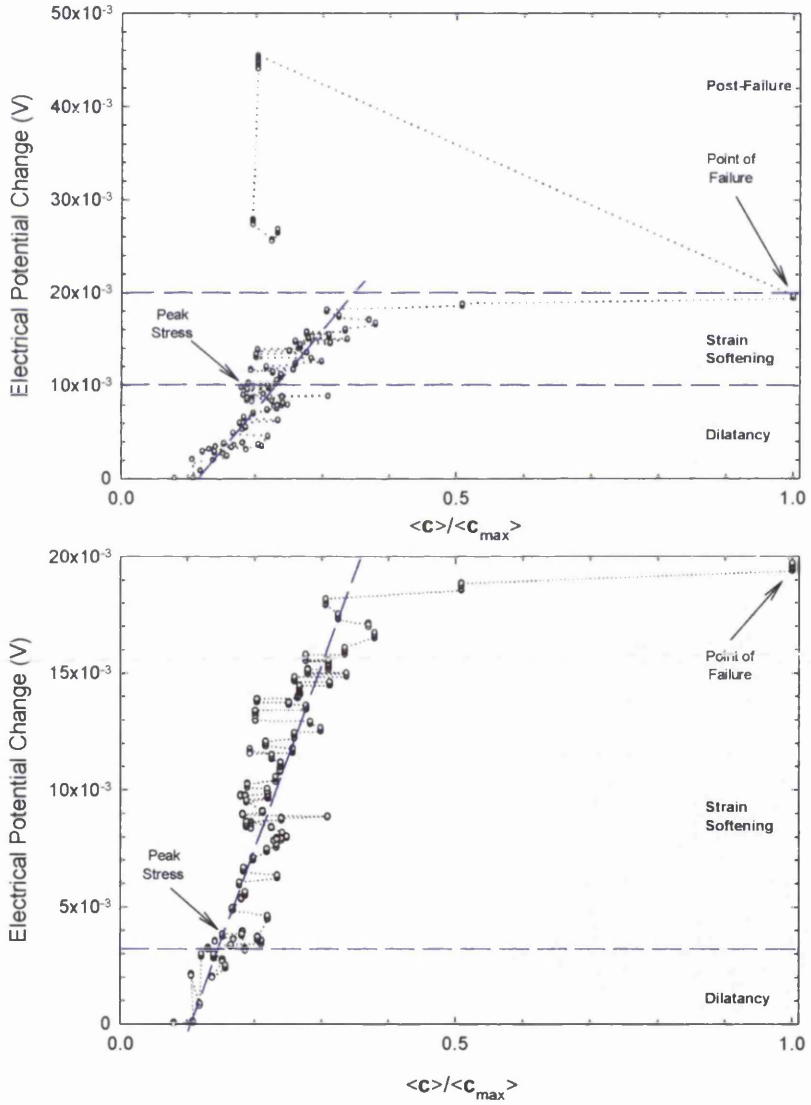

Figure 6-11 Electrical potential change as a function of the normalised mean crack length. [Experiment No.: 41]

6.5 Chapter Summary

I. The electrical potential difference generated from sandstone deformed without pore fluid and undergoing brittle fracture shows an increase or decrease at a stress level close to peak stress between effective pressures ranging from 20 to 100MPa. The onset of the signal change corresponds strongly to the exponential increase in AE event rate.

II. Cataclastic flow mechanisms are characterised by an increasing electrical potential difference, which correlates with a constant rate of AE activity.

III. Triaxial deformation of sandstone under drained conditions produces a decreasing total electrical potential difference during compaction and increasing electrical potential difference during dilatancy. Undrained conditions however produce no measurable electrical potential deviations during compaction though comparable changes to the drained case are produced when dilatancy is dominant.

IV. The absolute electrical potential difference during compaction increases exponentially with effective pressure and corresponds to a linear increase in absolute pore volume change with increasing effective pressure.

V. During dilatancy, the absolute electrical potential difference increases linearly with effective pressure. In this situation the pore volume change remains constant with increasing effective pressure, though a positive correlation with increasing cumulative AE events is found.

VI. Pre-seismic electrical anomalies decrease under drained conditions with increasing effective pressure. The voltage range of the measurements is comparable for both. Co-seismic signals increase up to 30MPa with increasing effective pressure and then remain constant with further effective pressure increases under drained conditions.

VII. The electrical potential increases as the instantaneous mean crack length, inferred from AE, increases. The majority of dilatancy is dominated by a large electrical potential increase over a relatively small increase in mean crack length. Just before fracture, a large increase in mean crack length occurs with a small associated electrical potential change. Fracture is associated with the largest electrical potential increase coupled with an associated significant decrease in the mean crack length.

7. The Effect of Pore Fluid Salinity on Electrical Potential Signals During Deformation.

7.1 Introduction

Numerous investigations have centred on the effects of varying stages of deformation on resistivity and conductivity of fluid saturated rock samples. These studies are conducted because important physical properties such as porosity, permeability and damage can be determined from the electrical conductivity of fluids within rock formations. Since natural pore fluids in the crust contain varying concentrations of salts, the effect of these salt concentrations must be investigated to allow accurate measurements and conclusions. Solutions of varying conductivity are expected to alter the coupling strength between the fluid and electric currents since fluid conductivity is an important parameter in the coupled equations for electrokinetic behaviour.

To investigate the effects of pore fluid conductivity, binary symmetric 1:1 electrolytes between 2 and 30% wt NaCl have been used as the pressurised pore fluids during the deformation of Darley Dale sandstone. NaCl has been chosen because it comprises the greatest percentage of typical crustal brines (Table 7-1). For discussion purposes the range will be separated into low (0.2M), intermediate (1.0M) and high ionic strength solutions (5.0M). The rock samples have been deformed under a triaxial stress at an effective pressure of 40MPa and a strain rate of 1.5×10^{-5} s^{-1}, while simultaneous measurements of electrical potential and acoustic emission have been recorded.

Ion	%
CO_2	1.1
Cl	34.5
SO_4	3.9
Na	25.4
K	3.5
Ca	0.51
Mg	Trace
SiO_2	30.3
Fe	0.009
Al	0.003
H_2S	10.5
As	0.15

Table 7-1 Chemical composition of typical crustal brines. The pH of this brine is 8.92.

7.2 Mechanical Properties of NaCl Saturated Rocks

A family of stress/strain curves is presented in Figure 7-1 representing the drained deformation of Darley Dale sandstone using pore fluids with varying NaCl molarity, deionised water and without water.

A similar quasi-elastic behaviour for the varying strength brine solutions up to approximately 0.75% strain is seen in all the experiments with the exception of 5.14M molarity brine which shows a good comparison with the deformation of Darley Dale using deionised water. This similarity experienced for the range of brine pore fluids indicates negligible effect of pore fluid salinity on mechanical behaviour during compaction.

The non-linear section of the stress/strain curves, however, varies with the salinity of pore fluid used. A peak stress value is achieved as seen on each curve varying between 76 and 118 MPa. The peak strength of each sample is given in Table 7-2. After peak stress however, a period of strain softening occurs before ultimate failure of the sample, the duration of this period being controlled by the pore fluid salinity. The relationship is described as non-linear between strain softening duration and pore fluid salinity.

The presence of deionised water produces a 32% reduction in the peak strength of Darley Dale sandstone under this set of conditions. The samples, saturated with low ionic brine pore fluids (0.34M) however are 25% higher in strength than those saturated with deionised water. Samples deforming with intermediate strength ionic solutions (1.2M) are up to 17.5% stronger than the water saturated samples while the greatest reduction in strength is found for high ionic brine solutions (5M). The effect of pH is not considered here as pH range was narrow, between 8.1 – 8.7, for the brine pore fluids utilised however it is reported elsewhere to have a less important effect on mechanical properties (Feucht and Logan, 1990).

The cumulative AE and b-values are shown in Figure 7-2b for the deformation of Darley Dale sandstone using 0.34M (2% wt) NaCl pore fluid and these curves are typical for all the brine saturated experiments performed. A very low acoustic emission period is observed up to 400 seconds after which, an exponential increase in the cumulative number of AE is observed. This activity represents crack opening becoming the dominant deformation mechanism over compaction. This exponential relationship is determined from the fit to the cumulative AE data seen in the inset of Figure 7-2a. It is also characterised by a decreasing b-value, which implies an increasing percentage of large amplitude AE events from a more diffuse area. For comparison the cumulative AE and b-value changes for an experiment under similar conditions using deionised water as pore fluid are shown in (Figure 7-2a). An exponentially increasing AE activity is observed simultaneously with a decreasing b-value during the dilatancy stage of deformation. The b-values are of the same magnitude as the brined saturated rock but the total cumulative AE, in this case, is 2.5 times less. This result suggests a chemical effect of saline fluids on micro-mechanical activity, i.e. a possible enhancement of the micro-cracking mechanism.

Pore Fluid	Peak Strength (MPa)	Salinity	pH
No pore fluid	118	-	-
Deionised water	80	-	7.2
0.34 M NaCl brine	100	2.0% wt NaCl	8.1
0.63 M NaCl brine	96	3.7% wt NaCl	8.3
0.85 M NaCl brine	94	5.0% wt NaCl	8.7
1.29 M NaCl brine	94	7.5% wt NaCl	8.5
1.71 M NaCl brine	106	10.0% wt NaCl	8.1
5.14 M NaCl brine	76	30.0% wt NaCl	8.7

Table 7-2 Peak strengths of Darley Dale sandstone and type of pore fluid used.

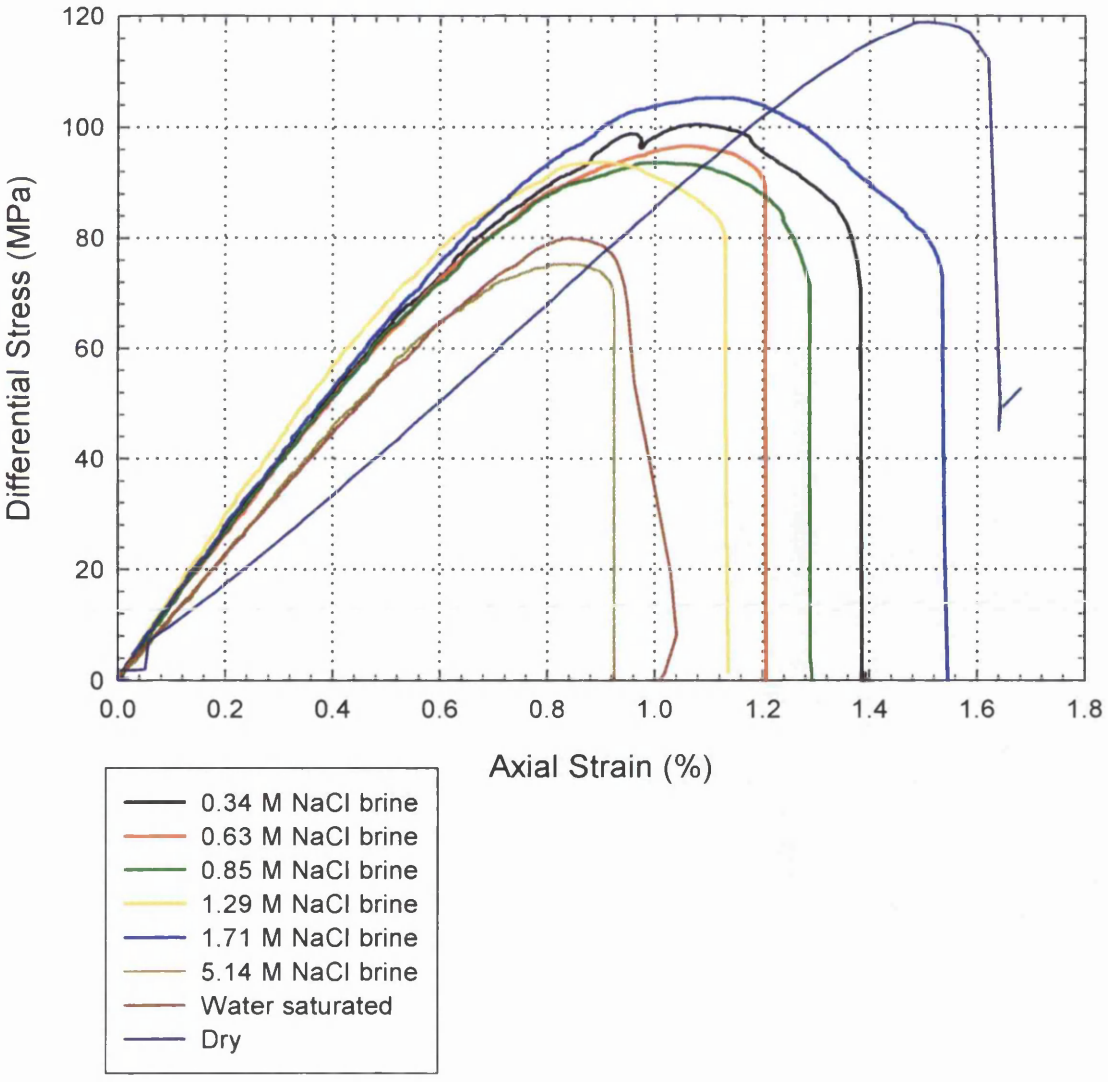

Figure 7-1 Plot of stress-strain curves for 'wet (drained)' and 'dry' deformation of Darley Dale sandstone using deionised water and pore fluids with increasing concentrations of NaCl. The effective pressure was 20MPa and deformation occurred at a strain rate of 1.5×10^{-5} s^{-1}. [Experiment No.: 25, 33, 51, 52, 53, 55, 56, 57]

(a)

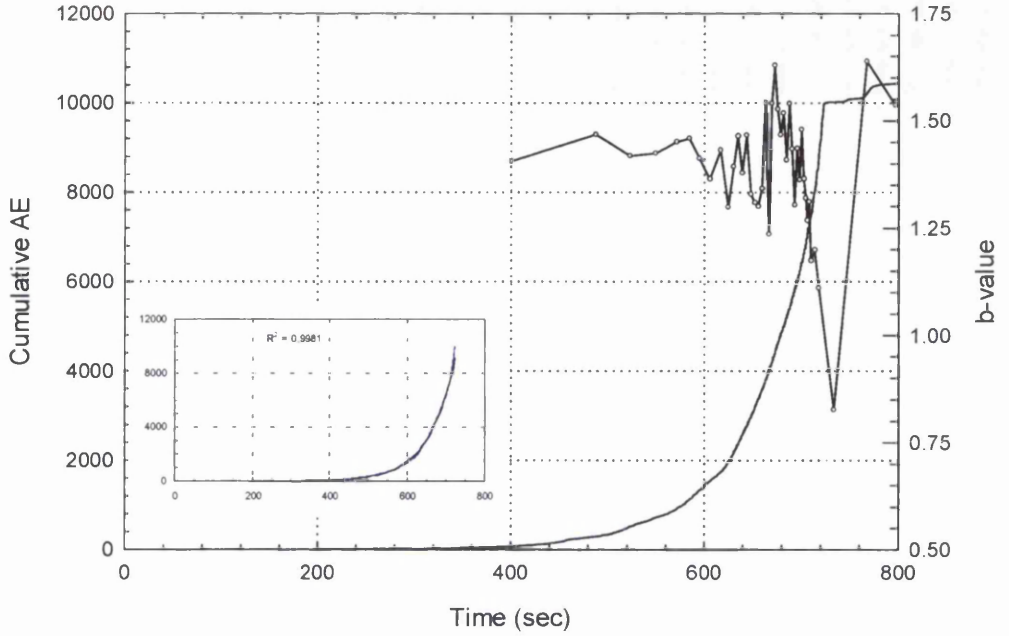

(b)

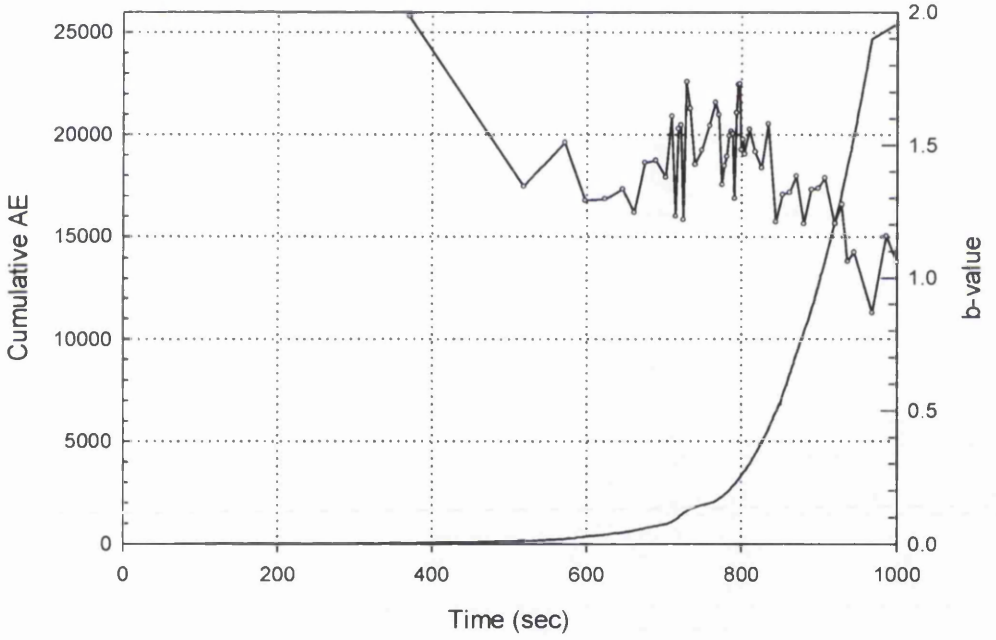

Figure 7-2 Cumulative acoustic emission curves and b-value changes for Darley Dale sandstone using (a) deionised water and (b) 2% wt NaCl solution as pore fluid. Inset in upper plot shows an exponential fit to the cumulative AE data and the threshold amplitude for b-value calculation was 41dB. [Experiment No.: (a) 41, (b) 52]

7.3 Electrical Potential during Deformation

The electrical potential variation due to the increasing pore fluid salinity from 0.34M (2% wt) to 1.71M (10% wt) NaCl and the corresponding pore fluid variation are shown in Figure 7-3.

Changes in the electrical potential difference can be separated into four major components. A decreasing electrical potential signal is observed between 0 and approximately 300s for all the curves with the steepest drop obtained for 7.5% wt (1.29M) NaCl brine.

This overall decrease in electrical potential corresponds directly to the pore volume decrease determined from the decreasing pore fluid volume (Figure 7-3b). The decrease in pore volume, of approximately $0.1cm^3$, is due to the increased axial differential stress causing compaction. Compaction is associated with small levels of AE activity, as shown in Figure 7-2b, and therefore fluid is being forced out of the connected porosity. The flow of fluid from the connected pores and cracks will carry convection currents resulting in a redistribution of the electrical charge and so a varying electrical potential difference.

The second component of the electrical potential signal results in a period of constant potential difference being maintained. It corresponds with a region of constant pore volume change, corresponding to the onset of AE activity at 360s. The AE, due to microcracking, suggests the onset of dilatancy and this region of constant potential difference and constant pore volume can be understood as a competition between dilatancy and compaction.

Later the pore volume again increases with increasing deformation, followed closely by an increase in the electrical potential, indicating the dominance of dilatancy. The direction of fluid flow has now changed, as fluid is forced into the newly forming cracks by a constant pore pressure. The convection current carried by the fluid may change direction leading to a change in the electrical potential difference.

The pore volume increases non-linearly until failure with an average pore volume change of $0.65cm^3$ observed. After fracture a drop in the pore fluid volume is evident before a constant value is maintained. The electrical potential difference increases during this period until a peak electrical potential is reached and this is followed by a decreasing potential difference until failure. The position of this peak is dependent on the pore fluid salinity and does not correlate with any corresponding position in pore volume change or stress.

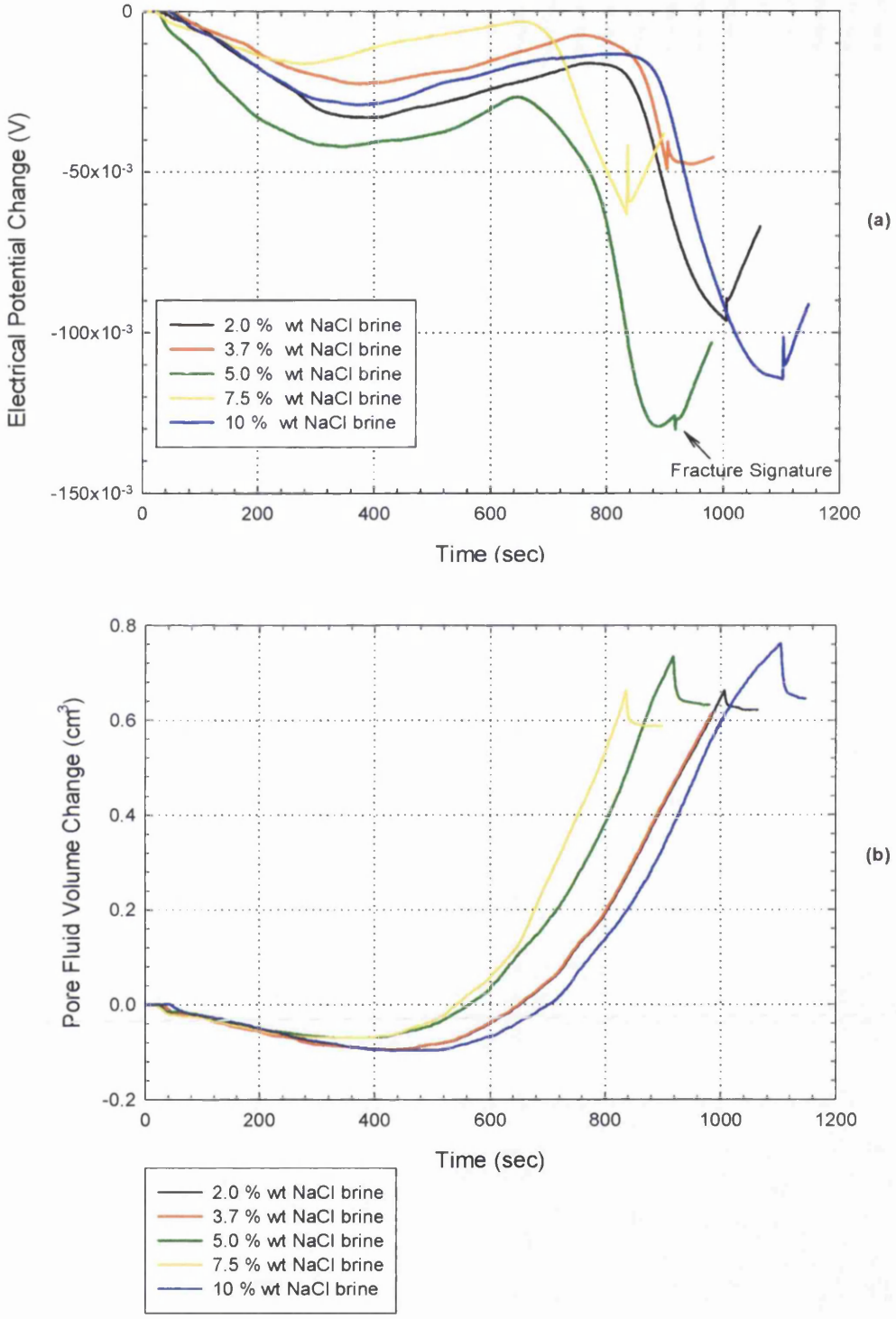

Figure 7-3 Temporal evolution of (a) electrical potential signals during deformation using varying salinity pore fluids and the corresponding (b) pore fluid volume changes which indicates directly pore volume changes in the rock sample. Deformation occurred at an effective pressure of 20MPa using a strain rate of 1.5 x 10^{-5} s^{-1} and data is normalised to zero. [Experiment No.: 51, 52, 53, 55, 56, 59]

Dilatancy is still occurring as observed from pore volume and AE measurements and therefore this anomalous electrical potential behaviour must reflect a change in the microcracking mechanism. The effect is only found when brine pore fluids are used; a similar signal change was not observed for deionised water during triaxial deformation (Chapter 6).

The final component of the electrical potential change is the signal generated during macroscopic fracture of the sample. The signal is spike-like for all experiments reported and varies between 5 and 20mV in magnitude with all signals showing initial upward positive polarity.

7.4 The Effect of Differential Stress on Electrical Potential Signals.

The increase in differential stress during the course of a triaxial experiment causes compaction and dilatancy to occur and these processes were shown to produce significantly different electrical potential signals. During compaction, increasing differential stress reduces pore space and to aid in understanding the effect on changes in electrical potential some data is extracted from the appropriate sections of the experimental curves and re-plotted. Firstly the values of axial stress and electrical potential are plotted up to the onset of dilatancy, which can be defined as the deviation from linearity on the volumetric strain curves. This is equivalent to the deviation from the initial linear section of the pore volume change curves.

In Figure 7-4a the pore volume is plotted against differential vertical stress and the resulting electrical potential change is displayed in Figure 7-4b for Darley Dale sandstone deformed at a strain rate of 1.5 x 10^{-5} s^{-1} using a pore fluid of 3.7% wt NaCl concentration.

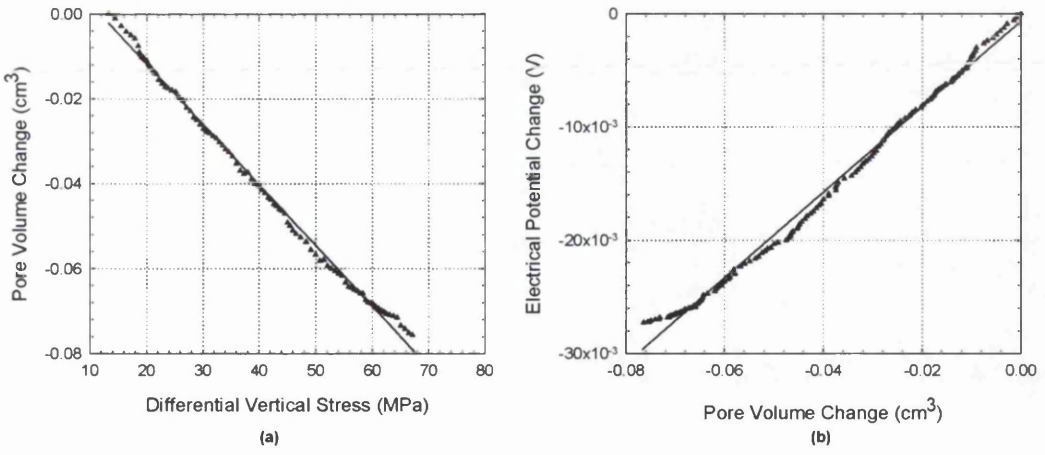

Figure 7-4 Pore volume change with (a) effective vertical stress and (b) electrical potential change during compaction for the deformation of Darley Dale sandstone at an effective pressure of 20MPa and strain rate of 1.5 x 10^{-5} s^{-1} using a NaCl brine of 3.7% wt concentration. [Experiment No.: 51]

A decreasing pore volume occurs with increasing effective vertical stress (Figure 7-4a) due to compactive processes, which leads to a decline in permeability. The closure occurs linearly at a rate of -1.5 x 10^{-3} cm^3 /MPa and the slight deviation from linearity at 62MPa (63% of sample peak strength) is considered to be the onset of dilatancy. The electrical potential during this period decreases linearly with decreasing pore volume (Figure 7-4b) at a rate of 357.1 mV/cm^3, suggesting the possible use of electrical potential signals as an indirect measurement of effective stresses during compaction.

The onset of AE activity (Figure 7-2a) corresponds to micro-cracking associated with dilatancy. This volume increase will allow fluid flow to occur under the constant pressure gradient. The variation in pore volume change and electrical potential is displayed in Figure 7-5.

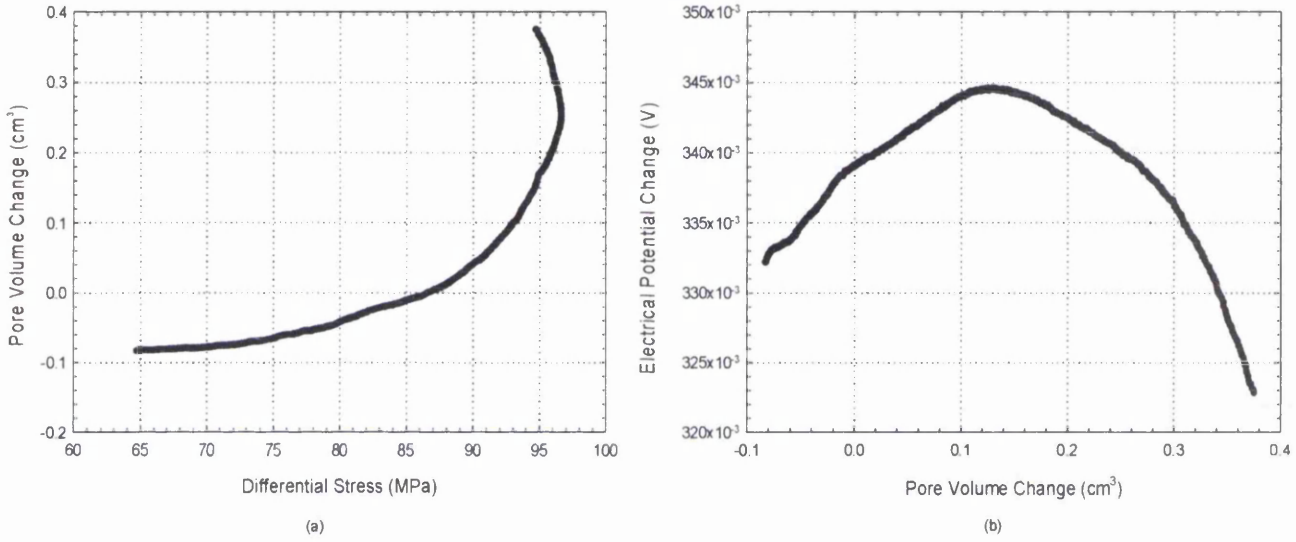

Figure 7-5 Pore volume change with (a) effective vertical stress and (b) electrical potential change during dilatancy for the deformation of Darley Dale sandstone at an effective pressure of 20MPa and strain rate of 1.5 x 10^{-5} s^{-1} using a NaCl brine of 3.7% wt concentration. [Experiment No.: 51]

An exponential law relates the pore volume change to differential stress during dilatancy, as shown by the fit to the data in Figure 7-5a. The pore volume change of 0.4cm^3 created through dilatancy is a factor of four greater than the pore volume change during compaction. The electrical potential change associated with this pore volume change is shown in Figure 7-5b. The relationship is significantly different from the case of compaction when the electrical potential change was directly related to the pore volume change.

The decrease in the electrical potential from zero to approximately -12.5mV can be attributed to a convection current carried by the fluid into newly forming dilatant cracks. This flow is in the opposite direction to that during compaction changing the electrical potential. Beyond this minimum value the electrical potential increases as dilatancy continues to increase the pore volume change. This feature is not observed during similar experiments conducted using deionised pore fluid (Figure 6-6) which tends to suggest some different mechanism operating due to brine pore fluids at this stage of deformation.

7.5 Microstructural Analysis

To understand fully the anomalous electrical potential change due to brine pore fluid, thin sections of Darley Dale sandstone were made and relevant micro-structural information extracted. Figure 7-6 shows photomicrographs of Darley Dale sandstone under cross-polarised light. In Figure 7-6a, the photomicrograph shows the microstructure of Darley Dale sandstone, which has undergone dilatancy up to the anomalous point of electrical potential difference change. The deformation was stopped and the sample removed carefully. In Figure 7-6b the microstructure of Darley Dale sandstone is shown for a sample which has undergone complete dynamic fracture. A sample of fractured Bentheim sandstone is shown in Figure 7-6e including a developed fault plane and finally in Figure 7-6f, fractured basalt is shown including a section of the macroscopic fault plane. All photomicrographs are shown for the axial direction and represent a cross section between the top and bottom of the sample. Figure 7-6c, d, g and h are the corresponding edge detected versions of Figures 7-6a, b, e and f. The edge detection method calculates the first derivative and therefore is useful in delineating boundaries and cracks.

An examination of the thin sections shows brittle deformation processes to be the most obvious deformation feature. In Figures 7-6b and d, quartz and feldspar grains are fractured and fragments displaced relative to each other. A conspicuous development of axially aligned cracks is apparent across both sections.

In Figure 7-6a and c, angular quartz grains form the majority of the photograph with minor clays and feldspars also evident. A comparison of the two photomicrographs reveals the absence of significant cracks within the quartz and feldspar grains in the Darley Dale sandstone, Figure 7-6a. This can be observed more clearly in Figure 7-6b and d. The cracking, which is evident in Figures 7-6b and d may therefore have an important role in causing the observed changes electrical potential difference. More specifically this cracking, seen in the quartz grains, can be called intragranular in contrast to intergranular cracking, which occurs between the grains. A period of intergranular cracking must operate during dilatancy, which increases the pore volume allowing influx of pore fluid, while the secondary intragranular cracking occurs at a later stage. In Figure 7-7 it is seen that the onset of the anomalous electrical potential difference changes is near to the time of peak stress of the sample.

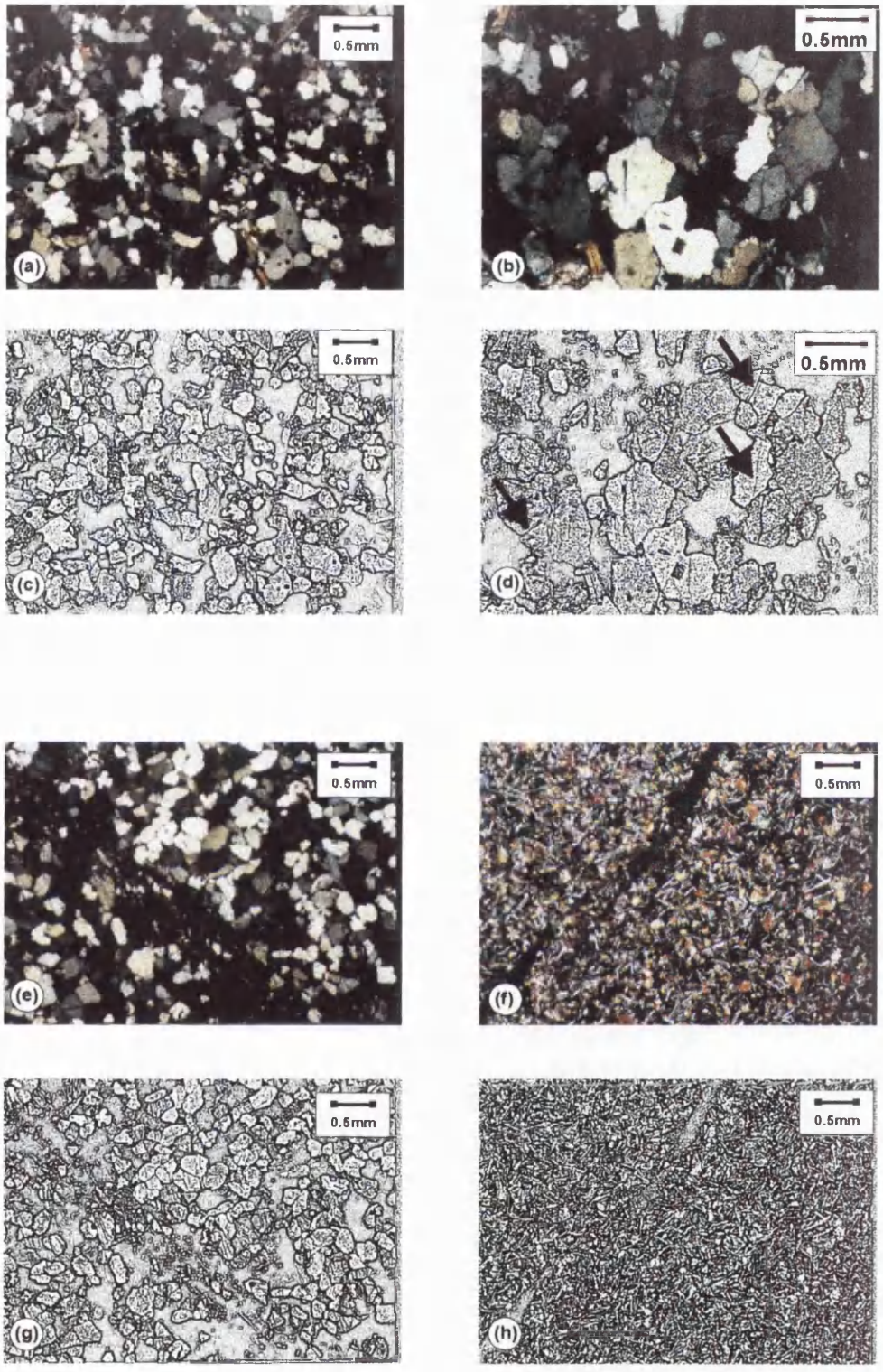

Figure 7-6 Photomicrographs of (a) Darley Dale sandstone deformed during dilatancy but non-fractured, (b) fractured Darley Dale sandstone, (e) fractured Bentheim sandstone, (f) fractured Icelandic basalt. The photos in (c), (d) –arrows indicate intragranular microcracks, (g) and (h) are the edge-detected results of (a), (b), (e) and (f).

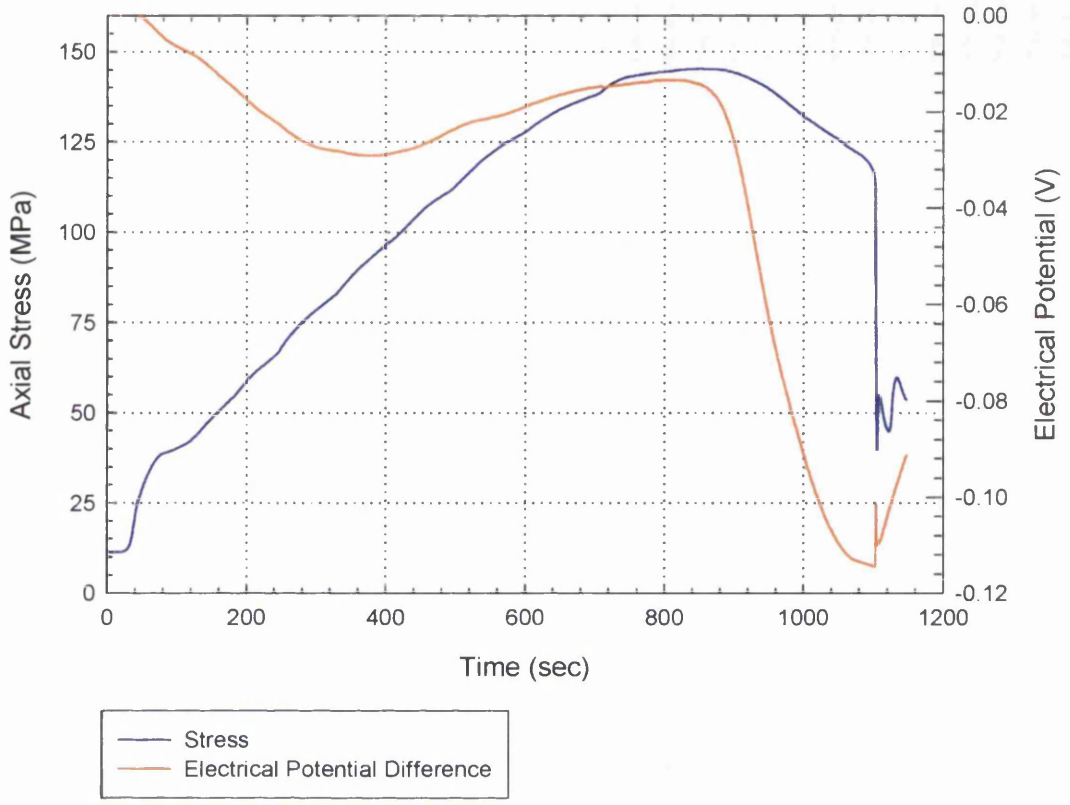

Figure 7-7 Electrical potential difference and axial stress change for deformation of Darley Dale sandstone. [Experiment No.: 51]

7.6 Electrical Potential Changes during Dynamic Fracture.

The coseismic electrical potential changes and corresponding stress drops during dynamic failure of Darley Dale sandstone are presented in Figure 7-8 for the range of brines investigated. Electrical pre-seismic signals, such as those detected in Chapter 5 for water saturated rocks, are not detectable above the

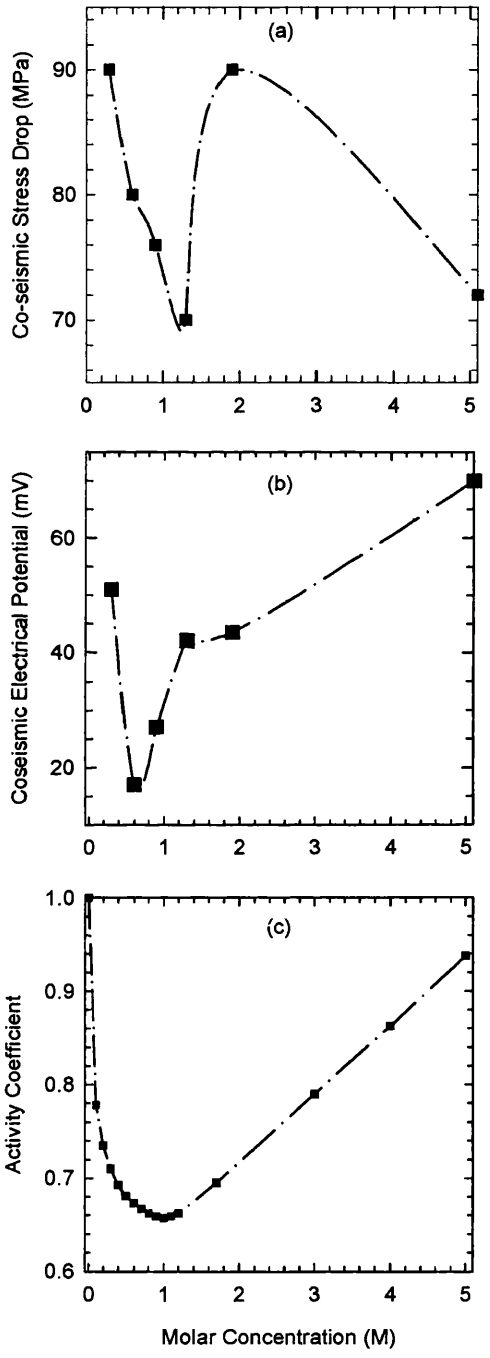

Figure 7-8 (a) Stress drop at fracture and (b) electrical potential changes during dynamic fracture of Darley Dale sandstone at an effective pressure of 20MPa and strain rate of 1.5×10^{-5} s^{-1} using NaCl brines varying between 0 and 5M (c) electrochemical activity coefficient for a NaCl monovalent ion pair. [Experiment No.: 51, 52, 53, 55, 56, 59]

noise level when brines are used (Figure 7-9). Also shown in Figure 7-8c are the activity coefficients for the concentration of the ionic species of NaCl in solution.

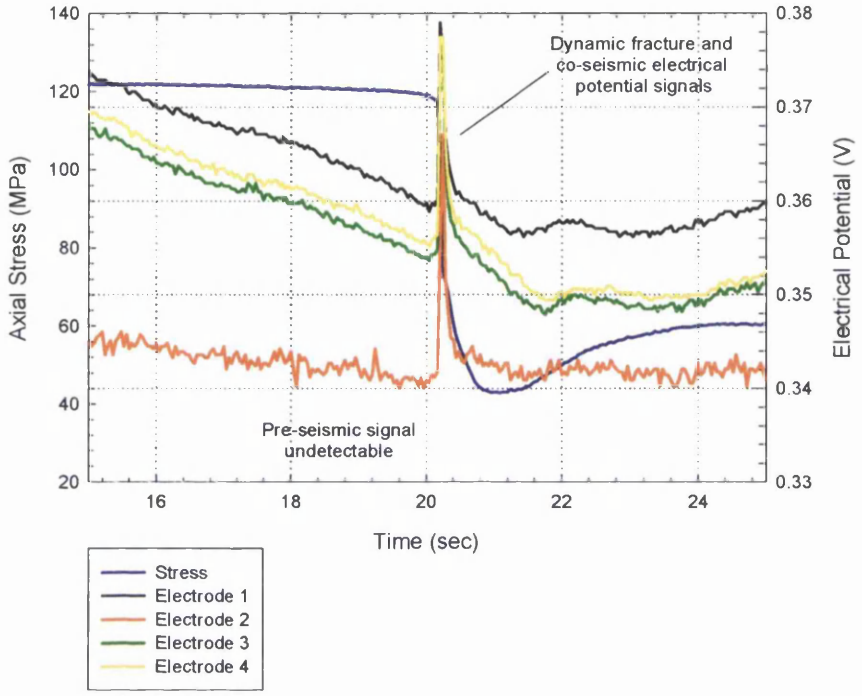

Figure 7-9 Electrical potential difference prior to and during dynamic failure of Darley Dale sandstone saturated with 0.63M NaCl pore fluid. [Experiment No.: 51]

In Figure 7-8b, the electrical potential coseismic signal decreases between 0 and 0.6M, after which an increase occurs over the higher pore fluid concentrations. The values of co-seismic electrical potential range between 15 and 70mV with an associated error of ± 0.5mV. From Figure 7-9 the fracture signature was identical for all the experiments and consisted of a positive polarity spike and succeeding decay signal, similar to those reported in Chapter 5. Electrical potential changes were of similar magnitude for all the electrodes (1 to 4) which differs from the case using deionised water where greater magnitudes were recorded for electrodes 3 and 4, approximately twice those of electrode 1 and 2.

An correlation between the coseismic electrical potential signals and the dynamic stress drop (Figure 7-8a) up to 1.3M concentration is seen. Low coseismic stress drops are associated with high electrical potential signals, with a peak stress drop of 93MPa generating a co-seismic electrical signal of 17mV. Above 2M a decrease of dynamic stress drop with increasing molar concentration corresponds to an increase of the coseismic electrical signal.

The activity coefficient (γ) of the ionic monovalent ion pair (Na^+ & Cl^-) calculated from Debye-Hückel theory is plotted in Figure 7-8c against molar concentration. The coefficient relates the ionic charge (z), hydrated radius (α) and concentration (m) of the ions in solution through the equation

$$\log \gamma = \frac{-0.51z^2\sqrt{m}}{1+(\alpha\sqrt{m}/305)} \tag{8-1}$$

The variation of activity coefficient shows excellent correlation with the electrical potential difference at fracture (Figure 7-8b). A minimum value of the electrical potential, at 0.6M, corresponds with the lowest value of the activity coefficient and an increase of electrical potential with activity coefficient occurs above this ionic concentration.

7.7 Chapter Summary

I Rocks saturated with low ionic brine solutions (≈ 0.34M) are ≈ 5% stronger than water-saturated samples. Intermediate concentration solutions (≈ 1.2M) are ≈ 17.5% stronger than water saturated samples while the greatest reduction in strength (≈ 5%) is found for high strength brine solutions (≈ 5M).

II The b-value variation is the same for the brine solutions as the water-saturated condition although the cumulative AE in brine saturated rocks are increased by 2.5 when compared to the water-saturated condition.

III A decreasing electrical potential signal occurs during compaction which is associated with a pore volume decrease and small levels of AE activity. A period of competition between compaction and dilatancy corresponds to a constant electrical potential and an increase in AE activity. Decreasing values of b-value represent higher magnitude AE over a more diffuse area and represent dilatancy. During this period the electrical potential becomes less negative, also corresponding to a pore volume increase. A decrease in b-value and an increase in pore volume is then found upto failure. The electrical potential near to peak stress becomes more negative and continues so until failure. The point at which this change occurs depends on the pore fluid salinity.

IV The rock pore volume decreases linearly with effective vertical stress and leads as does the electrical potential difference with pore volume decrease. An exponential relationship exists between pore volume change and differential stress during dilatancy. The relationship between electrical potential difference and pore volume change and hence differential stress is however distorted due to anomalous signal changes.

V Microstructural analysis reveals no significant cracking within the quartz and feldspar grains of Darley Dale sandstone prior to the point at which this electrical potential signal changes. After dynamic fracture however clear intragranular and transgranular cracking can be observed. This condition is also apparent in Bentheim sandstone, but deformation induced microcracking in basalt creates large continuous cracks within the compact and impermeable matrix.

V1 Electrical potential variations before dynamic fracture are not detectable above the background noise level when brine pore fluids are used. The co-seismic signals are the same recorded on all electrodes and decrease with molar concentration up to 0.6M and then increase with increasing concentration. A correlation between co-seismic electrical potential signal and activity coefficient is apparent.

8. The Effect of Strain Rate on Electrical Potential Signals

8.1 Introduction

Strain rate effects are however important in shear fracture (Odedra, 1998), frictional strengths and nucleation processes (Kato et al., 1992). For example, Kemeny (1991) extended a model for the interaction of collinear wing cracks (Kemeny and Cook, 1987) to include sub-critical crack growth governed by Charles' Law (Charles, 1958) and showed agreement with laboratory observed stress-strain behaviour with strain rate. If the processes of sub-critical crack growth play an important role in the deformation process then only a strain rate dependent model will account for the observed unsteady growth of cracks (Renshaw and Schulson, 1998). A realistic geological strain rate of 10^{-14} s^{-1} is difficult to obtain within the laboratory and is very time-consuming, for example even a strain rate of 10^{-10} s^{-1} would take approximately 2 months to reach 2% shortening. It is therefore important to provide experimental data from a range of strain rates to form a basis for extrapolation.

The effect of strain rate on the electrical potential is investigated, using strain rates of 1.5×10^{-4} s^{-1} to 1.5×10^{-6} s^{-1} under drained conditions. The electrical potential difference and acoustic emissions during deformation have been measured and analysed in order to give some indication of how electrical potential difference might vary over geologically significant time-scales.

8.2 Mechanical Effects due to Strain Rate Variations

The mechanical properties of Darley Dale sandstone deformed at constant strain rates ranging from 10^{-4} s^{-1} to 10^{-6} s^{-1} are summarised by the stress-strain curves in Figure 8-1. The specimens were deformed in the presence of deionised water held at a constant pore pressure. The confining pressure was maintained at 40MPa corresponding to a depth of 1.6km in the crust. A strain rate of 1.5×10^{-7} s^{-1} was attempted three times and each time an experimental failure was recorded due to electrical cut-outs. The duration of the experiment was 27 hours and therefore due to time restrictions it was not possible to continue to try and complete this experiment.

A quasi-linear-elastic increase in the stress as a function of strain is observed for strain rates of 1.5×10^{-4} s^{-1} and 1.5×10^{-5} s^{-1} until approximately 0.7% strain when a departure from linearity is encountered. In the case of 1.5×10^{-6} s^{-1} strain rate the limit of the quasi-linear-elastic behaviour occurs at 0.5% strain. At this point, the yield stress is 81%, 78%, and 69% of the peak strength of the sample at 1.5×10^{-4} s^{-1}, 1.5×10^{-5} s^{-1} and 1.5×10^{-6} s^{-1} respectively. Stress then increases non-linearly with strain to a peak stress level when a decrease occurs representing a strain-softening period. However peak differential stress values obtained of 67.5, 80 and 72.5MPa are not considered to vary significantly with strain rate. Dynamic failure is characterised by a rapid decrease to a residual stress. The maximum elongation measured varies between 1.125% and 1.225% for these samples.

Figure 8-2 shows the acoustic emission data from the experiments where the samples are deformed in the presence of water as pore fluid under drained conditions. Cumulative AE are shown together with the seismic b-value for each strain rate experiment performed.

An exponential increase in AE activity is seen for each strain rate. Also a change in total cumulative AE from 7200 in Figure 8-2a to 11,200 in Figure 8-2c as strain rate decreases from 1.5×10^{-4} s^{-1} to 1.5×10^{-6} s^{-1} is observed. The decreasing cumulative AE with strain rate suggests the rock is becoming weaker and since similar experimental conditions exist, this weakening effect is predominantly due to mechanical properties rather than chemical influences.

The seismic b-value initially decreases steadily as deformation proceeds. The decrease in b-value from values of 1.75 (Figure 10-2a), 1.4 (Figure 10-2b) and 1.9 (Figure 10-2c) continues directly to failure, with a marked b-value drop prior to dynamic fracture to 0.7, 0.8 and 0.4 at dynamic failure for strain rates of 1.5×10^{-4} s^{-1}, 1.5×10^{-5} s^{-1} and 1.5×10^{-6} s^{-1} respectively. After this point, recovery to a value between 1 and 1.5 occurs as frictional sliding commences (N.B these experiments are terminated after dynamic fracture and frictional sliding is generally not represented).

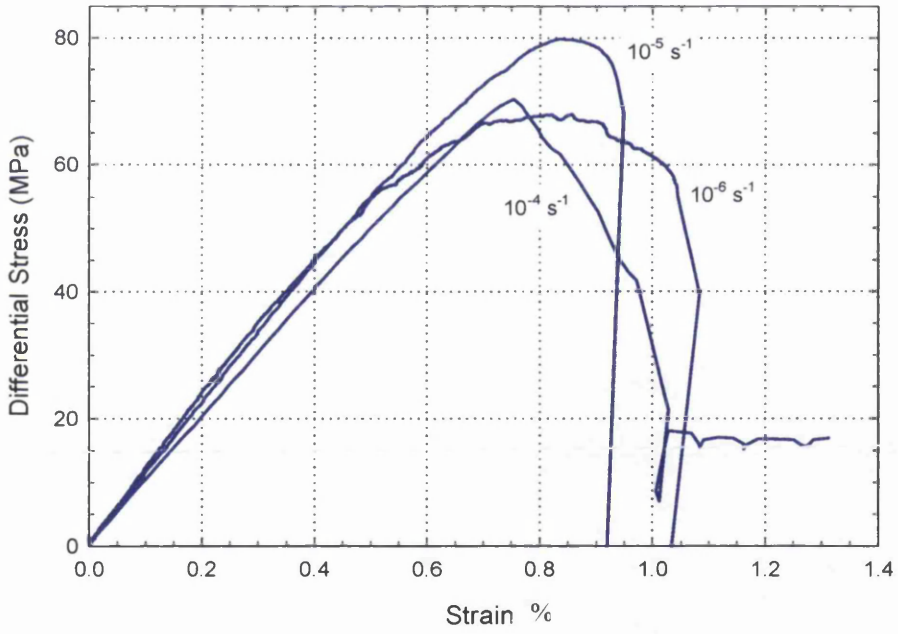

Figure 8-1 Stress-strain curves from experimental deformation of Darley Dale sandstone at strain rates varying from 1.5×10^{-4} s^{-1} to 1.5×10^{-6} s^{-1}. Effective pressure was maintained at 20MPa for each experiment and deionised water was used as pore fluid. [Experiment No.: 41, 42, 43]

After fracture the b-value recovers to a value comparable with the initial values. Similar fault styles are produced in all samples and these extending across the sample in question at an angle of approximately 30° to the axial principal stress.

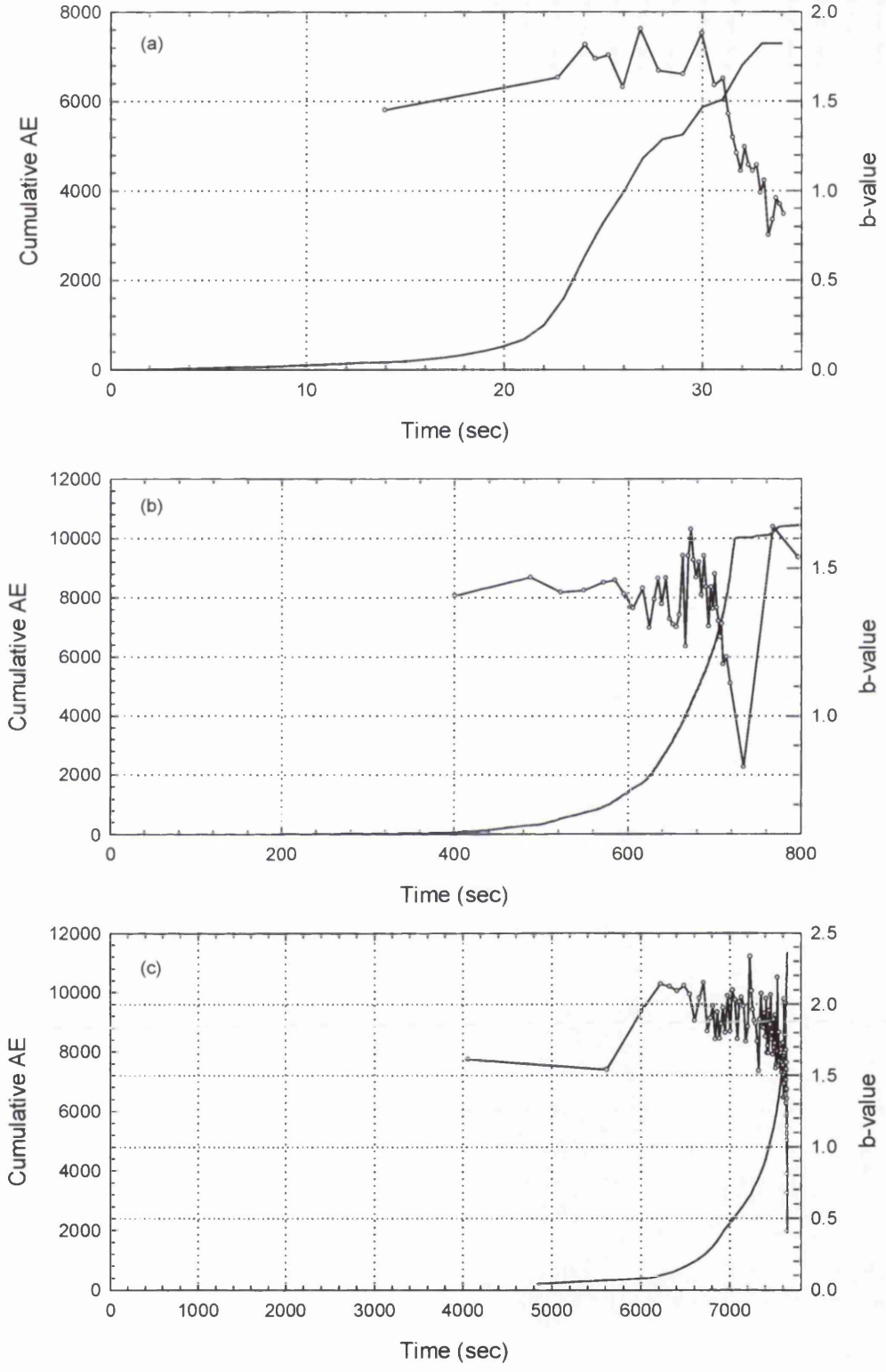

Figure 8-2 Cumulative AE and b-value changes for deformation of Darley Dale sandstone under drained conditions for a strain rate of (a) 1.5 x 10^{-4} s^{-1}, (b) 1.5 x 10^{-5} s^{-1} and (c) 1.5 x 10^{-6} s^{-1}. [Experiment No.: (a) 41, (b) 42, (c) 43]

8.3 Electrical Potential Changes

The change in the electrical potential difference has been measured during compaction and dilatancy and plotted as a function of strain rate in Figure 8-3. Also shown are the associated measurement errors.

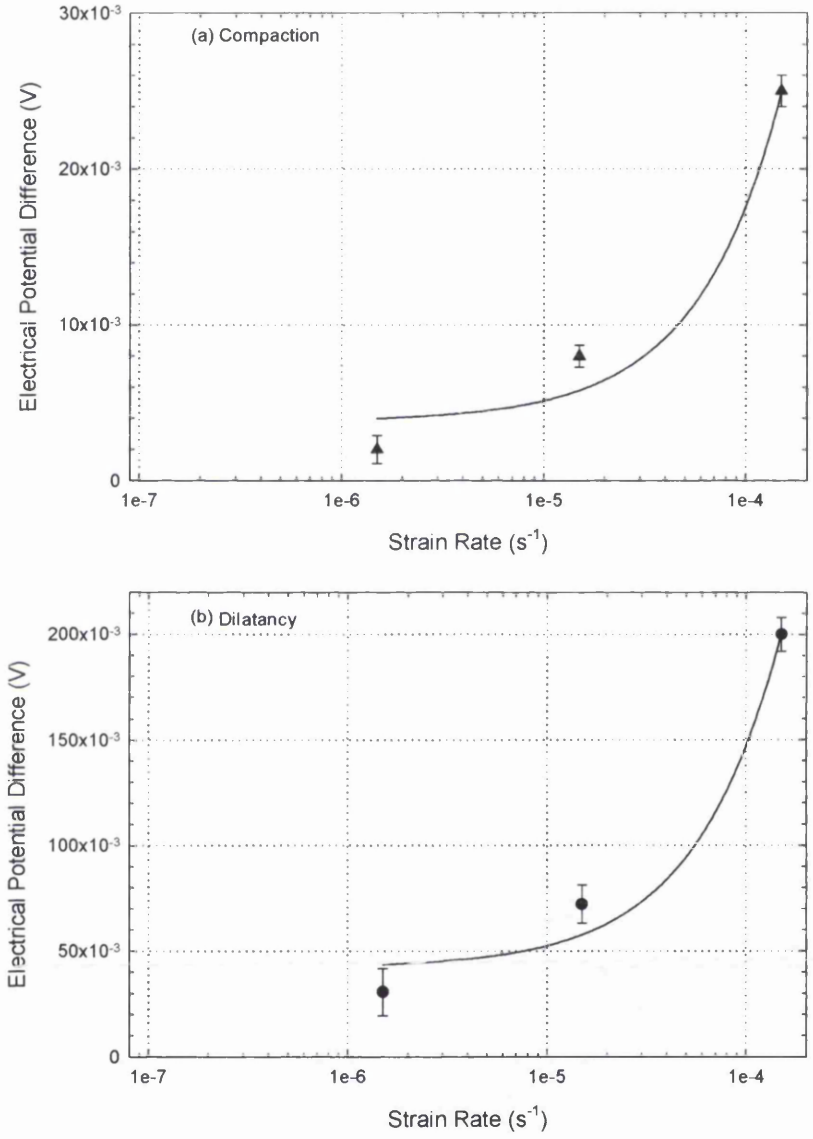

Figure 8-3 Variation of electrical potential difference with strain rate for Darley Dale sandstone for (a) compaction and (b) dilatancy (taken up to failure). The data plotted is the absolute change in electrical potential difference and does not indicate any information on polarity changes. [Experiment No.: 41, 42, 43]

During compaction the absolute value of electrical potential difference change decreases with strain rate. This period is associated with low AE event rate for all strain rates and closure of cracks have the effect

of expelling pore fluid from the rock interior. This fluid will transport charge created in electrical double layers by means of convection currents. In the case of a quartz/water system a pressure gradient causing fluid flow will transport positive charges (Chapter 3). As the fluid carrying this positive charge leaves the compacting rock a decrease in the electrical potential results, as is observed by the electrical potential difference during deformation (Chapter 6).

The pore volume change, which occurs in a sandstone sample during compaction, is shown in Figure 8-4. A constant pore volume change of approximately $0.06cm^3$ occurs over the range of strain rate investigated and therefore is independent of strain rate. This implies the same mechanism for both crack and pore closure. Since the stress-strain data shows similar quasi-elastic behaviour, the electrical potential differences noted can be attributed to changes in pore fluid velocity caused by local pressure gradient change.

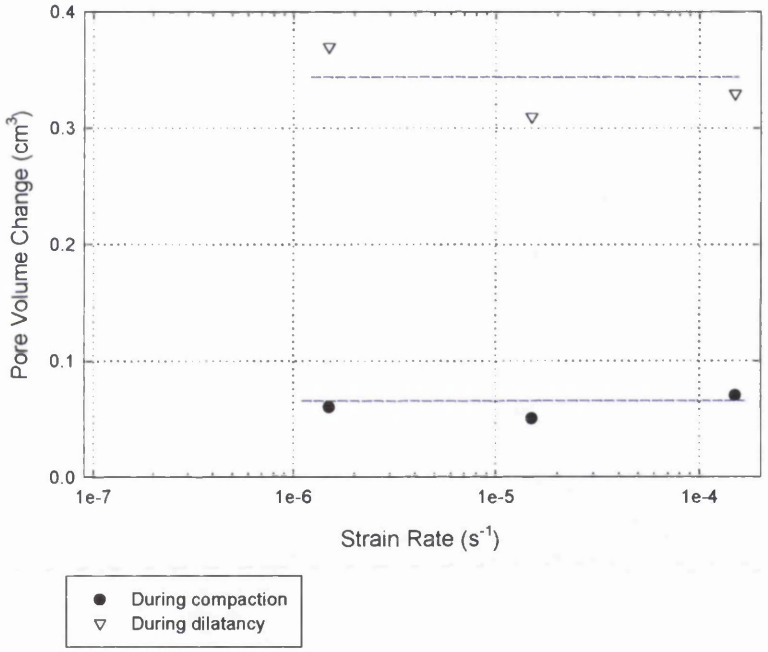

Figure 8-4 Variation of pore volume change with strain rate during compaction of Darley Dale sandstone. [Experiment No.: 41, 42, 43]

At the onset of dilatancy, as determined from the rise in AE activity (Figure 8-2a, b, c), crack closure ceases and newly forming cracks open in the most favourable orientations according to the Griffith criterion. Pore fluid will now be forced into these cracks and a reversal in the convection current direction can occur. The fluid entering the rock rapidly forms EDL's with the new grain surfaces. The positive charge will therefore be carried from the diffuse layer into the rock causing an increase in the electrical potential difference. This will be manifested by increasing electrical potential differences as already outlined in Chapters 6, 7 and 8.

The increase in pore volume due to new dilatant crack growth can be measured through pore fluid volumometry. The absolute pore volume increase up to dynamic failure is plotted in Figure 8-4. A constant volume change is again observed with an average pore volume change of $0.34cm^3$. The electrical potential difference occurring during dilatancy for each strain rate is shown in Figure 8-3b. A decrease in the absolute potential occurs with decreasing strain rate identical to the change during compaction. A redistribution of charge will occur, specifically more positive charge will be introduced into the rock sample as an influx of fluid into the sample caused by local pressure gradient increases will carry positive charge from the newly forming electrical double layers.

8.4 Strain Rate Effects on Pre-Seismic and Co-Seismic Electrical Potential Signals

In the case of water saturated samples, clear pre-cursory and co-seismic electrical potential signals have been identified (Chapter 5) and the effects of effective pressure have been described (Chapter 6). How the electrical potential signal varies with strain rate is important in this type of study and quantitative values will be required in future models and for interpretation of field observations. In Figure 8-5 the variation of the electrical potential difference prior to and during dynamic fracture is plotted. The values are tabulated in Table 8-1.

	Pre-seismic signal (mV)				**Co-seismic signal (mV)**			
Strain Rate (s^{-1})	Electrode 1	Electrode 2	Electrode 3	Electrode 4	Electrode 1	Electrode 2	Electrode 3	Electrode 4
1.50e-4	110	105	137	143	33	28	49	23
1.50e-5	30	20	40	40	49	52	70	70
1.50e-6	2	7.5	22	17.5	50	60	95	100

Table 8-1 Pre-seismic and co-seismic electrical potential signals measured from each electrode during triaxial deformation of Darley Dale sandstone at a range of strain rates.

In Figure 8-5a the absolute value of pre-seismic signal decreases from an average value of 123.75mV to 12.25 mV over a strain rate range from 1.5×10^{-4} s^{-1} to 1.5×10^{-6} s^{-1}. The electrical potential differences are found to be generally greater for electrodes 3 and 4 for the majority of measurements in this study. During this period, the rate of microcrack activity is high; linkage and intersection of cracks can therefore be expected. This interlinking will create pathways available for fluid flow. As explained in the preceding section the velocity of the pore fluid is expected to be higher with increasing strain rate, therefore if pore fluid travels faster in the newly forming pathways, charge will be redistributed at a greater rate. As fluid is flowing into the sample from top to bottom, positive charge is being transported vertically downwards and therefore increasing the electrical potential at the electrodes.

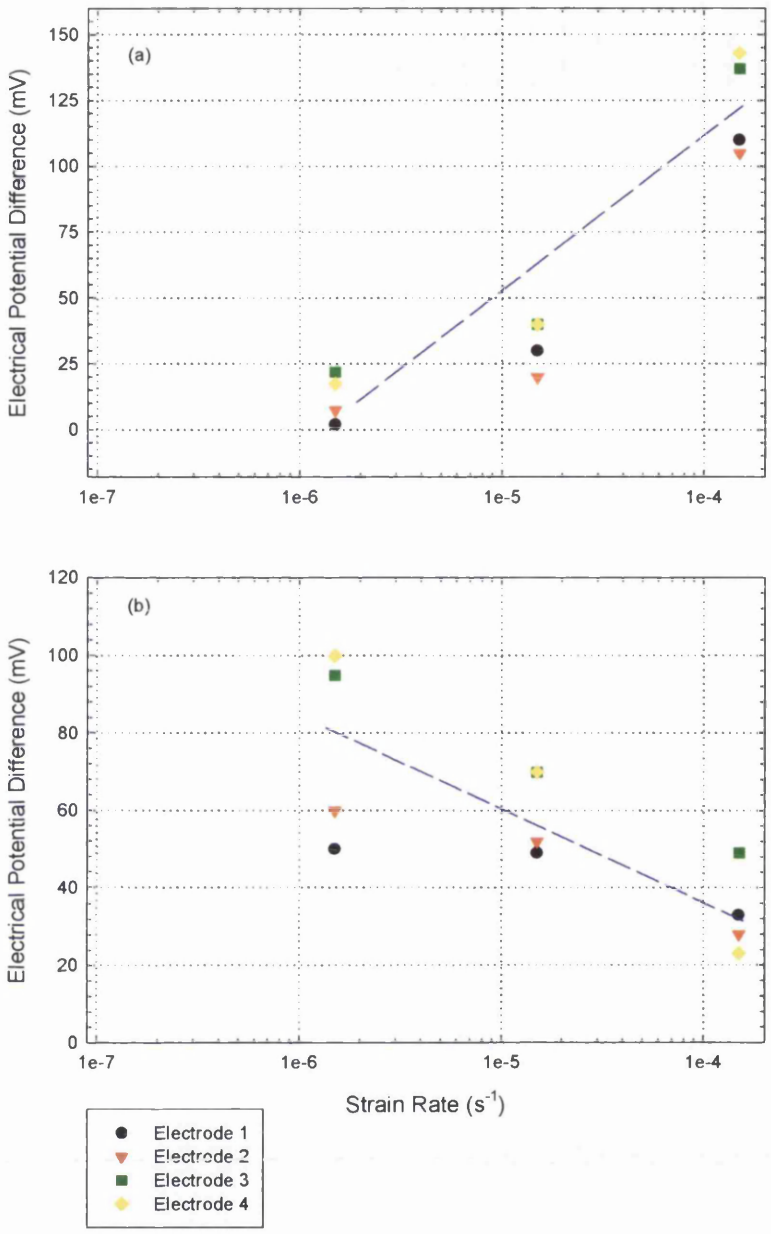

Figure 8-5 Variation of electrical potential difference (a) prior to failure and (b) during dynamic fracture as a function of strain rate. [Experiment No.: 41, 42, 43]

The co-seismic signals associated with dynamic fracture of the samples are plotted in Figure 8-5b. A decrease of the electrical potential difference from an average value of 76.25 to 33.25mV occurs with increasing strain rate. Higher potential differences are recorded for the electrodes 3 and 4 similar to the co-seismic signals. The dynamic stress drops associated with the electrical potential signal were 45, 76 and 61MPa for strain rates of 1.5×10^{-4} s^{-1}, 1.5×10^{-5} s^{-1} and 1.5×10^{-6} s^{-1} respectively. From this evidence, no qualitative relationship can be made between the stress drop and the electrical potential difference.

As the test progresses, a macroscopic fault plane is formed in the sample, which consists of a region of highly fractured and crushed grains forming a fault gouge (Figure 7-6g). The ability of fluid to flow will be interrupted by this region and therefore current flow will be disturbed. This effect would decrease the electrical potentials measured at the electrodes because less charge is being distributed within the sample. The decrease in the number of AE recorded with increasing strain rate also implies fewer pathways available for fluid and current flow.

8.5 Chapter Summary

I The amount of rollover varies with strain rate while the strength does not vary significantly. The varying rollover causes an increase in the cumulative AE with decreasing strain rate.

II A decrease in the electrical potential difference occurs with decreasing strain rate during compaction. Pore volume decreases and associated corresponding low levels of AE activity do not vary with strain rate. A fluid velocity mechanism is suggested as producing the electrical potential differences.

III Dilatancy is detected using the onset of AE activity with an exponential increase in the cumulative AE and a decrease in b-value. The absolute electrical potential differences produced during dilatancy up to dynamic fracture also decrease with decreasing strain rate. The pore volume change does not vary significantly for the strain rates investigated. Fluid flows in the opposite direction during dilatancy in all these experiments and the velocity of the fluid/current is expected to determine the charge distribution in the rock.

IV Pre-seismic electrical potential differences increase with increasing strain rate during drained triaxial deformation of Darley Dale sandstone. The co-seismic signal decreases with strain rate over the same range of strain rates. No effect of magnitude of the dynamic stress drop on the co-seismic electrical potential is seen and microstructural processes may be important in generating these signals.

9. Investigation of Streaming Potential Signals

9.1 Introduction

The generating mechanism of the streaming potential is well established in relation to rock-fluid formations. The effects of properties such as fluid pH and conductivity have been extensively studied. Disagreement arises though, when temperature effects, stress variations and pressure gradients are considered.

This chapter will present the results of high-pore fluid pressure gradients and the associated streaming potentials. The variation of streaming potential during deformation and after fracture is investigated using deionised fluids and brines. The effects of pH and conductivity will not be investigated due to the existence of previous work. Temperature effects were not investigated due to time limitations.

Finally a 2D finite element model has been used to simulate the variation of theoretical streaming potentials expected before and after sample failure. The methods used to construct this model are outlined.

9.2 Streaming Potentials at High Pore-Fluid Pressure

In this study high pore fluid pressures up to 40MPa have been used. Figure 9-1 shows the electrical potential waveform obtained during a typical streaming potential measurement. The electrical potential is constant until an isolation valve at the downstream side of the sample is opened. This causes a steady fluid flow rate under the applied pressure gradient, 20MPa in this case.

The fluid flow strips off the charged outer layer of the EDL causing a convection current to flow in the direction of flow. A potential difference is created across the sample, which generates a back conduction current flowing in the opposite direction. When the two currents equilibrate a constant streaming potential is obtained, as shown. Finally when flow is terminated, by closing the valve the streaming potential decays as the charge diffuses. This signature is typical of all the measurements performed in this study.

Using this type of signal, the streaming potential is measured for a range of pore fluid pressures between 10 and 30MPa. The results, in Figure 9-2, are plotted for experiments on undeformed samples of Darley Dale and Bentheim sandstone under hydrostatic conditions of 50MPa, saturated with deionised water.

A linear relationship is observed between streaming potential and applied pore pressure variation for the values measured at all four electrodes; regression coefficients are between 0.95 and 0.98. The values at electrode 3 and 4 are approximately twice those of electrode 1 and 2, as they are located further down the sample, away from the upper-grounded surface of the sample. This result, together with the fact that the

applied pressure difference is proportional to the fluid flow rate (Figure 9-3) suggests that streaming potentials are directly proportional to flow rate.

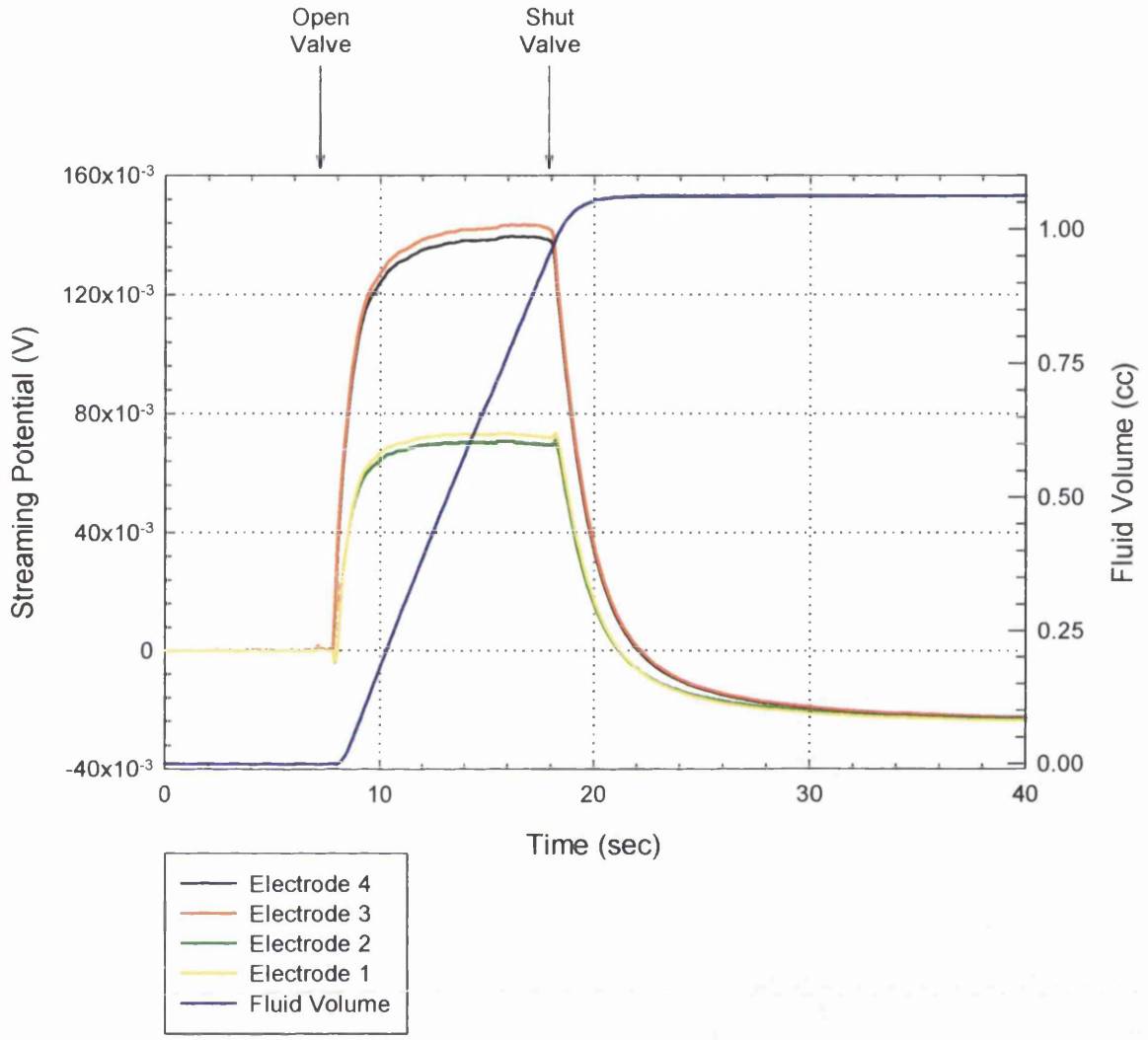

Figure 9-1 Plots of streaming potential with time for the four measuring electrodes from Darley Dale sandstone under hydrostatic pressure of 50MPa. The streaming potential is generated when a valve at the bottom of the sample is opened and ceases when the valve is closed, both positions are shown. Note the rapid decay of the streaming potential when the valve is closed. The pore pressure difference is 20MPa and the fluid volume change indicates a constant flow rate. The fluid conductivity is 250μS/cm and permeability of the rock is 1×10^{-15} m^2 at 40MPa confining pressure. [Experiment No.: 41]

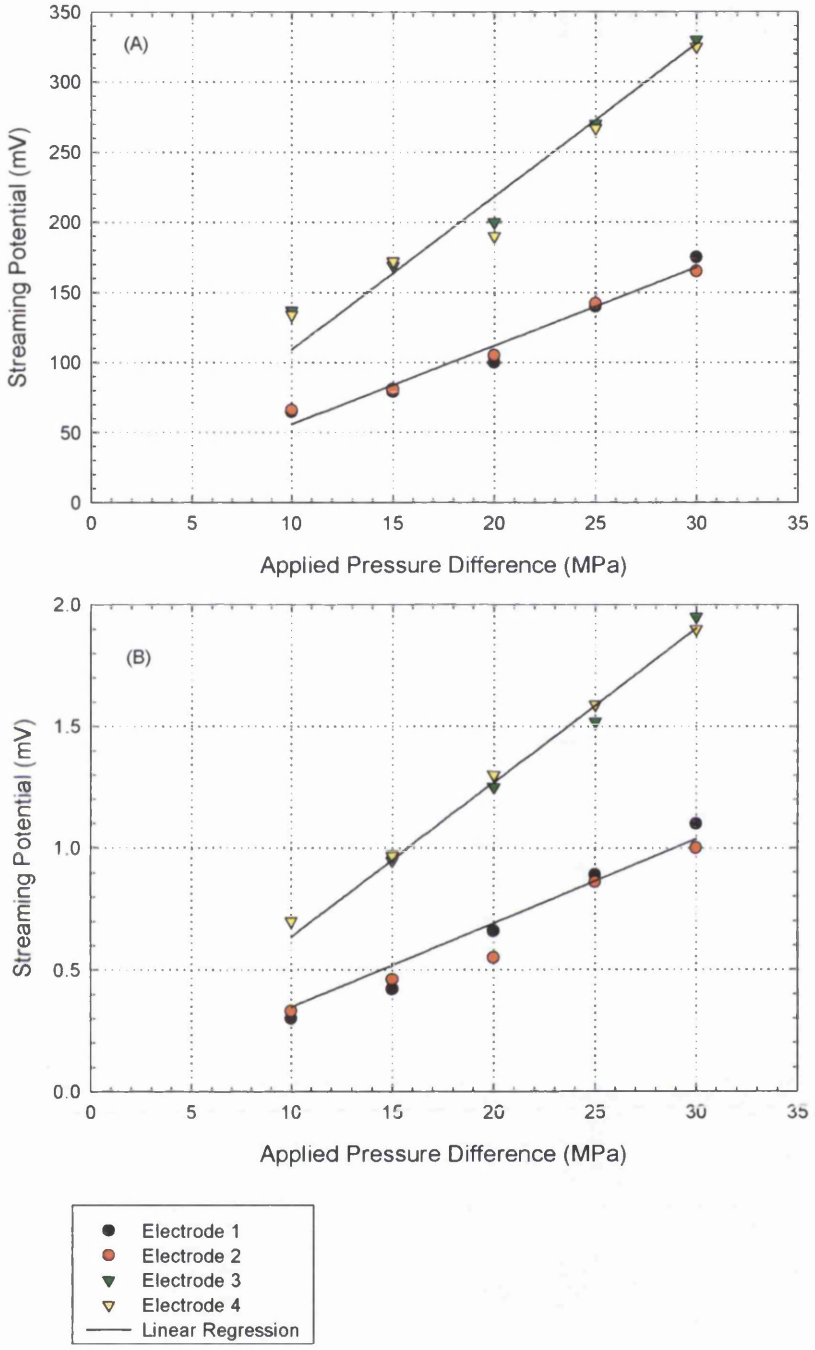

Figure 9-2 Plots showing streaming potential generated under increasing pore pressure differences for (A) Darley Dale and (B) Bentheim sandstone. A linear relationship is obtained for both samples at all electrodes. Regression coefficient range is between 0.95 and 0.98. Samples are confined under a hydrostatic pressure of 50MPa and deionised water of 250μS/cm is used as pore fluid. [Experiment No.: (a) 41, (b) 49]

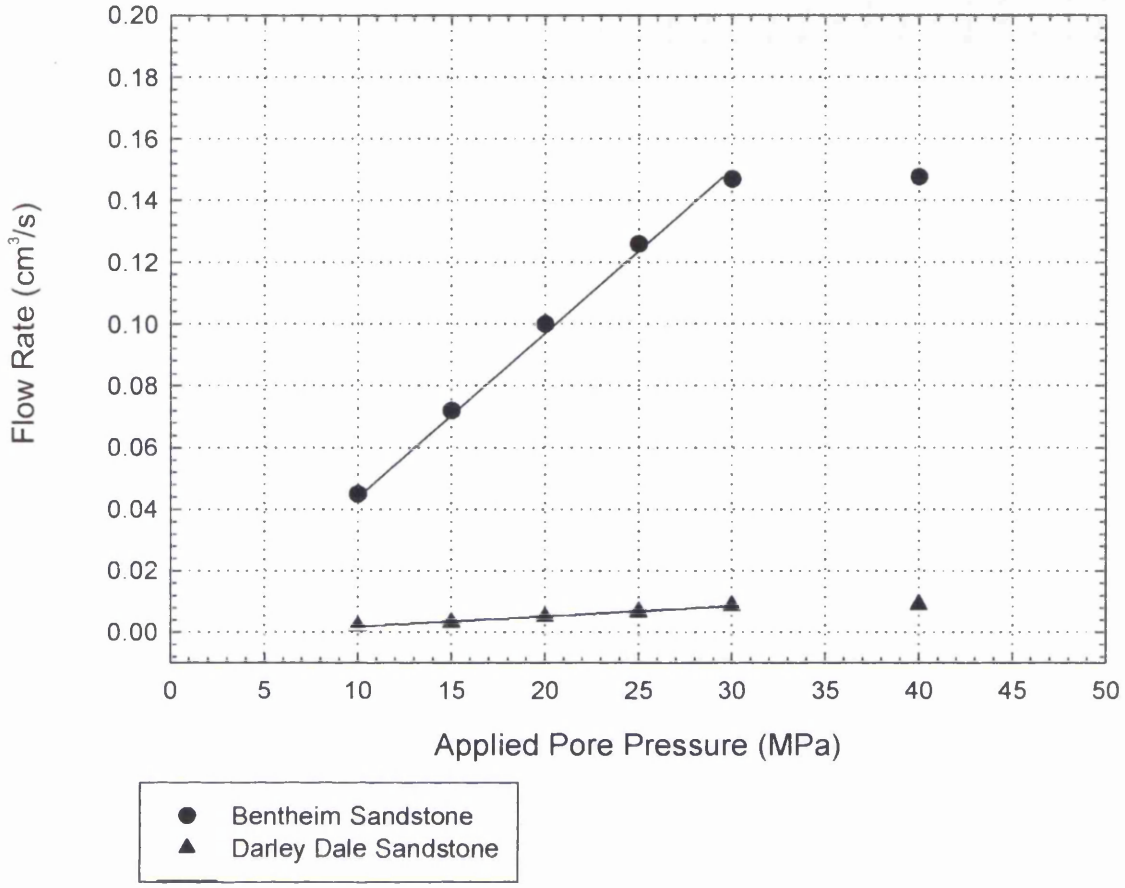

Figure 9-3 Plot showing proportionality between flow rate and applied pore pressure through Darley Dale and Bentheim sandstone under hydrostatic conditions of 50MPa. This result suggests laminar flow through the sample. [Experiment No.: (a) 41, (b) 49]

A constant streaming potential was not obtainable for pore fluid pressure differences greater than 30MPa as depicted in Figure 9-4. It is possible that pressures above this value correspond to the onset of turbulent flow, which by its nature cannot form a constant streaming current.

The Reynolds number (R_e, equation 2-24) determines whether the flow will be laminar or turbulent and is given by the equation $\rho v l/\eta$ where density $\rho = 1 \times 10^3$ kg m^{-3}, v is the velocity of the fluid in the pore matrix, l is a characteristic pore dimension and η is the fluid viscosity (1×10^{-3} Pa s). Using the average grain size of 0.5mm and 150μm for l, the Reynolds number is calculated to be 0.46 for Darley Dale sandstone and 0.75 for Bentheim sandstone. Since Darcy's Law is valid for $R_e < 1$ (Gueguen and Palciauskas, 1994), laminar flow can be assumed.

The magnitude of the maximum streaming potentials generated in Darley Dale ($\approx$ 325mV) is an order of magnitude greater than Bentheim sandstone ($\approx$ 2mV). Bentheim sandstone has a permeability greater than Darley Dale sandstone. Streaming potentials are expected to decrease with increasing permeability

(Jouniaux and Pozzi, 1995b) for a given pressure gradient but from Figure 9-3, it can be seen that the flow rate is significantly different for both sandstones.

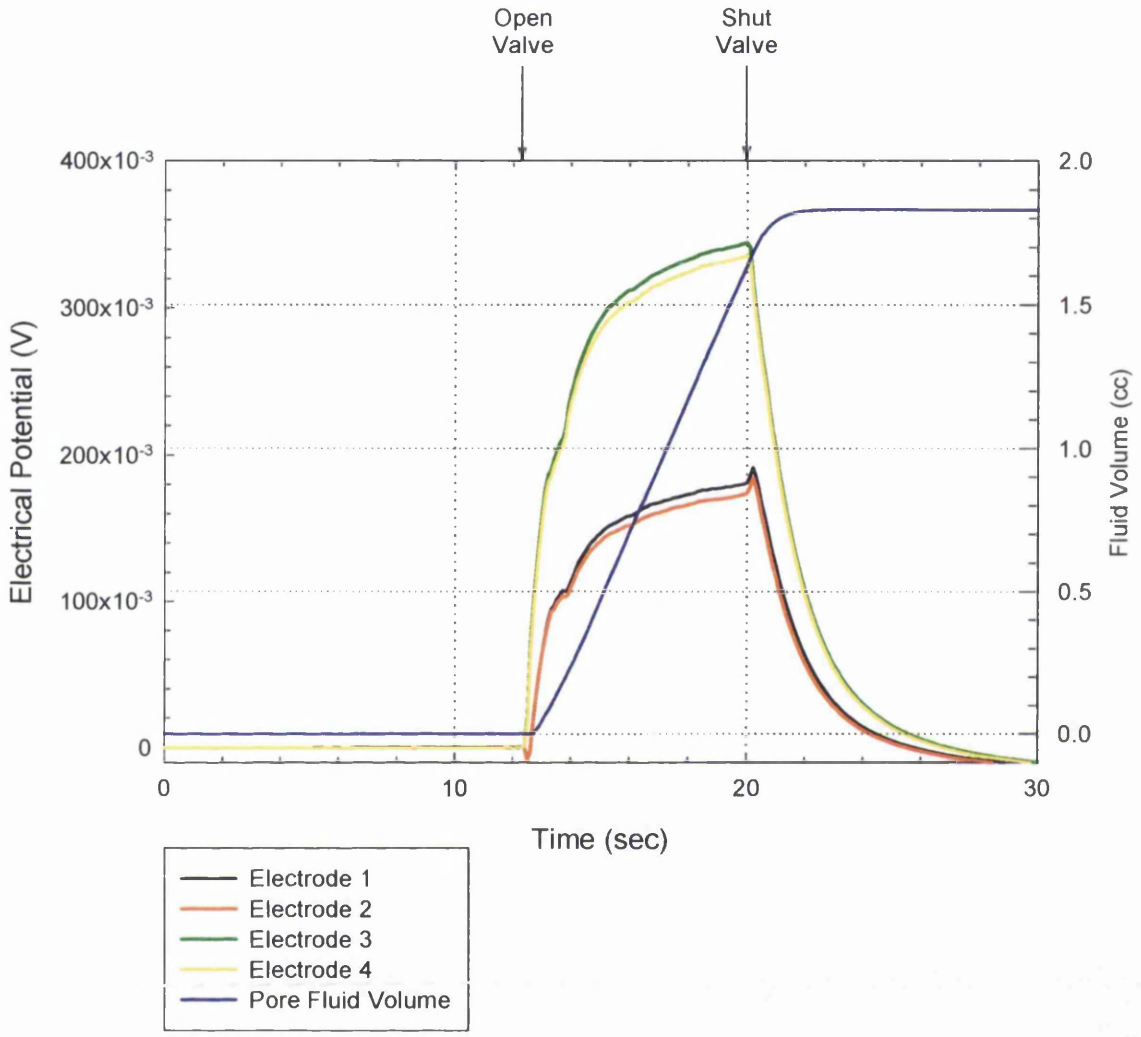

Figure 9-4 Electrical potential variation during application of 40MPa pore fluid pressure difference across Darley Dale sandstone. A constant streaming potential gradient is not obtained suggesting a turbulent flow regime. [Experiment No.: 41]

9.3 Streaming Potential Variation with Stress Perturbation

The effect of a slowly varying axial compressive load on the streaming potential is investigated. A constant streaming potential was achieved for a Darley Dale sandstone sample under hydrostatic conditions of 40MPa. The pore fluid used was deionised water and the fluid pressure gradient applied was 20MPa. As the streaming potential was maintained constant a compressive pulse was applied to the sample by increasing and decreasing the axial compressive load (Figure 9-5).

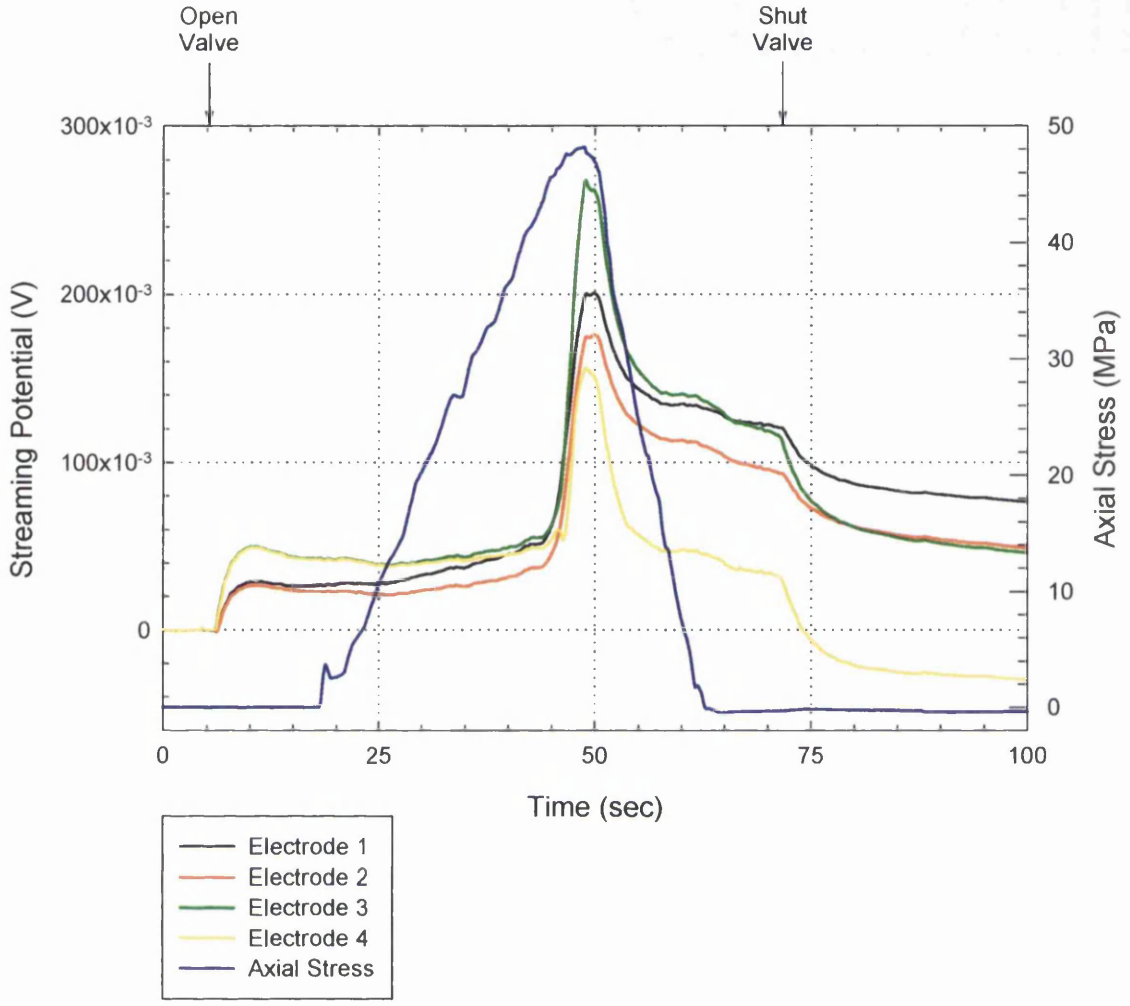

Figure 9-5 Plot of streaming potential change as a slowly varying axial compressive load is applied to the sample. Confining pressure was 50MPa and fluid pressure was maintained at 20MPa. The load was increased manually and the signal change is recorded on all four electrodes. [Experiment No.: 41]

The results show a constant streaming potential during the increasing axial load and a rapid increase, of approximately 200mV (for electrode 3), as the stress rate changes. This peak value decreases rapidly at first and then more slowly as the axial load decreases. When the valve is closed and the streaming potential decays characteristically as the convection current ceases.

It therefore appears that an increased streaming potential is produced by means of the change in stress direction. Plotting streaming potential versus stress rate can further delineate this observation. In Figure 9-6a the first derivative of stress and the inverse electrical potential show an excellent correlation. The magnitude of the stress pulse is varied between 10 and 50MPa and the results are plotted in Figure 9-6b.

(a)

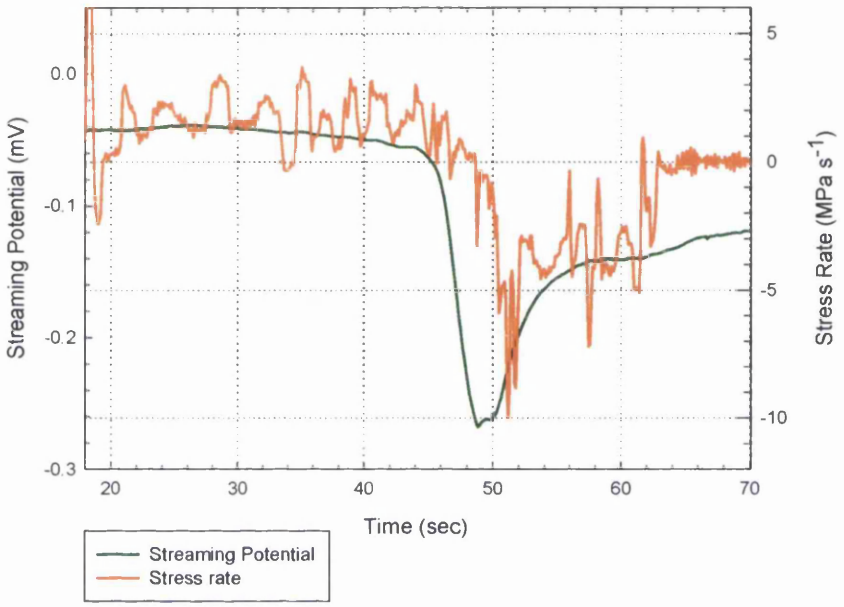

(b)

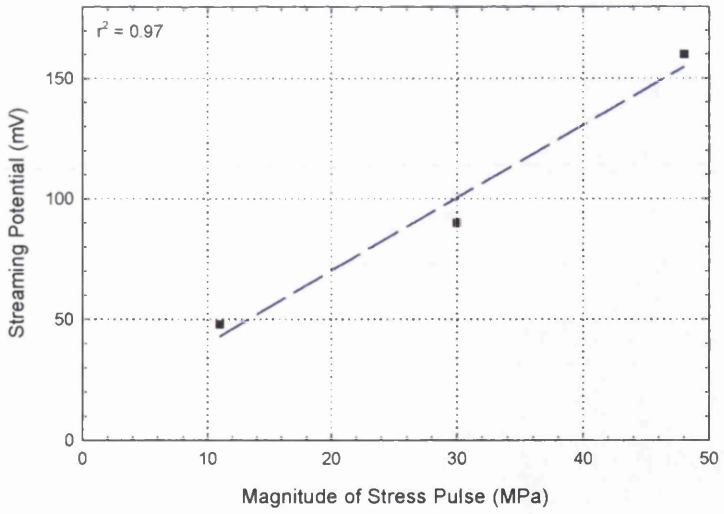

Figure 9-6 (a) The inverse streaming potential plotted against the first derivative of axial stress and (b) Streaming potential as a function of stress pulse magnitude. [Experiment No.: 41]

A relationship can therefore be proposed between streaming potential (Vs) and stress rate ($\dot{\sigma}$)

$$1/V_s = C\dot{\sigma} \tag{9-1}$$

where C is a positive or negative multiplication factor.

The stress change can be thought of as a stress pulse, which is transmitted into the fluid as a pressure pulse causing relative fluid motion across the EDL's, generating a streaming potential. The generation of streaming potentials through application of seismic waves is the basis of the electroseismic effect (Pride and Morgan, 1991). Similar behaviour is obtained for all four electrodes surrounding the sample and can be explained by Pascal's principle that a change of pressure applied to an enclosed fluid is transmitted undiminished to every portion of the fluid and to the walls of the containing vessel.

9.4 Streaming Potential Variations during Deformation.

The measurement of the streaming potential at different stages of deformation could prove useful in delineating structural damage (Al-Saigh et al., 1994) or inversely predicting the stress state of the crust. The streaming potential was measured before and after sample failure using a range of pore fluid pressure differences not exceeding 30MPa. Figure 9-7 illustrates how the streaming

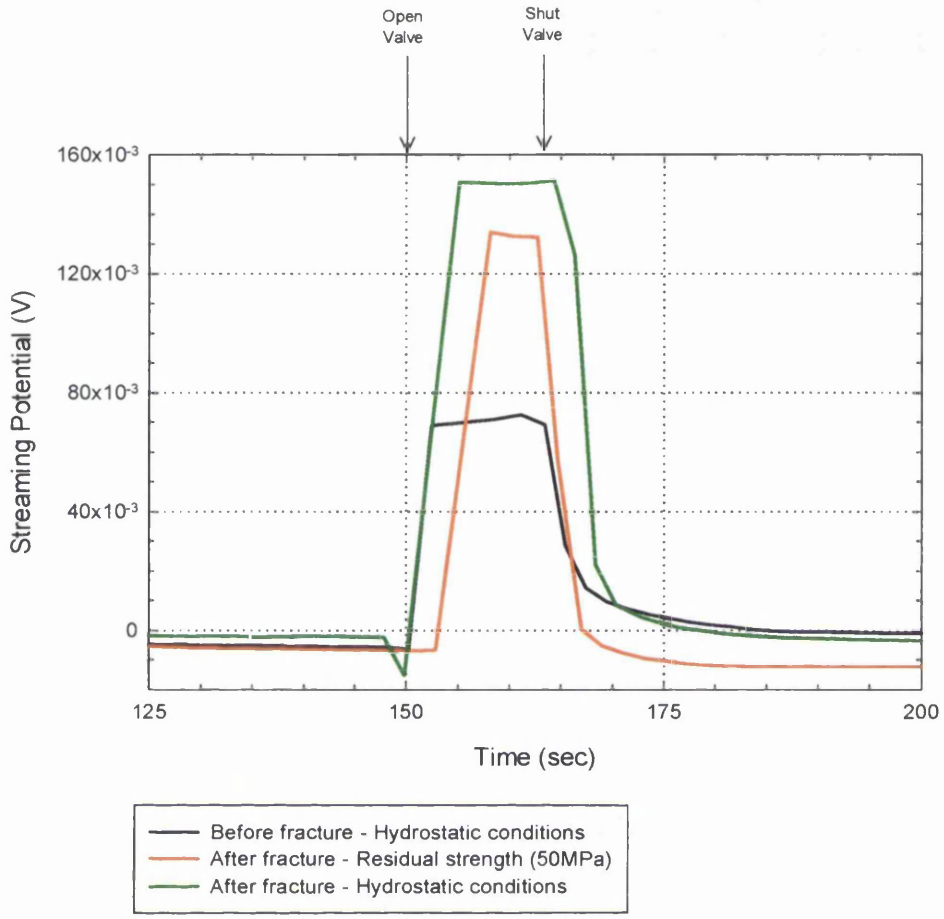

Figure 9-7 Variation of streaming potential before and after fracture with a pressure difference of 20MPa applied. The magnitude of the streaming potential results plotted are the values from electrode 3 minus the value from electrode 1. Confining pressure was 40MPa and deionised water acted as pore fluid. [Experiment No.: 41]

potential increases before and after deformation and fracture of the sample. The streaming potential measured at the residual stress level, increases by a factor of 1.7 after failure. This increase could be due to permeability evolution during deformation induced dilatancy. When the axial load is removed completely, the streaming potential has increased by a factor of 1.9 compared with the magnitude of the undeformed initial signal. This suggests that horizontal cracks and intergranular pore space, closed during application of an axial deviatoric stress, enhance the streaming potential when stress is removed. This offers evidence that crack aperture is important for streaming potential development.

9.4.1 Effect of Pore Pressure.

The combination of pore pressure difference and deformation on the streaming potential is observed from Figure 9-8. A range of pore pressure differences has been applied at the same three stages as shown in Figure 9-7, at hydrostatic pressure conditions of 50MPa before and after fracture. Pore fluid was deionised water and a strain rate of 1×10^{-5} s^{-1} was used.

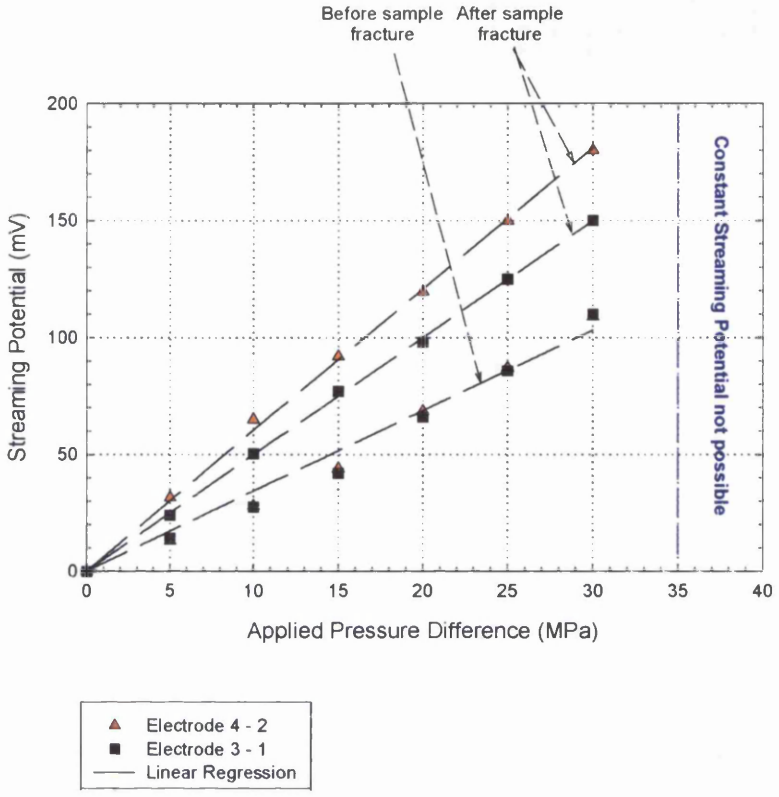

Figure 9-8 The variation of streaming potential with pore pressure differences for Darley Dale sandstone. [Experiment No.: 41]

For plotting purposes the values used are the differences between the streaming potentials measured between electrode 3 and electrode 1 on one side of the sample and between electrode 4 and 2 on the other. A linear relationship is observed between streaming potential and applied pressure difference as shown in Figure 9-2 and this is also shown to exist before and after fracture. Similar streaming potentials are found on both side of the sample before deformation, i.e. from electrode 3 - 1 and electrode 4 - 2, indicating a degree of homogeneity across the sample. After deformation the streaming potential value increases, the magnitude of the increase depending on increases in pore fluid pressure. The streaming potential at electrode 3 - 1 is lower in value than those at electrode 4 - 2 indicating some inhomogenity in the sample. This can be expected due to dilatancy and the later generation of a macroscopic fault across the sample.

The sample is shown in Figure 9-9 together with the positions of the electrode dipoles. It can be seen that electrodes 3 and 1 (dipole 2) are located on the hanging wall of the faulted sample while electrode 4 and 2 (dipole 1) are adjacent to the footwall. The macroscopic fault plane may act as a barrier to fluid flow causing variations of streaming potential above and below the fault.

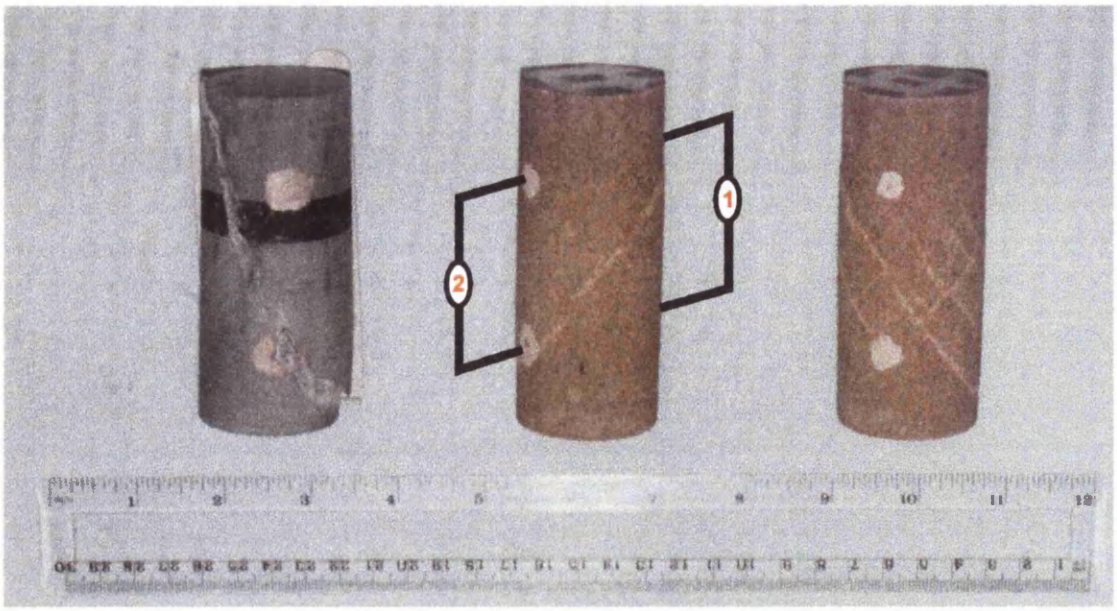

Figure 9-9 Location of dipole 2 (electrode 3-1) and dipole 1 (electrode 4-2) with respect to the macroscopic fault surface.

9.5 Streaming Potential during A Typical Deformation Cycle.

The streaming potential evolution is now investigated during a complete deformation cycle to try to understand the information obtainable from streaming potential signals on the stress-strain fields. Figure 9-10 shows the streaming potential and axial stress variation with axial strain for Darley Dale sandstone. Deformation occurred at a strain rate of 1.5×10^{-5} s^{-1} with an effective pressure of 20MPa using deionised water as pore fluid. In this experiment, deformation is stopped at chosen strain intervals and the streaming potential measured using the steady state flow technique by applying a constant pore pressure gradient of 20MPa across the sample. The flow rate is also measured and used to compute the hydraulic permeability.

In Figure 9-10a, up to the point **A** which is 86.5% of the compressive strength (Point **B**) of the sandstone, and represents the quasi-elastic stress limit of the sample above which, permanent deformation is induced. This period corresponds to compaction and closing of the pore and crack network. The streaming potential decreases by –42% during this period. A decrease in the hydraulic permeability (Figure 9-10b) of –43% is also seen in the same interval. Both transport properties therefore appear to be sensitive to the closing of the pore network.

Between **A** and **C** unrecoverable deformation occurs due to the formation of microcracks as dilatancy becomes the dominant mode of deformation. The streaming potential continues to decrease during this period. The point **C** represents the point of ultimate failure of the rock. In this region the streaming potential increases by a factor of 5 while the hydraulic permeability increases by a factor of only 1.2. It therefore appears that the streaming potential can not be only dependent on the hydraulic pore/crack network.

Continued deformation in the form of stable sliding occurs after dynamic fracture during which the streaming potential decreases by 78% and remains relatively constant during frictional sliding. In

contrast the permeability initially does not change significantly from the value at failure though it begins to decrease slightly with increasing strain showing a 15% decrease at 1.6% strain.

In Figure 9-11 the streaming potential and hydraulic permeability changes during deformation are shown when a 0.63M brine solution was used as pore fluid. The strain rate and effective pressure were kept the same and streaming potentials were measured when deformation induced fluid flow had ceased.

The streaming potentials are reduced on average by a factor of 0.33 when the brine is used. During the compaction stage, up to point **A** which is 79.4% of the compressive strength, the streaming potential decreases by -24% from 10mV to 7.6 mV. In comparison the permeability decreases by almost -25% in the same period from 1.0×10^{-15} m^2 to 6.2×10^{-16} m^2.
The streaming potential then increases non-linearly during dilatancy by +121% at 0.98% strain and by 9.4mV at dynamic fracture. Dilatancy causes the permeability in this interval to decrease to 6.7×10^{-16} m^2 and then decrease to 6.0×10^{-16} m^2 at failure. No streaming potential was obtained during stable sliding. The streaming potential evolution is therefore similar to using either brine or deionised pore fluids. It is also noted that the permeability is one order of magnitude higher when the 0.63M brine is used as pore fluid.
These varying streaming potentials and hydraulic permeabilities will be discussed again in Chapter 10.

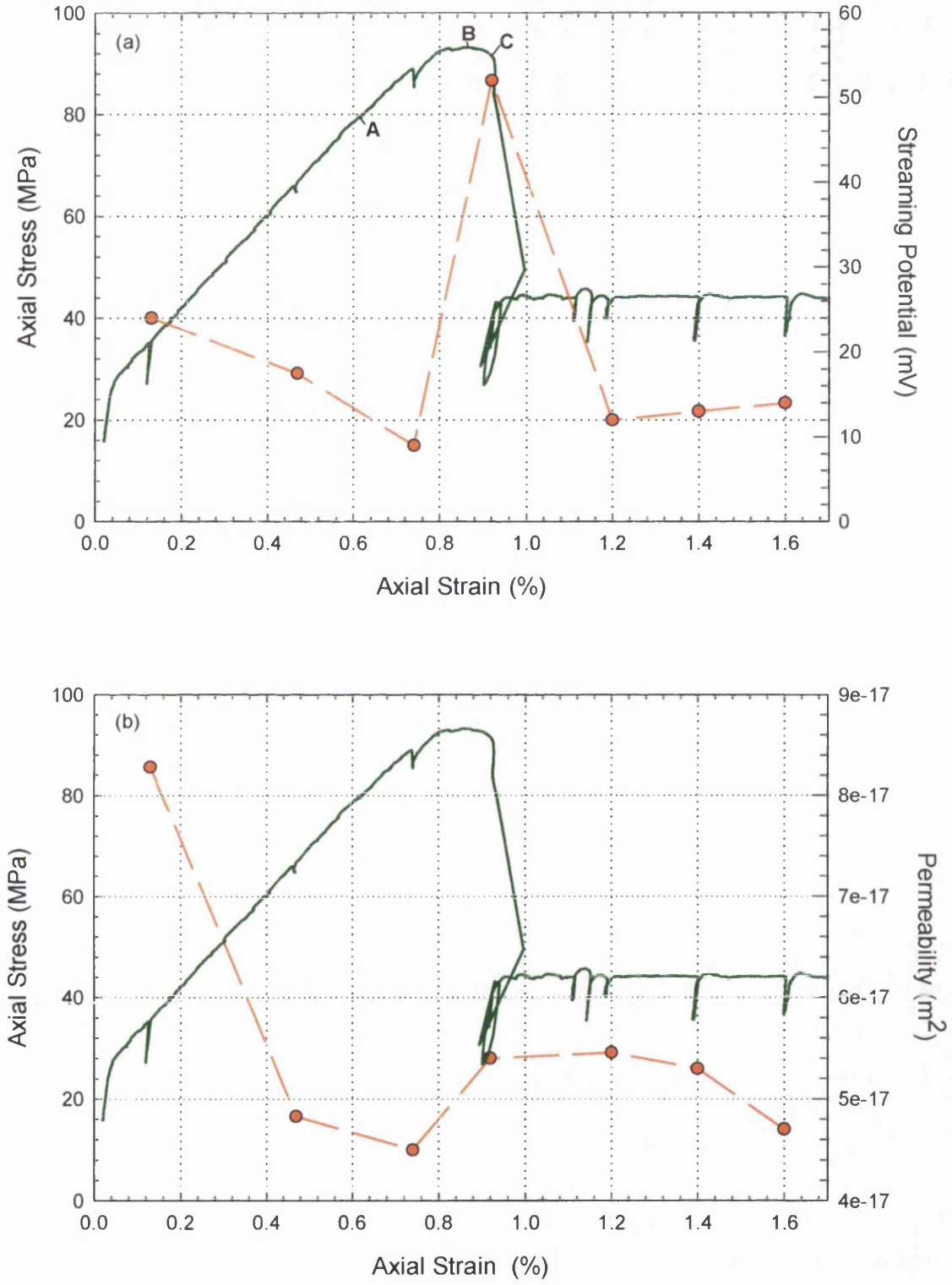

Figure 9-10 Plot of (a) streaming potential and (b) permeability variation during a deformation cycle on Darley Dale sandstone. The stress-strain curve, involving compaction, dilatancy, fracture and stable sliding indicate deformation. A strain rate of 1 x 10^{-5} s^{-1} was used and an effective pressure of 20MPa with deionised water was maintained. The point A shows the limit of quasi-elastic deformation, B the peak strength and C the point of dynamic fracture. [Experiment No.: 57]

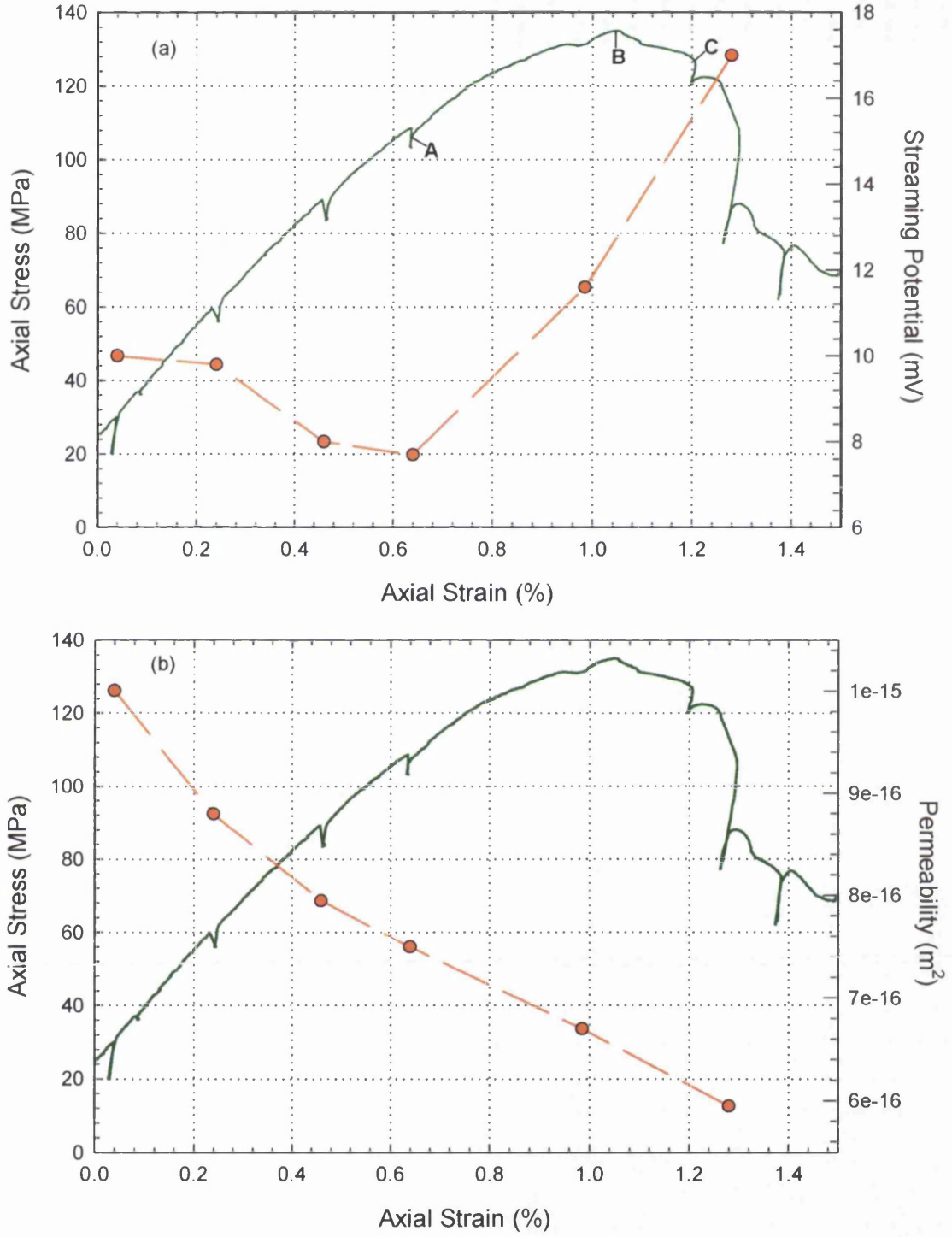

Figure 9-11 Plot of (a) streaming potential and (b) permeability variation during deformation with conditions similar to those described in Figure 9-10. Pore fluid was changed to 0.63M NaCl brine solution. Points **A**, **B** and **C** are the same for Figure 9-10. [Experiment No.: 58]

9.6 Finite Element Modelling of Streaming Potentials

To investigate theoretically the spatial variation of streaming potentials during deformation, a finite element mesh is used to model steady-state flow governed by Laplace's equation (9-2) (Smith and Griffiths, 1998).

$$k_x \frac{\partial^2 \phi_p}{\partial x^2} + k_y \frac{\partial^2 \phi_p}{\partial y^2} = 0 \qquad (9\text{-}2)$$

where ϕ_p is the fluid potential and k_x and k_y are the permeability in the x and y directions.

The problem is to determine the streaming potential variation caused by steady state flow in a porous medium undergoing deformation. The individual values of k_x and k_y in equation 9-2 allow anisotropy to be introduced into the model. A model consisting of 160, 4-node, elements (Figure 9-12) were constructed to simulate the experimental set-up and represent a 2D vertical plane through the 3D cylindrical sample.

Numerical applications were performed for this model, representing an experimental streaming potential measurement, for a range of permeability, k_y listed in Table 9-1. Laplace's equation can be solved using the appropriate boundary conditions as follows. Since the sides of the model represent the jacketed sample, they are therefore impermeable and the natural boundary condition of $\partial\phi_p / \partial n = 0$ is required. The top of the sample is maintained at an electric potential of 0V and the bottom of the sample is fixed at an electrical potential of 3.5mV, which is calculated from the Helmholtz-Smoluchowski equation (3-25). The values used are $\varepsilon = 7.08 \times 10^{-10}$ F/m, $\zeta = -10$mV, $\eta = 33.6 \times 10^{-3}$ Pa s and $\sigma_f = 1.2$ S/m for a high conductivity pore fluid which means the surface conductivity contribution to the electrical potential is small.

Model No	k_x	k_y
1	$1 \times 10^{-17} m^2$	$1 \times 10^{-19} m^2$
2	$1 \times 10^{-17} m^2$	$1 \times 10^{-18} m^2$
3	$1 \times 10^{-17} m^2$	$1 \times 10^{-17} m^2$
4	$1 \times 10^{-17} m^2$	$1 \times 10^{-16} m^2$
5	$1 \times 10^{-17} m^2$	$1 \times 10^{-15} m^2$

Table 9-1 Permeability in the x and y direction for the finite element models.

The results from the model are the electrical potential at each node due to a constant pressure gradient inducing steady-state flow.

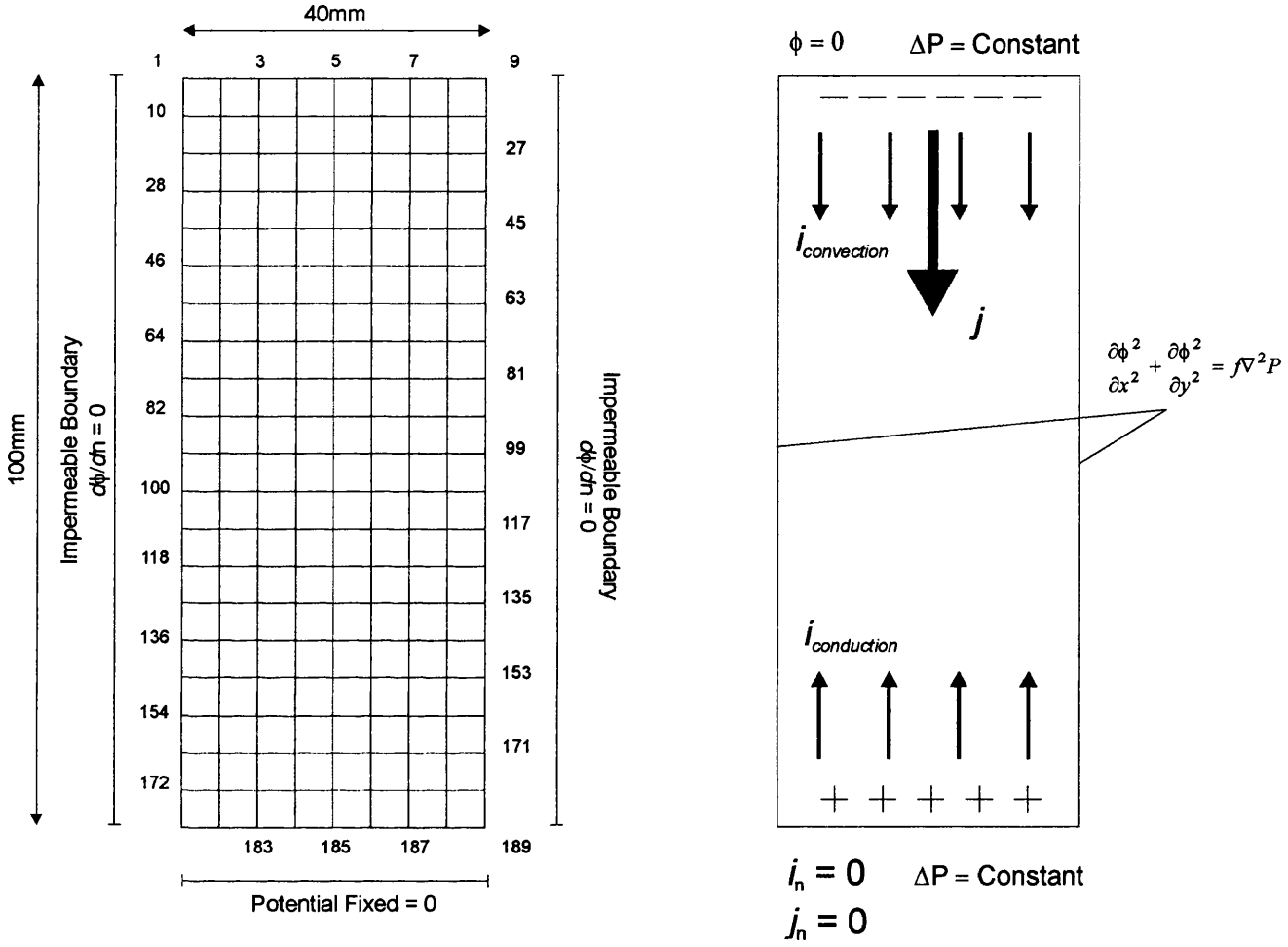

Figure 9-12 Finite element mesh and boundary conditions for input to streaming potential calculations.

The spatial variation of the fluid pressure and streaming potential due to a pressure gradient of 20MPa is plotted in Figure 9-13. A range of permeability over five orders of magnitude is investigated (increasing rightwards) as listed in Table 9-1. The fluid pressure decreases steadily vertically downwards in regular steps. At a permeability of 1 x 10^{-15} m^2 the pressure distribution becomes more varied. The streaming potential increases vertically downwards due to the zero voltage maintained at the top and the spatial variation increases with increasing permeability.

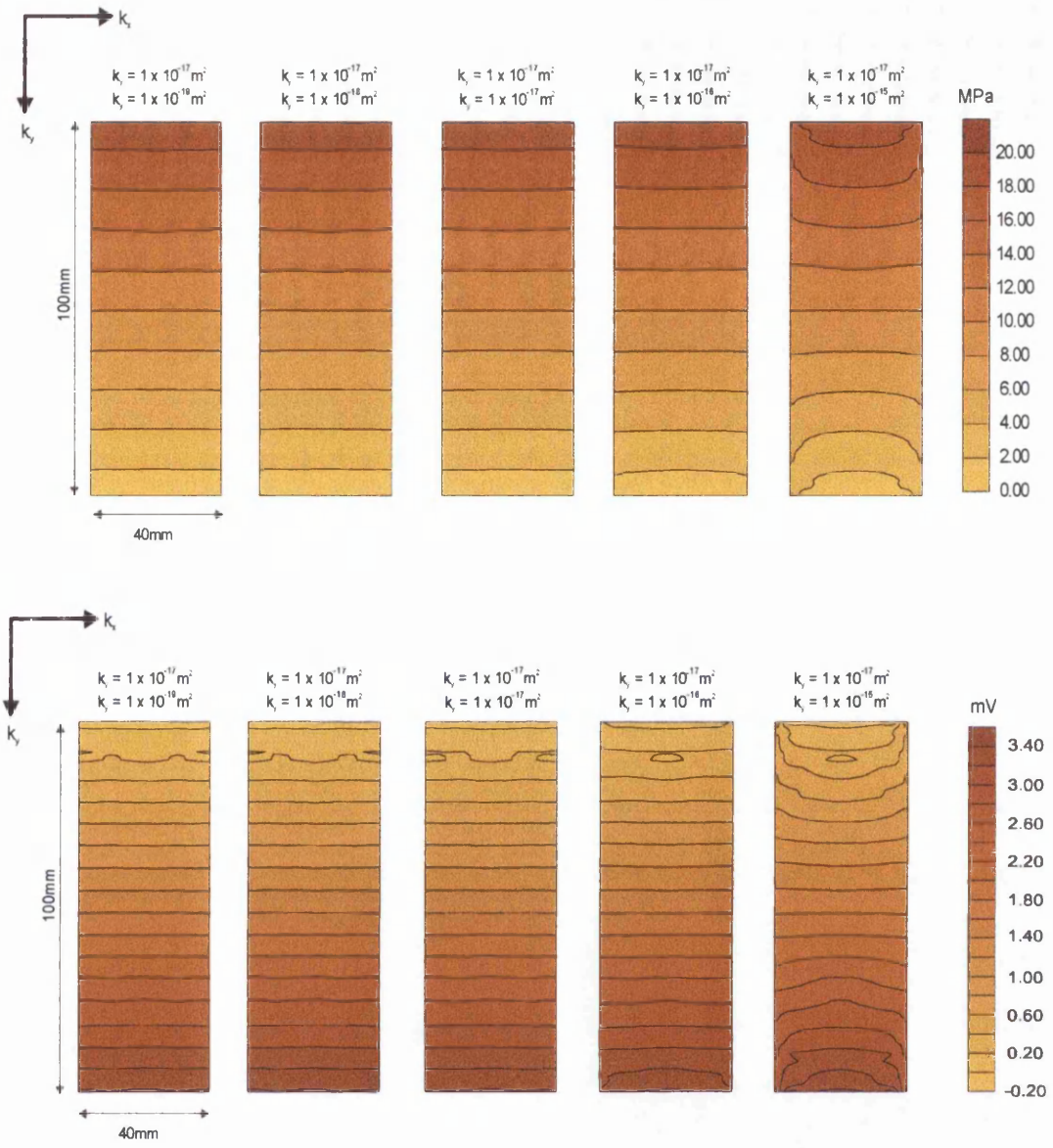

Figure 9-13 Finite element models of pressure (top) and associated streaming potential (bottom) variation during application of a 20MPa pressure gradient using a high conductivity pore fluid. Increasing vertical permeability is shown in from left to right

Assuming fault zones to exhibit higher permeabilities then increased fluid flow will be expected. The fluid flow rate is increased at a number of node in the finite element mesh allowing the presence of a fault to be simulated (Figure 9-15). The angle between the fault surface and the vertical is 45° whereas experimentally observed fault angles vary between 20° and 50° as shown in Figure 10-3 for the case of Darley Dale sandstone. The resulting streaming potential variation from this model is plotted in Figure 9-16.

The vertical permeability is set to 3.5 x 10^{-17} m^2 determined from Figure 9-10 which is the value after dynamic fracture of the rock sample.

The simulated fault has a clear effect on the streaming potential variation. It causes a constant streaming potential in the upper, hanging wall, area of the models and an increasing streaming potential in the footwall area under the fault. Measured values of streaming potential will therefore vary depending on position, i.e. if the electrodes are located above the fault then different streaming potentials can be expected relative to the footwall.

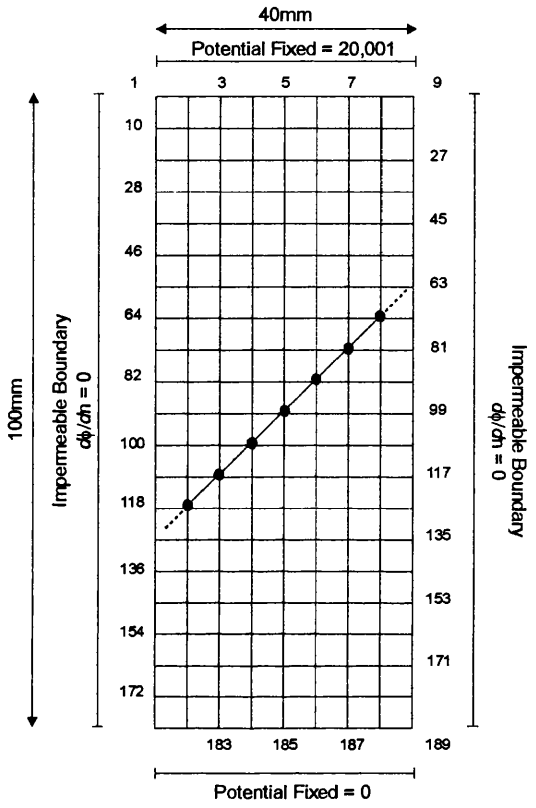

Figure 9-15 Finite element mesh, boundary conditions and position of fault like discontinuity for input to streaming potential calculations.

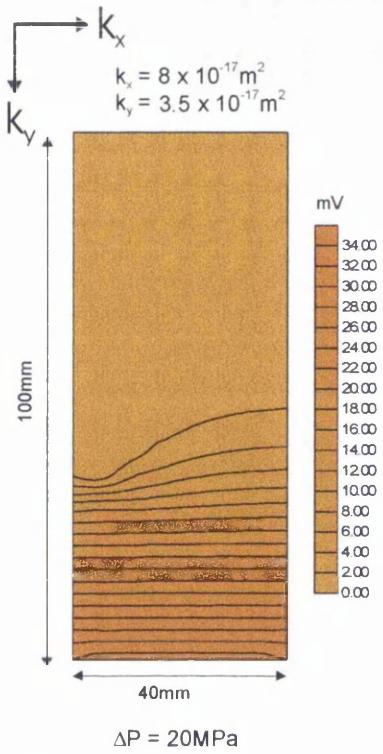

Figure 9-16 Streaming potential variation around simulated fault positioned in centre of model.

9.7 Chapter Summary

I. Streaming potentials are shown to increase linearly with applied pore fluid pressure for Darley Dale and Bentheim sandstone. The signal magnitudes are of the order of mV, which is comparable with field and previous experimental measurements. The linearity between pore fluid pressures and streaming potential is valid up to a value of 30MPa, above that a constant streaming potential can not be obtained.

II. Slowly varying stresses applied to a rock produce a constant streaming potential inducing a high amplitude electrical signal. The waveform can be described by a simple relationship relating the streaming potential amplitude to the stress rate.

III. The streaming potential is found to vary during deformation. The magnitudes typically increase by a factor of 1.9 after dynamic failure of the sample. This result recognises the possibilities of streaming potentials delineating fractured mediums. The linear relationship between streaming potential and applied pore pressure difference also holds before and after macroscopic sample failure.

IV. The evolution of the streaming potential consists of a decrease during compaction followed by an increase during dilatancy. The peak streaming potential is obtained immediately after fracture after which a decrease to a constant value is obtained during stable sliding on a macroscopic fault plane. The permeability is also found to decrease during compaction and

increase during dilatancy for deionised water and continue to decrease during compaction and dilatancy for brine pore fluid. The relative decrease in permeability is greater than that for the streaming potential during compaction and less during dilatancy and fracture. A small permeability decrease occurs during the stable sliding stage while the streaming potential is constant.

V. The effect of using brines, as pore fluid is to decrease the streaming potential by a factor of 0.33 while its evolution during deformation is comparable to that described in summary point IV.

VI. A 2D finite element model utilising steady state flow laws and the Helmholtz-Smoluchowski equation is used to determine theoretically the spatial variation of the streaming potential. An increase in the spatial variability of the streaming potential occurs with increasing vertical permeability.

VII. When a fault zone is included in the finite element model the streaming potential is dependent on the position of the fault. This agrees with the experimentally determined values.

10. Discussion of Results

Experimental rock deformation on sandstone and basalt produces measurable electrical potential, streaming potential and acoustic emissions. It is recognised, through this investigation, that these electrical signals are dependent on effective pressure and pore fluid type together with saturation, strain rate, initial permeability and quartz content. The streaming potential signal is the result of an electrically induced conduction current reaching an equilibrium level with a pressure-induced convection current. This process typically occurs within two to three seconds for a 100mm long sample and is the result of hydraulic diffusion in the sample (Gueguen and Palciauskas, 1994). Electrical processes and therefore diffusion occur over much faster time scales e.g. for Darley Dale sandstone with deionised water as pore fluid, a representative electrical decay time is 0.3μs. The implication being that, pressure induced convection currents generated by the closure and opening of pores is quickly equilibrated by the electrically induced conduction current. During deformation the closure of pores and cracks during compaction or crack generation during dilatancy do not allow a steady state fluid flow field to establish and therefore a steady equilibrated streaming potential cannot be obtained. The observed electrical potential signals are therefore transitory even though the strain field is constant. These observations are important in the discussions to follow.

10.1 Electrical Potential Response due to Shear Fracture in rocks

The results presented in Chapter 5 have demonstrated the existence of d.c. electrical potential signals, during the fracture of crustal rocks under crustal stresses. Shear faulting is the failure mode in all the rock samples tested. This is utilised and is indeed expected under moderate confining pressures at inclinations of less than 45° to the axial compressive stress (Jaeger and Cook, 1979). Sandstone deformed under water-free conditions produced a measurable but small pre-seismic anomaly (20mV) during strain softening and a much larger co-seismic signal (100mV) at dynamic fracture, both in mV. Electrokinetic contributions to this signal can be discounted as no fluid is present in the pore space and therefore other methods such as piezoelectricity or charge separation mechanisms are considered responsible for their existence.

The large electric potential co-seismic signal during dynamic failure can be explained using the model of Yoshida et al. (1997). A large instantaneous stress drop during dynamic fracture and slip within the dry rock produces an effective polarisation in the quartz crystals which when summed over all the quartz crystals present is detectable on the surface (Figure 3-1). A previous study (Yoshida et al., 1994) shows that the electrical potential signal is due to the dynamic stress drop and not the frictional slip on the fault plane although shear movements in quartz crystals are known to produce piezoelectric signals. Similar experiments on granite confirm this mechanism by measurement of electrical currents at varying stress rates (Sasaoka et al., 1998). The polarities of the measured signals vary which is to be expected if the effective polarisation at each electrode is produced from randomly orientated quartz crystals.

In the model of Yoshida et al. (1997) it was deduced that a rapid stress drop is necessary to produce a bulk effective polarisation. This however, did not explain the occurrence of the smaller pre-seismic electrical signals. If the small stress decrease recorded before failure is depicted as a series of discrete stress drops caused by microcracking in localised areas, then a similar mechanism as that of dynamic failure may exist at a microlevel. The presence of localised areas of damage is observed using AE source location techniques. Figure 10-1 shows the evolution of AE with strain and highlights the progressive localisation of AE around the future developed macroscopic fault plane. The AE that occur during strain softening i.e. stage (e) and (f) of Figure 10-1, produce small stress drops and they can theoretically generate electrical potential signals through piezoelectric mechanisms.

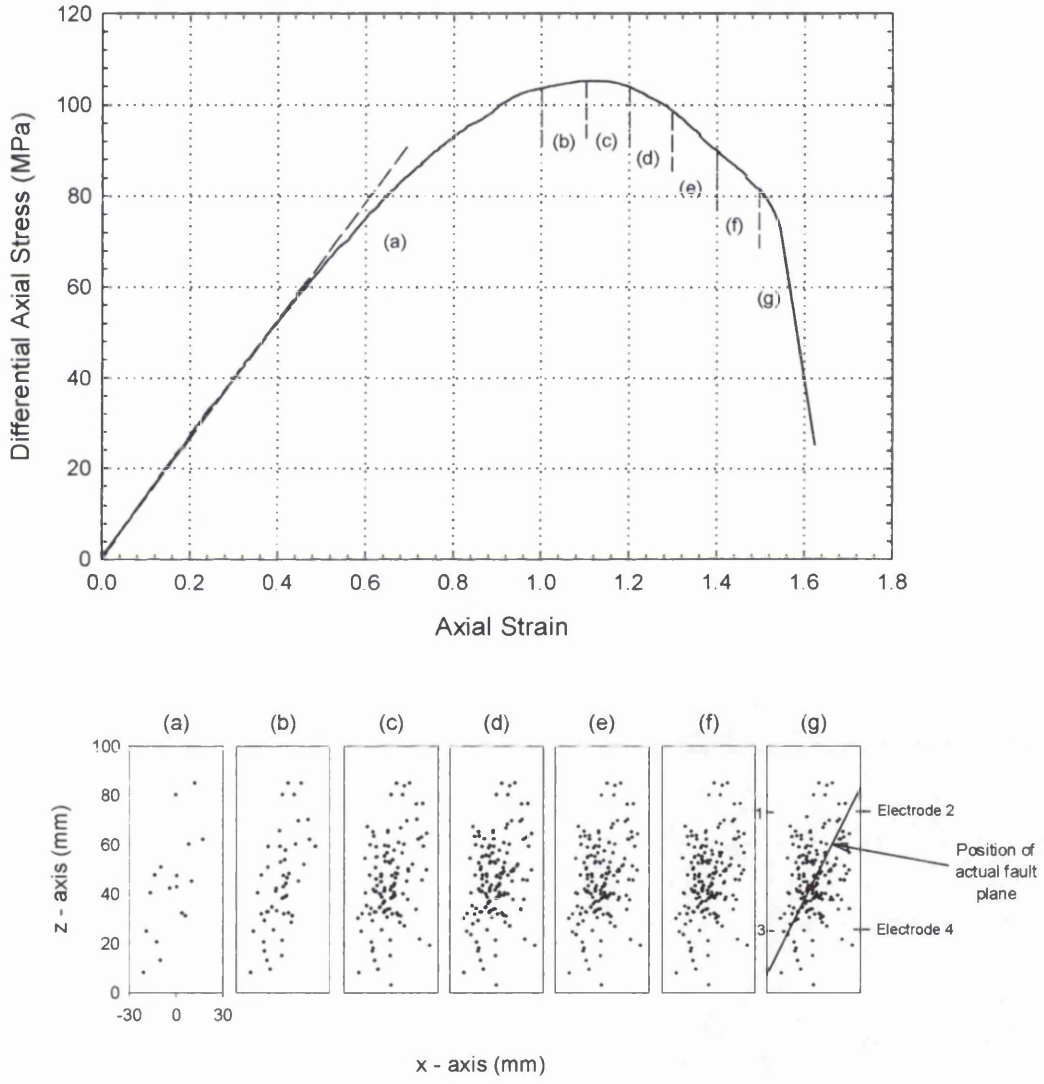

Figure 10-1 Source located AE events during triaxial deformation of Darley Dale sandstone at constant strain rate. [Experiment No.: 51]

Due to the localised nature of the damage as shown in area (f) of Figure 10-1, represented by a inclined area of microcracking extending from top right to bottom left corner, the polarity of the electrical potential measured at the four electrode positions will differ which is observed.

The introduction of pressurised pore fluid results in an alteration of the mechanical strength of Darley Dale sandstone, effectively reducing fracture strength by 31%. This has been observed in Darley Dale sandstone (Sammonds et al., 1992, Read et al., 1995) and also in Berea sandstone (Brace, 1968; 1969). The effect of embrittlement of rocks due to pore pressure variation is a subject of intense discussion (Kirby, 1984) and continued research. These changing mechanical properties will cause changes in the electrical and hydraulic transport properties of rocks.

During strain softening prior to dynamic fracture electrical potential signals from each electrode show similar time-dependent behaviour and magnitudes (Figure 5-4b). It is known that during strain softening, the coalescence of newly forming dilatant microcracks is occurring, which may or may not create a more continuous pathway for fluid and current flow. The pore volume increases, (Figure 10-2), measured through pore fluid volumometry, indicate a dilatant volume increase and resulting fluid flow. This theory is embedded in the dilatancy-diffusion hypothesis of seismic precursory activity (Nur, 1972, Scholz et al., 1973) and comparable laboratory results are explained using a model of time-varying applied stress and crack growth (Sammonds, 1992).

Under drained conditions the pore pressure is maintained constant, therefore fluid is forced to flow into the newly forming crack network. As a new crack opens a pressure gradient is set-up causing fluid flow. This flux induces transport of electrical charge, from the diffuse layer, as convection currents. An electrical potential gradient is set-up across the crack inducing an instantaneous conduction current in the opposite direction. Before an equilibrium potential or streaming potential can be maintained a new crack opens which may link with existing cracks and the process repeats.

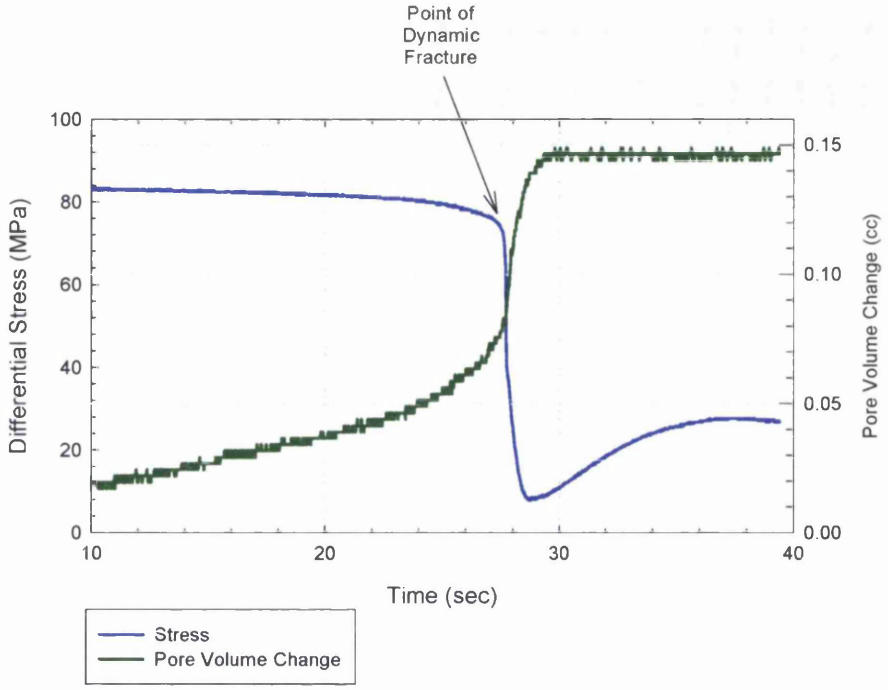

Figure 10-2 Pore volume change and differential stress variation for Darley Dale sandstone during shear fracture. Pore volume increase is determined indirectly from the fluid leaving the pore fluid intensifier. Effective pressure was 20MPa, strain rate was 1.5 x 10^{-5} s^{-1} and pore fluid was distilled water. [Experiment No.: 25]

The convection current $I_{convection}$ is given as

$$I_{convection} = \phi\tau^{-2}\frac{\varepsilon_p\zeta}{\eta}\nabla P \qquad (10\text{-}1)$$

following the nomenclature of Ishido and Mizutani (1981). The zeta potential is usually negative for quartz-water systems (Ishido and Mizutani, 1981) which means a greater percentage of positive ions are situated in the diffuse layer of the EDL. Under a positive pressure gradient positive charge is transported in the direction of flow and as the charge is redistributed within the sample an increase in electrical potential occurs at all the electrode positions. The existence of the same electrical potential signal at each electrode indicates that the source mechanism in the damaged zones produces similar electrical perturbations in areas outside the region of microcracking. An explanation may be that the increasing axial stress produces long range electrical and streaming potentials across the entire rock volume or alternatively the streaming potentials produced in the microcracking zone induce fluid perturbations in a zone of 'quiescence'. These types of models are also proposed by and applied to field measurements by Bernard (1992) leading to the deduction that a mechanism based on triggering of strain instabilities by strain perturbation was put forward to account for some of the observations in the field.

Co-seismic electrical signals, which are comparable in magnitude to the pre-seismic signals, can be explained in a similar fashion. The high level of microcracking, as evidenced through exponentially increasing AE rate, is distributed broadly along a plane as shown in Figure 10-1. The dynamic stress drop results in shear fault formation along this plane, which is orientated at approximately 30° to the axial compressive stress. This macroscopic fault plane can be envisaged initially as a macroscopic fluid conduit creating the conditions necessary for enhanced fluid flow. The increase in the number of cracks formed during deformation can be seen in the photomicrographs of Figure 7-6. The enhanced fluid flow carries increased positive charge under a pressure gradient resulting in an instantaneous rise in the electrical potential.

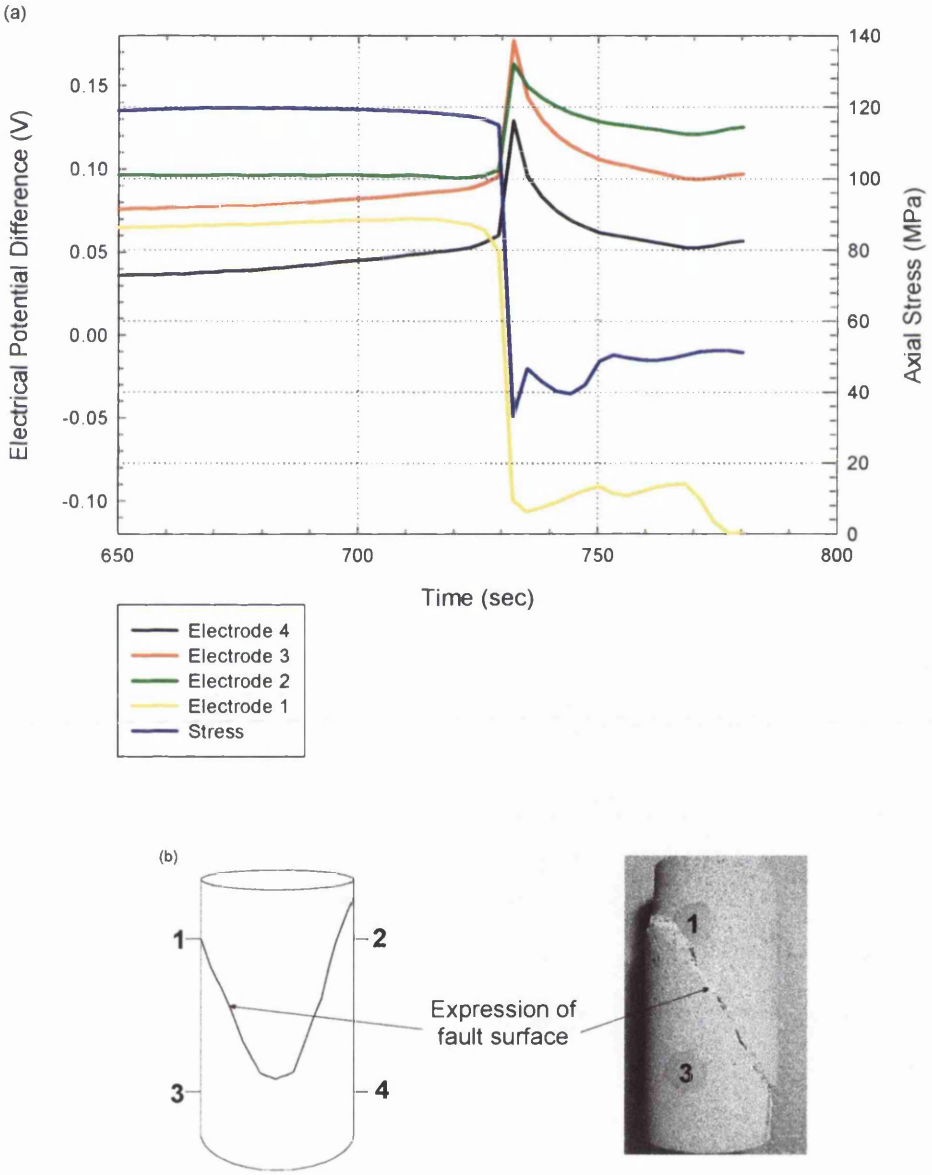

Figure 10-3 (a) Pre-seismic and co-seismic electrical potential signals during shear fracture of Darley Dale sandstone. The electrical potential difference recorded at electrode 1 exhibits opposite polarity to the other three electrodes. The position of this electrode (1) in relation to the actual fault plane is shown in (b). [Experiment No.: 40]

It is also recognised that a decrease in permeability can occur after fracture for sandstone (Zhu and Wong, 1996; Keaney, 1998) and therefore an increased fluid flow pathway may not be expected. It is noted that this behaviour is actually later seen during frictional sliding on the fault plane and not immediately after dynamic fracture. The relationship between streaming potential and hydraulic permeability discussed in Chapter 10.5 will help to clarify this point.

The character of the pre and co-seismic signal is however dependent on location on the specimen. In Figure 10-3a it can be seen that a decreasing electrical potential signal occurs both prior to and during dynamic fracture as recorded by electrode 1. In Figure 10-3b the position of electrode 1 is shown and it is seen that the macroscopic fracture intersects the immediate area around the electrode. Fluid moving within this fracture zone can therefore be expected to remove positive charge from this area thereby reducing the potential difference in that particular zone. It is concluded that the position of the electrodes can provide spatial information on the fracture location.

The effective polarisation of quartz crystals is responsible for a piezoelectric signal, which is indirectly proportional to electrical conductivity (Chapter 3.4.1). The increased bulk conductivity will decrease significantly when pore fluids are used, suggesting a much smaller piezoelectric effect under saturated experimental conditions. As seen in figure 5-4c a quartz free rock produces no pre-seismic electrical potential signals while the co-seismic signal are negligible for a stress drop of 30 MPa. This suggests that any effect due to point defects or charge separation is unimportant in the generating mechanism of electrical potential signals under these conditions. A final conclusion, which can be drawn from this experiment, is that the sole generating mechanism for electrical pre-seismic signals in water-free sandstone during shear fracture is piezoelectricity within quartz crystals.

The co-seismic signals observed in dry basalt occur with an audible bang as the elastic energy of the sample and loading apparatus is released. This released energy is sufficient to produce shock waves, which can cause some AE transducers to become detached introducing noise contamination. The source of these signals is unclear but may be due to electron emissions from crack tips at dynamic fracture (Yamada et al., 1989; Guo et al., 1994). This explanation however is not conclusive because in a deformation experiment on Icelandic basalt, at a confining pressure of 75MPa, no electrical potential signal was recorded on the upper electrodes during dynamic failure, a result which is confirmed by Sasaoka et al. (1998). A measurable signal was found however, at the lower electrodes, which are located close to the surface expression of the fault plane, and again noise from the catastrophic energy release is suspected. This experiment strongly suggests that the piezoelectric effect of quartz is important in producing electrical potential signals in water-free sandstone.

When pore fluid (distilled water) is introduced into the basalt both pre-seismic and co-seismic electrical potential signals are now observed. The low porosity (ϕ) of 3% implies a low permeability and therefore the ability of fluid to flow within the rock and hence the capacity to transport electrical convection currents is reduced. During dilatancy the newly forming cracks do not coalesce with existing fluid pathways until dynamic failure due to the high strength and competency of basalt. This is indicated in Figure 7-6f, where deformation is only manifested by a macroscopic fracture with little matrix

deformation. The pre-seismic electrical signals therefore represent complex hydraulic and current flow patterns within isolated damaged zones occurring before coalescence occurs and is manifested by the varying polarities observed. During fracture however, a macroscopic fault develops across the sample. In general it is not a continuous fault plane, c.f. sandstone, but a region of interconnecting smaller faults. This type of fault allows fluid and electrical current to flow in varying directions giving rise to vari-directional co-seismic electrical potential signals.

10.1.1 Effect of Increased Quartz Content on Electrical Potential Signals during Shear Fracture

It was observed that an increased percentage of quartz decreases preseismic and coseismic electrical potential signals in sandstone. From equation 3-6 it can be seen that the resulting voltage is directly proportional to the density of quartz crystals and therefore the Bentheim sandstone (99% quartz) is expected to show greater electrical potentials differences than the Darley Dale sandstone (75% quartz). Clays are known to have high conductivity when immersed in low salinity fluids (Revil and Glover, 1998) but the effect in dry conditions has not been studied extensively. The clays, which are composed of layers of silica tetrahedrons, have high surface areas ($750m^2/g$ for montmorillonite) which are typically negatively charged and have a high surface conductivity (Ruffet et al., 1995). For dry rocks, cation movement will compensate the negative surface charge of the clay and become bonded to the surface forming mobile conductive layers. It is these conductive layers which may be responsible for the increased electrical potential differences found in dry Darley Dale sandstone over Bentheim sandstone.

In the presence of pore fluid, electrical double layers form in both Bentheim and Darley Dale sandstone on the grain fluid interfaces. Increased surface conductivity occurs in double layers and it is more dominant for low conductivity fluids (Bussian, 1983; Revil and Glover, 1997). It has been shown experimentally that the value of surface conductivity extrapolated to low conductivity values is greater for rocks containing a higher percentage of clays. This is demonstrated in Figure 2-19, which shows a higher surface conductivity for Darley Dale sandstone (clay bearing) than the non clay-bearing Berea sandstone. A similar result is shown for clay rich Vosges sandstone compared to non clay-bearing Fontainebleau sandstone (Lorne et al., 1999b).

Surface conductivity (σ_s) in this manner is given by

$$\sigma_s = 2\frac{S_s}{r} \tag{10-2}$$

where r is the radius of the grains and S_s is the specific surface conductance (O'Konski, 1960). Typical values of S_s are 8.9×10^{-9} S for quartz and 2.5×10^{-9} S for clay (Revil and Glover, 1998) values results which manifest how the clay component can contribute greatly to conduction currents on the surface. Clay can also interact with pore fluids forming electrical double layers and hence an excess of charge will exist. This increase of the counter-ions would be expected to increase the streaming convection currents.

The co-seismic electrical potential signals produced from Bentheim sandstone have an average magnitude of 40mV, which is smaller by a factor of 10 than those detected from Darley Dale sandstone (Table 10-1). It might be expected that Bentheim sandstone would produce an electrical signal of greater magnitude due to its higher permeability. Conceptually a higher permeability rock suggests a greater bulk conductivity and therefore an increased convection current. This should in turn give an increased conduction current which will reduce the streaming potential. A reduction of the streaming potential can also occur with decreasing grain size due to increasing surface conductivity effects. This is demonstrated in Figure 10-4, using the model of Revil (1999a), also plotted are the streaming potentials for Darley Dale and Bentheim sandstone where the average grain size of both is used to calculate the theoretical streaming potentials assuming zeta potential is equal to 100mV for DDS and Bentheim sandstone.

	Darley Dale Sandstone		**Bentheim Sandstone**		**Icelandic Basalt**	
	Pre-seismic	**Co-seismic**	**Pre-seismic**	**Co-seismic**	**Pre-seismic**	**Co-seismic**
Water Free	20	107	20	40	0	35
Drained	100	115	30	65	20	232
Undrained	27	27	26	56	-	-

Table 10-1 Magnitude of pre-seismic and co-seismic signals for sandstone and basalt under a range of experimental conditions. All values are given in millivolt. Replotted from Table 5-1.

10.1.2 Effect of Undrained Conditions on Electrical Potential Signals during Shear Fracture

The effect of undrained conditions are investigated since they represent the conditions of many geological situations. Under this condition fluid flow due to pressure redistribution can have marked effects on the mechanical properties of rock. Earthquakes, for example, are suggested to be generated through naturally forming overpressured compartments, which reduce shear stresses in rocks leading to fracture (Blanpied et al., 1992). The resulting aftershocks may then be produced from the reduction in rock strength attributed to fluid redistribution (Nur and Booker, 1972; Sammonds et al., 1992).

The pre- and coseismic signals in both Darley Dale and Bentheim sandstone show varying polarity electrical potential signals under these undrained conditions. In the case of basalt, similar variation in signal polarity was explained in terms of a closed system where fluid pathways are not connected until dynamic fracture. A fully connected flow path is not necessarily formed at this point. A continuous fluid network is therefore not present in order to create a uniform direction for convection currents. Pore fluid pressure decreases as dilatancy progresses but the increasing effective pressure causes a closure of pores and cracks. Maintaining a constant fluid equilibrium is then not possible and therefore a dominant fluid direction is not possible. The electrical potential signals are then dependent on the local fluid flow field at each electrode position and consequently varying electrical potential polarities can be expected.
Electrical co-seismic signals from sandstone become approximately equal in magnitude to the pre-seismic signals for all the electrode positions. It is at this point that the macroscopic fault plane forms and hence enhanced fluid flow is possible as discussed previously. The transport of an increased convection current

should occur due to local pressure gradient increases but because the pore fluid pressure inducing the convection current has decreased, the convection current will decrease as predicted in equation 10-1. The result is decreased electrical potential differences.

10.2 Discussion of Effective Pressure Dependency on Electrical Potential Signals.

Rocks can undergo deformation by a wide variety of mechanisms including dilatancy, pore collapse and normal consolidation depending on effective pressure. Pore collapse and consolidation lead to permeability reductions while dilatancy can cause an increase or decrease in the hydraulic network. Both these processes occur in natural and man-made deformation and therefore the consequences of effective pressure on electrical potential difference may offer information on the microscopic processes occurring.

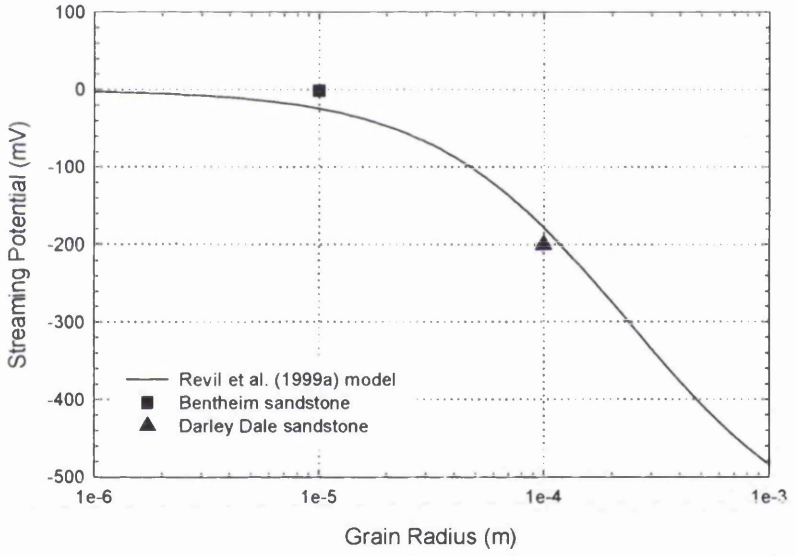

Figure 10-4 Variation of streaming potential with mean grain radius using the model of Revil et al. (1999a). The streaming potentials for Darley Dale and Bentheim sandstone are plotted for a pressure gradient of 20MPa and de-ionised water as pore fluid with conductivity of 4×10^{-3} S/m. A zeta potential of –100mV was used in the calculation.

A rapid stress drop generates a piezoelectric signal in dry sandstone; this was the conclusion from observations of stress drops across saturated and water-free sandstone and basalt samples. In the time immediately prior to the stress drop a smaller piezoelectric signal is also generated through piezoelectric mechanisms.

The evolution of electrical potential difference during a deformation cycle of 'dry' sandstone cannot be interpreted using the same mechanism. An increasing stress should create piezoelectricity by inducing

strain in crystals such as quartz. This is not observed. If a system of randomly orientated quartz crystals exists then an effective polarisation created in one quartz crystal will be cancelled by that of neighbouring crystals. This is supported by the results in Figure 10-5, which shows the non-dependence of electrical potential difference on increasing differential stress. Between 80 and 90MPa, a random variation of the signal occurs which correlates well with the onset of an exponentially increasing AE event rate (Figure 6-3a). Similar behaviour is seen for confining pressures up to 100MPa. An exponentially increasing AE event rate indicates cracking which causes an increase or decrease in the electrical potential difference.

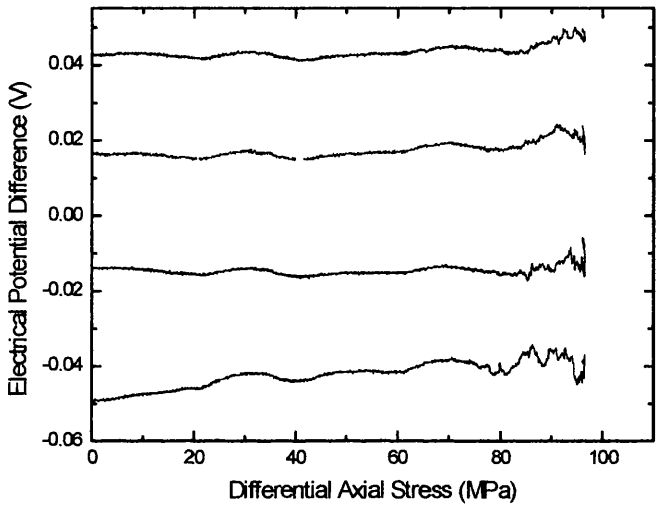

Figure 10-5 Electrical potential difference as a function of differential axial stress for the four electrodes around sample generated from deformation of 'dry' DDS. [Experiment No.:12]

Each individual non stable cracking event is assumed to emit an elastic wave, which in the case of quartz crystals will produce a piezoelectric signal. This type of signal should take the form of a high frequency spike and decay like the signals (Figure 10-6) such as those found in granite (Yoshida et al., 1994). It is concluded from the signal that the piezoelectric effect does not create measurable signals during compaction and dilatancy. The signals may be due to differences in capacitance changes between the electrode and rock because of the high sensitivity of capacitance to the intermediate spacing. The high confining pressures used, up to 100MPa, should however make this effect negligible.

An alternative explanation for the observed behaviour is a strain effect. In general the macroscopic strain rate is constant, though local strain fields may vary due to deformation in localised areas (Figure 10-1). Strain in these localised areas will create piezoelectric signals from a number of crystals which in a non-homogeneous area do not cancel each other out. The increase or decrease in the signals occurs because the location of the localised damage varies from sample to sample and hence the difference recorded between an upper and lower electrode can vary. At confining pressures of 200MPa, Darley Dale sandstone undergoes cataclastic deformation and the electrical potential difference increases slowly for the entirety of the deformation. Source located AE were seen to be distributed over a large volume of the sample and all the electrodes measured similar behaviour, therefore it is thought that the randomly

distributed microcracking produced from grain crushing and rotation induce strain induced piezoelectricity at all the electrodes.

Under saturated conditions, a pore fluid reduces the ultimate strength of the rock and a constant fluid pressure during deformation reduces the ultimate strength even further (Table 10-2). This is due to a reduction of the effective pressure.

	Dry	Undrained	Drained
Peak Strength	118 MPa	108 MPa	88 MPa

Table 10-2 Peak strength of Darley Dale sandstone under various conditions.

The absolute electrical potential difference occurring during compaction decrease exponentially with effective pressure and is associated with a linear decrease in pore volume change. A reduction of porosity occurs with mechanical loading leading to grain rotation followed by grain crushing. The critical effective pressure for this grain crushing, which would significantly alter fluid and electrical flow paths, has been formulated in a fracture model by Zhang et al. (1990). Recently Wong et al. (1997) using the model of Zhang et al. (1990) give a value of effective pressure equal to 360MPa for the onset of grain crushing. Read et al., (1995) showed that confining pressures of 400MPa are required to close completely the porosity of Darley Dale sandstone. The microstructural analysis in this investigation clearly shows the presence of pore space and open cracks. It is therefore assumed that a pore volume capable of allowing fluid flow exists at the effective pressures used in this investigation.

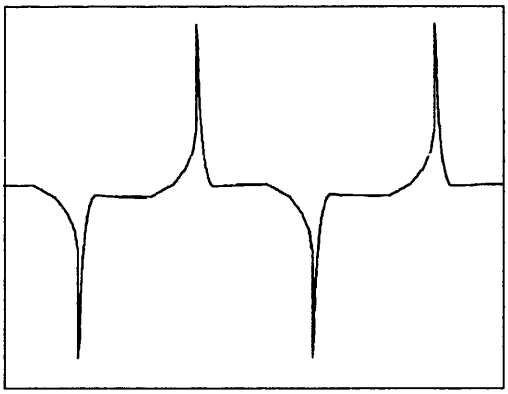

Figure 10-6 Expanded schematic representation of high frequency piezoelectric signals emanating from a deforming sandstone containing quartz crystals.

The relationship between electrical potential difference and effective pressure during compaction suggests that as closure of pore space and microcracks occurs, fluid is expelled from the rock reducing the pore volume. The fluid carries a convection current of positive charges, produced through electrokinetic mechanisms, out of the sample. No extra fluid enters the rock sample to form new EDL's and therefore the removal of positive charges will reduce the electrical potential measured across the sample.

Experimental observations also indicate a permeability dependence on fluid pathway type i.e. crack, pore or fracture porosity, and a non-dependence of electrical resistivity on pathway type (Mattisson, 1997). The application of hydrostatic pressure also appears to produce varying critical paths for electrical and hydraulic flow, with hydraulic flow controlled by length scales of the order l^4 and electrical conductivity controlled by l^2 length scales (David, 1993). As a result the pore geometry and distribution can be considered important in controlling fluid and electrical current flow in rocks (Bernabé and Bruderer, 1998) and semipermeable membranes (Saksena and Zydney, 1995). The presence of cracks with low aspect ratio appears to inhibit fluid flow but allow electrical current to be transported. Fluid within a connected pore network, containing pores above a critical aspect ratio, is expelled during compaction. Convection current will flow within this network but also within the lower aspect pores resulting in further current displacement. This reasoning may be applicable in the interpretation of the exponential relationship between electrical potential difference and effective pressure.

During dilatancy a linear increase in the cumulative AE occurs representing increased microcracking. This result intuitively suggests an increase in the connected fracture porosity available for fluid flow as interaction of the cracks occurs. This however is not the case, as the pore volume change appears to be independent of effective pressure. Permeability decreases are observed for sandstone during dilatancy (Tuefel, 1987, Zhu and Wong, 1996, Keaney, 1998) and explained in terms of increasing tortuosity, grain size reduction, gouge evolution and cataclasis. If the cracks are of low aspect ratio then they will inhibit fluid flow and an overall decrease in pore volume and permeability will not occur. Electrical current flow within these cracks is not inhibited as much as fluid flow and under a constant pore pressure gradient an increasing convection current will be carried through the rock increasing the electrical potential across it. Increasing effective pressure could be expected to close these low aspect cracks, however observations of water filled pore space contributing to electrical resistivity measurements at effective pressures of 1000MPa (Brace and Orange, 1968) show this assumption is not valid.

The electrical potential differences determined during compaction, dilatancy and shear fracture correspond to a maximum depth of 4km in the crust. Streaming potential measurements can only be measured from the surface down to a depth of 0.3km (Thompson and Gist, 1993) therefore electrical signals at depths of 4km are not likely to be detectable at the surface. Though with the presence of high conductivity zones and belts of fractured rock the fluid flow expelled during deformation could carry electrical current to more shallow levels. The possibility of strain perturbations in the earthquake preparation zone triggering far field fluid instabilities is also a plausible mechanism (Bernard, 1992).

Coseismic and Preseismic signals

As ultimate dynamic fracture is approached, crack growth occurs and pores fluid moves to fill the dilatant volume under conditions of a constant pressure gradient. This gives rise to precursory electrical potential signals as convection currents within the pore fluid redistributes ionic charge within the sample. The signals decrease at higher effective pressures due to the increased normal forces inhibiting crack opening.

Shear fracture is associated with co-seismic electrical potential signals as discussed in Chapter 5. The variation of this signal occurring during deformation at increasing effective pressure was outlined in Chapter 6. An initial increase of the electrical potential difference followed by a constant value was found between 30MPa and 50MPa with magnitudes of a similar order to those of the pre-seismic signals. The results indicate a different mechanism of electrical current transport during dynamic rupture. At this point macroscopic fracture formation occurs and the resulting signal is generated only by this mechanical process and is not influenced by sliding on the fault plane. It is suggested that the rock enters its most dilatant stage at this point when increased fluid flow occurs. From Figure 10-2 it can be seen that at the point of dynamic fracture a rapid increase in pore volume change occurs and 0.065ml of fluid enters the coseismic source region. An increase in the number of suitable pathways for fluid and electrical current flow occurs and local pressure gradients are increased . An increase in effective pressure causes an increase in this co-seismic signal up to 30MPa. During this period an increase in cumulative AE between 10MPa and 30MPa is also observed which suggests enhanced cracking and the presence of a greater number of electrical pathways. This could therefore explain the increasing co-seismic electrical potential signal with effective pressure. The non-dependence of electrical potential difference on effective pressures above 30MPa is unclear though it may be due to increasing widths of the localised damage zones causing variable flow patterns and reduced convection currents. Increasing gouge zone thickness has been reported in Coconino sandstone and used to explain decreases in hydraulic permeability (Teufel, 1987). An increase in cumulative AE was recorded at higher effective pressures and hence this explanation may be appropriate.

The fractal quantity 'mean crack length' is estimated from stress-strain relationships and AE data and as described by Main et al. (1992) is a measure of the average length of aligned cracks. If the cracks are aligned then there is a strong possibility they will interact forming a continuous pathway. Electrical current can then flow through such pathways resulting in charge distribution and electrical potential changes. The increase in cumulative mean crack length towards a maximum crack length at fracture occurs in a non-linear fashion during dilatancy, as shown in Figure 6-10. The electrical potential difference increases linearly with increasing cumulative mean crack length, suggesting that a increasing density of aligned cracks causes increased transport of the convection currents. There appears to be no critical threshold of AE above which current flow is possible. A sharp electrical potential increase occurs at fracture suggesting that the macroscopic shear fault is acting as an enhanced current pathway.

The electrical potential difference is seen to depend on the mode of deformation and so the resulting electrical signals might be used as a measure of the damage manifested through these processes.

10.3 Discussion of Effects of Pore Fluid Salinity on Electrical Potential Signals.

Fluid interaction through stress corrosion has significant effects on deformation and is assumed to be important in crustal deformation (Rutter, 1976, Sleep and Blanpied, 1992). Interactions are directly dependent on effective stress, temperature, mean grain diameter and indirectly dependent on ionic strength and the pH of the intergranular fluid (Revil, 1999).

From this study it has been deduced that samples saturated with low ionic brine pore fluids (0.34M) are 20% higher in strength than the those saturated with water. Samples deformed with intermediate strength ionic solutions (1.2M) are up to 16% stronger than water saturated samples while the greatest reduction in strength is found for high ionic brine solutions (5.14M) (see Table 10-3). Ishido and Mizutani (1980) suggested an electromechanical effect where fracture strength is non-linearly dependent on the zeta potential during uniaxial compression. A parabolic relationship between strength and zeta potential was obtained for the pore fluids used. In this study the zeta potential decreases non-linearily with increasing NaCl salinity due to a decreasing Debye length, as shown in Figure 3-3 and no relationship with peak strength can be found. The relationship between a binary electrolyte and concentration is given by Revil et al. (1999a) and discussed below.

Pore Fluid	Peak Strength (MPa)	Number of AE
No pore fluid	118	
Deionised water	80	10400
0.34 M NaCl brine	100	25000
0.63 M NaCl brine	96	
0.85 M NaCl brine	94	
1.29 M NaCl brine	94	
1.71 M NaCl brine	106	
5.14 M NaCl brine	76	

Table 10-3 Peak strengths of Darley Dale sandstone deformed with pore fluids of varying salinity.

A brine solution of 0.63M concentration caused the number of AE events during deformation to be more than double that occurring using deionised water as the pore fluid, for the same threshold (Table 10-3). This effect is considered to be due to the high concentration of pore fluid influencing the stress corrosion processes. The increased cracking is seen to have an enhanced effect on the electrical potential difference producing changes one order of magnitude greater than those found from deformation using deionised water. It can be assumed that cracking creates further electrical paths as crack density increases. It can also be noted, over the range of brine concentrations used, the peak strength of the rocks vary. It appears that the peak strength is higher for brine than water saturated rocks for the low and intermediate brine concentrations (0.2M), while significant reductions in strength, compared to water saturated rocks, occur for rocks with brines of high concentration (5.14M). No microscopic analysis of the brine-saturated rocks was made due to time restrictions. The above result can be explained mathematically using equation

10-3, which describes how the deformation rate will increase with increasing molar volume of the pore fluid (Guéguen and Palciauskas, 1994).

$$\dot{\varepsilon} = \frac{\sigma \upsilon}{RT} \frac{D'}{h^3} \tag{10-3}$$

where $\dot{\varepsilon}$ is strain rate, σ is stress, ν is the molar volume, D' is the diffusion coefficient, R is the universal gas constant, T is the temperature in degrees centigrade and h is the grain length.

These mechanical results are in close agreement to those of Feucht and Logan (1990) who investigated the effects of chemically active solutions on triaxial deformation of Tennessee sandstone. It was shown here, using SEM observations, that the friction surfaces from rocks deformed containing high ionic strength solutions have very rough surfaces and little gouge material. The cause of this effect was suggested to be pressure solution related.

The evolution of the electrical potential difference during deformation is significantly different for brine saturated rocks during the dilatancy phase of deformation. During compaction a decrease of the electrical potential difference occurs as connected pore volume is closed expelling fluid and electrical charge through convection current flow. The electrical potential difference during dilatancy begins to increase as found in earlier experiments. At a particular point an anomalous decrease in the signal occurs for all the investigated brine saturated samples. This decrease continues until dynamic fracture occurs where a signal similar to that found in the water-saturated samples is recorded.

To explain this anomalous behaviour it is necessary to consider a number of factors, which are shown to affect electrokinetic phenomenon. The effect of changes in pH causes the polarity of the zeta potential to alter from a positive value to more negative values with increasing pH as seen in Figure 10-7 (Ishido and Mizuntani, 1981; Lorne et al., 1999a; Johnson, P. R., 1999). The value of pH can be altered by the addition of ions such as SO_4^{2-} or Al^{3+}, which can alter the zeta potential significantly (Ishido and Mizutani, 1981; Lorne et al., 1999a). An increase in electrolyte concentration also causes a decrease in the zeta potential for 1:1 electrolytes (Lorne et al., 1999a; Revil et al., 1999a). The value predicted for a 1M NaCl binary solution in contact with a silica surface is –15mV using the model of Revil et al. (1999a).

The change in electrical potential difference may therefore be due to a changing zeta potential caused by a pH change of the saturating fluid. The availability of pH altering ions, specifically SO_4^{2-} could be produced through reactions occurring in the cement between quartz grains, as suggested by Lorne et al. (1999b) or from opening of fresh crack surfaces. Dilatancy generally occurs at around 50% of the peak strength of Darley Dale sandstone (Figure 6-6 and Sammonds et al., 1989; Glover et al., 1997) and these interactions would be expected to occur around this time. However, the electrical potential difference anomaly during dilatancy occurs at approximately 95% of the peak stress and so an explanation based on chemical reactions in the quartz cement cannot account for the behaviour. In Figure7-6a, b photomicrographs of Darley Dale sandstone are shown before and after the average stress level (σ_{avg}) for the change in electrical potential occurs. It can be seen that after σ_{avg} a significant production of axial

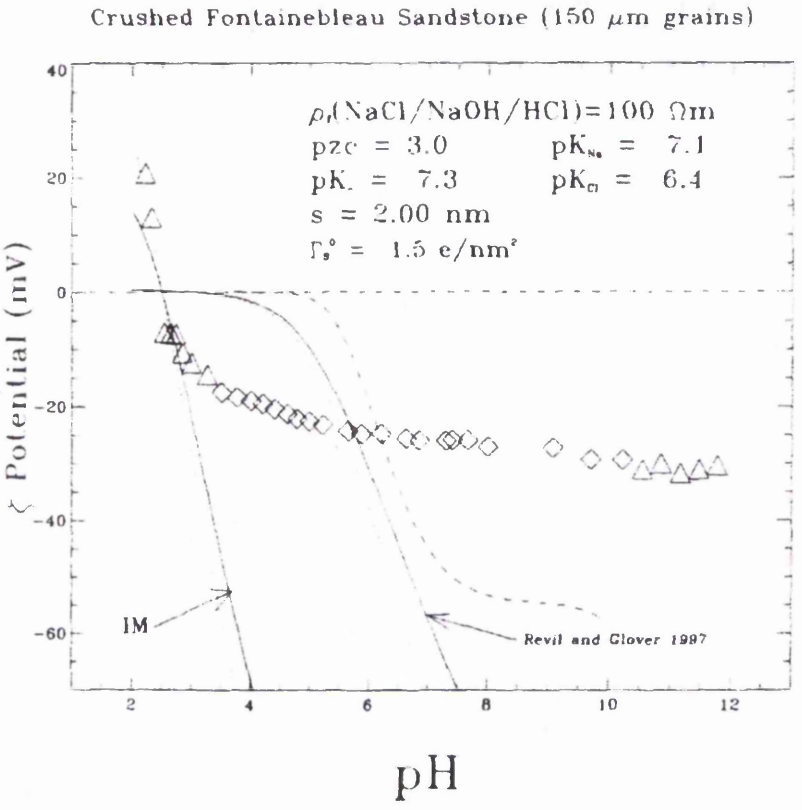

Figure 10-7 Zeta potential variation with pH determined from streaming potential measurements showing decrease from positive values to negative values with increasing pH. Triangles are values for which the fluid resistivity could not be maintained at 100 Ωm (From Lorne et al., 1999a).

intragranular crack has occurred. Since AE activity is observed during all the dilatant period, I suggest that up to 95% of peak stress, intergranular cracking in the form of shearing and pore opening is dominant and that after this point, intragranular is initiated. The presence of these intragranular cracks occurring at this stress level agrees with previous studies on sandstone by Menéndez et al. (1996) though the early production of intragranular cracks followed by intergranular cracks has also been suggested (Dunn et al., 1973). Rapid decreases of V_s and V_p wave velocities well after the onset of dilatancy have also been attributed to more dominant axial cracking (Sammonds et al., 1989; Ayling et al., 1995). This mechanism of cracking, creating new reactive crack surfaces is thought to alter conductivity and pH of the fluid, which has a direct influence on the zeta potential resulting in electrical potential changes (Ishido and Mizutani, 1981; Lorne et al., 1999b). The actual mechanism of fluid resistivity change may be through production of SO_4^{2-} ions. These ions have been observed during triaxial deformation of Fontainebleau sandstone at 75% of the fracture strength and are a strong candidate for the observed resistivity changes (Lorne et al., 1999b).

Coseismic and Preseismic signals

Significantly, precursory electrical potential signals to dynamic fracture can not be found when NaCl brines over the range investigated here are used as pore fluid. During strain softening subcritical crack growth coupled with crack coalescence leads to fluid flow and electrical current flow as discussed in the preceding sections. This leads to an electrical potential difference across the solid rock medium. When pure water is used as pore fluid the mobility of the ions is lower compared to those comprising brine solution. This is because the ionic radii of OH^- ions are smaller than CL^- ions (Table 10-4) and therefore have a higher charge density, which attracts more water of hydration, lowering the mobility. The high mobility of the ions in the brine solution and the high fluid conductivity lead to a increased time constant (Appendix A) suggesting that spontaneous electrical signals rapidly decay and hence precursory signals may not be detectable.

Ionic Species	Ionic Radius / pm
O^-	126
Na^+	95
Cl^-	181
OH^-	155

Table 10-4 Ionic radii of most common species in NaCl brine solution.

Coseismic signals however are evident during dynamic rupture. The variation of the electrical potential difference shows a correlation with the variation of the activity coefficient of the pore fluid. It is not entirely know why such a relationship exists and more information is required to alleviate this behaviour. It is possible that the pore fluids with high and low activity coefficients (Figure 7-8) produce fault surfaces with high gouge content or rough surfaces with little gouge content respectively as found by Feucht and Logan (1990) in Tennessee sandstone. This type of fault plane inhibits fault closure and therefore current flow can be maintained through the crack network. The pore fluids with intermediate values of activity coefficient produce smooth surfaces with little gouge material and therefore under a confining pressure the fault surface will close more, reducing the connectivity of paths for electrical current flow.

10.4 Discussion of Effects of Strain Rate on Electrical Potential Signals.

Experimental rock deformation over a range of strain-rates is essential to provide a basis for extrapolation to typical geological settings. As shown in Figure 8-3 a decrease in electrical potential difference is found with decreasing strain rate between 1.5×10^{-4} s^{-1} and 1.5×10^{-6} s^{-1}. Absolute electrical potential differences approach zero as strain rate becomes low: a phenomenon, which has also been reported, in moist bone (Gross and Williams, 1982).

Mechanically the deformation characteristics, as observed from the stress strain curves (Figure 8-1), show similar behaviour with no significant variation in peak stress. Since absolute pore volume change is similar for each of these experiments (Figure 8-4), a mechanism resulting in increased charge distribution in the sample due to increased pore volume change can be excluded. Moreover the effects of different hydraulic and electrical conductivity (see Chapter 10.5) are not expected to be important in these results because an effective pressure of 20MPa was used in all experiments. The indication is therefore that the rate of fluid flow may be responsible for the observed electrical potential changes.

A linear relationship is obtained between electrical potential difference and flow rate as shown in Figure 10-8. In equation 10-4 the total current density is the sum of a pressure induced convection current (1st term on the right) and an electrically induced conduction current (2nd term on right). The decreasing flow rate causes a decrease in the convection current rate through the sample, which will reduce the conduction current contributions. These reduced contributions will each lower the total charge density flowing within the sample and the resulting electrical potential across the rock,

$$J = -\frac{\varepsilon\zeta}{\eta}\nabla P - \sigma_f \nabla V \tag{10-4}$$

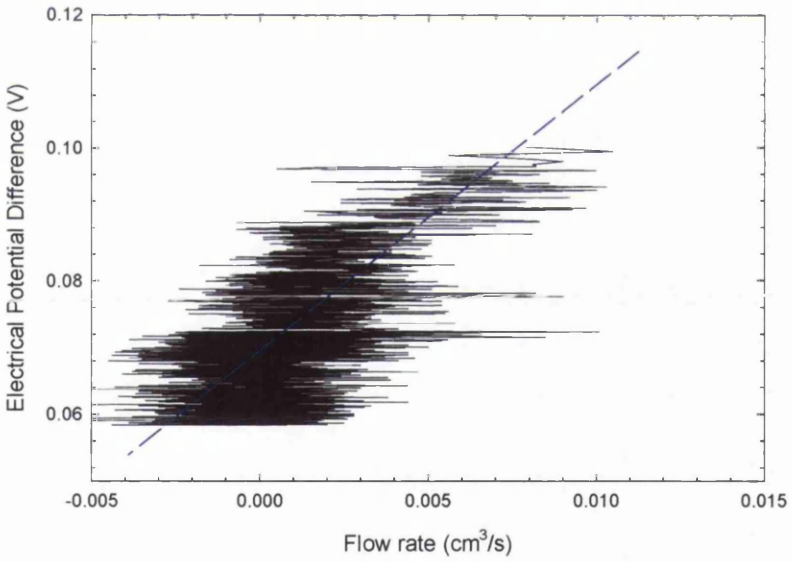

Figure 10-8 Electrical potential difference as a function of fluid flow rate. Data is taken during compaction and dilatancy up to dynamic fracture during triaxial deformation of Darley Dale sandstone. De-ionised water was used as pore fluid and data plotted is from a 1.5 x 10^{-5} s^{-1} strain rate experiment. [Experiment No.:40]

10.5 Discussion of Streaming Potential Signals from Porous Sandstone.

The process of crack generation during dilatancy could change the streaming potential due to an increase in the zeta potential (Jouniaux and Pozzi, 1995b). Effective pressure is also expected to alter the streaming potential, altering the pore and crack network ability to transmit fluid and electrical current. Compaction and dilatancy under drained and undrained conditions will alter pore pressure and the behaviour of streaming potentials at various pressures is therefore required. Consequently, if a systematic change in streaming potential during deformation can be determined then important information concerning the deformation can be obtained. Hydraulic permeability will also be affected by the matrix alterations during deformation (Tuefel, 1987; Zhu and Wong, 1996; Keaney, 1998) and the relationship between the two is important to produce accurate models (David, 1993).

It has been found here that the streaming potential increases linearly with pore fluid pressure up to a pressure gradient of 30MPa for Darley Dale sandstone (Figure 9-2). The maximum pressure gradients used in previous investigations are given in Table 10-5. This linear relationship has been observed on Fontainebleau sandstone samples (Jouniaux and Pozzi, 1995) under hydrostatic pressure of 11.5MPa using pore pressure gradients up to 0.2MPa. Investigations without hydrostatic pressure also show a linear relationship on crushed haematite (Korpi et al, 1971), crushed quartz samples (Ishido et al, 1981), arkosic sand mixtures (Brown, 1997) and crushed Fontainbleau sandstone (Lorne et al., 1990a, 1999b). A non-linear relationship is observed for Berea sandstone without application of confining pressure (Tuman, 1963) while both linear and non-linear behaviour has been reported for unconfined Triassic sandstone and fractured granites (Middleton, 1997).

The surface conductivity for both Berea and Darley Dale sandstone is comparable, i.e., 0.5 – 0.7mS/m therefore the non-linearity observed by Tuman (1963) may be due to turbulent flow related to the high permeability of Berea sandstone. $k = 2 \times 10^{-12}$ m^2 has been measured in Berea sandstone (Zhu and Wong, 1996), which is five orders of magnitude greater than Darley Dale sandstone.

To understand why a constant streaming potential signal is not obtainable above 30MPa requires the consideration of the Reynolds number (R_e) which indicates whether laminar flow is established. Using the experimentally determined flow rate of 0.00114 ms^{-1} occurring at 40MPa through Darley Dale sandstone the Reynolds number can be determined. The expression for (R_e) is given as

$$R_e = \rho v l / \eta \qquad (10\text{-}5)$$

where density $\rho = 1 \times 10^3$ kg m^{-3}, v is the velocity of the fluid in the pore matrix, l is a characteristic pore dimension (0.5mm) and η is the fluid viscosity (1×10^{-3} Pa s). Using these data a value of 570 is obtained for R_e which is suggestive of non-laminar flow and hence Darcy's law is not valid.

This study therefore confirms the linear relationship between streaming potential and applied pressure gradient as predicted by equation 3-26 but suggests that there may be a maximum pressure gradient above which streaming potentials cannot be maintained. The results agree well with the linear relationships determined by previous investigations as shown in Figure 10-9.

Study	Maximum Pressure Gradient (MPa)
Lorne et al. 1999a	0.2500
Middleton 1997	0.0125
Brown and Haupt 1997	0.0250
Jouniaux and Pozzi. 1995b	0.2000
Ishido et al. 1981	0.0100
Korpi et al. 1971	0.0930
Tuman 1963	9.6000

Table 10-5 Maximum pressure gradients used in streaming potential measurements from previous studies.

This linear behaviour between streaming potential and pressure gradient is also seen in Bentheim sandstone. This sandstone has a hydraulic permeability two orders of magnitude greater than Darley Dale sandstone. The streaming potentials recorded from this rock however are two orders of magnitude lower (Figure 9-2). Equation 3-26 predicts that the streaming potential is scale invariant, i.e. has no dependence on permeability assuming constant zeta potential, and therefore this result is unexpected. Lorne et al. (1999a) report no clear intrinsic dependence of streaming potential coefficient on permeability using crushed samples performed without confining pressure. Jouniaux and Pozzi (1995b) on the other hand found an increase in streaming potential coefficient with increasing permeability at a confining pressure 10MPa, a relationship found for the macroscopic streaming potential coefficient using numerical simulations (Bernabé, 1998).

The increase in permeability will give rise to an increased bulk electrical conductivity through the rock (Stesky, 1986; David and Darot, 1989) and an increased convection current. The ohmic conduction will quickly equilibrate this convection current because of the increased bulk conductivity causing a reduction of the streaming potential.

The effect of permeability on streaming potential is vital in understanding how these signals are produced within a heterogeneous earth model. So to are the effects of stress variation on these types of signals. The level of stress can induce significant levels of damage (increased crack and pore porosity) and therefore warrants detailed investigation. An initial experiment (Figure 9-8) shows how the streaming potential increases after shear fracture. The increase is observed at pore-fluid pressure gradients up to and including the limiting value of 30MPa (discussed earlier). The removal of the residual stress from the sample also increases the streaming potential by a factor of 1.3 and is considered a result of the opening of sub-horizontal cracks, which were closed by an axial normal stress. This opening and relaxation of cracks can significantly increase the fluid flow rate through fractures (Tsang and Witherspoon, 1981). Frictional sliding did not occur on the fault plane as deformation was stopped at the moment of fracture and therefore the fracture processes enhance the streaming potential.

This increase in streaming potential at the point of dynamic rupture may be related to an increase in permeability, although it should be noted, an increase in permeability does not always occur for porous sandstone. Zhu and Wong (1996) found a decrease in permeability during dilatancy and shear fracture for Berea sandstone. The results show good agreement with network models (Zhu and Wong, 1996). The increase of streaming potential noted immediately after fracture also increases further with pore pressure gradient. The streaming potential measured at varying parts of a rock sample will therefore depend on the measurement position when heterogeneities are introduced. This is comparable with the electrical potential measurements produced after fracture as shown in Chapter 5. Finite element models also suggest variations of the theoretical streaming potential when a discontinuity is introduced.

If a constant pore pressure gradient is maintained then a streaming potential will be generated which will be maintained until interrupted. A compressive stress pulse applied to the system causes an enhanced streaming potential superposed on the original signal. The peak magnitude of the enhanced signal increases with stress change and the time evolution of the signal correlates well with the stress-rate of the pulse. The stress pulse will cause the closure of sub-horizontal cracks forcing fluid out of connected pores as shown schematically in Figure 10-10. This process does not affect the streaming potential as

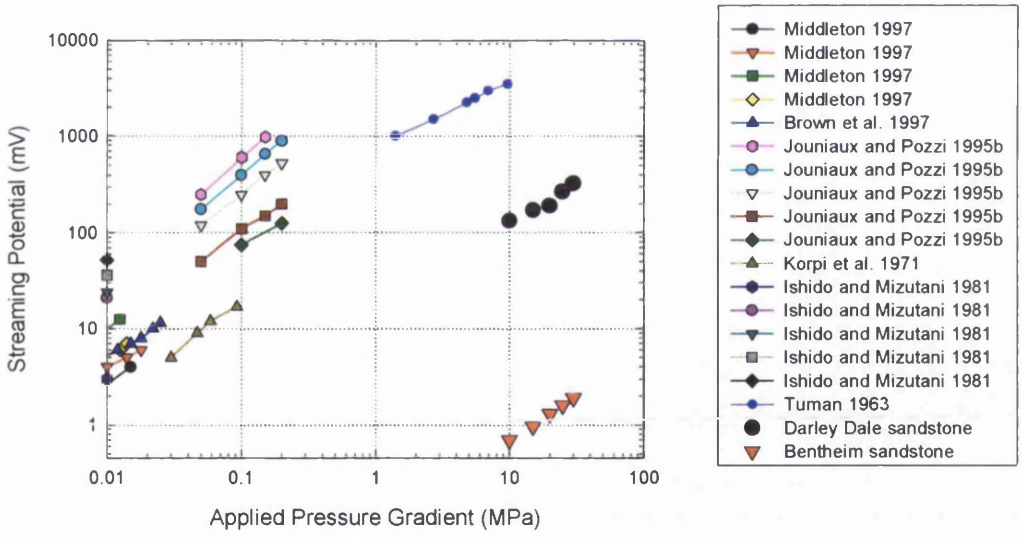

Figure 10-9 Comparison of streaming potentials measured from Darley Dale and Bentheim sandstone with values from the literature. Sources of data are given in the legend.

shown in Figure 9-5 and therefore increasing compressive stress has negligible effect on the electrical flow-path. As the stress is removed the streaming potential increases rapidly. This may be due to the fact that a fraction of the pores relax and contribute to the convection current. An increased transport of electrical charge occurs causing an increased conduction, in turn leading to an increased streaming potential. The result suggests an additional source of streaming potentials in addition to those predicted by Sill (1983) (equation 3-36).

The evolution of permeability and streaming potential during deformation will bring out the difference between hydraulic and electrical flow in rocks and help to explain the above observations. Note that the permeability is not corrected for the electro-osmotic contribution due to the first term of equation 3-29 and is an apparent permeability. A 42% decrease in hydraulic permeability using deionised water and 25% decrease for brine saturated rock occur during compaction. The streaming potential decreases by only 42% and 24% respectively during this period indicating a complex relationship between hydraulic and electrical flow. This complex relationship has also been reported for compaction of crushed Fontainebleau sandstone samples (Lorne et al., 1999b).

It is now appropriate to discuss the electrical (τ_e) and hydraulic tortuosities (τ_h). The processes of fluid and electrical fluid flow are described by similar equations and therefore it is assumed that ions flowing through a rock under a potential gradient follow the same path as fluid flowing under a pressure gradient (Tsang, 1984). It has been observed that transport properties vary significantly from sample to sample in sandstone (David and Darot, 1989) and from formation to formation (Wyble, 1958). Numerical evaluations show clearly a higher hydraulic tortuosity compared to electrical flow patterns, manifested as

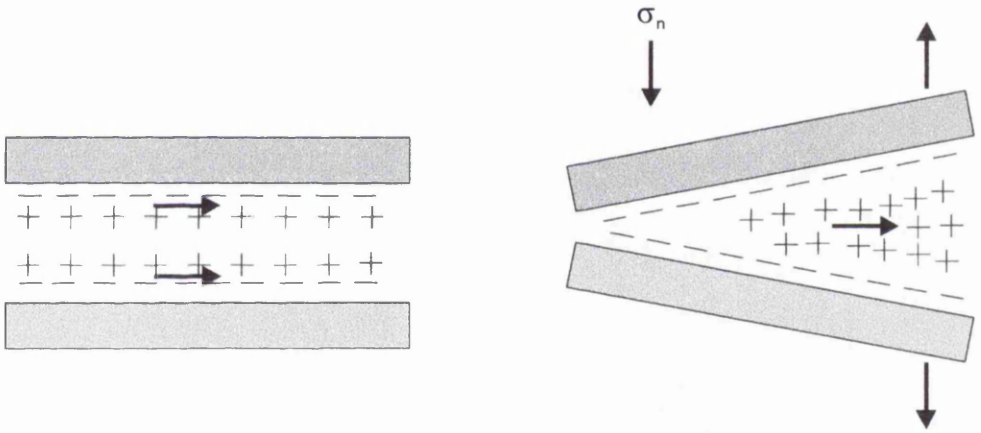

Figure 10-10 Schematic plot of streaming current in (a) pore space and (b) closing pore space.

an order of magnitude difference at low porosity (Brown, 1989; David, 1993; Zhang and Knackstedt, 1995). Experimental observations also indicate a permeability dependence on fluid pathway type, i.e., crack or fracture porosity, and a non-dependence of electrical resistivity on pathway type (Mattisson, 1997). The application of hydrostatic pressure also appears to produce varying critical paths for electrical and hydraulic flow with hydraulic flow controlled by length scales of the order l^4 and electrical conductivity controlled by l^2 length scales (David, 1993). As a result the pore geometry and distribution can be considered important in controlling fluid and electrical current flow (Bernabé and Bruderer, 1998) and therefore a single value transport coefficient cannot be used. The pore size distribution effect on fluid flow and streaming potential in semipermeable membranes has also been examined (Saksena and Zydney, 1995).

The difference between hydraulic permeability and streaming potential can now be understood as being due to different tortuosity. The results suggest that the hydraulic tortuosity increases faster than the electrical tortuosity. During compaction a decrease in pore volume occurs which is due to closure of sub-horizontal cracks and pores resulting in a less continuous pore network for fluid flow and significant reduction of permeability as predicted by equation 2-24. The electrical current, which is dependent on an even smaller crack aperture (David, 1993), is still able to permeate through the sample and hence an equivalent reduction in streaming potential does not occur. This explanation confirms the simple model proposed by Lorne et al. (1999b).

When further compaction can no longer accommodate the stress induced strain in the sample, dilatant induced microcracking becomes prevalent. This process is associated with an exponentially cumulative rise in AE, decreasing b-values and a spatial variation of the cracks along a future macroscopic fault plane. The onset occurs around 55% of the peak strength of the sample, which agrees with previously reported values (Glover et al., 1994).

During this period, which continues up to dynamic fracture, the streaming potential and permeability continue to decrease and are still decreasing at 90% of the peak strength of Darley Dale sandstone, for example. Lorne et al. (1999b) report this streaming potential phenomena up to 73-79% of the peak strength of Fontainebleau sandstone while 72-86% was reported by Jouniaux and Pozzi (1995b) for the same rock. Therefore the onset of dilatancy does not cause a significant change in the electrical and hydraulic flow patterns in a deforming rock. Using AE source locations it is observed that initial microcracking occurs in isolated upper and lower regions of the sample, which begin to coalesce along a macroscopic plane after peak stress. The new dilatant cracks are responsible for increases in bulk pore volume but this is not reflected in a permeability increase also evidenced by Zhu and Wong (1996). The cracks will create a more tortuous fluid pathway causing a decrease in hydraulic permeability.

In Chapter 10.3 I suggested that intergranular cracking is the primary cracking mechanism occurring during this period with no significant increase in low aspect cracks, through which convection currents can flow, are produced. The grain rotation and shear mechanisms actually increase the electrical tortuosity leading to a decrease in streaming potential.

These ideas have led me to develop of a simple model illustrated in Figure 10-11, which has been constructed using microscopic analyses presented earlier in this report. This model describes the evolution of the hydraulic and electrical network during dilatancy, which is separated into two stages on the basis of microstructural analyses and frictional sliding. The idea is comparable to the conceptual model of Lorne et al. (1999b), which outlines a process for hydraulic and electrical tortuosity evolution during compaction but is a one-stage dilatant period only and has no microstructural information included.

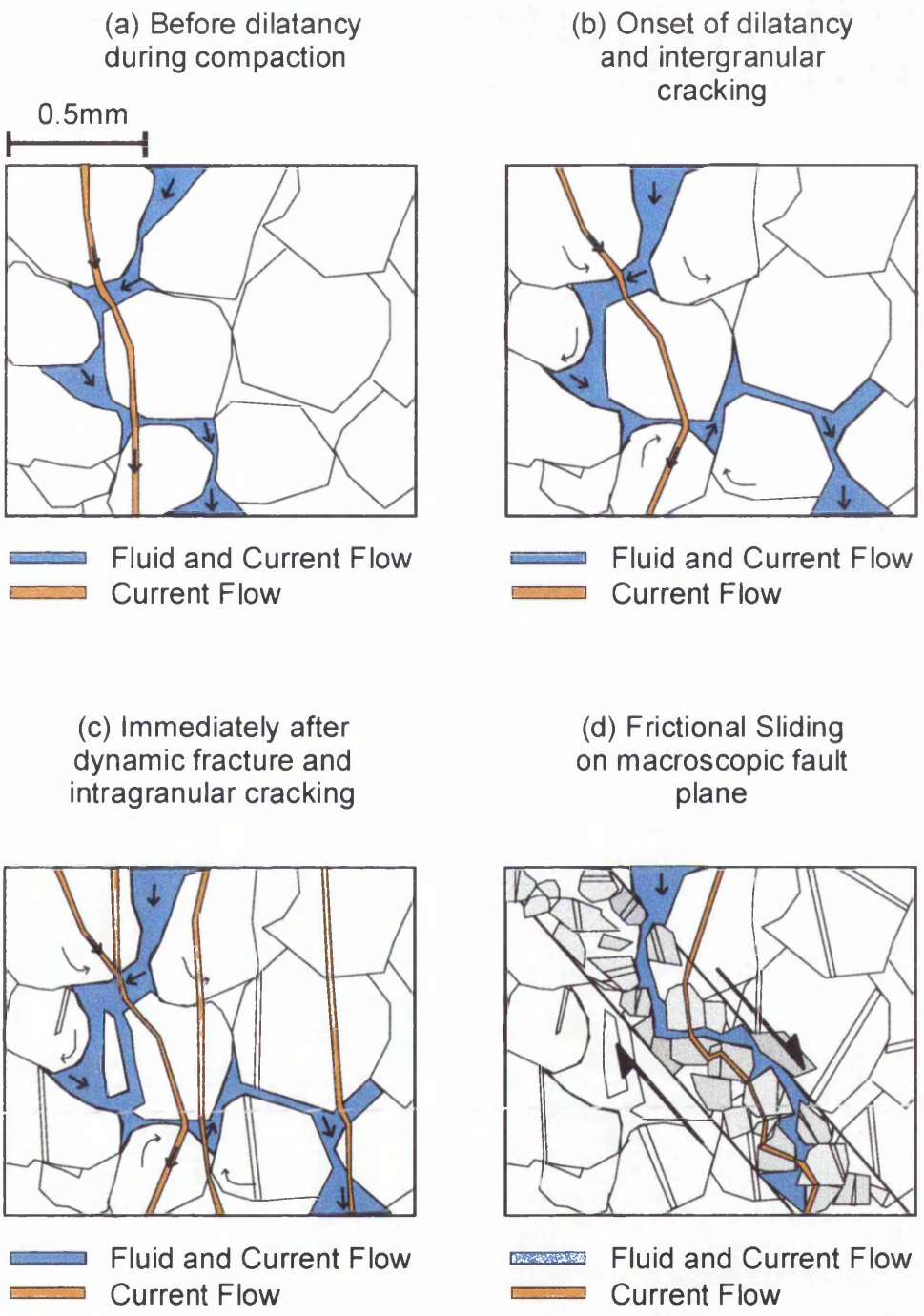

Figure 10-11 Evolution of electrical and hydraulic flow paths during (a) compaction, (b) onset of dilatancy, dominated by intergranular cracking and grain rotation (c) between peak stress and immediately after dynamic fracture, dominated by intragranular cracking and (d) during stable sliding on macroscopic fault plane. N. B. increases in pore volume in (b) and (c) during dilatancy and the detail of grain geometry at each stage has been obtained from microscopic analyses.

In Figure 10-11a the state of the rock before dilatancy is shown with a representative fluid pathway which also carries the convection current. Also shown is an electrical current path, which has lower aspect ratio than the fluid pathway thereby restricting fluid movement, although these are not prevalent. In Figure 10-11b the onset of dilatancy is depicted. Intergranular cracking causes a shearing of grain boundaries, which dilates the pore space, increasing the pore volume. Grain rotation in this period causes the hydraulic tortuosity to increase, which decreases the permeability while only slightly affecting the electrical tortuosity. The model therefore adequately describes the observations during compaction.

As peak stress is approached grains can become locked into rigid positions and the cracking process changes to intergranular cracking as explained in Chapter 10.3. The streaming potential increases during this period exhibiting a maximum value of 120% and 278% of the initial values immediately after dynamic fracture for water and brine fluids respectively. Permeability however does not increase in this way exhibiting only an increase of 20% of the initial permeability for water saturated samples and a decrease of -20% of the initial permeability for brine saturated samples. This behaviour can be explained using Figure 10-11c, which represents an area away from the macroscopic fracture i.e. away (3mm) from the localised fault zone area. An increase in pore volume occurs due to grain boundary shearing while grain rotation will also increase the tortuosity of the hydraulic network. Axial cracks within grains link up to form low aspect pathways through which current can flow. The result is that a hydraulic permeability decrease will occur and an increased streaming potential is expected. The permeability could be expected to increase slightly if a series of large aspect cracks occur such as shown in Figure 10-11c. Grain rotation may also create a link between two parts of a tortuous fluid path.

A decrease in permeability has been reported in sandstone during stable (frictional) sliding (Jouniaux and Pozzi, 1995b; Zhu and Wong, 1996; Keaney, 1998) during which interaction of asperities is occurring. Numerical simulations show rough fracture surfaces cause decreased permeability (Waite et al., 1998), complex flow patterns including channelling (Brown, 1995; Glover et al., 1998), and obvious differences between electrical current and hydraulic flow patterns (Brown, 1989). Furthermore the relationship between surface roughness and asperity deformability can cause the fracture permeability to increase (Olsson and Brown, 1993) or decrease (Olsson, 1992).

The observations from this study show the permeability of Darley Dale sandstone is initially constant but, then decreases during stable sliding on the macroscopic fracture plane. The streaming potential decreases rapidly by 77% after only a small increment of strain (0.3%) before maintaining a constant value as sliding progresses. Microstructural analysis reveals that the majority of grains in the sample are fractured while a region of localised deformation exists around the fracture zone. The region is highly fractured with varying amounts of fault gouge and range of quartz and feldspar grain sizes. This feature is also reported from Tennessee sandstone (Keaney, 1998) and Coconino sandstone (Teufel, 1987). The fault zone will increase the hydraulic tortuosity as shown in Figure 10-11d thereby reducing the hydraulic permeability. Increased sliding is expected to cause further surface interaction and crushing of asperities. This crushing will further reduce the porosity and permeability as sliding continues. Such results have

been shown in Coconino sandstone (Teufel, 1987). The electrical current is also reduced in the model due to the large increase in electrical tortuosity in the fault region. Current flow is dependent on the successful connection of the intragranular cracks in the fault gouge, which increases the electrical tortuosity. Due to the large number of fractured crystals in the fault region a continuous electrical path can be expected resulting in a more or less constant streaming potential.

10.6 Application to Geological Environments

10.6.1 Earthquake Prediction Implications

These results can now be discussed in the context of earthquake prediction. Considering a dilatant region undergoing fracture nucleation and coalescence a situation can arise when fluid is forced into the region by a positive pore pressure gradient. Through electrokinetic phenomena a convection current will redistribute positive charge formed at the fracture/fluid interfaces causing increasing electrical potential anomalies of the order of millivolts. A resulting seismic event involving large scale faulting would be expected to produce an instantaneous, similar magnitude, electrical potential signal, which would decay as equilibrium is reached. If a constant pore pressure gradient is maintained then a streaming potential will be generated which will also be maintained until interrupted. An interruption may include a stick slip event or local compressive stress pulse. The latter will cause an enhanced signal on the existing streaming potential the size of which is directly linked to the magnitude of the stress change.

Whether the above behaviour, recognised through laboratory testing, can occur on kilometre scales requires the relationships between fracturing and fluid/current flow to exhibit self-similar behaviour. Fault growth exhibits a linear dependence between fault displacement and fault length (Scholz et al., 1993) for the three fault types studied (Schlische et al., 1996). This self-similarity is also recognised through a power law distribution of earthquake sizes. The above relationships are questioned through studies which reveal linear (Cartwright et al., 1993) and exponential (Cowie, 1993) relationships between fault length and displacement during fault growth.

Also normal fault segments show an increase in displacement while fault length remains fixed (Moreland and Roberts, 1999) and it is suggested that the fault length is established early in the fault evolution. The explanation for these types of relationships is that segment or fracture interaction and linkage perturbs the stress field leading to a departure from the power law scaling principles. The clustering of cracks/fractures seen during deformation (Figure 10-12) can increase the electrical conductivity of a region as suggested in Figure 10-11. A quantitative relationship for this process is shown in Figure 10-13 where a linear increase between cumulative mean crack length, determined from AE, and electrical potential exists. Fracture is easily identified as a sharp rise in the electrical potential as dynamic fracture ultimately forms a fault plane.

In Figure 10-14 the electrical potential difference is plotted as a function of the number of source located AE occurring in the region around each electrode. A power law relationship between the electrical potential difference and number of AE is obtained for electrodes 1 and 2. Both these electrodes are found to be located closely to the surface expression of the fault (Figure 10-3b). The electrical potential generated through current flow may therefore scale with the size of the fault preparation zone as suggested by Vallianatos and Tzanis (1999). The distribution of source located AE can be considered a measure of the damage-zone dimension and power-law relationships between earthquake source dimensions and parameters such as seismic moment have been found to exist in field studies (Abercrombie, 1995 and Figure 2-4). It appears therefore that the dimension of the source zone may control the electrical potential difference as it does the magnitude of a seismic event.

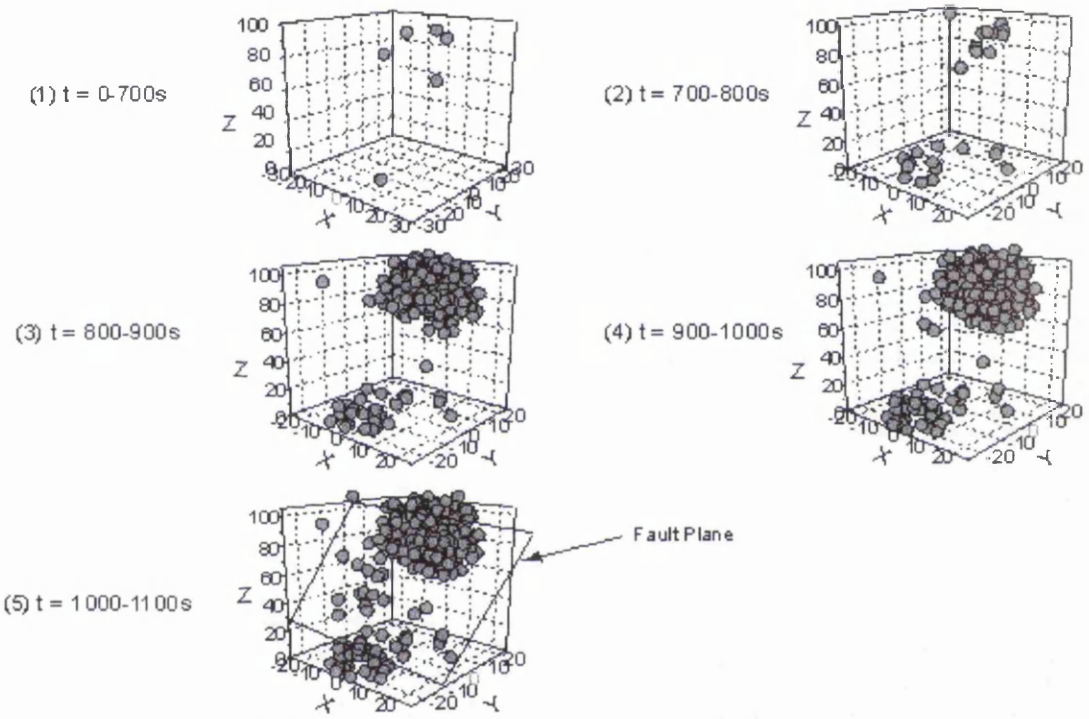

Figure 10-12 Evolution of AE during deformation and fracture of Darley Dale sandstone. [Experiment No.: 40]

A result of using brine solutions as pore fluid means that precursors cannot be detected above a certain noise level. This fluid which is more typical of crustal pore fluids suggests that short-term precursory electrical potential signals may not be produced in the preparation zone of an earthquake.

NaCl brines are more representative of fluids in the earth's crust (Roedder, 1984) and therefore the absence of precursory electrical potential signals to dynamic fracture suggests that electrokinetic precursory signals prior to seismic events may not be detectable. However the brines used in this study consists only of Na^+, Cl^-, H_3O^-, and OH^- ions which does not fully represent the entire ionic content of real crustal brines as outlined in Table 7-1. The possibility of typical crustal brine generating electrical potential signals cannot be ruled out.

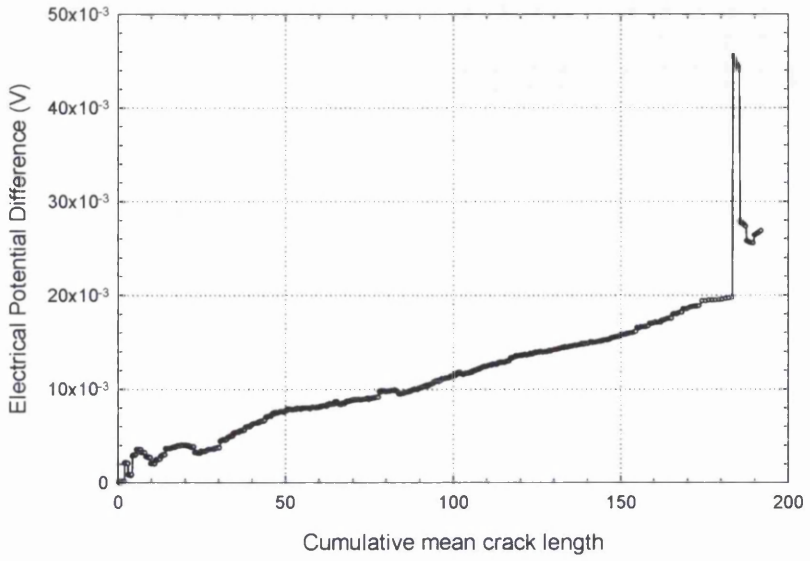

Figure 10-13 Electrical potential difference as a function of cumulative mean crack length during dilatancy and shear fracture during deformation. [Experiment No.: 40]

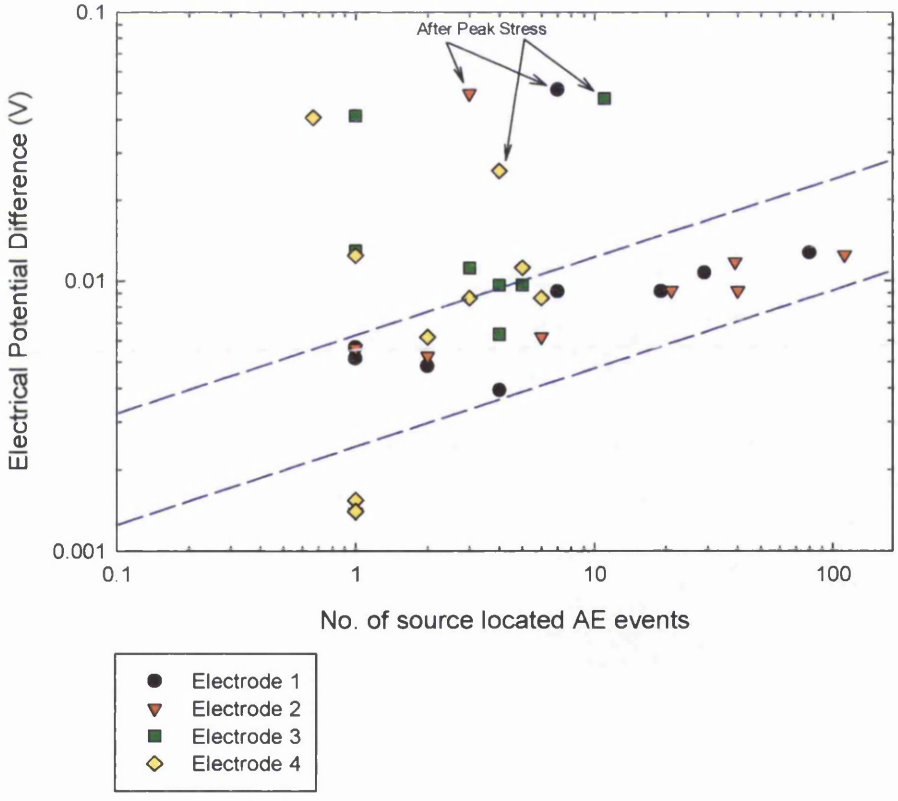

Figure 10-14 Electrical potential difference as a function of number of source located AE positioned in the region around each electrode. [Experiment No.: 40]

10.6.2 Implications for Shallow Crustal Exploration

The power of electrokinetic measurements is that they allow us to determine the microscopic information from macroscopic measurements on bulk samples. The electrokinetic signal can be measured directly from the surface down to depths of 300m (Thompson and Gist, 1993) using electroseismic methods of application of a mechanical pulse. The method has the advantage that it does not alter the stress state of the rock by invading it with pressure gradients or pressurised pore fluids. Shallow boundaries can be mapped by recording the electric fields induced through seismic sources at formation boundaries (Mikhailov et al., 1996; Russell et al., 1997) which agree with synthetic electrograms (Mikhailov et al., 1996). The results are also in accordance with the theoretical predictions of Sill (1983) where sources of electrical potential exist in regions of convection current divergence (Chapter 3.4.4).

Fitterman (1978, 1979) shows the existence of electrokinetic-magnetic anomalies across faulted areas and within dilatant regions due to variation of streaming potential coefficient across the region and the existence of a pressure gradient. Numerical models indicate that the streaming potential response caused by pumping down oil well boreholes is of the order of a few millivolts but is transmitted over only small distances (Wurmstich and Morgan, 1994). An increase in streaming potential produced through fractured rock (Chapter 10-4) could be used to delineate damaged zones or fracture aperture ahead of drilling direction. Streaming potentials increase with the applied pressure gradient and therefore an optimum pressure pulse could be found to increase the detectability of the resulting signals.

In the case of the Darley Dale sandstone tests, a limiting pressure of 30MPa is found above which turbulent flow is expected to occur. The streaming potential is found to decrease with increasing permeability therefore this technique is perhaps not suited to oil and water exploration because high permeability and porosity sandstone is required for economic resource extraction. The model presented in Figure 10-10 deduced from the observations in this study indicates differences between electrical and hydraulic flow patterns and therefore a direct link cannot be assumed. Calibrated results for specific rock types could however be used to predict the Darcy permeability from a streaming potential measurement.

10.6.3 Scaling Issues and Fractal Behaviour

Due to the heterogeneity of rocks in the field the results produced from small homogeneous rock samples in the laboratory are questioned (Leary, 1997). This arises due to the presence of seismic and electrical anisotropy in the crust and is thought to be due to the presence of fluid filled fractures and faults (Bernard et al., 1997). Experiments performed on heterogeneous samples would of course be hard to interpret though a complete understanding of the fundamental effects contributes greatly to our understanding of these processes. A link between experimental studies of fundamental electrokinetic phenomena (Ishido and Mizutani, 1981; Lorne et al., 1999a; Revil et al., 1999a) streaming potentials during deformation (Jouniaux and Pozzi, 1995b; Lorne et al., 1999b) and electrical potential changes during shear fracture (Yoshida et al., 1998) must be linked with field studies (Thompson and Gist, 1993; Russell et al., 1997; Beamish, 1999).

Macroscopic electrokinetic equations have been developed incorporating flow rates, temperature, pressures, fluid concentrations and pore geometry (Revil et al., 1999b; Ishido and Pritchett., 1999). Realistic values of behaviour of streaming potentials with each of these parameters have been taken from experimental work and used in supercomputer simulations of large scale features. The results successfully fit naturally observed self-potential profiles across geothermal fields, volcanoes and faults. Both models which, incorporate electrokinetic mechanisms, show positive self-potential anomalies associated with fluid discharge areas and negative anomalies over fluid recharge areas.
These results show the importance of this current research. The electrical potential results presented here occur throughout compaction, dilatancy, crack coalescence and propagation; features observed in typical earthquake cycles. The dependence of mechanical and fluid flow properties on fracture roughness suggest that the size of a rock sample should be larger than the typical wavelength of the roughness undulations (Tsang and Witherspoon, 1983). Increasing mis-matched fracture surfaces allowed more accurate stress-strain behaviour to be recreated. Numerically produced fracture surfaces show that synthetic fractures should be matched at long wavelengths and unmatched at short wavelengths (Glover et al., 1998a). The results can be used to model accurately the natural transmissivity and stress response of fluid flow in geothermal rocks (Glover et al., 1998b).

The results between a number of source located acoustic emissions and the electrical potential during dilatancy, up to peak stress, show self-similar behaviour in the areas of most intense microcracking (Figure 10-12). It is concluded therefore that the interaction of cracks in an increasingly damaged area creates the conditions necessary for increased current flow. The power law relationship suggests scale invariance and fractal behaviour. A fractal scaling law relating electrical field and earthquake magnitude has been determined using polarised spherical volumes of increasing size in an earthquake preparation zone (Vallianatos and Tzanis, 1999). No specific polarisation mechanism is implied but the present results could explain this behaviour through a fractal distribution of crack volumes polarised through electrokinetic mechanisms. Vallianatos and Tzanis (1999) using a fractal dimension (D) of 2.3 corresponding to dynamic crack propagation suggest that transient precursors may result from microfracturing processes in the earthquake source region. As noted in Figure 10-14, a deviation from the power law relationship is observed after peak stress when sub-critical crack growth occurs. True self-similar behaviour may therefore only be possible during the period leading to peak stress of the rock.

The electrical potential difference time series is plotted in Figure 10-15 as a series of cluster plots for 100s intervals with a few smaller intervals around dynamic fracture. The data is plotted in space as $x_{n+2} - x_{n+1}$ as a function of $x_{n+1} - x_n$, which is a measure of future events on the current value. A clear correlation exists in all time intervals indicating a non-random process. The result could be a signature of a self-organising 'system'. If such a self-organisation reached a critical point, self-organised criticality (SOC), such as that described for fault populations, could be observed and power law scaling then exists. One aspect of SOC is that the critical point is maintained and is insensitive to external dynamic controls. In Figure 10-15 the system is maintained up to 600s which includes the compaction and early dilatancy cycle of the deformation cycle. Between 600s and 700s the correlation becomes more random as the

directionality of the correlation is disturbed. At 700s, peak stress is reached and between 700s and 730s, strain softening occurs prior to dynamic fracture. The system has now evolved once again into a non-random correlated sequence, which is maintained after fracture at 730s. The system therefore reorganises itself after peak stress most likely due to a different deformation process such as e. sub-critical crack growth. The time of occurrence of the system organisation correlates with the deviation from a power law scaling behaviour between electrical potential difference and microcracking zones (Figure 10-14). The results suggest that a state of SOC does not exist. On the other hand the present research deals with an initial 'time equal to zero' state which cannot be recognised in field conditions. SOC therefore may be reached immediately prior to an earthquake and maintained at a critical point during further deformation, further experiments at high strain are needed to clarify this point. If this were so, it would agree with the constant b-value obtained by Sammonds and Ohnaka (1998) in frictional experiments.

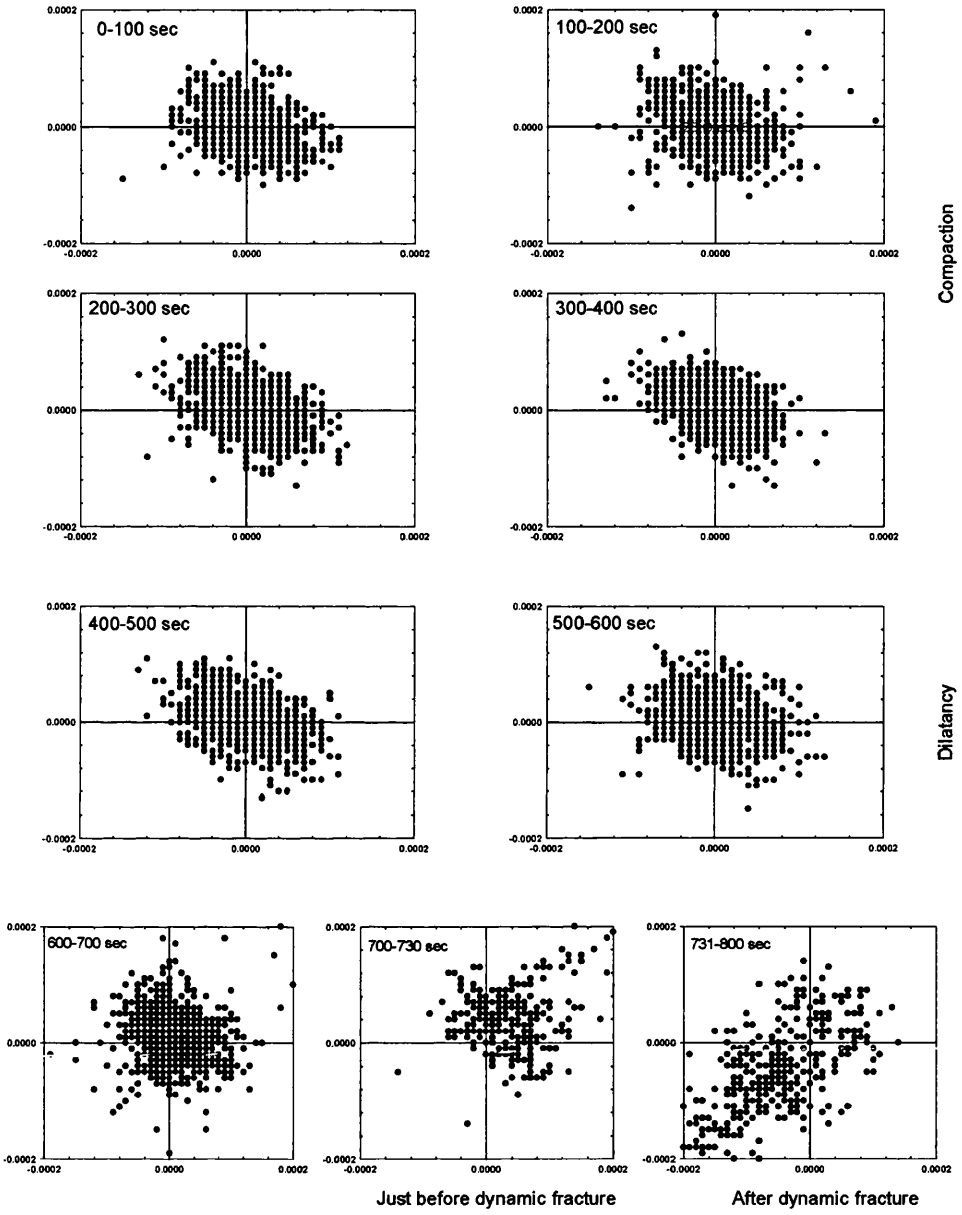

Figure 10-15 Cluster diagrams of an electrical potential difference time series during a deformation cycle. Values are plotted as $x_{n+2} - x_{n+1}$ as a function of $x_{n+1} - x_n$ where x is an electrical potential measurement at time t_n. [Experiment No.: 40]

11. Conclusions and Future Work

In this study the acoustic emission, electrical potential difference and streaming potential signals during experimental rock deformation are investigated. Triaxial deformation techniques are employed carried out under constant strain rate control. Electrical potential signals are measured using an electrode array while streaming potentials are determined using a steady-state flow method. An array of eight piezoelectric transducers allows acoustic emission events to be located in space and time during deformation. Effective pressure, strain rate and pore fluid salinity and rock type are varied and the resulting effects are used to investigate the electrical potential generation mechanism.

The results show that in a saturated rock such as sandstone or basalt deformed at an effective pressure of 20MPa equivalent to a depth of 1.33km, dynamic fracture is associated with precursory and co-seismic electrical potential anomalies. This is the case for deionised water and a mechanism of electrokinetic current flow through newly forming intragranular cracks is strongly suspected. For the case of brine saturated sandstone no pre-seismic electrical potential anomaly can be detected. The high mobility of the NaCl ions, rapidly equilibrating the electrical potentials produced, is believed to be the cause of this behaviour.

Channel flow through pore and crack networks appears to control electrical current flowing through rocks under simulated crustal conditions. The alteration of crack and pore networks through compaction, dilatancy and shear fracture significantly modify the resulting electrical potential difference. Electrical and streaming potentials are increased through microcracking and instantaneous faulting. Frictional sliding is not expected to create increased electrical signals as evidenced by a constant streaming potential. A favourable channelling of electrical current in this manner has been shown to produce signals of tens of millivolts per kilometre from a 1km deep reservoir maintained a near-lithostatic pore pressures (Bernard, 1992). It is therefore possible that electrical currents could emanate from a source region creating electrical fields at far-field distances through fluid flow mechanisms and may therefore form SES prior to earthquakes.

The decrease of electrical potential difference with effective pressure during compaction suggests that as closure of pore space and microcracks occurs, fluid is expelled from the rock reducing the pore volume. The fluid transports a convection current of positive charges out of the rock reducing the electrical potential across the sample. During dilatancy an increase in the electrical potential occurs across the sample. Increasing damage is occurring but the pore volume change within the rock does not alter significantly. This suggests that the cracks are of low aspect ratio preventing fluid flow but electrical current can be transported within this crack network causing an increase in the electrical potential difference as increased charge accumulates at boundaries in the rock sample.

Hydraulic permeability in deforming rocks is more affected by flow-path tortuosity than are electrical currents for the cases of pure water and brine saturated rocks. This conclusion is drawn from the results of the variation of streaming potential and permeability during deformation. During compaction, permeability decreased more rapidly under pressure than streaming potential while dilatancy induces greater increases in streaming potential than hydraulic permeability. An explanation includes the fact that a more effective crack network allows enhanced current flow while inhibiting fluid flow.

Streaming potentials are linearly related to the driving fluid pressure gradient for Darley Dale and Bentheim sandstone up to pressures of 30MPa. Non-laminar flow occurs above this pressure gradient and constant streaming potentials cannot be obtained. The streaming potentials measured are lower for Bentheim sandstone, which has a higher permeability than Darley Dale sandstone. If the permeability is greater then bulk conductivity will be greater leading to a greater conduction current, the convection current equilibrates this conduction current, leading to a reduction in the streaming potential assuming a constant pressure gradient and zeta potential and no change in the formation factor.

The fluid flow rate controls the current flow within rocks during deformation with a linear relationship existing between flow rate and electrical potential difference. The potential differences produced are such that the absolute value of the change in potential difference observed during compaction and dilatancy decreases with decreasing strain rate down to 1.5×10^{-5} s^{-1}. The physical process is a result of decreasing amounts of ionic charge being distributed within the sample. It is therefore possible that electrical potential differences are not measurable due to deformation at typical crustal strain rates.

Pore fluid salinity effects include greater peak strength of rocks saturated with pore fluids of concentration between 0 and 0.2M compared to peak strengths at higher pore fluid salinity (5M). Enhanced cracking occurs in sandstone when brines are used over deionised water with a doubling of cumulative AE during deformation evident. This increased cracking causes larger electrical potential differences due to the availability of more effective crack networks creating conditions for enhanced current flow. A significant change in the electrical potential gradient occurs during dilatancy when brine pore fluids are used. The occurrence of this point is suggested to be the onset of intragranular cracking evidenced through microscopic analysis. The presence of these cracks is suspected to alter the resistivity and pH of the pore fluid resulting in changes in the zeta potential and hence electrical potential differences.

The co-seismic stress drop and hence magnitude of the dynamic rupture event appears to be dependent on the salinity of the pore fluid. The resulting electrical potential difference shows a dependency on the stress drop for NaCl brines up to 1.6M concentration while a correlation is found up to a concentration of 5M with activity coefficient of the solution.

11.1 Future Work

The effects of temperature on streaming potential and electrical potential require a comprehensive investigation. Early experiments showed that self-potential surveys offer a powerful tool in delineating areas of high heat flow beneath the surface (Dorfman et al., 1977) but the underlying effects of temperature on electrokinetic parameters such as the zeta potential are not well known. Morgan et al. (1989) presents results showing a small effect of 0.05mV/°C on the zeta potential, for granite samples. In contrast Ishido and Mizutani (1981) showed the zeta potential to decrease with increasing temperature at a rate of -6.5×10^{-1} mV/°C for quartz in a solution of pH=6.1. Numerical models however predict an increase in zeta potential by approximately 7×10^{-2} mV/°C to which the experimental data of Ishido and Mizutani (1981) can be fitted. The above studies are conducted below 80°C and to therefore allow successful modelling and understanding of geological applications this effect must be quantified accurately at a greater temperature range. The influence of two phase flow is a necessary future problem for example in a recent volcanological simulation, two-phase flow (wet steam) at high temperature including an upward moving steam front was found to produce electrical potential gradients of opposite polarity to the smaller electrical anomalies produced during a downward liquid flow (Antraygues and Aubert, 1993).

To further understanding of electrokinetic phenomena in the field, the geophysical database must be expanded while streaming potentials should be measured during stick-slip, torsion and creep experiments. This depends on additional experiment programs on more rock types including volcanic and carbonate which are expected to exhibit streaming potential signals. Electrical potentials and streaming potential must be investigated over a wider permeability range such as the range investigated by Brace (1980).

The power law relationship found in Figure 10-14 between the electrical potential difference and number of source located acoustic emissions should be investigated by field experiments. Monitoring these data in a borehole experiment could be used to prove this empirical relationship and the results could be directed to the general question of upscaling from the laboratory to the field.

References

ABERCROMBIE, R., 1995, Earthquake source scaling relationships from –1 to 5ML using seismograms recorded at 2.5km depth. *J. Geophys. Res.* **100**, 24,015 – 24,036

ACEVES, R. L., PARK, S. K. AND STRAUSS, D. J., 1994, Statistical evaluation of the VAN method using the historic earthquake catalog in Greece. *Geophys. Res. Lett.* **23** (11), 1425 - 1428

ALDRICH, M. J., 1969, Pore pressure on Berea sandstone subjected to experimental deformation. *Geol. Soc. Am. Bull.* **80**, 1577 – 1586

AMBRASEY, N. N., 1970, Some characteristic features of the Anatolean fault zone. *Tectonophys.* **9**, 143 - 156

ANDERSON, L.A. AND JOHNSON, G.R., 1976, Application of the Self-Potential Method to Geothermal Exploration in Long Valley, California. *J. Geophys. Res.* **81** (8)

ANTRAYGUES, P. AND AUBERT, M., 1993, Self-potential generated by two-phase flow in a porous medium: Experimental study and volcanological applications. *J. Geophys. Res.* **98** (B12), 22,273 – 22,281

ARCHIE, G. E., 1942, The electrical resistivity log as an aid in determining some reservoir characteristics. *Trans. Am. Inst. Min. Metal. and Petr. Eng.* **146**, 54 – 62

ATKINSON, B. K., 1982, Sub-critical crack propagation in rocks: Theory, experimental results and applications. *J. Struct. Geol.* **4**, 41 - 56

ATKINSON, B. K., 1984, Subcritical crack growth in geological materials. *J. Geophys. Res.* **89** (B6), 4077 – 4114

ATKINSON, B. K. AND MEREDITH, P. G., 1987, The theory of subcritical crack growth with application to minerals and rocks. In: *Fracture Mechanics of Rock.* 111 – 166 (ed) Atkinson, B., Academic Press, London

AL-SAIGH, N. H., MOHAMMED, Z. S. AND DAHHAM, M. S., 1994, Detection of water leakage from dams by self-potential method. Eng. Geol. 37, 115 - 121

AVES, P., 1995, Mechanics of compaction and dilatancy in triaxially stressed rocks, under simulated crustal conditions studied by pore volumometry. *PhD Thesis*, University of London

AVELLANEDA, M. AND TORQUATO, S., 1991, Rigorous link between fluid permeability, electrical conductivity and relaxation times for transport in porous media. *Phys. Fluids* **A 3** (11), 2529 - 2540

AYLING, M. R., 1991, An experimental study of physical property changes in crustal rocks undergoing triaxial deformation. *PhD Thesis*, University of London

AYLING, M. R., MEREDITH, P. G., AND MURRELL, S. A. F., 1995, Microcracking during triaxial deformation of porous rocks monitored by changes in rock physical properties, I. Elastic wave propagation measurements on dry rocks. In: C. J. Spiers and T. Takeshita (eds), Influence of fluids on Deformation Processes in Rocks. *Tectonophys*, **245**, 195 - 211

BAK, P., TANG C. AND WIESENFELD K., 1988, Self-organised criticality. *Phys. Rev., **A38***, 364-74

BAK, P. AND TANG C., 1989, Earthquake as a self-organised critical phenomenon. *J. Geophys. Res., **94***, 15,635-15,637

BARRIERE, B. AND TURCOTTE D. L., 1991, A scale-invariant cellular-automata model for distributed seismicity. *Geophys. Res. Let.* ***18***, 2011-2014

BARRIERE, B. AND TURCOTTE D. L., 1994, Seismicity and self-organised criticality. *Phys. Rev.* ***E49***, 1151-1160

BATZLE, M. L., SIMMONS, G AND SIEGFRIED, R. W., 1980, Microcrack closure in rocks under stress: Direct observation. *J. Geophys. Res.* **85** (B12), 7072 – 7090

BEAMISH, D., 1999, Characteristics of near-surface electrokinetic coupling. *Geophys. J. Int.* **137**, 231 - 242

BERNABÉ, Y., 1998, Streaming potential in heterogeneous networks. *J. Geophys. Res.* **103** (B9), 20,827 – 20,841

BERNABÉ, Y. AND BRUDERER, C., 1998, Effect of the variance of pore size distribution on the transport properties of heterogeneous networks. *J. Geophys. Res.* **103** (B1), 513 – 525

BERNARD, P., CHOULIARAS, G., TZANIS, A., BRIOLE, P., BOUNIN, M.-P., TELLEZ, J., STAVRAKAKIS, G. AND MAKROPOULOS, K., 1997, Seismic and electrical anisotropy in the Mornos delta, Gulf of Corinth, Greece, and its relationship with GPS strain measurements. *Geophys. Res. Lett.* **24** (17), 2227 - 2230

BERRYMAN, J. G., 1992a, Exact effective stress rules in rock mechanics. Phys. Rev. A **46** (6), 3307 – 3311

BERRYMAN, G., 1992b, Effective stress for transport properties of inhomogeneous porous rock.' *J. Geophys. Res.* **97**, 17409-17424

BIOT, M. A., 1941, *J. App. Phys.* **12**, 155

BLAKE, E. W AND CLARKE, G. K. C., 1999, Subglacial electrical phenomena. *J. Geophys. Res.* **104** (B4), 7481 - 7495

BLANPIED, M. L., LOCKNER, D. A. AND BYERLEE, J. D., 1992, An earthquake mechanism based on rapid sealing of faults. *Nature* **358**, 574 - 576

BOTT, M. H. P., 1982, The Interior of the Earth; its Structure, Constitution and Evolution. 2nd edn, Edward Arnold, London, and Elsevier, New York.

BRACE, W. F. AND BOMBOLAKIS, E. G., 1963, A note of brittle crack growth in compression. *J. Geophys. Res.* **68**, 3709 - 3953

BRACE, W. F., 1964, Brittle fracture of rocks. *In State of Sress in the Earth's Crust.* Judd, W. R., (ed). New York, Elsevier, 111 - 174

BRACE, W. F. AND ORANGE, A. S., 1966, Electrical resistivity changes in saturated rocks under stress. *Science.* **153**, 1525 – 1526

BRACE, W. F., PAULDING, B. W. AND SCHOLZ, C., 1996b, Dilatancy and the fracture of crystalline rocks. *J. Geophys. Res.* 77 (16), 2939 - 3953

BRACE, W. F. AND ORANGE, A. S., 1968, Electrical resistivity changes in saturated rocks during fracture and frictional sliding. *J. Geophys. Res.* **73** (4), 1433 - 1445

BRACE, W. F., 1968, The mechanical effects of pore pressure on fracturing of rocks. *Conference on research in tectonics: Geol. Soc. Can.* Paper **68-52**, 113 - 124

BRACE, W. F., 1971, Resistivity of saturated crustal rocks to 40km based upon laboratory measurements, in Structure and physical properties of the earth's crust, *Geophys. Monogr. Ser.*, **14**, 243 - 255

BRACE W. F., ORANGE, A. S. AND MADDEN, T. R., 1976, The effect of pressure on the electrical resistivity of water-saturated crystalline rocks. *J. Geophys. Res.* **70**, 22, 5669 – 5678

BRACE, W. F., 1980, Permeability of crystalline and argillaceous rocks. *Int. J. Rock Mech. Min. Sci. and Geomech. Abstr.* **17**, 241 – 251

BREDEHOEFT, J. D. AND NORTON, D. L., 1990, Mass and energy transport in a deforming earth's crust. *Studies in Geophysics*, National Research Council, National Academy Press, Washington

BROWN, S. R. AND SCHOLZ, C. H., 1985a, Broad bandwidth study of the topography of natural rock surfaces. *J. Geophys. Res.* **90**, 12,575 – 12,582

BROWN, S. R. AND SCHOLZ, C. H., 1985, Closure of random elastic surfaces in contact. *J. Geophys. Res.* **90**, 5531 - 5545

BROWN, S. R. AND SCHOLZ, C. H., 1986, Closure of rock joints. *J. Geophys. Res.* **91**, 4939 – 4948

BROWN, S. R., 1989, Transport of fluid and electric current through a single fracture. *J. Geophys. Res.* **94**, 9429 – 9438

BROWN, S. R., 1998, Simple mathematical model of a rough fracture. *J. Geophys. Res.* **100**, 5941 - 5952

BROWN, S. R. AND HAUPT, R. W., 1997, Study of electrokinetic effects to quantify groundwater flow. *Rep. SAND94-2607*, Sandia Natl. Lab., Albuquerque, N. M.

Bruner, W. M., 1976, Seismic velocities in dry and saturated solid. *J. Geophys. Res.* **81**, 2573 - 2576

BUCHER, M., FOSTER, D.A. AND GRAY, D.R., 1996, *Geol. Soc. Am. Abs. Prog.* **28**, p.A-439.

BUSSIAN, A. E., 1983, Electrical conductance in a porous medium. *Geophysics* **48**, 1258 - 1268

BUTLER, D. B. AND KNIGHT, R. J., 1998, Electrical conductivity of steam-flooded clay-bearing geologic materials. *Geophys.* **63** (4), 1137 - 1149

BYERLEE, J., 1993, Model for Episodic Flow of High Pressure Water in Fault Zones before Earthquakes. *Geology* **21**, 303 – 306

CARTWRIGHT, J. A., MANSFIELD, C. AND TRUDGILL B., 1996, The growth of normal faults by segment linkage. In *Modern Developments in Structural Interpretation, Validation and Modelling*, Geol. Soc. Lon. Special Publication **99**, Buchanan, P. G. and Nieuwland, D. A. (eds), 163 - 177

CHANDLER, R., 1981, Transient streaming potential measurements on fluid-saturated porous structures: An experimental verification of Biot's slow wave. *J. Acoust. Soc. Am.* **70** (1), 116 -121

CHARLES, R. J., 1958, Static fatigue of glass. *J. Appl. Phys.* **29**, 1549 - 1560

COHEN, R. R. AND RADKE, C. J., 1991, Streaming potentials of nonuniformly charged surfaces. *J. Colloid Interface Sci.* **141** (2), 338 – 347

CORWIN, R. F., AND MORRISON, H. F., 1977, Self-potential variations preceding earthquakes in central California. *Geophys. Res. Letts.* **4** (4), 171 - 174

CORWIN, R. F. AND HOOVER, D. B., 1979, The Self-Potential method in geothermal exploration. *Geophysics* **44**, 226 – 245

COSTIN, L. S., 1985, Damage mechanics in the post failure regime. *Mech. Mat* **4**, 149 - 160

COVEY-CRUMP, S. J., 1998, Evolution of mechanical state in Carrara marble during deformation at 400° to 700°C. *J. Geophys. Res.* **103**, 29781-29794.

COWIE, P., VANNESTE, P. C. AND SORNETTE, D., 1993, Statistical physics model for the spatio-temporal evolution of faults. *J. Geophys. Res.* **98**, 21809

COWIE, P., SCHOLZ, C. H., EDWARDS, M. AND MALINVERNO, A., 1993, Quantitative fault studies on the East Pacific Rise – a comparison of sonar imaging techniques. *J. Geophys. Res.* **98**, 17,911 – 17,920

COWIE, P., 1997, Cracks in the earth's surface. *Phys. World* February, 31 – 35

COX, S. J. D. AND MEREDITH, P. G., 1993, Microcrack formation and material softening in rock measured by monitoring acoustic emissions. *Int. J. Rock Mech. Min. Sci & Geo. Abst.* **30**, 1, 11 – 24

CRAMPIN, S. AND ZATSEPIN, S. V., 1997, Modelling the compliance of crustal rocks - II. Response to temporal changes before earthquakes. *Geophys. J. Int.* **129**, 495 – 506

CRESS, G. O., BRADY, B. T. AND ROWELL, G. A., 1987, Sources of electromagnetic radiation from fracture of rock samples in the laboratory. *Geophys. Res. Lett.* **14**, 331 - 334

CUOMO, V., LAPENNA, V., MACCHIATO, M., SERIO, C. AND TELESCA, L., 1998, Linear and non-linear dynamics in electrical precursory time series: implications for earthquake prediction. *Tectonophys.* **287**, 279 - 298

DAVID, C. AND DAROT, M., 1989, Permeability and conductivity of sandstones. In *Rocks at Great Depth*, ed, V. Maury and D. Fourmaintraux, Balkeme, 203 - 210

DAVID, C., GUEGUEN, Y. AND PAMPOUKIS, G., 1990, The effective medium theory applied to the transport properties of rocks. *J. Geophys. Res.* **95**, 6993 - 7006

DAVID, C., 1993, Geometry of flow paths for fluid transport in rocks. *J. Geophys. Res.* **98**, B7, 12,267 - 12,278

DERR, J. S., 1973, Earthquake lights A review of observations and present theories. *Bull. Seismol. Soc. Am.* **63**, 2177 - 2187

DONATH, F. A. AND FRUTH, L. S. JR., 1971, Dependence of strain-rate effects on deformation mechanism and rock type. *J. Geol.* **79**, 347 - 371

DORFMAN, M. H., OSKAY, M. M. AND GADDIS, M. P., 1977, Self-Potential Profiling - A New Technique for Determination of Heat Movement in a Thermal Oil Recovery Flood. *Proc. Soc. Pet. Eng. AIME*, **SPE 6790**, Colorado

DUBA, A., HEIKAMP, S., MEURER, W., NOVER, G. AND WILL, G., 1994, Evidence from borehole samples for the role of accessory minerals in lower crustal conductivity. *Nature* **367**, 59 - 61

DUNN, D. E., LAFOUNTAIN, L. J. AND JACKSON, R. E., 1973, Porosity dependence and mechanism of brittle fracture in sandstones. *J. Geophys. Res.* **78**, 14, 2403 - 2417

DZIEWONSKI, A. M. AND ANDERSON, D. L., 1981, Preliminary reference earth model. *Phys. Earth Planet. Int.* **25**, 297 – 356

EDWARDS, S. T., MEREDITH, P.G. AND MURRELL, S. A. F., 1998, An investigation of leak-off test data for estimating in situ-stress magnitudes: application to a basinwide study in the North Sea. In: *Proc. Rock Mechanics in Pet Eng.* Trondheim, Norway. SPE. 357 - 367

ENGELDER, T. AND SCHOLZ, C. H., 1981, Fluid flow along very smooth joints at effective pressures up to 200 megapascals. Mechanical Behaviour of Crustal Rocks, *Geophys. Mono.* **24**, AGU, 147 – 152

FEUCHT, L. J. AND LOGAN, J. M., 1990, Effects of chemically active solutions on shearing behaviour of a sandstone. *Tectonophys.* **175**, 159 - 176

FENOGLIO, M. A., JOHNSTON, M. J. S. AND BYERLEE, J. D., 1995, Magnetic and Electric Fields Associated with changes in High Pore Pressure in Fault Zones: Application to the Loma Prieta ULF emissions. *J. Geophys. Res.* **100**, (B7), 12,951 - 12,958

FOWLER, C. M. R., 1990, The solid earth. Cambridge University Press, 472pp

FISCHER, G. J. AND PATERSON, M. S., 1992, Measurements of permeability and storage capacity in rocks during deformation at high temperature and pressure. In *Fault Mechanics and Transport Properties of Rocks*, Evans, B. and Wong, T.-f. (eds), Academic Press, New York

FITTERMAN, D. V., 1978, Electrokinetic and magnetic anomalies associated with dilatant regions in a layer in a layered earth. *J. Geophys. Res.* **83** (B12), 5923 – 5928

FITTERMAN, D. V., 1979, Theory of electrokinetic-magnetic anomalies in a faulted half-space. *J. Geophys. Res.* **84** (B11), 6031 - 6040

FRANKLIN, J., A., 1971, Triaxial strength of rock materials. *Rock Mech* **3**, 86 - 98

FREIMAN, S. W., 1984, Effects of chemical environments on slow crack growth in glasses and ceramics. *J. Geophys. Res.* **89** (B6), 4072 – 4076

FREUND, F., WHANG, E-J AND LEE, J., 1994, Highly mobile hole charge carriers in minerals: Key to the enigmatic electrical earthquake phenomena. *Electromagnetic Phenomena related to Earthquake Prediction.* Ed. Hayakawa, M. and Fujinawa, Y., Terra Scientific, Tokyo, 271 - 292

GARCIA-CASTELLANOS, D., FERNANDEZ, M. AND TORNE, M., 1997, Numerical modelling of a foreland basin formation: A program relating subsidence, thrusting, sediment geometry and depth dependent lithosphere rheology. *Computers & Geosciences* **23** (9), 993 – 1003

GELLER, R. J., 1996, Earthquake Prediction: a critical review. *Geophys. J. Int.* **131**, 425 - 450

GLOVER, P. W. J. AND VINE, F. J., 1992, Electrical conductivity of carbon-bearing granulite at raised temperatures and pressures. *Nature* **360**, 723 - 726

GLOVER, P. W. J., MEREDITH, P. G., SAMMONDS, P. R. AND MURRELL, S. A. F., 1994, Ionic surface electrical conductivity in sandstone. *J. Geophys. Res.* **99**, (B11), 21,635 - 21,650

GLOVER, P W J., GOMEZ, J B., MEREDITH, P G., BOON, S. A., SAMMONDS, P. R. AND MURRELL, S. A. F., 1996, Modelling the stress-strain behaviour of saturated rocks undergoing triaxial deformation using complex electrical conductivity measurements. *Surv. Geophys.*, **17**, 307 - 330

GLOVER, P W J., GOMEZ, J B., MEREDITH, P G., HAYASHI, K., SAMMONDS, P. R. AND MURRELL, S. A. F., 1997, Damage of Saturated Rocks undergoing Triaxial Deformation using complex electrical conductivity measurements: Experimental results. *Phys.Chem.Earth,* **22** (1-2), 57-61

GLOVER, P. W. J., MATSUKI, K., HIKIMA, R. AND HAYASHI, K., 1998a, Synthetic rough fractures in rocks. *J. Geophys. Res.* **103** (B5), 9609 - 9620

GLOVER, P. W. J., MATSUKI, K., HIKIMA, R. AND HAYASHI, K., 1998b, Fluid flow in synthetic rough fractures and applications to the Hachimantai geothermal hot dry rock test site. *J. Geophys. Res.* **103** (B5), 9621 - 9635

GODANO, C., ALONZO, M. L. AND CARUSSO V., 1993, Self-organised criticality and earthquake predictability. Phys. *Earth Planet Int. **80,*** 117-123,

GRIFFITH, A. A., 1924, The theory of rupture. *In: Proc. 1st Int. Cong. Appl. Mech.* (eds. Biezeno, C. B. and Burgers, J. M.). Delft: Tec. Boelhandel en Drukkerji. 56 - 63

GRIGGS, D. T., 1936, Deformation of rocks under high confining pressure. *J. Geol.* **44**, 541 – 577

GROSS, D. AND WILLIAMS, W., 1982, Streaming potential and the electromechanical response of physiologically moist bone. *J. Biomech.* **15** (4), 277 - 295

GRUSZOW, S., ROSSIGNOL, J. C., TZANIS, A. AND LEMOUEL, J. L., 1996, Identification and analysis of electromagnetic signals in Greece: the case of the Kozani earthquake VAN prediction. *Geophys. Res. Lett.* **23**, 2025 – 2028

GUEGUEN, Y. AND PALCIAUSKAS, V., 1994, *Introduction to the Physics of Rocks.* Princeton University Press, Princeton, New Jersey, pp 294

GUO, Z., LIU, B. AND WANG, Y., 1994, Mechanism of electromagnetic emissions associated with microscopic and macroscopic cracking in rocks. In: *Electromagnetic Phenomena Related to Earthquake Prediction*, (eds) Hayakawa, M. and Fujinawa, Y., 523 – 529, Terrapub, Tokyo

HAARTSEN, M. W., DONG, W. AND TOKSÖZ, M. N., 1998, Dynamic streaming currents from seismic point sources in homogeneous poroelastic media. *Geophys. J. Int.* **132**, 256 - 274

HATTON, C. G., MAIN, I. G. AND MEREDITH, P. G., 1994, Non-universal scaling of fracture length and opening displacement. *Nature* **367**, 160 – 162

HEARD, H. C., 1963, Effect of large changes in strain rate in the experimental deformation of Yule marble. *J. Geol.* **71**, 162 - 195

HEINSON, G. AND SEGAWA, J., 1997, Electrokinetic Signature of the Nankai Trough Accretionary Complex: Preliminary modelling for the Kaiko - Tokai program. *Phys. Earth Planet. Int.* **99**, 33 – 53

HORII, D. AND NEMAT-NASSER, S., 1985, Compression induced microcrack growth in brittle solids: axial splitting shear failure. *J. Geophys. Res.* **87 (B4)**, 3105 - 3125

HORII, D. AND NEMAT-NASSER, S., 1986, Brittle failure in compression: Splitting, faulting and brittle-ductile transition. *Philos. Trans. R. Soc. London. Ser. A*, **319**, 337 - 374

HUBBERT, M. K., 1940, The theory of groundwater motion. *J. Geol.* **48** (8), 785 - 944

HUBBERT, M. K. AND RUBEY, W. W., 1959, Role of fluid pressure in mechanics of overthrust faulting. I. Mechanics of fluid filled porous solids and its application to overthrust faulting. *Bull. Geol. Soc. Am.* **70**, 115 – 166

IKEYA, M., TAKAKI, S., MATSUMOTO, H., TANI, A AND KOMATSU, T., 1997, Pulsed charges model of fault behaviour producing seismic electric signals (SES). *J. Cir. Sys. Comp.* **7** (3), 153 - 164

ISHIDO, T. AND MIZUTANI, H., 1980, Relationship between Fracture Strength or Rocks and ζ - Potential. *Tectonophysics* **67**, 13-23

ISHIDO, T. AND MIZUTANI, H., 1981, Experimental and theoretical basis for electrokinetic phenomena in rockwater systems and its applications to geophysics. *J. Geophys. Res.* **86**, 1763-1775

ISHIDO, T., MIZUTANI, H. AND BABA, K., 1983, Streaming Potential Observations, using Geothermal Wells and In Situ Electrokinetic Coupling Coefficients under High Temperature. *Tectonophysics* **91**, 89-104

ISHIDO, T. AND PRITCHETT, J. W., 1999, Numerical simulation of electrokinetic potentials associated with subsurface fluid flow. *J. Geophys. Res.* **104** (B7), 15247 – 15 259

ISMAIL, I. A. H., 1974, Experimental studies of mechanical instabilities in rocks with particular reference to earthquake focal mechanisms. *Ph.D. Thesis*, University of London

ISMAIL, I. A. H. AND MURRELL, S. A. F., 1976, Dilatancy and the strength of rocks containing pore water under undrained conditions. *Geophys. J. Roy. Astr. Soc.* **44**, 107 - 134

JAEGER, J. C. *Elasticity, fracture and flow*. Chapman and Hall, 1969

JAEGER, J. C. AND COOK, N. G. W., 1979, *Fundamentals of Rock Mechanics* (3rd edition). Chapman and Hall, London, 593 pp

JOHNSON, D. L. AND SCHWARTZ, L. M., 1989, Unified theory of geometrical effects in transport properties of porous media. *Trans. SPWLA Annu. Logging Symp.*, **30th** paper E, 25 pp, SPE

JOHNSON, P. R., 1999, A comparison of streaming potential and microelectrophoresis methods for obtaining the zeta potential of granular porous media surfaces. *J. Coll. Interface. Sci.* **209**, 264 - 267

JOHNSTON, M. J. S., MUELLER, R. J., MYREN, G. D. AND KELLER, V., 1999, Tilt, strain and magnetic field measurements, *Proj. No's*: 7460-10590, 7460-11590, 7460-11592, 7460-16590 7460-18590, USGS, AGU

JONES, C., 1989, An experimental study of the relationship between P-wave velocity, Acoustic emission and deformation in rocks under simulated crustal conditions. *Ph.D. Thesis*, University of London

JONES, C. AND MEREDITH, P. G., 1998, An Experimental Study of Elastic Wave Propagation Anisotropy and Permeability Anisotropy in an Illitic Shale. In *Eurock '98, Proc. SPE/ISRM* International Conference, 8-10 July, 1998, Trondheim, Norway, Society of Petroleum Engineers (1998).

JOUNIAUX, L., POZZI, JP., BROCHOT, M. AND PHILIPPE, C., 1992, Resistivity changes induced by triaxial compression in saturated sandstones from Fontainebleau. *C. R. Acad. Sci. Paris* **315**, (II), 1493 - 1499

JOUNIAUX, L. AND POZZI, JP., 1995a, Permeability Dependence of Streaming Potential in Rocks for various Fluid Conductivities. *Geophys. Res. Let.* **22** (4), 485-488

JOUNIAUX, L. AND POZZI, JP., 1995b, Streaming potential and permeability of saturated sandstones under triaxial stress: Consequences for electrotelluric anomalies prior to earthquakes. *J. Geophys. Res.* **100**, 10,197 - 10,209

KAGAN, Y. Y. AND JACKSON, D.D, 1996, Statistical tests of VAN earthquake predictions: Comments and reflections. *Geophys. Res. Lett.* **23**, 1433 – 1436

KAGAN, Y.Y., 1997, Are earthquake predictable. *Geophys. J. Int.* **131**, 505 - 525

KAGAN, Y. Y., 1999, Is earthquake seismology a hard, quantitative science? *Pageoph.* **155** (2-4), 233 – 258

KANAMORI, H. AND ANDERSON, D. L., 1975, Theoretical bases of some empirical relations in seismology. *Bull. Seis. Soc. Am.* **65**, 1073 - 1095

KARMAN, TH. VON., 1911, Festigkeitsversuche unter allseitigem Druck. Z. *Ver. Dt. Ing* **55**, 1749 - 1757

KATO, N., YAMAMOTO, K, YAMAMOTO, H. AND HIRASAWA, T., 1992, Strain-rate effect on frictional strength and the slip nucleation process. *Tectonophys.* **211**, 269 - 282

KATZ, A. J. AND THOMPSON, A. H., 1985, Fractal sandstone pores: Implication for conductivity and pore formation. *Phys. Rev. Lett.* **54**, 1325 - 1328

KATZ, A. J. AND TRUGMAN, S. A., 1988, Residual water saturation, electrical conductivity and rough rock/pore interfaces. *J. Colloid Int. Sci* **123**, 8 - 13

KEANEY, G. M., 1998, Evolution of permeability in low porosity rocks under simulated crustal stress conditions. *PhD Thesis,* University of London.

KEILIS-BOROK, V. I, 1990, The lithosphere of the earth as a non-linear system with implications for earthquake prediction. *Rev. Geophys.* ***38***, 19-34

KELLER, G. V., 1987, Rock and mineral properties. *Electromagnetic methods in Applied Geophysics*, **1**, ed. M. N. Nabighian, Series: *Investigations in Geophysics*, **3**, Soc. Expl. Geophys., Tulsa, Okla.

KEMENY, J. M., AND COOK, N. G. W., 1987, Crack models for the failure of rock under compression. *Proc. 2nd Int. Conf. Constitutive Laws for Engng. Materials* **2**, 879 – 887

KEMENY, J. M., 1991, A model for non-linear rock deformation under compression due to sub-critical crack growth. *Int. J. Rock Mech. Min. Sci. & Geomech. Abstr.* **28**, 459 - 467

KILBURN, C. R. J. AND VOIGHT, B., 1998, Slow rock fracture as eruption precursor at Soufriere Hills volcano, Montserrat. *Geophys. Res. Lett.* **25** (19), 3665 - 3668

KIRBY, S. H., 1984, Introduction and digest to the special issue on chemical effects of water on the deformation and strengths of rocks. *J. Geophys. Res.* **89** (B6), 3991 - 3995

KIRKPATRICK, S., 1971, Classical transport in disordered media; Scaling and effective medium theories. *Phys. Rev. Lett.* **27**, 1722

KLIGFIELD, R., HUNZIKER, J., DALLMEYER, R.D. AND SCHAMEL, S., 1986. *Jour. Struct. Geol.* **8,** 781-798.

KORVIN, G., 1992, *Fractal Models in the Earth Sciences,* Elsevier, New York.

LEARY, P. C., 1997, Rock as a critical-point system and the inherent implausibility of reliable earthquake prediction. *Geophys. Res. Int.* **131**, 451 - 466

LEBEDEV, E. B., RYZHENKO, B. N., DORFMAN, A. M., ZEBRIN, S. R., SOKOLOVA, N. T., BURKHARDT, H., MORIG, R. AND WULFF, A., 1996, Influence of fluids on the elastic properties of sandstone at high pressure and temperature. *Geophys. Res. Let.* **23** (22),3115 - 3118

LOCKNER, D. A. AND BYERLEE, J. D., 1985, Complex resistivity measurements of confined rock. *J. Geophys. Res.* **90** (B9), 7837 - 7847

LOCKNER, D. A. AND BYERLEE, J. D., 1986, Changes in complex resistivity during creep in granite. *Pageoph* **124** (4/5), 659 - 676

LOCKNER, D. A., BYERLEE, J. D., KUKSENKO, V., PONOMAREV, A. AND SIDORIN, A., 1991, Quasi-static fault growth and shear fracture energy in granite. *Nature* **350**, 39 – 42

LOCKNER, D. A., BYERLEE, J. D., KUKSENKO, V., PONOMAREV, A. AND SIDORIN, A., 1992, Observations of quasi-static growth from acoustic emissions. In: *Fault Mechanics and Transport Properties of Rocks*, Evans, B., & Wong, T-f., (eds), Academic Press, London

LOCKNER, D. A., 1993, The role of acoustic emission in the study of rock fracture. *Int J. Rock Mech. Min. Sci. & Geomech. Abstr.* **30** (7), 883 - 899

LOCKNER, D. A., 1995, Rock Failure. In *Rock physics and Phase Relations.* A handbook of physical constants. AGU reference shelf 3, 127 – 147, USA

LONG, L. T. AND RIVERS, W. K., 1975, Field measurement of the electroseismic response. *Geophysics* **40** (2), 233-245

LORNE, B., PERRIER, F. AND AVOUAC, J-P., 1999b, Streaming potential measurements 2. Relationship between electrical and hydraulic flow patterns from rock samples during deformation. *J. Geophys. Res.* **104** (B8), 17,879 – 17,896

MAIN, I. G., MEREDITH, P. G. AND JONES, C., 1989, A reinterpretation of the precursory seismic b-value anomaly from fracture mechanics. *Geophys. J.* **96**, 131 - 138

MAIN, I. G., MEREDITH, P. G., SAMMONDS, P. R. AND JONES, C., 1990, Influence of fractal flaw distributions on rock deformation in the brittle field. In *Deformation Mechanisms, Rheology and Tectonics*, R. J. Knipe and E. H. Rutter (eds), Geol. Soc. Lond., Special Publication **54**, 81 – 96

MAIN, I. G., 1991, A modified Griffith criterion for the evolution of damage with a fractal distribution of crack lengths: application to seismic events and b- values. *Geophys. J. Int* **107**, 353 - 362

MAIN, I. G., SAMMONDS, P. R., AND MEREDITH, P. G., 1993, Application of a modified Griffith criterion to the evolution of fractal damage during compressional rock failure. *Geophys. J. Int.* **115**, 367 - 380

MAIN, I., 1996, Statistical physics, seismogenesis and seismic hazard. *Rev. Geophys.* **34** (4), 433 – 462

MAIN, I., 1997, Long odds on prediction. *Nature* **385**, 19 - 20

MANDELBROT, B. B., 1983, *The Fractal Geometry of Nature.* New York, Freeman

MASUDA, K., NISHIZAWA, O., KUSUNOSE, K. AND SATOH, T., 1993, *Int. J. Rock. Mech. Min. Sci. & Geomech. Abstr.* **30** (1), 1 – 10

MATTISSON, C., KNACKSTEDT, M. A. AND SENDEN, T. J., 1997, Transport in fractured porous solids. *Geophys. Res. Lett.* **24** (5), 495 - 498

MAVROMATOU, C. AND HADJICONTIS, V., 1994, Highly mobile hole charge carriers in minerals: Key to the enigmatic electrical earthquake phenomena. *Electromagnetic Phenomena related to Earthquake Prediction.* Ed. Hayakawa, M. and Fujinawa, Y., Terra Scientific, Tokyo, 293 - 305

MAZZELLA, A. AND MORRISON, H. F., 1974, Electrical resistivity variations associated with earthquakes on the San Andreas Fault. *Science* **185** (4154), 855 – 857

MAZUR, P. AND OVERBEEK, J. TH. G., 1951, On electro-osmosis and streaming-potentials in diaphragms, II, General quantitative relationship between electro-kinetic effects. *Recl. Trav. Chim. Pays Bas* **70**, 83 – 91

MCLINTOCK, F. A. AND WALSH, J. B., 1962, Friction on Griffith cracks in rocks under pressure. In: *Proc. 4th U.S. Nat. Congr. Appl. Mech.*, **II**. New York: Am. Soc. Mech. Eng., 1015 - 1021

MEREDITH, P. G., MAIN, I. AND JONES, C. J., 1990, Temporal variations in seismicity during quasi-static and dynamic rock failure. *Tectonophys.* **175**, 249 - 268

MENENDEZ, B., W. ZHU. AND WONG, T.-F., 1996, Micromechanics of brittle faulting and cataclastic flow in Berea sandstone. *J. Struct. Geol.* **18**, 1 – 16

MERZER, A. M. AND KLEMPERER, S. L., 1992, *Geophys. J. Int.* **108**, 895 - 905

MICHAEL, A. J., 1997, Testing prediction methods: Earthquake clustering versus the Poisson model. *Geophys. Res. Lett.* **24** (15), 1891 – 1894

MIKHAILOV, O. V., HAARTSEN, M. W. AND TOKSOZ, M. N., 1996, Electroseismic investigations of the shallow subsurface: Field measurements and numerical modelling. *Geophys.* **62** (1), 97 – 105

MIZUTANI, H., ISHIDO, T., YOKOKURA, T. AND OHNISHI, S., 1976, Electrokinetic phenomena associated with earthquakes. Geophys. Res. Letts. 3 (7), 365 - 368

MOGI, K., 1968, Source locations of elastic shocks in the fracturing process in rocks. *Bull. Earthq. Res. Inst.* **46**, 1103 – 1125

MOGI, K., 1985, *Earthquake Prediction.* Academic, London, 243 pp

MORELAND, N. C. AND ROBERTS, G. P., 1999, Lateral propagation of the surface of the South Alkyonides normal fault segment, central Greece: its impact on models of fault growth and displacement-length relationships. *J. Struct. Geol.* **21**, 635 - 652

MORGAN, F. D., WILLIAMS, E. R. AND MADDEN T. R., 1989, Streaming potential properties of Westerly granite with applications. *J. Geophys. Res.* **94** (B9), 12,449 - 12,461

MORROW, C. AND BRACE, W. F., 1981, Electrical resistivity changes in tuffs due to stress. *J. Geophys. Res.* **86** (B4), 2929 - 2934

MUIR-WOOD, R. AND KING, G. C. P., 1993, Hydrological signatures of earthquake strain. *J. Geophys. Res.* **98** (B12), 22,035 - 22,068

MULGARIA, F. AND GASPERINI, P., 1992, Analysing the statistical validity of earthquake precursors, an application to the VAN method. *Geophys. J. Int.* **111**, 32 - 44

MURRELL, S. A. F., 1963, A criterion for brittle fracture of rocks and concrete under triaxial stress and the effect of pore pressure on the criterion. *J. Appl. Phys.* 15,

MURRELL, S. A. F., 1964, The theory of the propagation of elliptical Griffith cracks under various conditions of plane strain or plane stress. *Part I. Br. J. Appl. Phys.*, 1195 - 1210

MURRELL, S. A. F, 1965, The effect of triaxial stress systems on the strength of rocks at atmospheric temperatures. *Geophys. J. R. Astron. Soc.* **10**, 231 – 281

MURRELL, S. A. F. AND DIGBY, P. J., 1970, The theory of brittle fracture Initiation under triaxial stress conditions. *I. Geophys. J. R. Astron. Soc.* **19**, 309 - 334

MURRELL, S. A. F. AND ISMAIL, I. A. H., 1976, The effect of decomposition of hydrous minerals on the mechanical properties of rocks at high pressures and temperatures. *Tectonophysics* **31**, 207 - 258

NESBITT, B. E., 1993, Electrical resistivities of crustal fluids. *J. Geophys. Res.* **98** (B3), 4301 – 4310

NEEV, J. AND YEATTS, F. R., 1989, Electrokinetic effects in fluid-saturated poroelastic media. *Phys. Rev. B* **40** (13), 9135 – 9141

NISHIZAWA, O., ONAI, K., AND KUSUNOSE, K., 1985, Hypocenter distribution and focal mechanism of AE events during two stress stage creep in Yugawara andesite. *PAEGEOPH* **122**, 36 - 52

NOUBEHECHT, B., 1963, Irreversible thermodynamics in homogeneous media and its application to certain geoelectric problems, *Ph.D. Thesis*, Mass. Inst. Of Tech., Cambridge

NUR, A. AND BYERLEE, J. D., 1971, An exact effective stress law for elastic deformation of rock with fluids. *J. Geophys. Res.* **76**, 6414 - 6419

NUR, A., 1971, Effects of stress on velocity anisotropy in rock with cracks. *J. Geophys. Res.* **76**, 8, 2022

NUR, A., 1972, Dilatancy, pore fluids, and premonitory variations of ts/tp travel times. *Bull. Seis. Soc. Am.* **62**, 1217 - 1222

NUR , A. AND BOOKER, J. R., 1972, Aftershocks caused by pore fluid? *Science* **10**, 885 – 887

NUR, A. AND WALDER, J., 1990, Time dependent hydraulics of the earth's crust. In: *The Role of Fluids in Crustal Processes*. National Research Council. 113 - 140

ODEDRA, A., 1998, Laboratory studies on shear fracture of granite under simulated crustal conditions. *PhD Thesis*, University of London

O'KONSKI, C. T., 1960, Electric properties of macromolecules. Theory of ionic polarisation in polyelectrolytes. *J. Chem. Phys.* **64**, 605 – 619

OGAWA, T., OIKE, K. AND MIURA, T., 1985, Electromagnetic radiation's from rocks. *J. Geophys. Res.* **90** (D4), 6245 - 6249

OHNAKA, M. AND MOGI, K., 1982, Frequency characteristics of acoustic emission in rocks under uniaxial compression and its relation to the fracturing process to failure. *J. Geophys. Res.* **87** (B5), 3873 - 3884

OHNAKA, M., 1992, Earthquake source nucleation: A physical model for short-term precursors. *Tectonophysics* **211**, 149 – 178

OHSHIMA, H., MAKINO, K. AND KONDO, T., 1987, Electrostatic interaction of two parallel plates with surface charge layers. *J. Colloid. Interface. Sci.* **116** (1), 196 - 199

OLHOEFT, G. R., 1981, Electrical properties of granite with implications for the lower crust. *J. Geophys. Res.* **86** (B2), 931 – 936

OLSSON, W. A., 1992, The effect of slip on the flow of fluid through a fracture. *Geophys. Res. Lett.* **19**, 541 – 543

OLSSON, W. A. AND BROWN, S. R., 1993, Hydromechanical response of a fracture undergoing compression and shear. *Int. J. Rock Mech. Min. Sci. Geomech. Abstr.* **30**, 845 - 851

OVERBEEK, J. TH. G., 1952, Electrochemistry of the double layer, in *Colloid Science*, **1**, *Irreversible Systems*, (eds) H. R. Kruyt, Elsevier, New York, 115 - 193

PALACKY, G. J., 1987, Resistivity characteristics of geologic targets. *Electromagnetic methods in Applied Geophysics*, **1**, ed. M. N. Nabighian, Series: *Investigations in Geophysics*, **3**, Soc. Expl. Geophys., Tulsa, Okla.

PARK, S. K., 1996, Precursors to earthquakes: Seismoelectromagnetic signals. *Surv. Geophys.* **17** (4), 493 - 516

PARSONS, B. AND MCKENZIE, D. P., 1978, Mantle convection and the thermal structure of the plates. J. *Geophys. Res.* **83**, 4485 - 4496

PATERSON, M. S., 1970, A high-pressure, high-temperature apparatus for rock deformation. *Int. J. Rock. Mech. Min. Sci.* **7**, 517 - 526

PATERSON, M. S., 1978, Experimental Rock Deformation: The Brittle Field, Springer – Verlag, 254 pp

PERRIER, F., TRIQUE, M., LORNE, B. AND AVOUAC, JP., 1998, Electric potential variations associated with yearly lake level variations. *Geophys. Res. Lett.* **25**, (11), 1955 - 1958

PIKE, G. E. AND SEAGER, C. H., 1974, Percolation and conductivity. *Phys. Rev B* **10** (4), 1421 - 1434

PLATT, J. P., SOTO, J., -I, WHITEHOUSE, M. J., HURFORD, A. J. AND KELLEY, S. P., 1998, thermal evolution, rate of exhumation, and tectonic significance of metamorphic rocks from the floor of the Alboran extensional basin, western Mediterranean. *Tectonics*, **17** (5), 671 – 689

PRICE, N. J., 1975, Rates of Deformation. *J. Geol. Soc.* **131**, 553 – 575

PRICE, N. J. AND COSGROVE, J. W., 1990, Analysis of Geological Structures. Cambridge University Press. 502 pp

PRIDE, S. AND MORGAN, F. D., 1991, Electrokinetic dissipation induced by seismic waves. *Geophys.* **56**, 914 - 925

PRIDE, S., 1994, Governing equations for the coupled electromagnetics and acoustics of porous media. *Phys. Rev. B* **50** (21), 15,678 – 15,697

RANALLI, G., 1995, *Rheology of the Earth.* Chapman and Hall, 413pp, UK

READ, M. D., AYLING, M. R., MEREDITH, P. G. AND MURRELL, S. A. F., 1995, Microcracking during triaxial deformation of porous rocks monitored by changes in rock physical properties, II. Pore volumometry and acoustic emission measurements on water saturated rocks. *Tectonophys.* **245**, 223 - 235

REID, H. F., 1910, The mechanics of the earthquake, *in The California earthquake of April 18, 1906.* Rept. State. Earthquake Invest. Com., Carnegie Inst., Washington D.C.

RENSHAW, C. E. AND SCHULSON, E. M., 1998, Non-linear rate dependent deformation under compression due to state variable friction. *Geophys. Res. Lett.* **25** (12), 2205 - 2208

RESTON, T. J., 1987, Spatial interference, reflection character and the structure of the lower crust under extension. Results from 2D seismic modelling. *Ann Geophys* **5B**, 339 – 348

REVIL, A , DAROT, M. AND PEZARD, P. A., 1996, From surface electrical properties to spontaneous potentials in porous media. *Surv. Geophys* **17**, 331 – 346

REVIL, A , DAROT, M. AND PEZARD, P. A., 1996, Influence of the electrical diffuse layer and microgeometry on the effective ionic diffusion coefficient in porous media. *Geophys. Res. Lett.* **23**, 1989 – 1992

REVIL, A. AND GLOVER, P. W. J., 1997, Theory of ionic-surface electrical conduction in porous media. *Phys. Rev. B* **55** (3), 1757 – 1773

REVIL, A. AND GLOVER, P. W. J., 1998, Nature of surface electrical conductivity in natural sands, sandstones and clays. *Geophys. Res. Lett.* ***25*** (5), 691 - 694

REVIL, A., 1999a, Pervasive pressure-solution transfer: a poro-visco-plastic model. *Geophys. Res. Lett.* **26** (2), 255 – 258

REVIL, A., SCHWAEGER, H.; CATHLES, L. M., III AND MANHARDT, P. D., 1999b , Streaming potential in porous media, 2, Theory and application to geothermal systems. *J. Geophys. Res.* 104 (B9), 20,033

RIKITAKE, T. AND YAMAZAKI, Y., 1979, A resistivity precursor of the 1974 Izu-Hanto-Oki earthquake. *J. Phys. Earth* **27**, 1 - 6

RIST, M. A., SAMMONDS, P. R. AND MURRELL, S. A. F., 1991, Strain rate control during deformation of ice: An assessment of the performance of a new servo-controlled triaxial testing system. *Cold Regions Science and Technology* **19**, 189 - 200

ROBERTS, J. J., DUBA, A. G., MATHEZ, E. A., SHANKLAND, T. J. AND KINZLER, R., 1999, Carbon enhanced electrical conductivity during fracture of rocks. *J. Geophys. Res.* **104** (B1), 737 – 747

ROEDDER, E., 1984, Fluid inclusions, *Rev. Mineral* **12**, 664 pp.

RUFFET, C., GUEGUEN, Y. AND DAROT, M., 1985, Complex conductivity measurements and fractal nature of porosity. *Geophys.* **56** (6), 758 - 768

RUFFET, C., GUEGUEN, Y. AND DAROT, M., 1991, Rock conductivity and fractal nature of porosity. *Terra Nova* **3**, 265 - 275

RUFFET, C., DAROT, M. AND GUEGUEN, Y., 1995, Surface conductivity in rocks: A review. *Surv. Geophys.* **16**, 83 – 105

RUSSELL, R. D., BUTLER, K. E., KEPIC, A. W. AND MAXWELL, M., 1997, Seismoelectric exploration. *The Leading Edge, SEG*, **16** 1611 - 1615

RUTTER, E.H., 1995, Experimental study of the influence of stress, temperature and strain on the dynamic recrystallization of Carrara marble. *J. Geophys. Res.* **100**, 24651-24663.

SAMMIS, C. G., OSBORNE, R. H., ANDERSON, J. L., BANERDT, M. AND WHITE P., 1986, Self-similar cataclasis in the formation of fault gauge. *Pageoph, 124,* 53-78

SAMMONDS, P. R., AYLING, M. R., MEREDITH, P. G., MURRELL, S. A. F., AND JONES, C., 1989, A laboratory investigation of acoustic emissions and elastic wave velocity changes during rock failure under triaxial stresses. In *Rock at Great Depth – Rock Mechanics and Rock Physics at Great Depth*, Maury and Fourmaintraux (eds), Balkema, Rotterdam, **1**, 233 - 240

SAMMONDS P. R., MEREDITH P. G. AND MAIN I. G., 1992, Role of pore fluids in the generation of seismic precursors to shear fracture. *Nature* **359**, 228 – 230

SAMMONDS, P. R., MEREDITH, P. G. AND MURRELL, S. A. F., 1994, Modelling the damage evolution in rock containing pore fluid by acoustic emission. In *Eurock '94, Proc. SPE/ISRM* International Conference, Balkema, Rotterdam, Society of Petroleum Engineers (1994).

SAMMONDS, P. R. AND OHNAKA, M., 1998, Evolution of microseismicity during frictional sliding. *Geophys. Res. Lett.* **25** (5), 699 - 702

SASAOKA, H., YAMANAKA, C. AND IKEYA, M., 1998, *Geophys. Res. Lett.* **25** (12), 2225 - 2228

SAVAGE, J. C. AND PRESCOTT, W. H., 1979, Geodometer measurements of strain during the southern Californian uplift. *J. Geophys. Res.* **84**, 156 – 164

SCHEIDEGGER, A. E., 1974, The physics of flow through porous media, 353 pp., Univ. of Toronto Press, Toronto, Ont., Canada

SCHLISCHE, R. W., YOUNG, S. S., ACKERMANN, R. V. AND GUPTA. A., 1996, Geometry and scaling relations of a population of very small rift-related normal faults. *Geology* **24** (8), 683 – 686

SCHOLZ, C. H., 1968, The frequency-magnitude relation of microfracturing in rock and its relation to earthquakes. *Bull. Seismol. Soc. Am.* **58**, 399 – 415

SCHOLZ, C. H., 1968b, Microfracturing and the anelastic deformation of rock in compression. *J. Geophys. Res.* **73**, 1417

SCHOLZ, C. H., SYKES, L. AND AGGARWAL, Y., 1973, Earthquake prediction. *Science* **181**, 803 – 810

SCHOLZ, C. H., 1991, Earthquakes and faulting. Self-organised critical phenomena with a characteristic dimension. In *Spontaneous Formation of Space-Time Structures and Criticality,* eds. T. Riste and D. Sherington, Klawer Academic Publishers, Netherlands, 11-66

SCHOLZ, C. H., DAWERS, N. H., ANDERS, M. H., AND COWIE, P. A., 1993, Fault growth and fault scaling laws: preliminary results. *J. Geophys. Res.* **98** (B12), 21,951 – 21,961

SCHOLZ, C. H., 1996, *The Mechanics of Earthquakes and Faulting.* Cambridge University Press. 439 pp, UK

SCHMIDT, E., 1988, Wideband acoustic response of fluid-saturated porous rocks: Theory and preliminary results using waveguided samples. *J. Acoust. Soc. Am.* **83** (6), 2027 – 2042

SCHULSON, E. M., ILIESCU, D. AND RENSHAW, C. E., 1999, On the initiation of shear faults during brittle compressive failure: A new mechanism. *J. Geophys. Res.* **104** (B1), 695 - 705

SCLATER, J. G., JAUPART, C. AND GALSON, D., 1980, The heat flow through oceanic and continental crust and the heat loss of the earth. *Rev. Geophys. Space. Phys.* **19**, 394 - 406

SHANKLAND, T. J., DUBA. A. G., MATHEZ, E. A. AND PEACH, C. L., 1996, Increase of electrical conductivity with pressure as an indicator of conduction through a solid phase in mid-crustal rocks. *J. Geophys. Res.* **102** (B7), 14741

SHAW, H. R. AND GARTNER, A. E., 1986, On the graphical interpretation of palaeoseismic data. *United States Geological Survey Open File Report*, 86 - 394

SHAW, B. E., CARLSON, J. M., AND LANGER, J. S., 1992, Patterns of activity preceding large earthquakes. *J. Geophys. Res.* **97**, 479 - 488

SKAND, S. AND ZYDNEY, A. L., 1995, Pore size distribution on electrokinetic phenomena in semipermeable membranes. *J. Mem. Sci.* **105**, 203 - 215

SIBSON, R. H., 1980, Power dissipation and stress levels on faults in the upper crust. *J. Geophy. Res.* **85**, 6239 – 6247

SILL, W. R., 1983, Self-potential modelling from primary flows. *Geophys.* **48** (1), 76 – 86

SLEEP, N. H. AND BLANPIED, M. L., 1992, Creep, compaction and the weak rheology of major faults. *Nature* **359**, 687 - 692

SMITH, I. M. AND GRIFFITHS, D. V., 1998, Programming the finite element method. *John Wiley & Sons, Chichester, UK.* 534pp

SMITS, L. J. M., 1968, SP log interpretation in shaly sands. *Soc. Pet. Eng. J. Trans.* AIME **243**, 123 – 136

SPYROPOULOS, C., GRIFFITH, W. J., SCHOLZ, C. H. AND SHAW, B .E., 1999, Experimental evidence for different strain regimes of crack populations in a clay model. *Geophy. Res. Lett.* **26** (8), 1081 - 1084

STEPHENSON, L. P., PLUMLEY, W. J. AND PALCIAUSKAS, V. V., 1992, A model for sandstone compaction by grain interpenetration. *J. Sedim. Petr.* **62**, 11 – 22

STESKY, R. M., 1986, Electrical conductivity of brine-saturated fractured rock. *Geophys.* **51** (8), 1585 - 1593

SUNDARAM, P. N. AND FRINK, D., 1983, Electrical analogy of hydraulic flow through rock fractures. *Geotech. Test. J.* **6** (1) 3 – 9

SYKES, L. R., SHAW, B. E. AND SCHOLZ, C. H., 1999, Rethinking earthquake prediction. *PAGEOPH.* **155** (2-4), 207 - 232

TATE, J. AND DAILY, W., 1989, Evidence of electro-seismic phenomena. *Phys. Earth Planet. Inter.* **57**, 1 - 10

TERZAGHI, K., 1936, The shear resistance of saturated soils. *Proc. 1st Int. Conf. Soil Mech., Cambridge, Mass.* **1**, 54 – 56

TEUFEL, L. W., 1987, Permeability changes during shear deformation of fractured rock. *28th US Symp. Rock Mech., Tuscon*, US, 29 June, 473 - 480

THOMPSON, A. H., 1986. *Phys. Rev.* **B34**, 8179

THOMPSON, A. H. AND GIST, G. A., 1993, Geophysical applications of electrokinetic conversion. *The Leading Edge, SEG*, **12**, 1169 - 1173

THOMPSON, M. E. AND BROWN, S. R., 1991, The effect of anisotropic surface roughness on flow and transport in fractures. *J. Geophys. Res.* **89**, 9425 - 9431

TRIMMER, D., BONNER, B., HEARD, H. C. AND DUBA, A., 1980, Effect of pressure and stress on water transport in intact and fractured gabbro and granite. *J. Geophys. Res.* **85** (B12), 7059 – 7071

TSANG, Y. W., 1984, The effect of tortuosity on fluid flow through a single fracture. *J. Geophys. Res.* **20** (9), 1209 - 1215

TSANG, Y. W. AND WITHERSPOON, P. A., 1981, Hydromechanical behaviour of a deformable rock fracture subject to normal stress. *J. Geophys. Res.* **86**, 9287 – 9298

TSANG, Y. W. AND WITHERSPOON, P. A., 1983, The dependence of fracture mechanical and fluid flow properties on fracture roughness and sample size. *J. Geophys. Res.* **88**, 2359 - 2366

TUMAN, V.S., 1963, Streaming potentials at very high differential pressures. *J. App. Phys.* **34** (7)

TULLIS, T. E. AND TULLIS, J., 1986, Experimental rock deformation techniques. In: *Mineral and Rock Deformation: Laboratory Studies, geophys. Monogr. Am. Geophys. Un., Washington D.C.*, 297 – 324

TURCOTTE, D. L., 1991, Earthquake prediction. *Ann. Rev. Earth planet Sci.* **19**, 263 - 281

TURCOTTE, D. L., 1992, *Fractals and Chaos in Geology and Geophysics,* Cambridge University Press, Cambridge

VALLIANATOS, F. AND TZANIS, A., 1999, On possible scaling laws between electric earthquake precursors (EEP) and earthquake magnitude. *Geophys. Res. Lett.* **26** (13), 2013

VAROTSOS, P. AND ALEXOPOULOS, K., 1984a, Physical properties of the variations of the electric field of the earth preceding earthquakes, I. *Tectonophys.* **110**, 73 – 98

VAROTSOS, P. AND ALEXOPOULOS, K., 1984b, Physical properties of the variations of the electric field of the earth preceding earthquakes, II. *Tectonophys.* **110**, 99 – 125

VAROTSOS, P. AND ALEXOPOULOS, K., 1991, *Tectonophys.* **188**, 322 – 347

VAROTSOS, P., ALEXOPOULOS, K. AND LAZARIDOU, M., 1993, *Tectonophys.* **224**, 1 – 37

WAITE, M. E., GE, S., SPETZLER, H AND BAHR, D. B., 1998, The effect of surface geometry on fracture permeability: A case study using a sinusoidal fracture. *Geophys. Res. Lett.* **25** (6), 813 - 816

WALSH, J. B. AND BRACE, W. F., 1984, The effect of pressure on porosity and the transport properties of rock. *J. Geophys. Res.* **89**, 9425 – 9431

WALSH, J. B., 1965, The effect of cracks on uniaxial elastic compression. *J. Geophys. Res.* **70**, 381-389

WARWICK, J. W., STOKER, C. AND MEYER, T. R., 1982, Radio emission associated with rock fracture: Possible application to the great Chilean earthquake of May 22, 1960. *J. Geophys. Res.* **87**, 2851 – 2859

WONG, T –F., FREDRICH, J. T. AND GWANMESIA, G. D., 1989, Crack aperture and pore space fractal geometry of Westerly granite and Rutland quarzite: implications for an elastic contact model of rock compressibility. *J. Geophys. Res.* **94**, 10267 - 10278

WONG, T-F., 1990, A note on the propagation behaviour of a crack nucleated by a dislocation pileup. *J. Geophys. Res.* **95** (B6), 8939 - 8646

WONG, P., KOPLIK, J. AND TOMANIC, J. P., 1984, Conductivity and permeability of rocks. *Phys. Rev. B* **30** (11), 6606 – 6614

WORTHINGTON, A. E., HEDGES, J. H. AND PALLAT, N., 1990, SCA guidelines for sample preparation and porosity measurements of electrical resistivity samples, part I. *The Log Analyst* **31**, 20 – 28

SAMS, M. S., WORTHINGTON, M. H., KING, M. S. AND SHAMS KHANSHIR, M., 1993, A comparison of laboratory and field measurements of p-wave anisotropy. *Geophys. Prospect.* **41**, 189 – 206

WURMSTICH, B. AND MORGAN, F. D., 1994, Modelling of streaming potential responses caused by oil well pumping. *Geophys.* **59** (1), 46 - 56

WYBLE, D. O. 1958, Effect of applied pressure on the conductivity, porosity and permeability of sandstones. *Pet. Trans. AIME.* **2022**, 430 – 432, T. N

YAMADA, I., MASUDA, K. AND MIZUTANI, H., 1989, *Phys. Earth Planet. Int.* **57**, 157 – 168

YOSHIDA, S., MANJGALADZE, P., ZILPIMIANI, D., OHNAKA, M. AND NAKATANI, M., 1994, Electromagnetic emissions associated with frictional sliding of rock. In: *Electromagnetic Phenomena Related to Earthquake Prediction*, (eds) Hayakawa, M. and Fujinawa, Y., 307 – 322, Terrapub, Tokyo

YOSHIDA, S., UYESHIMA, M. AND NAKATANI, M., 1997, Electric potential changes associated with slip failure of granite: Preseismic and coseismic signals. *J. Geophys. Res.* **102** (B7), 14883 - 14897

YOSHIDA, S., CLINT, O. C. AND SAMMONDS, P. R., 1998, Electric potential changes prior to shear fracture in dry and saturated rocks. *Geophys. Res. Lett.* **25**, (10), 1577 – 1580

YOSHIOKA, N. AND SCHOLZ, C. H., 1989, Elastic properties of contacting surfaces under normal and shear loads, 2. Comparison of theory with experiment. *J. Geophys. Res.* **94** (B12), 17,691 – 17, 700

ZATSEPIN, S. V. AND CRAMPIN, S., 1997, Modelling the compliance of crustal rocks - I. Response of shear wave splitting to differential stress. *Geophys. J. Int.* **129**, 477 – 494

ZETA-METER INCORPORATED. 765 Middlebrook Avenue, PO Box 3008, Staunton, VA 24402, USA

ZHANG, J., WONG, T-F. AND DAVIS, D., 1990, Micromechanics of pressure-induced grain crushing in porous rocks. *J. Geophys. Res.* 95 (**B1**), 341 - 352

ZHANG, X. AND KNACKSTEDT, M. A., 1995, Direct simulation of electrical and hydraulic tortuosity in porous solids. *Geophys. Res. Lett.* **22** (17), 2333 - 2336

ZHU, W. AND WONG, T. -F., 1996, Permeability reduction in a dilating rock: Network modelling of damage and tortuosity. *Geophys. Res. Lett.* **23** (22), 3099 – 3102

ZHU, W. AND WONG, T. -F., 1996, The transition from brittle faulting to cataclastic flow: Permeability evolution. J. *Geophys. Res.*

ZOBACK, M. D. AND BYERLEE, J. D., 1975, The effect of microcrack dilatancy on the permeability of westerly granite. *J. Geophys. Res.* **80** (5), 752 - 755

ZOBACK, M. L. et al., 1989, Global patterns of tectonic stress. *Nature* **341**, 291 - 298

Appendix A - Mobility and Electrical Time Constant

Ionic Mobility

The mobility μ_m of a particular ionic species is equal to

$$\mu_m = \frac{q\lambda}{2mv} \tag{A-1}$$

where q is charge carrier charge, λ is average length of the free path of electrons, m is electron mass, v is the average speed of the thermal speed of electron in conductor and

Electrical Time Constant

Electrical signals decay according to the electrical time constant (11-5), which is inversely proportional to conductivity of the bulk medium and is the time required to attain electrical equilibrium in a medium

$$\tau_0 = \frac{\varepsilon_0 \varepsilon}{\sigma_b} \tag{A-2}$$

Appendix B – Computer Programs

All programs are written in C and compiled using a MS-DOS C Compiler.

B1 b-value Calculation

```
/*****************************************************************/
/*                                                               */
/*    Program which calculates b-value using AKI's weighting method*/
/*    Written by Oswald Clint September 1997                     */
/*                                                               */
/*****************************************************************/


#include<stdio.h>
#include<conio.h>
#include<math.h>


int main(void)                                  /* Main program */
{
            float amp[100];
            int rock, check, channel,q;
            int i, j, low_amp=0, high_amp=0, b_amp=0;
            int amp_temp=0, cum_hits=0, hits=0, no=1, hitint;
            float wgtime,time, para, amplitude, duration;
            float tot_amp=0.0, tot_dur=0.0, tot_time=0.0,
            calc_time=0.0;
            float U=0, levents, tamp, average, b_value=0.0,
            temp_time=0.0;
            char locan_file[50], b_file[50];
            FILE *fp, *fpp;


            for(q=0;q<8;q++)
            {


                  clrscr();
                        printf("Enter Locan ASCII Filename : ");
                        scanf("%s",locan_file);

                        fp = fopen(locan_file,"r+");

                  fp = fopen("c:\feb07new.asc","r+");


                        no=0;
                  if((fp = fopen(locan_file,"r+"))  == NULL)
                        {
                        printf("\nFile does not exist\n");
                        no=1;
                        }
```

```
        printf("\nEnter Output Filename : ");
        scanf("%s",b_file);
        fpp = fopen(b_file,"w+");


        printf("Enter Lower Amplitude Limit : ");
        scanf("%d",&low_amp);

        printf("Enter Higher Amplitude Limit : ");
        scanf("%d",&high_amp);

        printf("Enter Amplitude Limit for b-values : ");
        scanf("%d",&b_amp);



        channel = q+1;


              no=1;
        while(no==1)
              {
              printf("\nBasalt (1) or Sandstone (2) : ");
              scanf("%d",&rock);

              if(rock < 1 || rock > 2)
                    {
                    printf("\nEnter b or s please\n");
                    no=1;
                    }
              else
                    {
                    no=0;
                    }

              }

              switch(rock)
                    {                        /*dry basalt 100*/
                    case 1:                     hitint = 200;
                                             break;
                    case 2:                     hitint = 400;
                                             break;
                    default:                 exit(1);
                    }



        check = 1;
        for(j=0;j<100;j++)amp[j]=0;

        while(!feof(fp))
              {
              clrscr();
              printf("\n\nCalculating AE statistics");


fscanf(fp,"%f%f%f%f",&time,&para,&duration,&amplitude);

              if(check==1)
                    {
```

```
                        temp_time = time;
                        check=0;
                        }


            if(amplitude > low_amp && amplitude < high_amp && para ==
            channel)
                        {
                        tot_amp = tot_amp + amplitude;
                        tot_dur = tot_dur + duration;
                        tot_time = tot_time + time;
                        amp_temp = amplitude;
                        amp[amp_temp] = amp[amp_temp] + 1;
                        cum_hits+=1;
                        hits+=1;
                        calc_time = time - temp_time;
                                    /*basalt = 29.5-30.5*/
                                    /*sandstone = 49.5-50.5*/
            if(calc_time > 49.5 && calc_time < 50.5 || hits == hitint)
                              {
                              average = 0, levents = 0, tamp = 0;

                              for(i=b_amp;i<high_amp;i++)
                                    {
                                    levents = levents + amp[i];
                                    tamp = (amp[i] * (i+0.5)) + tamp;
                                    }
                              average = tamp/levents;
                              b_value = 8.6859 / (average - b_amp);

                              if(cum_hits<0)cum_hits*=-1;
fprintf(fpp,"%7.3f\t%7.3f\t%d\t%7.3f\t%7.3f\t%7.3f\n",tot_time/hits,
      hits/(time - U), cum_hits, tot_amp/hits, tot_dur/hits, b_value);
□

□
                              U = time, tot_amp=0, tot_dur=0;
□
                              tot_time=0; hits=0, amp_temp=0;
                              channel=0;

                              for(j=0;j<100;j++)amp[j]=0;

                              check=1;

                              }
                        }

            }

            }
            close(fp), close(fpp);
            return 0;
}
```

B2 AE Event Rate Calculation

```
/*****************************************************************/
□
/*                                                               */
/*    Program which calculates AE event rate                     */
/*    Written by Oswald Clint September 1998                     */
/*                                                               */
/*****************************************************************/

#include<stdio.h>
□
#include<stdlib.h>
□
#include<dos.h>
#include<conio.h>


void main(void)                                  /* Main program */
{
            int no=1,i,j;
            char asc_file[50], par_file[50], res_file[50];
            FILE *fp, *fpp, *fppp;

            unsigned long int nAE[2000];

            float time=0.0,load=0.0;
            float btime=0.0;

            int it;
            int dt=1;

            int duration, amplitude, energy, channel;
            unsigned long int lost=0, asc_cum, sum=0;

            int getout, count=0;


            for(i=0;i<2000;i++)
            {
                  nAE[i]=0;
            }

            while(no==1)
                  {
                  clrscr();
                  printf("Enter Locan ASCII Filename : ");
                  scanf("%s",asc_file);

                  fp = fopen(asc_file,"r+");
                  no=0;
                  if((fp = fopen(asc_file,"r+"))  == NULL)
                        {
                        printf("File does not exist\n");
                        no=1;
                        }
                   }
            no=1;
            while(no==1)
                  {
                  printf("Enter Lost Hits File Filename : ");
```

```
            scanf("%s",par_file);

            fpp = fopen(par_file,"r+");
            no=0;
            if((fpp = fopen(par_file,"r+"))  == NULL)
                  {
                  printf("File does not exist\n");
                  no=1;
                  }
             }

      printf("Enter Results Filename ");
      scanf("%s",res_file);
      fppp = fopen(res_file,"w+");



      clrscr();
      printf("\t\n\n\n\t\t\tWorking.....");




      while(!feof(fp))
      {
fscanf(fp,"%f%ld%d%d%d%d",&btime,&asc_cum,&channel,&duration,
                              &energy,&amplitude);
      printf("%f\n",btime);

      it = btime/dt;
      nAE[it]++;

      }

      it=0;
      while(!feof(fpp))
            {
            fscanf(fpp,"%f%ld",&time,&lost);



            it = time/dt;
            nAE[it] = nAE[it] + lost;

      }


      for(i=0;i<2000;i++)
      {
      for(j=i;j<i+60;j++)
      {
       sum = sum + nAE[j];

       }
            fprintf(fppp,"%ld\n",sum/60);

            sum=0;

      }
      close(fp), close(fpp), close(fppp);
}
```

B3 Mean Crack Length Calculation

```
/*********************************************************************/
/*                                                                   */
/*    Program which calculates Mean Crack Length                     */
/*    Written by Oswald Clint September 1998                         */
/*                                                                   */
/*********************************************************************/

#include<stdio.h>
#include<stdlib.h>
#include<dos.h>
#include<conio.h>
#include<math.h>

// Program to calculate mean crack density

void main(void)                                    /* Main program */
{

            int q, no=1;

            long time, bval, nt, frac_dim, pwr, ck_len1, mean_ck_len;
            long ck_len2, pwr2, pwr3, pwr4, pwr5, pwr6, pwr7;

            float time_lab, load, disp;

            long stress1, stress2, youngs, bsquared, mean_energy;
            long strain;
            long vol, cubed;

            long d1,d2,d3,d4,d5,d6, crack_den;

            char lab_file[50], loc_file[50], res_file[50];

            FILE *flab, *floc, *fres;


            while(no==1)
                  {
                  clrscr();
                  printf("Enter Labview Filename (*spd.asc): ");
                  scanf("%s",lab_file);

                  flab = fopen(lab_file,"r+");
                  no=0;
                  if((flab = fopen(lab_file,"r+"))  == NULL)
                        {
                        printf("File does not exist\n");
                        no=1;
                        }
                   }

            no=1;
            while(no==1)
                  {

                  printf("Enter B-Value Filename (*b.txt): ");
                  scanf("%s",loc_file);
```

```
            floc = fopen(loc_file,"r+");
            no=0;
            if((floc = fopen(loc_file,"r+"))  == NULL)
                  {
                  printf("File does not exist\n");
                  no=1;
                  }
             }

      printf("Enter Output Filename (*sts.asc): ");
      scanf("%s",res_file);
      fres = fopen(res_file,"w+");



      while(!feof(floc))
      {
      fscanf(floc,"%f%f%f",&time,&nt,&bval);
      printf("%f\t%f\t%f\n",time,nt,bval);
      clrscr();
      printf("\n\n\n\n\n\n\n\t\t\t\tWorking......");

      frac_dim = bval;

      pwr = 1/(frac_dim+1);

      pwr2 = 1-frac_dim;

      pwr3 = frac_dim/(frac_dim - 1);

      pwr4 = pwr2/(frac_dim+1);

      ck_len1 = (1 - (frac_dim*nt));

      pwr5 = pow(ck_len1,pwr4);

      ck_len2 = (1 - frac_dim*nt);

      pwr6 = (-1) * (frac_dim/(frac_dim+1));

      pwr7 = pow(ck_len2,pwr6);

      mean_ck_len = 0.000112 * pwr3 * (pwr5/pwr7);

      cubed = pow(mean_ck_len,3);

      vol = 3.14159265 * 0.04 * 0.04 * 0.1;

      crack_den = (nt * cubed) / vol;

      while(!feof(flab))
            {

fscanf(flab,"%f%f%f%f%f%f%f%f%f",&d6,&d5,&d1,&d2,&d3,&d4,&disp,&
                              load,&time_lab);


            if(time_lab < time + 0.5 && time_lab > time - 0.5)
```

```
                    {
                    stress1 = load * -119.7;
                    stress2 = stress1 * pow10(6);

                    strain = disp * -1;

                    youngs = stress2 / strain;

                    bsquared = 3.14159265 / youngs;

          mean_energy = bsquared * stress2 * stress2 * mean_ck_len;
                    }
              };
          rewind(flab);

          fprintf(fres,"%lf\t%f\t%f\t%lf\t%f\t%f\n",stress2,time,
                    mean_ck_len,mean_energy,crack_den,frac_dim);

          frac_dim=0,pwr=0,ck_len1=0,ck_len2=0,mean_ck_len=0;
          cubed=0,crack_den=0;
          pwr2=0, pwr3=0, pwr4=0, pwr5=0, pwr6=0, pwr7=0;


          };


          close(floc), close(flab), close(fres);


}
```

Appendix C

List of Triaxial Experiments Performed with Experimental Conditions and Data Plots

Conditions		1	2	3	4	5	6
Date (dd/mm/yy)		21/11/96	27/11/96	13/12/96	19/12/96	13/01/97	17/01/97
Rock Type		Darley Dale	Darley Dale	Darley Dale	Darley Dale	Darley Dale	Darley Dale
Confining Pressure (MPa)		40	20	25-20	40	40	40
Pore Pressure (MPa)		20	0	10	20	20	20
Strain Rate (s^{-1})		1.5×10^{-5}	1.5×10^{-5}	0.03	0.03	1.5×10^{-5}	1.5×10^{-5}
Mass (unsaturated) (g)		281.56	282.78	280.56	282.49	282.36	281.97
Mass (saturated) (g)		298.45	296.78	294.2	295.82	299.23	302.88
Locan Threshold (decibels)		45	45	47	43	48(1-7), 43(8)	43
Data Plot							Figure 4-13
							Figure 5-4b

7	**8**	**9**	**10**	**11**	**12**	**13**	**14**
15/01/97	20/01/97	24/01/97	02/04/97	02/07/97	19/2/97	20/2/97	28/2/97
Darley Dale	Icelandic	Icelandic	Icelandic	Darley Dale	Darley Dale	Darley Dale	Icelandic
40	30	10	30	20	20	20	30
20	20	0	20	0	0	0	20
0.03	1.5×10^{-5}	1.5×10^{-5}	1.5×10^{-5}	1.5×10^{-5}	1.5×10^{-5}	1.5×10^{-5}	1.5×10^{-5}
281.48	369.705	370.72	368.82	280.37	278.77	277.56	368.45
301.56	373.52	375.48	372.64	295.78	296.56	299.12	372.62
45	43(1-7), 54(8)	42	40 (No ch8)	50	52	55	40
Figure 5-1a	Figure 5-1b	Figure 5-4c		Figure 5-4a	Figure 10-5		
Figure 5-3	Figure 5-4d			Figure 6-5			

15	**16**	**17**	**18**	**19**	**20**	**21**	**22**
03/04/97	*18/6/1997*	*30/06/97*	*07/10/97*	21/07/97	30/07/97	01/10/97	08/10/97
Darley Dale	Icelandic	Darley Dale	Bentheim	Bentheim	Icelandic	Bentheim	Darley Dale
40	30	40	40	40	30	40	40
20	20	20			20	20	20
1.5×10^{-5}	1.5×10^{-5}	1.5×10^{-5}	1.5×10^{-5}	1.5×10^{-5}	1.5×10^{-5}	1.5×10^{-5}	1.5×10^{-5}
279.88	369.6	280.23	254.01	253.12	372.46	254.02	282.97
298.69	375.38	295.43	277.2	275.2	374.63	278.1	294.67
No AE recorded	48	48	48	45	50	47	48
	Heated Treated						
Figure 5-3	Figure 5-6			Figure 5-7a		Figure 5-7b	

23	**24**	**25**	**26**	**27**	**28**	**29**	**30**
18/11/97	21/11/97	23/11/97	25/11/97	26/01/98	27/01/98	02/02/98	03/02/98
Darley Dale	Darley Dale	Darley Dale	Bentheim	Darley Dale	Darley Dale	Bentheim	Darley Dale
40	40	40	40	200	75	75	100
20	20	20	20	0	0	0	0
1.5×10^{-5}	1.5×10^{-5}	1.5×10^{-5}	1.5×10^{-5}	1.5×10^{-5}	1.5×10^{-5}	1.5×10^{-5}	1.5×10^{-5}
281.15	280.32	282.96	252.03	282.51	282.28	253.67	280.04
299.54	298.45	294.44	273.05	298.23	296.54	297.312	299.37
42	44	46	45	38	38	38	38
Figure 5-3		Figure 5-8a	Figure 5-8b	Figure 6-1	Figure 6-1		Figure 6-1
Figure 6-4		Figure 6-5		Figure 6-2	Figure 6-2		Figure 6-2
Figure 6-5		Figure 6-6b		Figure 6-3	Figure 6-3		Figure 6-3
Figure 6-7		Figure 6-9			Figure 6-5		Figure 6-5
Figure 6-8		Figure 7-1					
Figure 6-9		Figure 10-2					

31	**32**	**33**	**34**	**35**	**36**	**37**	**38**
09/02/98	16/02/98	25/03/98	22/06/98	24/06/98	19/08/98	23/08/98	24/08/98
Icelandic	Darley Dale	Darley Dale	Darley Dale	Darley Dale	Darley Dale	Darley Dale	Darley Dale
75	95	20	100	60	100	80	20
0	20	0	25	30	50	40	10
1.5×10^{-5}	1.5×10^{-5}	1.5×10^{-5}	1.5×10^{-5}	1.5×10^{-5}	1.5×10^{-5}	1.5×10^{-5}	1.5×10^{-5}
365.89	281.67	282.19	281.79	280.99	282.84	281.57	282.13
370.02	295.22	279.75	297.46	294.23	296.95	296.05	293.02
38	38	50	55	40	40	47	45
Figure 5-5		Figure 6-1		Figure 6-4	Figure 6-4	Figure 6-4	Figure 6-4
		Figure 6-2		Figure 6-5	Figure 6-5	Figure 6-5	Figure 6-5
		Figure 6-3		Figure 6-7	Figure 6-7	Figure 6-7	Figure 6-7
		Figure 7-1		Figure 6-8	Figure 6-8	Figure 6-8	Figure 6-8
				Figure 6-9	Figure 6-9	Figure 6-9	Figure 6-9

39	**40**	**41**	**42**	**43**	**44**	**45**	**46**
22/09/98	25/09/98	07/10/98	12/10/98	15/10/98	28/10/98	05/11/98	06/11/98
Darley Dale	Darley Dale	Darley Dale	Darley Dale	Darley Dale	Darley Dale	Darley Dale	Darley Dale
50	40	40	40	40	80	20	60
30	20	20	20	20	20	10	30
1.5×10^{-5}	1.5×10^{-5}	1.5×10^{-5}	1.5×10^{-4}	1.5×10^{-6}	1.5×10^{-5}	1.5×10^{-5}	1.5×10^{-5}
280.49	282.71	282.13	287.89	282.13	280.97	282.55	282.13
298.63	297.01	298.71	295.38	296.92	294.14	296.89	295.46
40	41	41	43	45	45	45	45
		Streaming Potentials					
	Figure 9-8	Figure 6-6a	Figure 8-1	Figure 8-1		Figure 6-5	Figure 6-5
	Figure 10-3	Figure 6-10	Figure 8-2	Figure 8-2		Figure 6-9	Figure 6-9
	Figure 10-7	Figure 6-11	Figure 8-3	Figure 8-3			
	Figure 10-10	Figure 7-2	Figure 8-4	Figure 8-4			
	Figure 10-11	Figure 8-1, 8-2	Figure 8-5	Figure 8-5			
	Figure 10-12	Figure 8-3, 8-4					
	Figure 10-13	Figure 8-4, 8-5					
		Figure 9-1, 9-2					
		Figure 9-4, 9-5					
		Figure 9-6, 9-7					
		Figure 9-8					

47	**48**	**49**	**50**	**51**	**52**	**53**	**54**
09/11/98	11/11/98	13/01/99	29/01/99	30/01/99	02/02/99	03/02/99	07/02/99
Darley Dale	Darley Dale	Bentheim	Darley Dale	Darley Dale	Darley Dale	Darley Dale	Darley Dale
80	100	40	40	40	40	40	40
40	50	20	20	20	20	20	20
1.5×10^{-5}	1.5×10^{-5}	1.5×10^{-5}	1.5×10^{-5}	1.5×10^{-5}	1.5×10^{-5}	1.5×10^{-5}	1.5×10^{-5}
280.49	280.1	253.79	286.4	284.64	283.45	279.48	283.9
293.44	294.78	272.33	302.02	300.24	297.37	291.35	301.85
45	45	No AE recorded	45	45	46	45	48
			3.7% NaCl	3.7% NaCl	5% NaCl	7.5% NaCl	10% NaCl
Figure 6-5	Figure 6-5	Figure 9-2		Figure 7-1	Figure 7-1	Figure 7-1	
Figure 6-9	Figure 6-9	Figure 6-3		Figure 7-3	Figure 7-2	Figure 7-3	
				Figure 7-4	Figure 7-3	Figure 7-8	
				Figure 7-5	Figure 7-8		
				Figure 7-7			
				Figure 7-8			
				Figure 7-9			
				Figure 10-1			

55	**56**	**57**	**58**	**59**	**60**	**61**	
08/02/99	09/02/99	15/02/99	19/02/99	24/02/99	27/02/99	03/03/99	
Darley Dale	Darley Dale	Darley Dale	Darley Dale	Darley Dale	Darley Dale	Darley Dale	
40	40	40	40	40	40	40	
20	20	20	20	20	20	20	
1.5×10^{-5}	1.5×10^{-5}	1.5×10^{-5}	1.5×10^{-5}	1.5×10^{-5}	1.5×10^{-7}	1.5×10^{-7}	
284.44	280.7	281.23	279.79	282.4	282.8	280.5	
299.64	297.07	299.5	295.7	295.7	297.4	296.07	
48	42	45	43	43	41	40	
10% NaCl	2% NaCl	Streaming Potential	Streaming Potential	30% NaCl			
Figure 7-1	Figure 7-1	Deionized water	3.7% NaCl	Figure 7-1			
Figure 7-3	Figure 7-3			Figure 7-3			
Figure 7-8	Figure 7-8	Figure 9-10	Figure 9-11	Figure 7-8			

Table of Streaming Potential Experiments Performed and Pressure Gradients					
No.	Date	Rock Type	File Name	Conditions	Fracture
				Cp,Pp,Po	
1	13/01/97	DDS	jan1303.dat	40,20,0	before
	13/01/97	DDS	jan1305.dat	40,20,0	after at residual stress
3	13/01/97	DDS	jan1306.dat	40,20,0	after at intial stress
4	23/06/98	DDS	jun2301.dat	100,25,0	before
5	23/06/98	DDS	jun2302.dat	100,25,0	before
6	23/06/98	DDS	jun2304.dat	100,25,0	after at residual stress
7	23/06/98	DDS	jun2305.dat	100,25,0	after at initial stress
8	23/06/98	DDS	jun2306.dat	100,30,25	after
9	23/06/98	DDS	jun2307.dat	100,25,30	after
10	24/08/98	DDS	aug2402.dat	100,10,0	before
11	24/08/98	DDS	aug2403.dat	100,20,0	before
12	24/08/98	DDS	aug2404.dat	100,30,0	before
13	24/08/98	DDS	aug2405.dat	100,40,0	before
14	24/08/98	DDS	aug2409.dat	100,10,0	after
15	24/08/98	DDS	aug2411.dat	100,30,0	after
16	24/08/98	DDS	aug2413.dat	100,20,0	after
17	24/08/98	DDS	aug2414.dat	100,30,0	after
18	24/08/98	DDS	aug2415.dat	100,40,0	after
19	06/10/98	DDS	oct0602s.dat	100,10,0	before
20	06/10/98	DDS	oct0604s.dat	100,20,0	before
21	06/10/98	DDS	oct0605s.dat	100,30,0	before
22	06/10/98	DDS	oct0607s.dat	100,40,0	before
23	06/10/98	DDS	oct0608s.dat	100,50,0	before
26	07/10/98	DDS	oct0714s.dat	50,40,0	after
27	07/10/98	DDS	oct0716s.dat	50,30,0	after
28	07/10/98	DDS	oct0717s.dat	50,20,0	after
29	15/10/98	DDS	oct1503s.dat	40,20,0	before
30	15/10/98	DDS	oct1504s.dat	40,20,0	before(increasing load)
31	25/11/98	Bentheim	nov25sp6s.dat	50,10,0	before
32	25/11/98	Bentheim	nov25sp7s.dat	50,20,0	before
33	25/11/98	Bentheim	nov25sp8s.dat	50,30,0	before
34	25/11/98	Bentheim	nov25sp9s.dat	50,40,0	before
35	01/12/98	Bentheim	dec0106s.dat	100,50,0	before
36	01/12/98	Bentheim	dec0108s.dat	100,30,0	before
37	01/12/98	Bentheim	dec0109s.dat	100,20,0	before
38	01/12/98	Bentheim	dec0110s.dat	100,10,0	before
39	02/12/98	Bentheim	dec0201s.dat	75,50,0	before
40	02/12/98	Bentheim	dec0202s.dat	75,40,0	before
41	02/12/98	Bentheim	dec0203s.dat	75,30,0	before
42	02/12/98	Bentheim	dec0204s.dat	75,20,0	before
43	02/12/98	Bentheim	dec0205s.dat	75,10,0	before
44	15/12/98	Bentheim	dec1503s.dat	50,40,0	before
45	15/12/98	Bentheim	dec1504s.dat	50,40,0	before
46	15/12/98	Bentheim	dec1505s.dat	50,30,0	before
47	15/12/98	Bentheim	dec1506s.dat	50,30,0	before
48	15/12/98	Bentheim	dec1507s.dat	50,30,0	before
49	15/12/98	Bentheim	dec1508s.dat	50,20,0	before
50	15/12/98	Bentheim	dec1509s.dat	50,20,0	before
51	15/12/98	Bentheim	dec1510s.dat	50,20,0	before
52	16/12/98	Bentheim	dec1602s.dat	50,10,0	before
53	16/12/98	Bentheim	dec1604s.dat	50,40,0	before
54	16/12/98	Bentheim	dec1605s.dat	50,30,0	before
55	16/12/98	Bentheim	dec1606s.dat	50,20,0	before
56	16/12/98	Bentheim	dec1608s.dat	50,10,0	before
57	24/02/99	DDS	Feb-24	40,20,0	varying stress levels-brine
58	15/02/99	DDS	Feb-15	40,20,0	varying stress levels
59	04/03/99	DDS	Mar-04	40,20,0	varying stress levels

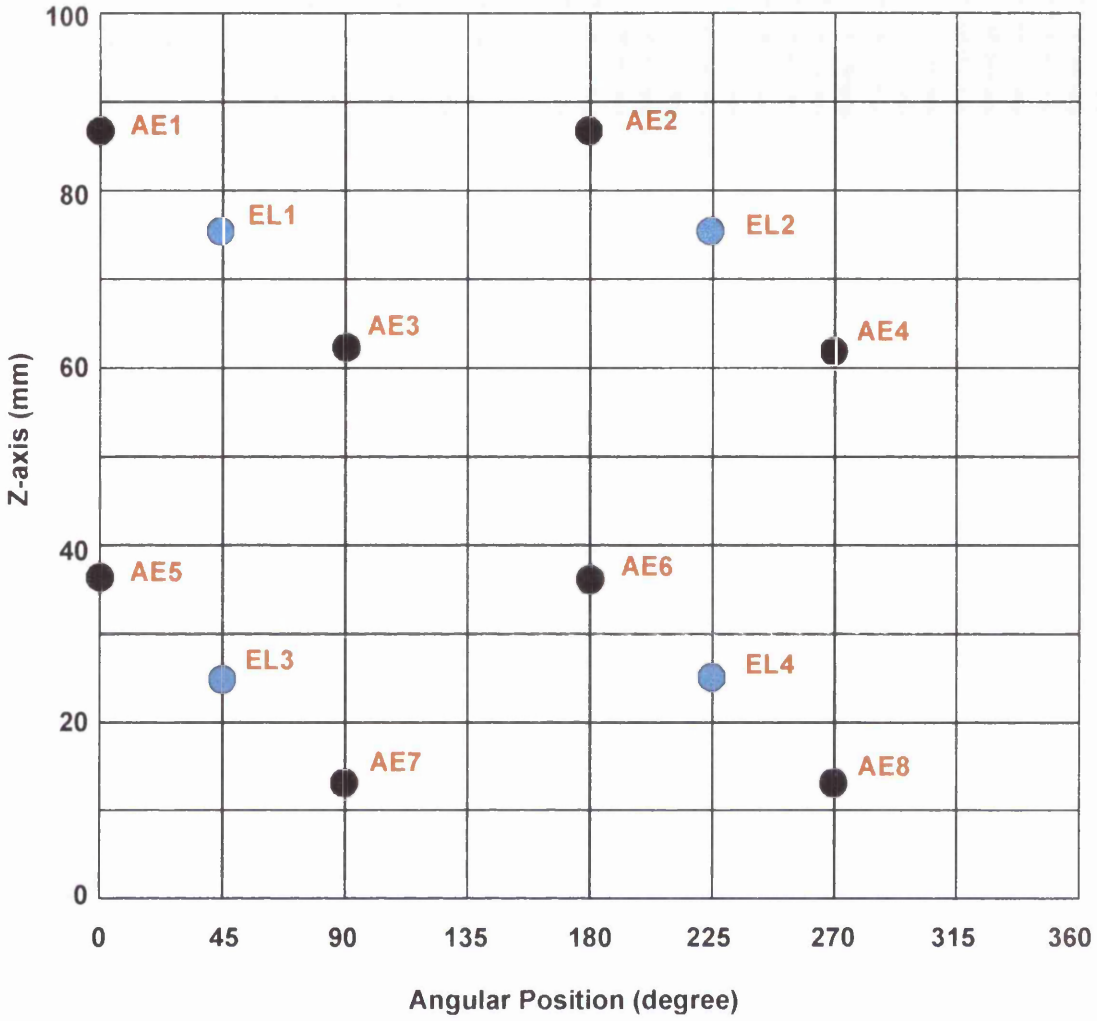

Figure C-1 Plan view of jacket with positions of AE and electrode inserts.

Appendix D - List of Symbols

ε_{ij}	Strain tensor
$\dot{\varepsilon}$	Strain rate
σ_{ij}	Stress tensor
$\dot{\sigma}$	Stress rate
σ_{ij}^{p}	Principal stress
σ_{ij}^{e}	Effective pressure
σ_N	Normal stress
$\sigma_S (\tau_s)$	Shear stress
p_f	Pore fluid pressure
μ'	Coefficient of internal friction
S_c	Cohesive strength
ϕ_f	Angle of friction
b	seismic b-value
D	Fractal dimension
ϕ	Porosity
S	Specific surface area
R	Grain radius
T_0	Uniaxial tensile strength
K_s	Bulk modulus
$q_x (Q)$	Darcy velocity
k	Hydraulic permeability
η	Pore fluid viscosity
S_I	Specific internal area
τ_h	Hydraulic tortuosity
τ_e	Electrical tortuosity
J_i	Electrical current density
E_j	Electric Field
F	Formation Factor
ρ_r	Resistivity of rock
ρ_f	Resistivity of fluid
m	Cememtation factor
a	Coefficient of saturation
D_p	Electric polarisation
ε_r	Relative permittivity
ε_p	Permittivity
d	Piezoelectric constant
C	Elastic constant
c_{ijk}	Piezoelectric modulus
p_i	Polarisation
φ	Electrical Potential
κ^{-1}	Debye length
k_b	Boltzmann's constant
T	Temperature
e	Elementary charge
ρ	Charge density
I	Electrical current
V	Streaming potential
ζ	Zeta potential
σ_f	Pore fluid conductivity
σ_B	Bulk conductivity
Σ_s	Specific surface conductance
P	Pore pressure gradient
γ	Activity coefficient